The role of phosphorus cycling in Early Earth oxygenation

Lewis James Alcott

Submitted in accordance with the requirements for the degree of Doctor of Philosophy

The University of Leeds

School of Earth and Environment

May 2020

The candidate confirms that the work submitted is his own, except where work which has formed part of jointly authored publications has been included. The contribution of the candidate and the other authors to this work has been explicitly indicated below. The candidate confirms that appropriate credit has been given within the thesis where reference has been made to the work of others.

The contents of Chapter 3 are published as:

Alcott, L. J.*, Krause, A. J.*, Hammarlund, E. U., Bjerrum, C. J., Scholz, F., Xiong, Y., Hobson, A. J., Neve, L., Mills, B. J. W., März, C., Schnetger, B., Bekker, A., Poulton, S. W. Development of Iron Speciation Reference Materials for Paleoredox Analysis, (2020)

L.J.A., A.J.K., B.J.W.M., C.M., A.B. and S.W.P collected sample material. L.J.A. and A.J.K prepared samples. L.J.A., A.J.K., E.U.H., C.J.B., F.S., Y.X., A.J.H., L.N., B.S performed geochemical analyses. All authors contributed to the manuscript. *Joint first authorship

The contents of Chapter 5 are published as:

Alcott, L. J., Mills, B. J. W. and Poulton, S. W. Stepwise Earth oxygenation is an inherent property of global biogeochemical cycling, *Science* **366**, pp.1333-1337 (2019)

L.J.A and B.J.W.M designed the research and developed the model. L.J.A performed model runs. All authors wrote the manuscript.

The contents of Chapter 6 are submitted as:

Alcott, L. J., Mills, B. J. W., Bekker, A. and Poulton, S. W. The rise of phosphorus recycling facilitated Earth's Great Oxidation Event, *Submitted*

S.W.P., L.J.A., B.J.W.M., and A.B. designed the research and collected the samples. L.J.A. and S.W.P. performed geochemical analyses and interpreted the data. L.J.A performed model runs. B.J.W.M. guided the biogeochemical modelling, and A.B. provided geological context. All authors contributed to the manuscript.

Acknowledgements

I must firstly thank my two unwavering supervisors, Benjamin Mills and Simon Poulton who without I would never have been given the opportunity to start or complete this PhD. Ben, as one of your first PhD students, I can only thank you for your openness in both offering your expertise and personal experiences in all stages of academia in addition to your unbroken positivity regardless of the quality of the work I put in front of you. Simon, since travelling with you to South Africa, I have always saved a quote that as soon as you said it, I knew it made to make it into my thesis. “I consider myself a geochemist Picasso I can appreciate art in many ways which is important for the two parts of what we’re doing, firstly the research and then writing the papers” – Simon Poulton, Nov. 2016. Your enthusiasm and encouragement have always been at the front of my mind when producing the work in this thesis. Andrey Bekker is gratefully acknowledged for his geological experience and his seemingly unlimited knowledge of Precambrian stratigraphy.

Without the help of Andy Connelly, Stephen Reid and Andy Hobson, my time in the lab would have been much more difficult and I only envy your unending tolerance that is required with the curse of knowing where everything is in the lab.

Over the course of this PhD, Alex Krause has shown the patience of a saint with my constant questioning and my more “off the wall” rather than useful ideas that accompany every coffee break. I’m sure we will look back and believe crushing the standards was “character building”. Thanks to Emma James for the much-needed lattes needed during certain periods of this PhD became very *sigh*.

Allyson Tessin, Fred Bowyer, and Martin Schobben are all thanked as oracles of wisdom both in science and life. All having our moments in the lab both early and late in the day. Countless other members of staff, postdocs and PhD students have made this thesis possible providing great feedback, much needed coffee breaks (seems to be a theme) and occasional tennis outings.

My family, who have always been supportive of my work. I only hope to inspire my nephew to do whatever he wants and be the best he can be much like our family have done for me. The Woods have supplied me with countless roast dinners, vegetarian or otherwise and have always managed to turn a Sunday from a day to dread the upcoming week to a day to stay relaxed.

Most of all, Annabelle Wood, you may not believe it but your guidance, support and patience at all stages of this PhD has made me smile each day and to always take more steps forward than back.

Abstract

Stepwise increases in oxygen abundance have been recognised as some of the most significant events throughout Earth history, but the mechanisms that drive these increases are still elusive. Atmospheric oxygen increased above 10^{-5} PAL (present atmospheric level) at approximately 2.3 Billion years ago (Ga). This rise, now termed the Great Oxidation Event (GOE), is the first of 3 canonical increases. The second is termed the Neoproterozoic Oxygenation Event (~0.8 - 0.5 Ga), and the third is termed the Palaeozoic Oxygenation Event (~0.4 Ga). Throughout the majority of the Precambrian (prior to ~0.5 Ga), the dominant redox state of the deep oceans has also been debated, with the common consensus being a ferruginous state with progressively more frequent restricted euxinic conditions on the continental shelves, which may have been better established following the GOE. Many studies have invoked changes in the input of the key limiting nutrient phosphorus as a driver of these changes, but the behaviour of phosphorus under these differing redox conditions has not been adequately explored. Through the use of biogeochemical modelling, palaeoredox proxies and phosphorus speciation, this thesis aims to shine a light on the behaviour of phosphorus throughout Earth history and its relative importance in creating a more habitable Earth for complex life. Biogeochemical models of the oxygen and phosphorus cycles have typically either considered an incomplete oxygen cycle or a simplified view of the redox dependant phosphorus cycle. A biogeochemical model was built to better constrain oxygen and the behaviour of phosphorus, and shows that stepwise changes in atmospheric oxygen may have been a consequence of the feedbacks between the carbon, oxygen and phosphorus cycles. This model is then used in conjunction with geochemical data from before the GOE (~2.6 Ga). The geochemical data show that the onset of oxidative weathering of sulfides on the continents drove euxinia and promoted phosphorus recycling from sediments to the water column. This benthic phosphorus flux would then have allowed for increased productivity and oxygenation on a planetary scale, facilitating the GOE. Other authors have begun to propose oscillatory rise of atmospheric oxygen following deglaciation of a Snowball Earth interval associated with the GOE. The use of phosphorus speciation across this interval highlights elevated phosphorus availability following deglaciation which stimulated oxygen production and resulted in the loss of MIF-S as atmospheric oxygen rose. However, the behaviour of phosphorus provided a self-limiting feedback on the rise of oxygen, as oxygenated conditions led to phosphorus sequestration and a return to predominantly anoxic conditions in the midst of the GOE.

Table of Contents

List of Tables

List of Figures

List of Equations

List of Abbreviations

O_2	Molecular Oxygen
pO_2	Partial pressure of oxygen
Fe	Iron
P	Phosphorous
H_2S	Hydrogen Sulfide
H_2	Molecular Hydrogen
Tl	Thallium
Mn	Manganese
Mo	Molybdenum
S	Sulfur
CO_2	Carbon Dioxide
Ce	Cerium
Pr	Praseodymium
Nd	Neodymium
La	Lanthanum
GOE	Great Oxidation Event
NOE	Neoproterozoic Oxygenation Event
POE	Palaeozoic Oxygenation Event
PAL	Present Atmospheric Level
Ma	Millions of years ago
Ga	Billion of years ago
kyr	Thousand years
Myr	Million years
Gyr	Billion years
MIF-S	Mass Independent Fractionation of Sulfur
C_{org}	Organic Carbon
C_{CARB}	Carbonate Carbon

(B)IF	(Banded) iron formation
Fe_{HR}	Highly reactive iron
Fe_{PRS}	Poorly reactive sheet silicate iron
Fe_{U}	Unreactive iron
Fe_{CARB}	Iron carbonate
Fe_{ox}	Iron (oxyhydr)oxide
Fe_{Mag}	Iron magnetite
Fe_{py}	Iron pyrite
Fe_{T}	Total iron
MSR	Microbial sulfate reduction
TOC	Total organic carbon
P_{Fe}	Iron bound phosphorus
P_{org}	Organic bound phosphorus
P_{aut}	Authigenic phosphorus
P_{cryst}	Highly crystalline phosphorus
P_{reac}	Reactive phosphorus
P_{mag}	Magnetite bound phosphorus

Thesis Summary

This thesis primarily concerns the abundance of free oxygen, both in the atmosphere and the ocean, throughout Earth history. Particular targets through time include the Great Oxidation Event (GOE; ~2.4 Ga; billions of years) and the Neoproterozoic Oxygenation Event (NOE; ~0.8 – 0.5 Ga). The Great Oxidation Event encompasses the first appreciable rise in atmospheric oxygen and is typically considered one of the largest disruptions to biogeochemical cycles throughout the history of the Earth. The GOE and NOE are commonly considered to be irreversible increases in oxygen availability in both the atmosphere and ocean. However recent work has contested this idea, while the drivers for these dynamic periods remain unclear. The work within this thesis uses both biogeochemical box modelling and high resolution geochemical analysis to investigate the drivers of these two oxygenation events, with a particular focus on the bio-limiting nutrient, phosphorus.

Chapter 1 provides a background to the studied intervals throughout Earth history. Chapter 2 describes the geochemical methods used throughout this thesis. Chapter 3 presents a manuscript on the description and results of the development of an international reference material for iron speciation (paper in revision). Chapter 4 presents the background and development of a biogeochemical model used throughout this thesis. Chapter 5 presents a modelling study suggesting that the oxygenation 'steps' described in the rock record can be driven by simple feedbacks within the carbon, oxygen and phosphorus cycles (published). Chapter 6 presents high resolution geochemistry prior to the GOE which demonstrates a key role for phosphorus recycling in the lead up to the event (submitted). Chapter 7 expands this geochemical study into the GOE and examines the nutrient response to intermittent oxygenation.

Chapter 1 Introduction

1.1 Precambrian Earth History

This chapter provides a summary of the evolution of the Earth and an overview of major geochemical transitions. A summary of these major events is surmised in Figure 1.1. Three canonical rises in atmosphere and ocean oxygen concentrations at ~2.3 Ga, ~0.6 Ga and ~0.4 Ga (Lyons et al., 2014b) are typically associated with snowball Earth glaciations, global redox and tectonic or biological revolutions (Lyons et al., 2014b).

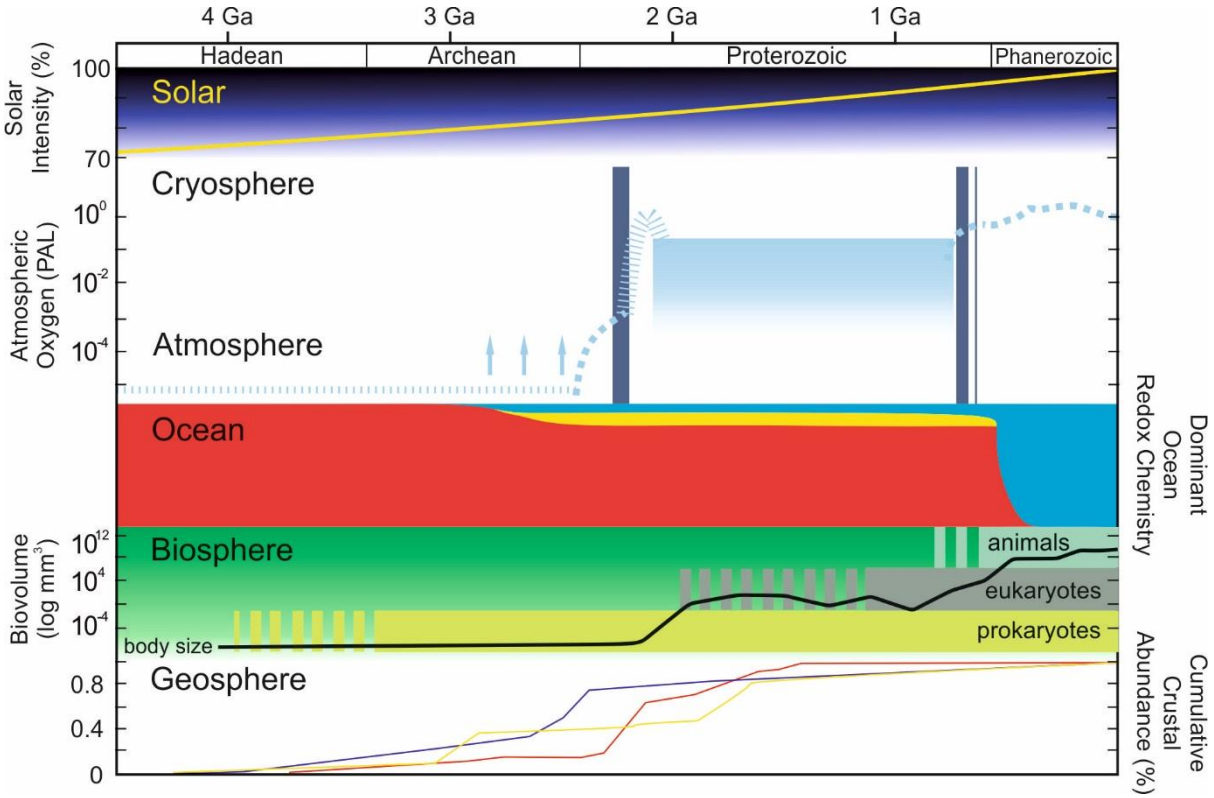

Figure 1.1. *Schematic evolution of the Earth System over geologic time, adapted from Lyons et al. (2014b); Poulton (2017); Crockford et al. (2019). Solar output relative to present levels calculated from Gough (1981). Atmospheric oxygen presented relative to Present Atmospheric Level (PAL). Overlaying that are the intervals of global glaciations. Predominant ocean redox state; red – ferruginous; yellow – euxinic; blue – oxic. The relative changes in the biosphere including onset of prokaryotes, eukaryotes and animals, dashed bars indicate uncertain origin. Example crustal abundance estimates from Jacobson (1988) (red), Ying et al. (2011) (green) and Taylor and McLennan (1985) (blue).*

1.1.1 The Hadean and Archean (4.5 – 2.5 Ga)

1.1.1.1 Evolution of a habitable Earth

The Earth is approximately 4.5 billion years old. The geological timescale begins with the Hadean Eon, in which the Earth was impacted by another large body, leading to the formation of the moon (Zahnle et al., 2007). The initially extremely hot surface would have eventually cooled and condensed, ultimately leaving a reducing atmosphere rich in CO_2 (Zahnle et al., 2007). It is not known whether the surface remained at higher temperatures (~70°C) suitable for extremophiles (Schwartzman, 2015) or cooled to more reasonably habitable or even freezing conditions (Sleep, 2010).

The transition from the Hadean to the Archean is not explicitly defined, with the dates between 4.0 – 3.8 Ga commonly cited. The rock record expands dramatically within the Archean in contrast to the Hadean, with Archean rocks being found on all continents except Antarctica. The original area of exposed continent during the Archean however continues to be debated (Cawood et al., 2013). The timing of the onset of modern-style plate tectonics is also still heavily debated with a general convergence of between 3 – 2.5 Ga (Cawood et al., 2018), but with the oldest estimates being 4.2 Ga (Maruyama et al., 2018).

The apparent lack of evidence for widespread glaciations throughout the majority of the Archean, in contrast to other periods in the Precambrian, suggests relatively temperate conditions. This is at odds with the fainter Sun earlier in time, leading to what is traditionally known as the faint young Sun paradox (Sagan and Mullen, 1972; Kasting, 1987; Feulner, 2012). The progressive rise in solar intensity as illustrated in Figure 1.1 is based upon the gradual increase in the abundance of He as opposed to the more primary H within the Sun leading to greater energy reactions (Sagan and Mullen, 1972). Under a present day atmospheric composition, the average surface temperature of the Earth would have been below freezing until 2 Ga (Condie, 2011) so a mechanism to allow for liquid water, as shown by several lines of evidence including the presence of aqueously deposited sedimentary successions, is required. Elevated levels of greenhouse gases have been proposed as a solution (Pavlov et al., 2000; Sagan and Mullen, 1972), however other mechanisms have been considered,

such as a lower planetary surface albedo due to the lack of exposed continents and clouds (Rosing et al., 2010).

Ferruginous ocean conditions (anoxic and rich is dissolved iron) are interpreted based on the presence of banded iron formations (Cloud, 1973), a limited sulfide mineral abundance, iron and sulfur systematics (Poulton and Canfield, 2011) and highly variable iron isotopes through dissimilatory iron reduction and partial oxidation of a dissolved iron pool (Rouxel et al., 2005).

1.1.1.2 First signs of Life

During these early stages in the history of the Earth, life became recognisable within the rock record. Metasedimentary rocks from Canada provide the first evidence at approximately 4.0 billion years based on negative carbon isotopes thought to have been formed biologically (Tashiro et al., 2017) in addition to the oldest recognisable life, stromatolites (macroscopic layers produced by microbial communities (Nutman et al. 2016). However, dates as early as ~4.3 Ga from fossil evidence (Dodd et al., 2017) and absolute maximums of 4.5 Ga (Betts et al., 2018) suggested based on molecular clock estimates. Molecular clocks utilise biomolecular data in order to estimate the timing of the origins of organisms through time, assuming a near constant rate of mutation and divergence over time and among different organisms (Ho, 2008). The earliest recognisable metabolisms were anaerobic, utilising more available chemical species such as H_2 and Fe^{2+} through anoxygenic phototrophy (Canfield, 2006). The remainder of the Archean provides more substantial evidence for life, including microbial mats at around 3.5 Ga, and more extensive stromatolite forms and comparative reef structures in the Mesoarchean (Nisbet and Fowler, 1999).

1.1.2 The Great Oxidation (2.5 – 1.8 Ga)

Prior to ~2.5 Ga, oxygen would have been considered a trace gas in the atmosphere-ocean system with estimates of 10^{-12} PAL (Kasting et al., 1979). Only when approaching the Archean-Palaeoproterozoic transition, do brief pulses of oxygen (“whiffs”) begin to emerge (e.g. Anbar et al. (2007)) (Figure 1.1). These “whiffs” of oxygen have been identified by sedimentary enrichments in redox sensitive trace metals such as rhenium and molybdenum, which are thought to have increased in concentration due to the onset of oxidative weathering of sulfide minerals as well as

being more efficiently buried in euxinic water column settings (anoxic with free H_2S) (Anbar et al., 2007). Euxinic conditions develop during "whiffs" as sulfate is supplied by oxidative weathering. This sulfate allowed for an intensification of microbial sulfate reduction, increasing the concentration of sulfide within the water column as well as increasing pyrite concentrations in the sediment (Reinhard et al., 2009). Whilst still widely accepted, mechanisms other than increases in atmospheric oxygen have been suggested to explain these increases in sulfide, such as volcanogenic sulfur input (Olson et al., 2019). More recent work has identified "whiffs" by redox sensitive isotope systems such as thallium, as its heavier isotope (^{205}Tl) is preferentially associated with manganese oxides (Ostrander et al., 2019). Manganese oxides require a heightened oxidizing potential to form, suggesting increased oxygen concentrations, however other work has suggested that earlier Mn deposits may have been deposited via a Mn oxidizing metabolism (Johnson et al., 2013; Daye et al., 2019), questioning the usefulness of Mn enrichments to constrain oxygenated conditions. The majority of these studies have focused on strata aged ~2.5 Ga (Anbar et al., 2007; Kendall et al., 2010; Kendall et al., 2015), however "whiffs" of oxygen have been recognised in strata as old as 3 Ga (Crowe et al., 2013; Eickmann et al., 2018).

The following 'Great Oxidation Event' (GOE) (Holland, 2002; Bekker et al., 2004) is the first of the three canonical rises in atmospheric oxygen (Figure 1.1; Lyons et al. (2014b)) and is commonly associated with four snowball Earth events (Evans et al., 1997; Kopp et al., 2005; Rasmussen et al., 2013).

1.1.2.1 Palaeoproterozoic Snowball Earth

The initiation of these snowball events is thought to have been related to the increased atmospheric oxygen concentration oxidizing the more abundant (relative to present) methane, reducing the greenhouse gas forcing, leading to a decrease in global temperature (Pavlov et al., 2000; Catling and Claire, 2005; Warke et al., 2020). It has been proposed that the glaciations themselves increased atmospheric oxygen concentrations by increasing the flux of nutrients during deglaciation stimulating productivity and oxygen production (Harada et al., 2015). Overall, there is a strong assumed association between the snowball Earth events and the GOE (Harada et al., 2015; Tajika and Harada, 2019).

Correlations of the snowball Earth events are often attempted via either radiometric dating of sediments overlying or underlying diamictite horizons or the presence of the MIF-S signal (e.g. Hoffman, 2013; Gumsley et al., 2017; Warke et al., 2020). Over the past few decades the correlation of strata has been heavily debated (e.g. Moore et al., 2001). Figure 1.2 offers one of the currently accepted correlations for the snowball Earth events and is primarily based on radiometric ages in addition to sedimentation patterns (Gumley et al., 2017).

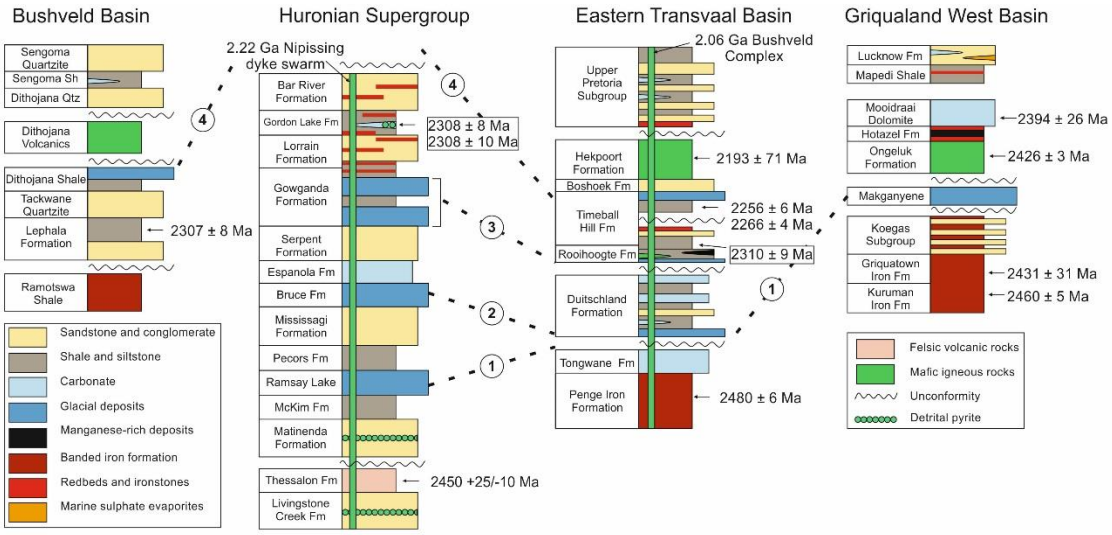

Figure 1.2. *Possible correlation of Paleoproterozoic strata from North America and southern Africa. Original figure from Rasmussen et al. (2013) with the re-interpretation of correlations from Gumsley et al. (2017).*

1.1.2.2 Defining the Great Oxidation Event

The GOE itself is commonly defined, both temporally and quantitatively by the loss of the signature of mass independent fractionation of sulfur (MIF-S; $\Delta^{33}S$) (Figure 1.3) (Farquhar, 2000; Farquhar and Wing, 2003). The definitive timing of the loss of the MIF-S signal is still debated, due to relatively poor correlation of sections across Palaeoproterozoic terraines. New work has recently shown that the initial disappearance of MIF-S occurred prior to the snowball Earth glaciations in Fennoscandia (~2.4 Ga; Warke et al., 2020) and due to regional unconformities suggests that the loss of MIF-S is broadly synchronous in globally disparate basins

including South Africa (Luo et al., 2016). The crustal memory effect must also be considered when defining the GOE, whereby there would be a delay in uplift, weathering and burial of sediments in order to fully transition to a mass dependant fractionation of sulfur (oxygenated) signal (Reinhard et al., 2013; Lyons et al., 2014b; Phillippot et al., 2018). A significant delay (100 Myr +) would however be unlikely due to the fast transfer rate between the atmosphere and the sediment (Farquhar et al., 2013; Halevy, 2013). The MIF-S signature itself is thought to be produced by the interplay between various "exit channels" (ways in which the MIF-S signature can leave the atmosphere) that must have existed in order to preserve the MIF-S value and the photolysis of sulfur species in the atmosphere at wavelengths that would be interfered with by the quantitative presence of oxygen (Halevy, 2013; Ono, 2017). More complicated mechanisms for the formation, magnitude and preservation of the MIF-S record are still being explored and developed such as the quantitative presence of organic haze formation altering the primary signal (Liu et al., 2019) or oxygenated surface waters leading to greater magnitude $\Delta^{33}S$ (Fakharaee et al., 2018). Haze formation could have diminished the photolysis of SO_2, which is the commonly invoked mechanism for initial MIF-S formation, leading to subdued $\Delta^{33}S$ earlier in the Archean, and once the haze disappeared more extreme $\Delta^{33}S$ values could be formed as seen in the rock record (Liu et al., 2019).

In addition to a more oxygenated environment influencing the MIF-S record, several other isotope systems respond throughout the late Archean and earliest Palaeoproterozoic. Carbon and sulfur isotopes have been used to identify the dominant metabolic pathways over the course of the late Archean and Palaeoproterozoic and how they have varied due to dramatic environmental redox changes (e.g. Havig et al., 2017).

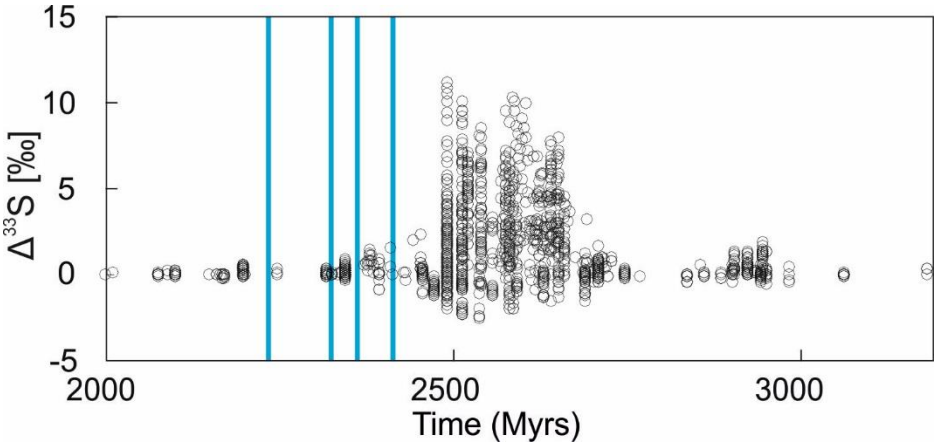

Figure 1.3. *Compilation of $\Delta^{33}S$ data (Izon et al., 2015). Glaciations overlain from Gumsley et al. (2017).*

Figure 1.4 shows the carbonate and organic $\delta^{13}C$ and sulfide $\delta^{34}S$ records from 3.5 to 1.5 Ga. These data have been used to distinguish four periods with varying metabolic drivers for the observed isotope record (Havig et al., 2017). Period 1 includes the Mesoarchean, where biogeochemical cycles became more established within the rock record, but the trends closely match the average mantle values. The f_{org} ratio obtained from the carbon isotope record in Period 1 indicates organic burial partition similar to today (0.2). The nitrogen cycle is thought to have been anaerobic, largely driven by a bioavailable ammonium pool as is consistent with the current view of Archean redox state (Stüeken et al., 2016). During period 2, all three isotope records demonstrate a buildup of oxygen concentrations. The decrease in the $\delta^{34}S$ sulfide envelope suggests an increased availability of sulfate above the limiting value for sulfate reduction (Habicht et al., 2002; Crowe et al., 2014). $\delta^{13}C_{ORG}$ in Period 2 suggests a greater role of methanogenic and methanotrophic organisms (Schidlowski et al., 1983). At the same time, periodically enriched $\delta^{15}N_{bulk}$ values suggest brief intervals of aerobic nitrogen cycling (Busigny et al., 2013; Garvin et al., 2009; Godfrey and Falkowski, 2009). This would have been facilitated by increased oxidant availability in addition to an increased flux of bio-limiting trace metals (e.g. Mo) allowing for nitrogen fixation and denitrification (Godfrey and Glass, 2011). However, it has been proposed that the dominant background state was still anaerobic nitrogen cycling (Mettam et al., 2019). Period 3 includes the GOE itself with more negative $\delta^{34}S$ sulfide values likely produced by greater sulfate availability due to the more established oxidative weathering. The widespread deposition of sulfate minerals in the

wake of the GOE is interpreted as an increase in sulfate concentrations, induced by the increased weathering of continental sulfides, and is based on large fractionations of $\delta^{34}S$ across the GOE (Havig et al., 2017; Habicht et al., 2002). These fractionations are thought to have been driven by MSR operating under non-limiting sulfate conditions (Habicht et al., 2002; Canfield et al., 2010; Farquhar et al., 2013). Also included within this the interval is the Lomagundi-Jatuli event with elevated $\delta^{13}C_{ORG}$ which suggests a greater proportion of fixed carbon within the sediment. The onset of the aerobic nitrogen cycle is proposed to have occurred at ~2.31 Ga as the nitrogen cycle variability becomes muted and moves towards zero as an expression of increased influence of diazotrophy (Stüeken et al., 2017). Period 4 highlights the relatively stability as envisioned for the remainder of the Mesoproterozoic with $\delta^{34}S$ sulfide values around zero. This return to higher values has been proposed to be related to preferential subduction of pyrite and removal of ^{34}S depleted sulfur from the Earth's surface (Canfield, 2005).

Several other independent lines of evidence exist for a rise in atmospheric oxygen at the GOE (Figure 1.5). Reduced detrital minerals are frequently found prior to the GOE within fluvial placers suggesting a lack of an oxidizing atmosphere (Rasmussen and Buick, 1999).

The loss of detrital pyrite and uraninite therefore provides an atmospheric O_2 threshold of 0.05 PAL (Johnson et al., 2014; Daines et al., 2017) for complete dissolution of 100μm^3 pyrite grain within 20,000 years (Anbar et al., 2007).

The emergence of red beds also occurs at the GOE transition, their formation associated with oxidizing conditions becoming more prevalent in continental settings, allowing ferric oxides (insoluble) to be preserved (hence the red colouration) as opposed to Fe^{2+} (soluble) (Eriksson and Cheney, 1992). The formation of these oxidized iron minerals is also linked to the preferential preservation of the earliest paleosols in the Palaeoproterozoic, and has been thought to suggest pO_2 concentrations >0.01 PAL (Rye and Holland, 1998).

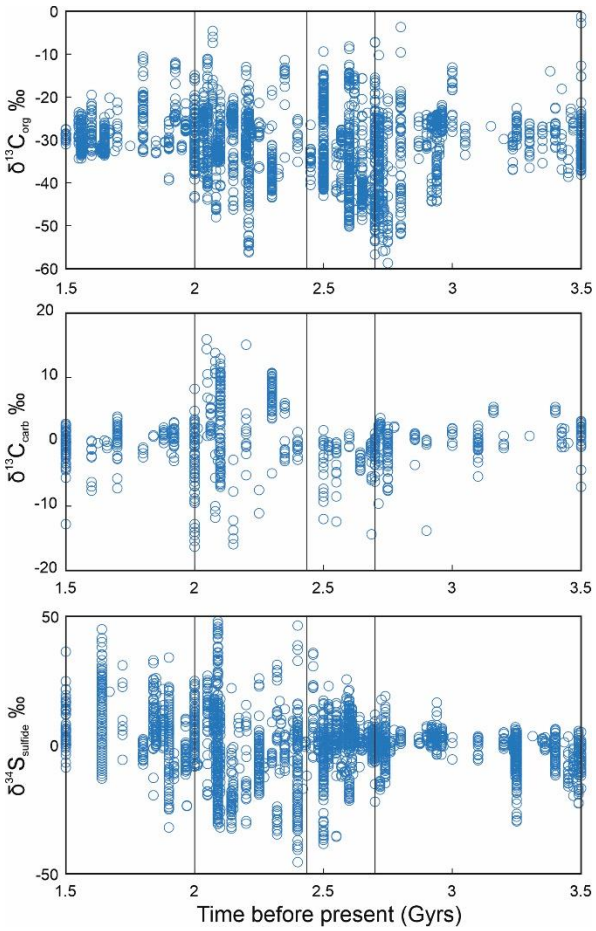

***Figure 1.4**. Compilation of $\delta^{13}C_{ORG}$, $\delta^{13}C_{CARB}$ and sulfide $\delta^{34}S$ records between 3.5 and 1.5 Ga (Adapted from Havig et al., 2017).*

1.1.2.1 Drivers for the GOE

Commonly invoked drivers for the GOE are defined by either changes in the sources or sinks of oxygen. Increases in the source of oxygen to the atmosphere-ocean system are often associated with increases in primary production and organic carbon burial (Des Marais et al., 1992; Melezhik et al., 2005). Several mechanisms have been hypothesised for the required increased nutrient delivery and by extension availability and primary production including; increased subaerial landmass (Bindeman et al., 2018), more acidic conditions associated with the wholesale production of sulfuric acid on the continents due to sulfide oxidation promoting nutrient release (Bekker and Holland, 2012) and an increase in the nutrient inventory of the continents (Cox et al., 2018).

Molecular clock estimates pose potential dates for the origin of oxygenic photosynthesis as early as 3.6 Ga (Garcia-Picel et al., 2019) whilst the earliest evidence for environmental oxygenation points towards a date of ~3.0 Ga (Buick, 2008; Crowe et al., 2013). These earlier periods of evolution pose the ongoing question of, 'if oxygenic photosynthesis evolved significantly prior to the GOE, then what caused the delay?' (e.g. Fischer (2008); Planavsky et al. (2014a)). This had led some research groups to propose the evolution of oxygenic photosynthesis to be coincident with (or at least immediately prior to) the GOE (e.g. Kopp et al. (2005)).

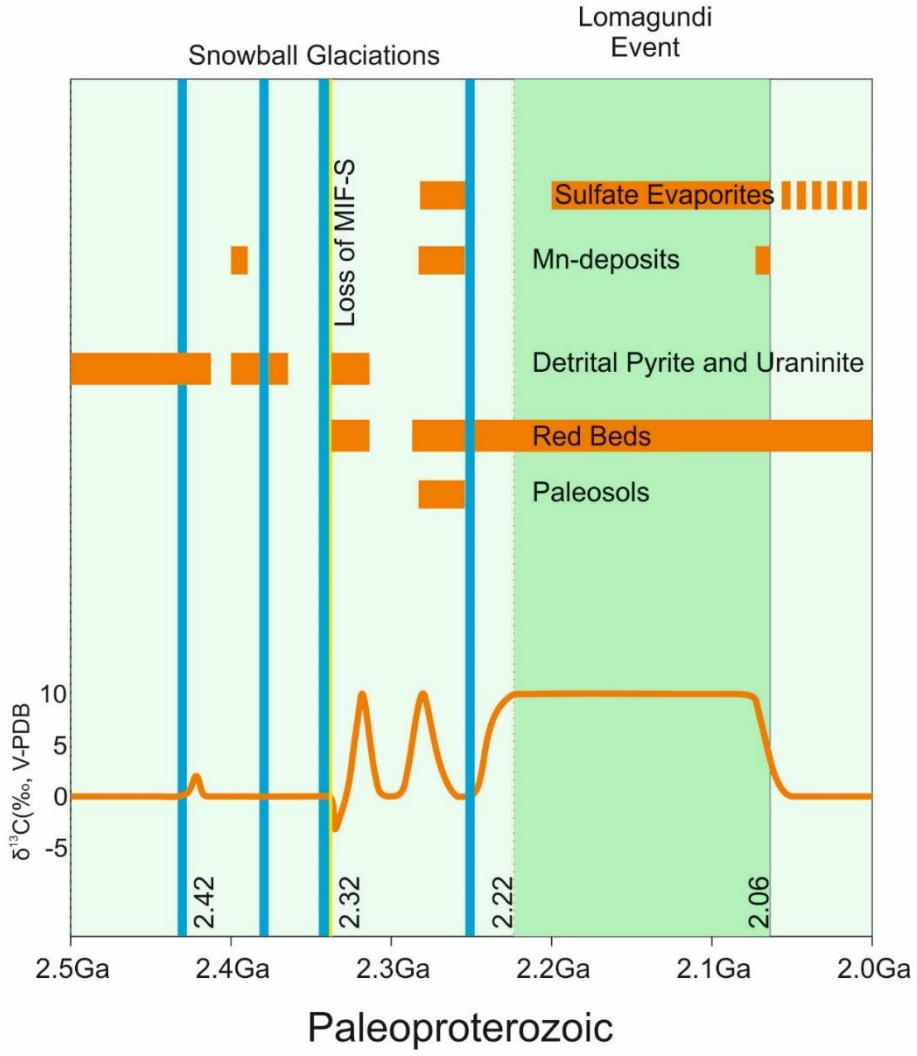

Figure 1.5. *Secular carbonate carbon isotope trend throughout the GOE and redox indicators for oxidations state of atmosphere –ocean system, adapted from Bekker and Holland (2012) and Bekker (2015). Blue vertical bars mark Palaeoproterozoic glacial events from Gumsley et al. (2017). Key dates; 2.42 Ga – End of Makganyene glaciation. 2.32 – Loss of MIF-S signature. Dashed record post GOE in marine sulfate evaporates to indicate that they became rare again during the later Palaeoproterozoic. Detrital pyrite and uraninite constraints defined by Johnson et al. (2014) and Bekker (2015). Red bed dates defined by Bekker (2015). Oxygenated paleosol interval defined by Bekker (2015) and Gumsley et al. (2017).*

Abiotic drivers postulated to have initiated the onset of the GOE focus on a decrease in the consumption of oxygen with reducing substances, the progressive escape of H_2 to space (e.g. Zahnle et al. (2013)), changes in the Archean greenhouse (e.g. Zahnle et al. (2006)) and changes to volcanic gas emission rates and composition (e.g. Holland (2002)). In addition to these, the increased subaerial landmass thought to drive increased nutrient delivery may have led to a net sink of oxygen due to an increase in the availability of exposed reducing material (Kump and Barley, 2007).

Studies have highlighted a bistable property of atmospheric oxygen (Claire et al., 2006; Goldblatt et al., 2006). These studies suggest that two different concentrations of oxygen in the atmosphere may persist under the same background conditions, as long as an initial "push" is imposed in order to shift from one state to another. This bistability relies on the formation of an ozone layer decreasing the rate of methane oxidation promoting further oxygenation (Goldblatt et al., 2006), consistent with the similar carbon isotope record before and after the GOE (Kasting, 2006).

Photochemical models have also predicted two stable states with regards to the presence or absence of an organic haze (Zerkle et al., 2012b). The transitions between the two states are thought to have been driven by variations in the production of methane, which may have varied due to availability of organic substrates (e.g. competition with other metabolisms), nutrient availability (e.g. nickel) or loss of methane via oxidation processes such as anaerobic oxidation of methane (Zerkle et al., 2012b). The elevated methane concentrations during haze episodes have been suggested to have expedited planetary oxygenation by promoting hydrogen loss and thus oxygen liberation (Izon et al., 2017).

1.1.2.4 Lomagundi Event

The Lomagundi-Jatuli event (commonly referred to as just the Lomagundi Event) is the largest and most prolonged positive isotope excursion in Earth history and occurs between ~2.2 – 2.05 Ga (Schidlowski et al., 1976; Bekker, 2015) (Figure 1.3). $\delta^{13}C_{CARB}$ values up to +8‰ on average and maximum values of +28‰ have been recorded and the event is often considered one of the defining characteristics of the

later stages of the GOE (Bekker and Holland, 2012). These high values traditionally suggest heightened deposition of organic carbon and extensive primary productivity as the lighter isotope is preferentially taken up by organisms (Bekker and Holland, 2012). A variety of mechanisms has been suggested to sustain such a profound event, including an increased phosphate flux from the continents to promote productivity (Bekker and Holland, 2012), or the preferential release of initially carbonate material from arc volcanoes alongside deep recycling of organic carbon driving the increase in carbon isotopes without the need for a change in the fraction of organic carbon relative to carbonate carbon burial (Eguchi et al., 2019). Estimates for the associated oxygen produced with the elevated production are thought to have led to atmospheric oxygen levels of up to 12 to 22 times present atmospheric levels (Karhu and Holland, 1996).

Oxygen isotopes ($\delta^{18}O$) of sedimentary sulfate suggests a collapse in productivity following the Lomagundi excursion (Hodgkiss et al., 2019) lending to the theory of the excursion being a primary signal in addition to supporting the seemingly accepted view of an oxygen overshoot accompanying the carbon isotope trend (Bekker and Holland, 2012). This collapse accompanies an oscillatory contraction of the sulfate reservoir in the ocean, as determined by sulfur isotopes (Schröder et al., 2008; Planavsky et al., 2012; Scott et al., 2014; Ossa Ossa et al., 2018). The surplus of sulfur may have been derived from the onset and sustained oxidative weathering flux of sulfate associated with increased atmospheric oxygen.

Alongside these higher concentrations of oxygen, it is often questioned if complex life evolved further (e.g. Kipp et al., 2017), as oxygen is commonly considered within the Neoproterozoic to be the limiting factor of faunal evolution (e.g. Canfield et al., 2007). Controversial work on the Francevillian section of Gabon (~2.1 Ga) at the tail end of the Lomagundi event proposes large colonial organisms with coordinated growth (El Albani et al., 2010) in addition to the first possible evidence for motility within the rock record (El Albani et al., 2019).

1.1.3 “The Boring Billion” (1.8 – 0.8 Ga)

The period from 1800 Ma to 800 Ma is thought to have been relatively stable with regards to the Earth surface system as a whole, alongside biological evolutionary stasis (e.g. Javaux and Lepot, 2018). This stability is derived by early studies from ‘uneventful’ carbon isotope compositions (Brasier and Lindsay, 1998) in addition to relatively muted trace element trends with respect to other periods of the Proterozoic (e.g. Planavsky et al. (2014b); Robbins et al. (2016)).

The concentration of atmospheric oxygen throughout the mid-Proterozoic is still heavily debated (Figure 1.1). Various proxies have been used in an attempt to constrain both oxygen within the water column and the atmosphere. Most notably iron speciation, redox sensitive metals and a suite of isotope systems (e.g. Doyle et al. (2018); Zhang et al. (2016)). Much of this debate has circled around the Xiamaling Formation (1.4 Ga) with no apparent consensus as to whether or not the section presents a globally open or restricted succession (Diamond et al., 2018; Zhang et al., 2019). This issue is further complicated by redox proxies offering differing interpretations of either limited oxygenation ($<10^{-3}$ PAL; Diamond et al., 2018) or relatively oxygenated conditions (> 4 – 6 % PAL; Zhang et al., 2017) in contrast to the earlier Palaeoproterozoic.

Methane is often considered to have played a major role in the regulation of climate throughout the Proterozoic (e.g. Pavlov et al., 2000). However, recent work has suggested that due to the abundance of oxidants (e.g. sulfate and oxygen), the net flux of methane out of the ocean was likely minimal leading to the paradox of the faint young sun to resurface (Olson et al., 2016). Methane climate regulation is still investigated, however, to test its relative importance (e.g. Zhao et al., 2018). This has called for other mechanisms for climatic stability to be investigated, especially as global glaciations are not witnessed throughout the Mesoproterozoic.

1.1.4 The Neoproterozoic Oxygenation Event (0.8 - 0.5 Ga)

The Neoproterozoic oxygenation event is considered the second of the three stepwise increases in atmospheric oxygen throughout Earth history (Lyons et al., 2014) and is defined by a suite of geochemical signatures.

Increasing Ce anomalies develop through scavenging by Mn and Fe oxides (Bau and Koschinsky, 2009), therefore providing a link between oxygenated conditions – that are needed to form the oxide minerals – and Ce depletion with respect to neighbouring rare elements such as Pr and Nd (Lawrence et al., 2006). La is not used in this calculation due to its typical overabundance relative to other neighbouring rare earth elements (De Baar et al., 1985). In short, negative Ce anomalies may indicate greater seawater oxygenation as seen throughout the Neoproteozoic and early Palaeozoic (Wallace et al., 2017).

Sulfur isotope discrimination (sulfate $\delta^{34}S$ – sulfide $\delta^{34}S$) increased to modern values across the Precambrian – Cambrian transition. This increase is thought to reflect a rise in atmospheric oxygen to above 0.05 PAL which is necessary for the metabolisms of sulfide-oxidizing bacteria (Canfield and Teske, 1996).

Redox sensitive trace metals such as molybdenum and vanadium are also used to infer redox conditions throughout the Neoproterozoic. An increase in Mo and V sedimentary concentrations across the Precambrian - Cambrian boundary are linked to an increased reservoir of these two metals from enhanced oxidative weathering associated with higher oxygen concentrations (Scott et al., 2008; Och and Shields-Zhou, 2012).

Within these clear trend changes, higher resolution studies have now begun to show the internal complexities of the Neoproterozoic oxygenation event. Oceanic oxygenation events as seen through the lens of redox sensitive trace metals (Sahoo et al., 2012; Sahoo et al., 2016; Tostevin et al., 2019) display brief pulses of oxygenation in contrast to the background anoxic state of the Precambrian ocean. Initially reported within late Neoproterozoic successions, Cambrian oxygenation events are now beginning to be documented (He et al., 2019).

The rise of animals, and their widespread diversification and proliferation is often considered to have driven drastic environmental change (Lenton et al., 2014;

Butterfield, 2018). However, inversely, appreciable concentrations of oxygen are commonly invoked to have been a determining factor in animal evolution and expansion (Tostevin et al., 2016; Wang et al., 2018). This “chicken and egg” scenario is a continued debate (Mills et al., 2014b) with animals having the potential to lead to oxygenation and the animals themselves having an oxygen requirement.

1.2 Iron

This section of the thesis provides a summary of the key components of the iron and phosphorus cycles for the modern day and through intervals of time addressed within this thesis. As highlighted previously, iron-rich conditions dominated a large portion of Earth's history with phosphorus being considered the ultimate limiting nutrient on geological timescales. The links between these two elemental cycles are explored in greater detail in the following chapters.

1.2.1 Iron

Iron can undergo redox transformations under surface (or near-surface) conditions (Poulton and Raiswell, 2002) and is important in biogeochemical cycles as a micronutrient, of which large regions of the modern ocean are limited by today (e.g. Watson et al. (2000)). Primary supplies of iron to the ocean are via rivers, dust, hydrothermal and glacial inputs (Poulton and Raiswell, 2002; Poulton and Canfield, 2011; Anderson and Raiswell, 2004; Raiswell et al., 2006). Riverine supply is noted to be depleted by up to 90% with respect to the original river composition due to esturine uptake via flocculation or precipitation (Poulton and Raiswell, 2002). The remaining present day riverine supply is predominantly in particulate phases (1000x larger than the dissolved fraction; Poulton and Raiswell, 2002) and is dominated by iron (oxyhydr)oxides and Fe in silicate minerals (Poulton and Raiswell, 2005). Aeolian supply is commonly considered to be the major supply to the Southern Ocean (Fung et al., 2000), however other studies have suggested that icebergs and glacially derived sediments are not entirely inert and can contribute comparable quantities of bioavailable iron to the Southern Ocean (Raiswell et al., 2008).

1.2.1.1 Precambrian iron cycle

The Precambrian iron cycle would have been notably different to present day, first and foremost due to the elevated concentrations of iron within the oceans (Poulton and Canfield, 2011). (Banded) Iron Formations (IFs/ BIFs) are prominent features of the Precambrian and typically contain appreciable concentrations of iron (>15 wt%;

Simonson, 2003). These chemically precipitated sediments predominantly occur between 2.7 – 1.8 Ga (Figure 1.6; Bekker et al. 2010) but recent work has identified both earlier and later examples (e.g. Li et al. (2018)). They are generally considered to have formed from upwelled hydrothermal iron sources based on rare earth element distributions (e.g. Danielson et al. (1992)).

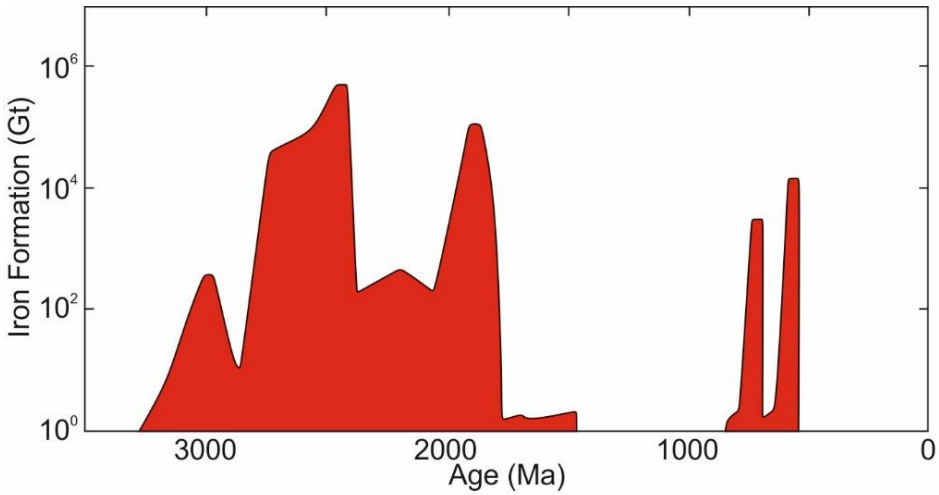

Figure 1.6. *Iron Formation tonnage over time, modified from (Chi-Fru et al., 2016)*

Iron formations typically form in one of two environments and lead to two distinctly different sedimentary facies. Banded iron formations consist of interlayered iron and silica rich layers and dominate the Archean and early Palaeoproterozoic successions, whereas granular iron formations display evidence for above storm wave base clastic deposition and start to occur at ~2.4 Ga (Bekker et al., 2010). In addition to these two facies types, a further classification can be used to differentiate IFs that are directly associated with volcanic sections (Algoma type) and those that generally lack associations with volcanic rocks and are thought to occur with large igneous province emplacement (Superior type) (Bekker et al., 2010).

Due to the chemical origin of these sediments, it is possible to infer the concentration of dissolved Fe^{2+} within the water column. For the Archean, proposed Fe concentrations range from 40 to 120 µM (Canfield, 2005; Holland, 1984) assuming equilibrium with siderite and calcite. This highlights the clear difference between the iron cycle of the Precambrian and the modern day, which has an average of ~1 – 2 nM Fe (Sarmiento and Gruber, 2006). An additional highly debated question is the original

mineral precipitated in order to form BIFs. Two prominent views are that the precursory minerals consisted of mainly oxidized iron phases (e.g. iron (oxyhydr)oxides; Robbins et al. 2019) or iron-silicate minerals (e.g. greenalite; Johnson et al. 2018). The mechanism behind Fe^{2+} oxidation within a dominantly anoxic ocean and the subsequent burial of iron (oxyhydr)oxides is currently controversial. There are three main hypothesises: photoferrotrophy or chemolithoautotrophic iron oxidation (Konhauser et al., 2002; Crowe et al., 2008), abiotic photodissociation of $FeOH^+$ (Cairns-Smith, 1978) and oxidation via oxygenic photosynthesis (Cloud, 1973; Cloud, 1965). The clarification of the precursory minerals formed within the Precambrian are of importance for adsorption potential of elements important to life such as phosphorus or arsenic.

Iron-silicate minerals however may have formed via several independent mechanisms: high concentrations of ferrous iron and silica exceeding greenalite saturation, iron oxidation in silica rich waters (although this would still call for a method of oxidation) and transformation of metastable phases such as green rust (Johnson et al., 2018). Recent hydrological constraints call for excessive oxygen concentrations and high permeability in order to form iron oxides within the sediment. These constraints suggest that primary iron (oxyhydr)oxides would had to have formed within the water column in order to have the concentrations of iron oxides preserved within IFs today (Robbins et al., 2019).

The understanding of the mid-Proterozoic ocean redox condition has developed over time. It was originally defined as fully oxygenated (Holland, 1984), and later the "Canfield Ocean" was envisaged (e.g. Canfield, 1998). The Canfield Ocean suggests extensive portions of the ocean were rich in free H_2S based on the apparent lack of BIFs post-GOE and a simple biogeochemical model utilizing estimates of both primary production and atmospheric oxygen concentrations (Canfield, 1998). The conditions would have been induced via the onset of oxidative weathering of the continents, stimulating dissolution of subaerial pyrite (previously just transferred as part of the detrital fraction to the ocean) leading to increased sulfate input into the ocean. Sulfate would have then ultimately been reduced to sulphide via microbial sulfate reduction. Further geochemical studies began to test this hypothesis, including iron speciation (Poulton et al., 2010), sulfur isotopes (Luo et al., 2015) and trace metal analyses (Scott et al., 2008; Gilleadeau et al., 2020). The conditions of the mid-

Proterozoic are now considered to be more similar to the Archean and Paleoproterozoic with elevated Fe^{2+} concentrations (Poulton et al., 2010; Poulton and Canfield, 2011; Planavsky et al., 2011). Investigations of globally sensitive proxies with long residence times (e.g. uranium isotopes) have now offered quantitative estimates of the extent of H_2S rich waters. Based on uranium isotope mass balance calculations, only up to 7% of the ocean is now thought to have presented "Canfield Ocean" conditions throughout the Mesoproterozoic (Gilleaudeau et al., 2019). This interpretation is based upon more negative $\delta^{238}U$ being prevalent in anoxic conditions due to reduced authigenic uranium accumulation (Andersen et al., 2014). However, this study provides a large error on the extent of anoxic vs. oxic conditions with values between 0 to 90% of the mid-Proterozoic ocean being oxygenated. Uranium isotopes are more typically used for discrimination between anoxic (sulfidic and non-sulfidic combined) and oxic waters as opposed to defining euxinic conditions (e.g. Andersen et al. (2014); Tissot and Dauphas, 2015).

1.3 Phosphorus

This section will highlight the behaviour of phosphorus under differing conditions in addition to exploring why phosphorus is considered to be the ultimate limiting nutrient over geological timescales.

The Phosphorus cycle

Riverine supply is the primary source of phosphorus to the ocean with smaller contributions of dust and glaciers sourced in both dissolved and particulate forms (Wallmann, 2003; Kanakidou et al., 2012). An increase in the continental P inventory through time is thought to have been associated with mantle cooling leading to changes in riverine supply (Cox et al., 2018). Laakso and Schrag (2014) suggest that in order to regulate oxygen during the Archean and Proterozoic, the flux of phosphorus to the oceans would have been greatly reduced with respect to present day. This reduced P flux would be regulated via the scavenging of phosphorus by an iron trap driven by

the greater mobility of ferrous iron in a low O_2 world. Although a reduced phosphate flux to the oceans is in accordance with their biogeochemical model, the mechanism derived by Laakso and Schrag (2014) is only theoretical and requires further investigation.

Due to the various mechanisms for phosphorus draw down and ultimate burial, the following section is separated into organic and inorganic burial.

Organic phosphorus burial

A key flux of P to the sediment is phosphorus associated with organic matter (P_{org}) (Froelich et al., 1982). Phytoplankton biomass forms in the uppermost surface ocean with a ratio of carbon to phosphorus of around 106:1 (Redfield, 1958), this ratio, in addition to the ratio of N:P of ~16:1 is coined the Redfield ratio (Redfield, 1958). The Redfield ratio is often quoted and used assuming no deviations from it, however this is not the case. Depending on the organism considered in addition to what environment it is living in, can lead to a wide range of primary organic matter elemental ratios (e.g. Moreno and Martiny (2018)). Environmental drivers include temperature, light and nutrient availability (Moreno and Martiny, 2018; Devries and Deutsch, 2014). Export production N:P is thought to vary between 6 – 26 with varying nitrate availability (Deutsch and Weber, 2012), with maximum ratios up to 100 (Geider and La Roche, 2002; Kuznetsov et al., 2008). These variations were most likely just as prominent on the early Earth as they are at present day. It has been hypothesised that this ratio varied predominantly based on the globally dominant physiology or redox state at the time (Planavsky, 2014). However, it is still acknowledged that despite regional variation the Redfield ratio persists to first order (Nature Geoscience Editorial, 2014; Gruber and Deutsch, 2014). The canonical Redfield ratio can be considered suitable for the work presented within this thesis, especially when factors such as latitudinal position as well as relative concentrations of nutrients are still questioned.

After being formed, organic matter sinks, where it is efficiently oxidized and respired releasing the phosphorus back to the water column (e.g. Harrison (1986)). A fraction of the organic matter escapes oxidation and is buried within the sediment. Phosphorus is then preferentially remineralized with respect to organic carbon leading

to elevated C:P ratios above 106:1 within the organic matter (Figure 1.5) (Ingall and Jahnke, 1994; Ingall et al., 1993).

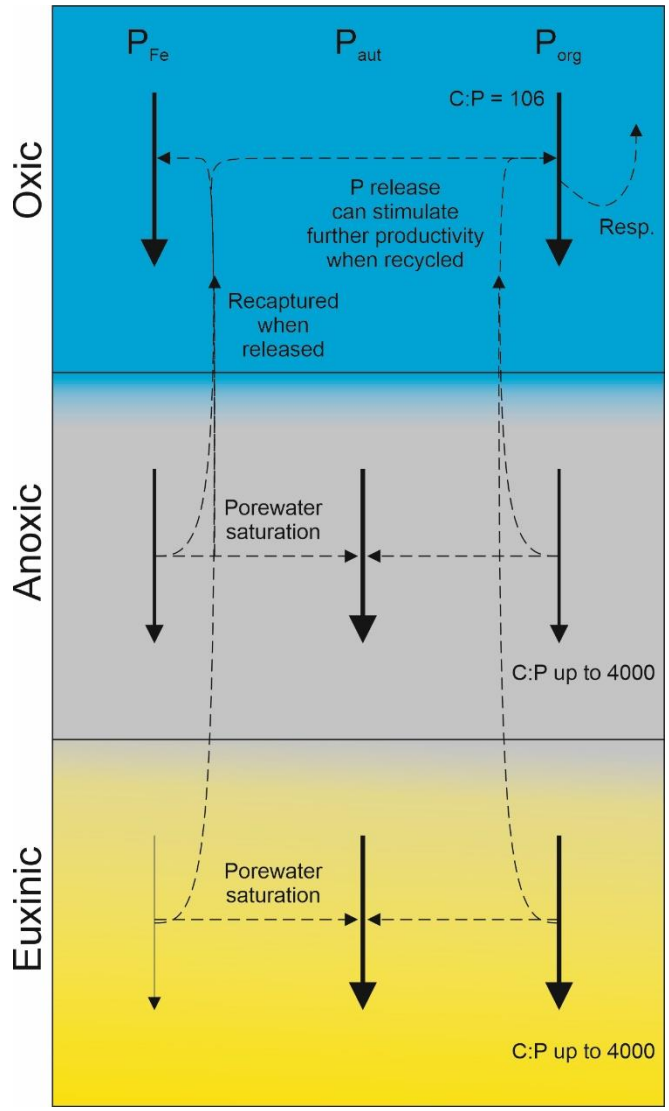

Figure 1.7. *Simplified phosphorus burial mechanisms under differing redox conditions.* P_{Fe} *– Iron bound P;* P_{org} *– Organic bound P;* P_{aut} *– Authigenic P. Solid lines denote sequestration of phosphorus. Dashed lines denote recycling or 'sink switching' of phases. Resp.-Respiration. C:P ratio is defined as the organic carbon to organic P ratio (Ingall et al., 1993).*

Several mechanisms have been proposed for this preferential remineralization associated with a variety of bacteria, including sulfate-reducing bacteria (Burnett, 1977; Arning et al., 2009). Other mechanisms include organisms such as large sulfide-oxidizing bacteria storing phosphorus under oxic conditions that, when transferred into an anoxic setting, release the stored phosphorus when under stress to the sediment pore waters in order to accommodate energy for other essential molecule storage (e.g. Gächter et al. (1988); Schulz and Schulz (2005)). This is thought to have been driven by the organisms switching to an oxygen independent metabolism and is found to be more extensive upon exposure to sulfide (Brock and Schulz-Vogt, 2011). The phosphorus that is released to the sediment pore waters then has the potential to be released back into the water column, further stimulating productivity and respiration. This positive productivity feedback is commonly invoked to explain oceanic anoxic events such as those in the Cretaceous (e.g. März et al. (2008)). This dynamic has led to the understanding that the organic C:P ratio, and thus the burial of P_{org} within the sediment, is dependent on the availability of oxygen (it is not fully known if it is dependent on the availability of other oxidants).

Inorganic phosphorus burial

Major inorganic fluxes of P to the sediment include P bound to iron minerals (P_{Fe}) and authigenic P (P_{aut}) (Figure 1.5; Ruttenberg and Berner (1993)). Phosphorus is known to be efficiently adsorbed to iron (oxyhydr)oxides (Berner et al., 1993). This iron-bound burial flux, much like P_{org}, is considered to be redox dependant (Van Cappellen and Ingall, 1994; Ingall et al., 1993; Van Cappellen and Ingall, 1996; Slomp et al., 2002; Poulton, 2017). Put simply, greater concentrations of oxygen allow for more iron (oxyhydr)oxides to form, meaning a greater quantity of phosphorus can be adsorbed and drawn down (e.g. Van Cappellen and Ingall (1994)).

In addition to traditional iron (oxyhydr)oxides, other iron minerals have recently been investigated with respect to their potential to capture phosphorus, which is important for oceans devoid of oxygen. One of these minerals includes green rust, a mixed Fe^{2+}/Fe^{3+} hydroxide, now commonly thought to be a precursor of magnetite, which efficiently adsorbs both P and Ni in modern day Archean analogues (Zegeye et al., 2012). As magnetite is often found within iron rich early Earth sedimentary

successions, it poses the question of whether green rust could have played a major role in the regulation of the phosphorus cycle under Archean-like conditions.

Once buried within the sediment, sedimentary processes may lead to reductive dissolution of the iron minerals leading to P being released to pore waters, including reaction with sulfides to form pyrite (Krom and Berner, 1980). Although reductive dissolution would be expected to lead to release of phosphorus from the sediment, it has been proposed that dissimilatory iron reduction leading to formation of other iron minerals such as vivianite can lead to effective retention of phosphorus within the sediment (Borch and Fendorf, 2007; Jilbert and Slomp, 2013; Egger et al., 2015; März et al., 2018; Xiong et al., 2019). Any pore water phosphorus can lead to saturation of P and form authigenic minerals such as calcium fluorapatite (CFA) (Ruttenberg and Berner, 1993; März et al., 2018). This transfer from one sink to another is commonly termed 'sink-switching' (Ruttenberg and Berner, 1993). Alternatively, the pore water phosphate can diffuse upwards back towards the redox interface and be re-adsorbed by other iron (oxyhydr)oxides (Slomp et al., 1996; Algeo and Ingall, 2007).

Under the majority of the modern day surface conditions, vivianite is commonly thought to form beneath the sulfate-methane transition zone (SMTZ) within the sediment (Egger et al., 2015; März et al., 2018) but can also be formed in a wide variety of settings including within the water column (Cosmidis et al., 2014). The mechanism of formation below the SMTZ relies on P becoming liberated from iron (oxyhydr)oxides due to interaction with free sulfide through dissimilatory Fe reduction, or via anaerobic oxidation of methane using Fe (oxyhydr)oxides as the electron acceptor (März et al., 2018). Within the SMTZ interval, high concentrations of P may lead to precipitation of CFA, however beneath this it has been understood that the abundance of Fe^{2+} and P within pore waters with low Ca concentrations, may lead to vivianite precipitation (e.g. März et al., 2018). It is these high iron and phosphorus concentrations and little available calcium and sulfur that allow vivanite to form in the variety of environments that it does (Rothe et al., 2016) making it a potentially important player in low sulfate systems (Xiong et al., 2019). This calls into question the relative contributions of the permanent burial phases of P over long timescales (Rothe et al., 2014; Rothe et al., 2015; Rothe et al., 2016), which can be

difficult as at present vivianite does not make a large proportion of sedimentary matrix and no sequential extraction specifically targets vivanite and it is instead extracted as part of the iron bound P fraction (Jilbert and Slomp, 2013; Xiong et al., 2019).

In the Archean, phosphorus is generally considered to be limiting due to the widespread ferruginous conditions, leading to P adsorption and drawdown associated with iron minerals (Bjerrum and Canfield, 2002). This consensus was however questioned via experiments testing the absorption potential of P to iron oxides in the presence of high concentrations of silica (proposed for the Archean oceans) (Konhauser et al., 2007). The hypothesis of limited P adsorption was later itself refuted by Jones et al. (2015) due to the lack of other sea water ions in the Konhauser et al. experimental design. The presence of these ions has a strong effect on the sorption of phosphorus by iron oxides. The formation of ternary complexes between phosphate and Ca^{2+} and Mg^{2+} surface species on the iron oxide, as well as aqueous ion pairing (which increases the non-specific adsorption of phosphorus onto negatively charged iron particles) may enhance phosphorus sorption in the presence of Ca^{2+} and Mg^{2+} so it may be these mechanisms in play within the Jones et al. study (Gao and Mucci, 2003). This debate seems to currently be resolved, the outcome being that on the early Earth, P was likely effectively adsorbed onto iron-oxides.

A restricted and minimal (relative to present) biosphere is thought to have existed throughout the mid-Proterozoic (Javaux and Lepot, 2017; Ozaki et al., 2019; Hodgskiss et al., 2019). This limitation is generally explained by the lack of bioavailable phosphorus due to either abundant ferruginous conditions scavenging phosphorus from the water column (Reinhard et al., 2017) or a diminished flux of phosphorus to the oceans (Laakso and Schrag, 2014).

1.3.2 Phosphorus vs. Nitrogen

Nitrogen is the local and short-term limiting nutrient at present day and is widely available through nitrogen fixation (diazotrophy), collecting N_2 from the atmosphere and converting it into biomass (Saltzman, 2005). At present day the dominant nitrogen sources to the biosphere are in the form of nitrite (NO_2^-) and nitrate (NO_3^-), which are formed via the recycling and oxidation of ammonium (NH_4^+)

produced by the remineralisation of diazotrophic organic matter (Casciotti, 2016). In the absence of oxygen, this recycling is diminished, but ammonium is still bioavailable to non-diazotrophic organisms (Mulholland and Lomas, 2008; Gilbert et al., 2016). In contrast, phosphorus has one primary source to the ocean in the form of riverine delivery (Froelich et al., 1982) with the open ocean surface waters being supplied by upwelling and diffusivity (Berner, 1990; Filippelli and Delaney, 1996).

Oxygen minimum zones offer a glimpse into the behaviour of nitrogen in low oxygen conditions. Nitrate can be used in denitrification or dissimilatory nitrate reduction (Granger et al., 2008) and nitrite is utilised in the anammox process (anaerobic oxidation of ammonium) (Kartal et al., 2007). These two processes lead to a loss of nitrogen from the marine reservoir, returning it to the atmosphere (Cline and Kaplan, 1975). Naafs et al. (2019) have proposed a collapse of the bioavailable nitrogen reservoir during oceanic anoxic events due to a decoupling between the various fluxes of the nitrogen cycle. Naafs et al. (2019) consider an increased phosphorus flux to the ocean, as assumed for many oceanic anoxic events, driving anoxia within a biogeochemical model framework. Under these conditions they propose that high rates of nitrification restrict the accumulation of ammonium, whilst at the same time high rates of denitrification keep the ocean nitrate inventory low (Naafs et al., 2019). This may be true for intervals of the Phanerozoic, however, for Precambrian conditions studied here, anoxia is not brought about by ample phosphorus availability and the nitrogen cycle explored further within a biogeochemical modelling framework.

The long standing question of P vs. N was potentially resolved by Tyrrell (1999) following contributions supporting both camps over several decades (e.g. Ryther and Dustan, 1971; Smith, 1984). Tyrrell (1999) utilized a two box model of the nitrogen and phosphorus cycles demonstrating the regulation of nitrate limiting surface waters (as is predominantly seen at present day) in concert with external phosphate inputs controlling long term primary production in the global ocean. At present day steady state there is a nitrogen deficit with a small population of nitrogen fixers adding nitrate to the system. An influx of nitrogen to the system would diminish the niche for nitrogen fixers, who then become outcompeted for other nutrients leading to a temporary increase in primary productivity. The new nitrogen input leads to a steady state similar to before but with the influx being offset by a smaller N_2-fixation input.

In contrast however, an additional flux of phosphate to the system would lead to an increased nitrogen deficit, leading to a greater input of nitrogen from N_2 fixers and an altogether greater steady state with elevated levels of primary production.

Geochemical studies of Proterozoic analogues and sediments have suggested adequate nitrogen availability for productivity (e.g. Michiels et al., 2017; Kipp et al., 2018). In modern ferruginous systems, the nitrogen cycle can lead to substantial quantities of nitrogen being recycled into bioavailable ammonium due to the lack of oxidants to stimulate full consumption via anammox or other mechanisms that remove nitrogen from the system (Michiels et al., 2017). As for the Neoarchean, several studies have interpreted a similar anaerobic nitrogen cycle, leading to abundant ammonium present in the anoxic ferruginous ocean (Mettam et al., 2019). A larger pool of bioavailable nitrogen may have fuelled the late Archean productivity due to a positive feedback of more primary production leading to greater subsequent release of ammonium further fuelling primary production (Mettam et al., 2019). The rise of oxygenic photosynthesis may have led to greater energy yields and elevated N_2 fixation rates, leaving a unique condition of extensive nitrogen availability (Yang et al., 2019).

Nitrogen fixation, the principle addition of nitrogen to the oceans, depends on the availability of redox sensitive trace metals, including Fe and Mo, as key components of the primary nitrogenase enzyme (Zerkle et al., 2006). As redox chemistry has evolved, so has the availability of these metals (Anbar and Knoll, 2002). The widespread ferruginous conditions of the Precambrian would not have led to Fe being the major limiting micronutrient for nitrogen fixation. However, molybdenum is efficiently removed to the sediment under euxinic conditions (Lyons et al., 2009). Prior to the GOE, due to the absence of prevalent sulfidic conditions, Mo is thought to not have been significantly taken up by sulfides (Li et al., 2019). In order to assess post-GOE and Mesoproterozoic conditions, bacterial culture studies have suggested that nitrogen fixation rates may have been impacted by Mo limitation (Zerkle et al., 2006). However, with more studies suggesting an decreasing extent of euxinia during the mid-Proterozoic, this metal limitation may not have been as prevalent as once considered (Reinhard et al., 2013).

At present day, established sulfide production and associated euxinia, requires nitrate depletion, as denitrifiers can outcompete sulfate reducers for the available organic carbon. The mid-Proterozoic offers several sections that suggest well-established euxinic wedges on productive shelf margins (e.g. Poulton et al., 2010). With this in mind, the simplest method to achieve this is to exhaust nitrate to accommodate the modern day redox ladder (Canfield and Thamdrup, 2009). This, however, leads to self-limitation as organic carbon supply would be diminished and an alternative source of fixed nitrogen is required. Boyle et al. (2013) developed a simplified upwelling margin model to demonstrate that mid-depth euxinia can be sustained when nitrogen fixation supports productivity at the surface. The result allows for a deficiency of nitrate leading to diazotrophic organisms to outcompete rivalling metabolisms allowing for sufficient fixed nitrogen for productivity. Alternatively, Boyle et al. (2013) hypothesised euxinia can persist with a sustained source of ammonium from the deep ocean as has been proposed for the Archean (Thomazo et al., 2011).

These feedbacks between euxinia and the nitrogen cycle are discussed further within Chapters 6 and 7 presenting geochemical data.

Chapter 2 Iron and Phosphorus Methods

2.1 Iron speciation

This section includes an introductory segment outlining the iron speciation technique followed by a brief description of iron behaviour under differing redox conditions. A more extensive review of iron speciation is described in Raiswell et al. (2018).

Iron speciation is used to distinguish between oxic or anoxic waters overlying sediments on the modern and ancient Earth. In addition to this, when classified as anoxic, the proxy can then aid in the discrimination between ferruginous (anoxic and Fe^{2+} rich) and euxinic (anoxic with free H_2S) conditions (Poulton and Canfield, 2011) (Figure 2.1).

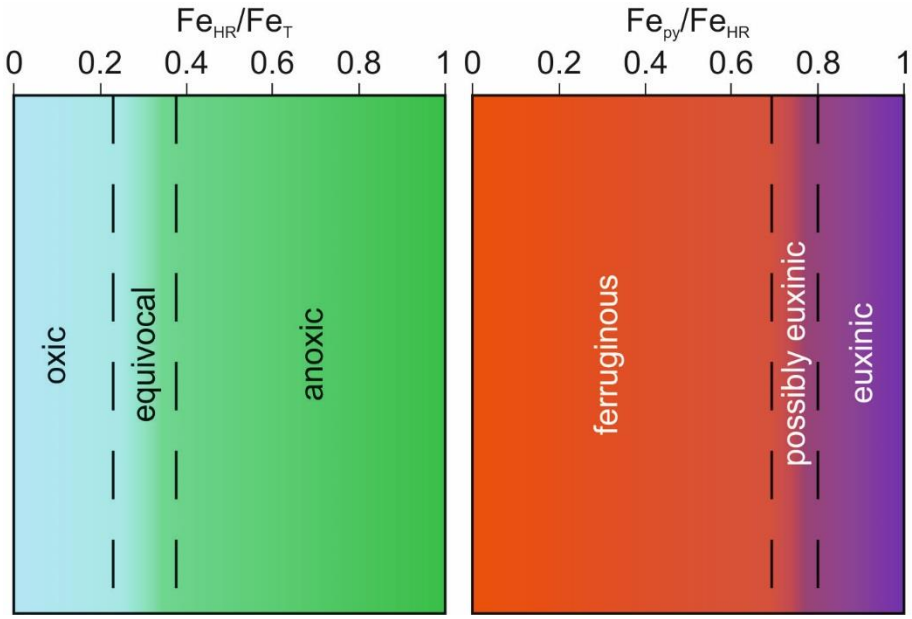

Figure 2.1. *Classification scheme used to distinguish between different redox states. Modified from Poulton and Canfield, 2011.* Fe_{HR} *– highly reactive iron;* Fe_T *– total iron;* Fe_{py} *– pyrite iron*

Iron speciation is conducted on fine grained siliciclastic sediments, most notably shales, and targets several operationally-define phases (Poulton and Canfield, 2005) including carbonate-associated iron (Fe_{carb}), ferric oxides (Fe_{ox}), mixed-valence iron oxides (principally magnetite; Fe_{mag}), and pyrite-associated Fe (Fe_{py}). The sum of these four phases determines the total fraction of highly-reactive iron (Fe_{HR}). The Fe_{HR} fractions are extracted following the protocol of Poulton and Canfield (2005) described as follows.

1) *Sodium acetate*: Samples were subjected to 10 ml of a 1 mol l^{-1} sodium acetate solution buffered with acetic acid (pH = 4.5) for 48 h, at a constant temperature of 50ºC. Carbonate-poor samples were degassed for 1 h after the addition of sodium acetate, and again after 6 h. Carbonate-rich samples were degassed 1, 2, 6 and 24 h after sodium acetate addition. This first step (Fe_{carb}) primarily targets iron associated with carbonate phases.
2) *Sodium dithionite*: The samples was then treated with 10 ml of a sodium dithionite solution (50 g l^{-1} sodium dithionite, 58.82 g l^{-1} tri-sodium citrate, 20 ml l^{-1} acetic acid) for 2 h. The sodium dithionite solution was always prepared immediately prior to use, to avoid oxidation of the solution and hence a lower extraction potential. This step (Fe_{ox}) primarily targets ferric oxide minerals.
3) *Ammonium oxalate*: The final step of the sequential iron extraction targets mixed ferric/ferrous oxides, such as magnetite (Fe_{mag}). This was achieved with 10 ml of a 0.2 mol l^{-1} ammonium oxalate/0.17 mol l^{-1} oxalic acid solution, with a treatment time of 6 h.
4) *Hot chromous chloride distillation*: This method dissolves sulphide minerals, primarily comprising acid-volatile sulphides (AVS) and pyrite (Fe_{py}; (Canfield et al., 1986)). The amount of sample required for this method depends on the amount of sulphide present to ensure a sufficient amount of Ag_2S precipitation for later quantification, and at the same time avoid supersaturation of the $AgNO_3$ solution by hydrogen sulphide released from the samples. The samples were initially treated with near-boiling 50% v/v HCl (8 ml) under a nitrogen atmosphere to test for the presence of AVS (Canfield et al., 1986). 16 ml of chromous chloride (533 g/L chromic chloride dissolved in 50% v/v HCl) was then added after determination of the presence of AVS. If AVS was present,

the $AgNO_3$ was replaced in order to separately quantify the phase. This chromous chloride solution was boiled for 1 h, also under a nitrogen atmosphere, and the released hydrogen sulphide was trapped (as Ag_2S) in a 1 mol l^{-1} $AgNO_3$ solution (with additional $AgNO_3$ added where appropriate to avoid saturation of the trap with sulphide). The Ag_2S precipitates were then filtered, dried and weighed, and the concentration of pyrite Fe was determined stoichiometrically.

Extractant solutions for the sequential extraction (steps 1-3) were analysed via atomic absorption spectroscopy. Supernatants were diluted 20 times with a calibration line created up to 10ppm Fe while ensuring a matrix match. Standard solutions of 0 and 5ppm Fe were measured every 10 samples to check for instrument drift.

Under "normal" oxygenated water column conditions, iron is oxidized from Fe^{2+} (ferrous) to insoluble Fe^{3+} (ferric), whilst anoxic conditions permit the water column transport of Fe^{2+} until precipitation is induced (Raiswell and Canfield, 1998). However, once buried, ferric iron can be reduced during early diagenesis via processes such as dissimilatory iron reduction (DIR) (e.g. Homoky et al. (2009)). This released Fe^{2+} then has the potential to be recycled within the sediment as the majority will be recaptured and re-oxidized although a fraction contributes to a benthic iron flux escaping the sediment (Raiswell and Canfield, 1998). This would lead to Fe_T/Al ratios within the range of oxic sediment (0.53 ±0.11 Raiswell et al. (2008)). Aluminium is used in an attempt to filter out enrichments of iron that are unrelated to the iron shuttle. This flux in oxygenated conditions leads to a loss of highly reactive iron to the water column leading to lower Fe_{HR}/Fe_T ratios (Fe_{HR}/Fe_T <0.22; Poulton and Canfield, (2011)). Highly reactive iron phases are determined by their reactivity towards biological and abiological reduction under anoxic conditions. The ratio is taken with respect to total iron in order to factor in the variable dilution of absolute Fe_{HR} by organic matter as well as silica or carbonate precipitation (Poulton and Canfield, 2011).

Released Fe^{2+} can be utilized in the formation of pyrite in a water column enriched in H_2S (e.g. Lyons and Severmann (2006)). The fraction of this highly reactive iron that ultimately forms pyrite can aid in the identification of euxinic water column conditions (where Fe_{py}/Fe_{HR}>0.7; free H_2S (Poulton and Canfield, 2011)),

most notably within the Black Sea but is now applied to a wide variety of depositional basins (e.g. Lyons and Severmann, 2006).

The formation of pyrite can be limited by the availability of either H_2S, highly reactive iron or organic carbon (Berner, 1970). Organic matter is utilized in microbial sulfate reduction (MSR) which reduces sulfate to form H_2S, which via several intermediary steps may lead to the formation of metastable iron monosulfides and the reaction of those phases with elemental sulfur to form pyrite (Berner, 1970).

Pyrite is also often analysed for a range of sulfur isotope measurements (e.g. Johnston (2011)). Frequently sulfur isotope measurements are not always conducted directly on pyrite grains, but instead on secondary precipitates such as Ag_2S produced via chromous chloride reduction in order to quantify iron sulfide concentrations (Canfield, 1986). In this thesis, only $\delta^{34}S_{py}$ will be investigated. During MSR, the product (sulfide) is depleted in ^{34}S relative to the sulfate source as ^{32}S contains weaker bonds and is more easily reduced (Sharp, 2017). It is this feature that allows for interpretation of the availability of sulfate for MSR and later pyrite formation as a greater negative $\delta^{34}S$ signature may suggest less sulfate limiting conditions (e.g. Luo et al., 2016).

Conditions that are both anoxic and limited in hydrogen sulfide allow for a build-up in the dissolved concentrations of ferrous (Fe^{2+}) iron in the water column. These ferruginous conditions do not effectively sequester iron as pyrite, instead the elevated concentrations of dissolved Fe^{2+} allow for the precipitation of non-sulfidized iron minerals such as siderite which augment the detrital flux of Fe_{HR} (Poulton et al., 2004). These water column redox conditions allow for elevated Fe_{HR}/Fe_T (>0.38) and low Fe_{py}/Fe_{HR} (<0.7) ratios defining ferruginous conditions (Poulton and Canfield, 2011).

Attempts have been made in order to utilize iron speciation on carbonate-rich sediments. Clarkson et al. (2014) show that the classification scheme outlined above also applies to carbonates, provided that Fe_T >0.5 wt%. This is due to diagenetic Fe addition having a greater impact on the ratios in addition to Fe_{ox} incorporation and very low lithogenic iron.

An additional feature must be considered when considering iron speciation, the transformation of non-sulfidized Fe_{HR} to poorly reactive silicate iron phases primarily clays (Fe_{PRS}). This process can take place during early diagenesis when there is insufficient free sulfide (Canfield et al., 1992; Poulton and Canfield, 2011). This transformation leads to lower Fe_{HR}/Fe_T ratios which would suggest oxic conditions when anoxic conditions may have prevailed (Doyle et al., 2018). In order to attempt to correct for this phenomena, an additional extraction can be conducted on sediments to quantify the reactive iron pool (Fe_R).

5) *Concentrated HCl*: To determine Fe_R, approximately 100 mg of powdered sample was weighed into a glass test tube. Concentrated HCl (5 ml) was added and the sample was immediately gently heated for 60 seconds to bring to the boil. The sample was then boiled more aggressively for a further 60 seconds (c.f. (Berner, 1970; Raiswell et al., 1994)). Samples were then immediately quenched with MilliQ water, transferred to 100 ml volumetric flasks and made up to volume. The difference between Fe_R and the sum of $Fe_{carb} + Fe_{ox} + Fe_{mag}$ gives Fe_{PRS}. Note however, that this extraction may also be performed sequentially after steps a – c (Table 1), which gives a direct measurement of Fe_{PRS} without the need to subtract Fe_{carb}, Fe_{ox} and Fe_{mag} (Poulton and Canfield, 2005).

This method is further explored in Chapter 3 and 7. By quantifying and comparing the Fe_{PRS}/Fe_T ratios to the ratio of the average modern day fraction, conversion to Fe_{PRS} can be determined.

It is important to understand that iron speciation is a local redox proxy in contrast to some other proxies (e.g. Uranium isotopes due to the long residence time of U; e.g. Tribovillard et al. (2006)). However, these other proxies do not clearly distinguish between oxic, ferruginous and euxinic conditions. For example Mo concentrations and isotopes are a valuable tool for determining the proportional extent of euxinia or oxygenated conditions but they depend on several assumptions such as the composition of the input and reservoirs considered in mass balance calculations (e.g. Tribovillard et al. (2006)).

2.2 Phosphorus speciation

The analytical speciation of phosphorus phases within the sediment has undergone numerous iterations and extensions to the originally envisaged extraction scheme (Benitez-Nelson, 2000). The original work of Aspila et al. (1976) determined the total and inorganic components of phosphorus, accounting the difference to organic bound phosphorus. This broad extraction scheme was later refined, defining individual P phases within the inorganic fraction. The SEDEX extraction developed by Ruttenberg (1992) allowed for the separation of the reactive inorganic phases and the unreactive detrital fraction. A total of five operationally-defined phosphorus reservoirs including exchangeable P (P_{sorb}), Fe (oxyhydr)oxide-bound P (P_{Fe}), authigenic P (P_{aut}; comprising authigenic CFA, $CaCO_3$-bound P and biogenic apatite), detrital P (P_{det}), and organic P (P_{org}). This method was then progressively developed upon, allowing for a greater number of components to fit the study's needs (e.g. fish bones and opal bound; März et al. (2014)). Following the widespread usage of SEDEX in the modern environment it was later employed to a host of palaeoenvironments. Oceanic Anoxic Events were primarily targeted most likely due to their better-defined characteristics than large swathes of Earth history (e.g. Mort et al. (2007); März et al. (2008); Kraal et al. (2010); Westermann et al. (2013)). Findings in these studies provided insight into the behaviour of phosphorus under contrasting redox conditions, however they also shined a light on some of the shortcomings of the method for ancient sediments. Ancient sediments often allow for minerals to increase in crystallinity (primarily the authigenic phase), this leads to a (possibly significant) portion of the P_{aut} phase to be extracted within the P_{det} extraction. In addition to this, the suite of environments studied also contain high iron concentrations (most notably ferruginous conditions) meaning additional steps were required in order to provide further clarity of the behaviour of phosphorus. These issues led Thompson et al. (2019) to further develop upon the SEDEX extraction scheme. As shown in Figure 2.2, the phosphorus speciation method for ancient sediments allows for the quantification of the phases defined by SEDEX but also magnetite bound P (P_{mag}) and more crystalline iron bound P (P_{Fe2}).

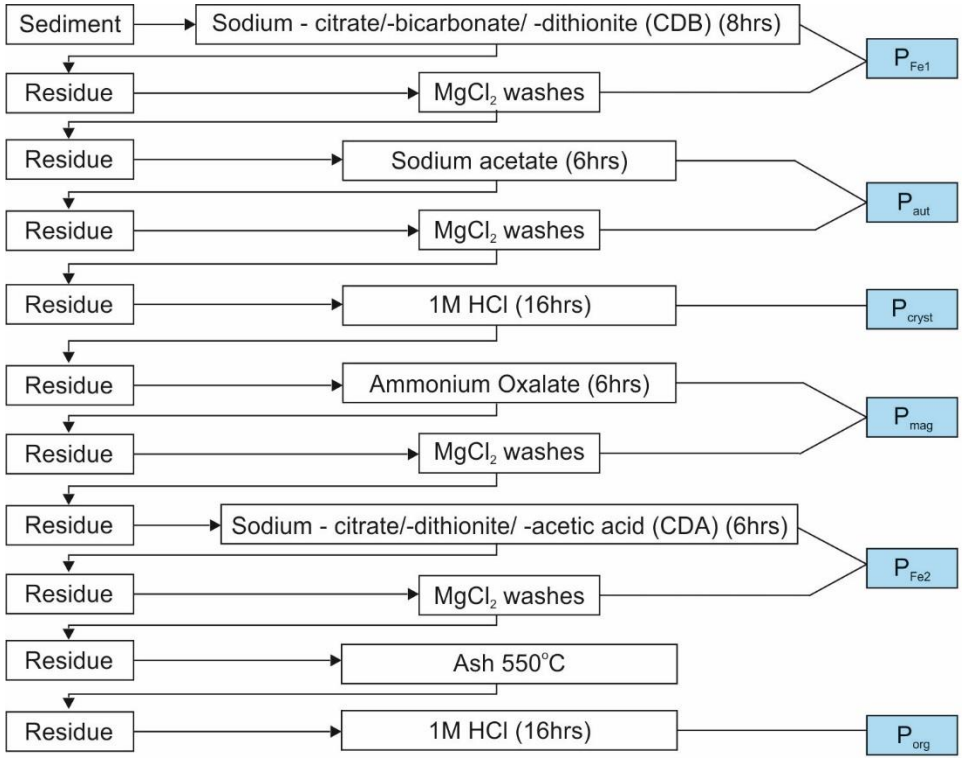

Figure 2.2. *Phosphorus sequential extraction for ancient sedimentary rocks. Modified from Thompson et al., 2019.*

During extractions the samples were constantly agitated and once complete were centrifuged for 4 minutes at 4000 rpm. Subsamples were taken after this for the appropriate analysis with the remaining supernatant being decanted to waste, similar to the method used in iron speciation.

Following the CDA extraction, residue was decanted into porcelain crucibles which were then dried and ashed for 2 hours at 550°C. Removal of the sample from the crucibles required gently scraping the walls with a spatula and decanting them back into the reactant centrifuge tubes. To ensure complete recovery of the sample, the crucibles were washed with 5 x 2 ml of 10% HCl which would make up the extractant solution for the P_{org} step.

Throughout this PhD, phosphorus concentrations for the sequential extraction were typically determined spectrophotometrically on a Spectonic GENESYS^{TM} 6 at 880 nm, using the molybdate-blue method (Strickland and Parsons, 1972; Koroleff, 1976). Molybdate blue (250 ml) was prepared using 45 ml of 10% vol/vol H_2SO_4, 31

ml of an antimony potassium tartrate solution and 62 ml of an ammonium molybdate tetrahydrate solution. The remainder of the volumetric flask was made to volume with Milli-Q. The addition of the molybdate-blue solution leads to the production of phospho-molybdate, which upon reduction produces a blue coloured complex, and it is the intensity of this blue that is measured spectrophotometrically (Benitez-Nelson, 2000). Due to the low pH of hydrochloric acid and relatively high pH of sodium acetate, a pH adjustment was required to allow for the molybdate-blue solution to develop correctly and stabilize over the time period of analysis. The ideal pH is between 1-2 (Thompson et al., 2019), this is corrected by the testing and ultimate addition of 1M sodium hydroxide (to the hydrochloric acid solutions) or 50% vol/vol sulfuric acid (to the sodium acetate solutions). This pH test is conducted for every run of phosphorus speciation to account for any differences in the molybdate-blue, hydrochloric acid or sodium acetate used. Additional issues are overcome by optimising the pH including: avoidance of interference by silica, arsenate and germanium and preventing formation of acid-labile compounds (Benitez-Nelson, 2000). A total of 1 ml of solution in cuvettes was used in analyses via spectrophotometer with 200 µl of molybdate blue added regardless of dilution. Colour development remained stable between 15 mins and 30 mins after initial molybdate-blue addition, providing the window of analysis. Calibration lines were developed based on dilution (to account for matrix difference with the addition of Milli-Q) and the maximum absorption allowed before colour saturation occurs (Up to ~1 ppm for a solution with no dilution).

The reagents in the P_{Fe} (CDB and CDA) and P_{mag} (ammonium oxalate) extractants interfere with colour development, and hence these solutions were analysed via ICP-OES. Solutions for ICP-OES analysis were made with 4.9 ml of each sample and 0.1 ml of an internal cobalt standard. Due to the preference for the CDB, CDA and ammonium oxalate solutions to precipitate over time, a weak acid solution (typically 10% hydrochloric acid vol/vol) was run in between each analysis solution as well as the introduction of an argon humidifier, to aid in preservation of the ICP-OES and stabilization of the results across the run. Quality checks were conducted every 10 samples to ensure negligible drift.

Throughout the course of the phosphorus speciation analyses conducted as part of this PhD, in-house reference materials were developed using the samples of Chapter 3.

The powdered sediment used for the extraction was between 0.15 – 0.19 g. On average, for the in-house materials, the summed sequential P extractions recovered 94% of the total P measured by bulk digest. Replicate analyses gave a RSD of ~10% for P_{aut} and P_{cryst}, in addition to P_{mag} and P_{org} both providing a RSD of <13%. These errors were collected at the University of Leeds from 7 users and 17 independent runs. P_{Fe} however is typically at very low concentrations in the ancient sediments studied here, but the RSD for such analyses is generally ~3% when P_{Fe} is present above trace concentrations (Thompson et al., 2019).

Total organic carbon concentrations were measured via the method outlined in Chapter 3. Due to the high Fe_{carb} concentrations in some of the samples studied, 50% vol/vol hydrochloric acid was used to effectively remove the inorganic carbon contents.

Total element concentrations (Fe, P, Al) were typically measured via a bulk rock digest. Here, ~50 – 80 mg of sediment was ashed (550°C overnight) and then subjected to a series of solutions. Initially 5 x 1 ml HNO_3 was added in order to transfer ashed sample to teflon beakers and aid in oxidation of organic compounds and removal of carbonate grains. Following this, 2 ml of HF was added to each sample in addition to 2 -3 drops of perchloric acid in order to ensure dissolution of silicate minerals and complete dissolution of organic material. The beakers were then heated overnight at 70°C, and once dry neutralised with 2 ml of boric acid ($50gl^{-1}$) and once again heated overnight. Samples were then brought back to solution using 5 x 1 ml 50% vol/vol HCl and gently heated on a hotplate. Ensuring all the sample is in solution, the sample was then decanted into a volumetric flask where it was made to volume with MilliQ. These solutions were then measured via ICP-OES with an Yttrium interal standard addition. Efficient elemental recovery was ensured with the use of typically 3 recognised standards (commonly either SBC-1 or SGR-1) and iron concentrations were also logged within a spreadsheet co-developed alongside this PhD in order to track any long term trends in analyses for Cohen lab users.

Chapter 3 Development of Iron Speciation Reference Materials for Paleoredox Analysis

Preface

The contents of this chapter is in minor revision for *Geostandards and Geoanalytical Research* as:

> Alcott, L. J., Krause, A. J., Hammarlund, E. U., Bjerrum, C. J., Scholz, F., Xiong, Y., Hobson, A. J., Neve, L., Mills, B. J. W., März, C., Schnetger, B., Bekker, A. and Poulton, S. W. Development of Iron Speciation Reference Materials for Paleoredox Analysis, *Geostandards and Geoanalytical Research* (in revision)

It is reproduced here in full and describes the main method used throughout this thesis to determine paleoredox conditions, iron speciation.

Abstract

The development and application of geochemical techniques to identify redox conditions in modern and ancient aquatic environments has intensified over recent years. Iron (Fe) speciation has emerged as one of the most widely used procedures to distinguish different redox regimes in both the water column and sediments, and is the main technique used to identify oxic, ferruginous (anoxic, Fe(II) containing) and euxinic (anoxic, sulphidic) water column conditions. While the Fe speciation technique has been revised over the years, some laboratories have adopted their own procedures that may differ from those of the original laboratories that developed and calibrated the method, as an international sediment standard has never been developed. This has led to concern over the consistency of results published by the many laboratories that now utilize the technique. Here, we report an interlaboratory comparison of four Fe speciation reference materials for paleoredox analysis, which span a range of compositions and reflect deposition under different redox conditions. We provide an update of the extraction techniques used in Fe speciation, and assess the effects of both sample size, and the use of different analytical procedures, on the quantification of different Fe fractions in sedimentary rocks.

Finally, we report the combined data of four independent Fe speciation laboratories to characterise the Fe speciation composition of the reference materials. These reference materials are available to the community to provide an essential validation of in-house Fe speciation measurements.

3.1 Introduction

Tracking the chemical evolution of Earth's atmosphere and oceans has long been a topic of considerable interest, with much focus on the changing state of ocean redox chemistry throughout Earth history, including its connection to the rise of atmospheric oxygen and the evolution of the biosphere (e.g., Canfield (2005)). Key to understanding Earth's past is the development and application of (bio)geochemical proxies to assess and track the redox state of the oceans. Currently used inorganic geochemical redox proxies include a variety of trace metal contents and ratios (e.g., (Brumsack, 2006; Robbins et al., 2016)), rare earth element ratios (e.g., (German and Elderfield, 1990; Planavsky et al., 2010a)), molybdenum isotopes (e.g., (Arnold et al., 2004; Asael et al., 2018), chromium isotopes (Frei et al., 2009), uranium isotopes (Weyer et al., 2008; Tissot et al., 2018), Fe/Al ratios (e.g., Lyons and Severmann 2006, Clarkson *et al.* 2014), and Fe speciation (Poulton and Canfield, 2005; Poulton and Canfield, 2011; Poulton et al., 2004; Raiswell et al., 2018).

Iron speciation is a particularly well-established and widely used paleoredox proxy for fine-grained siliciclastic sediments. We present a brief overview of its evolution here, and direct the reader to Raiswell *et al.* (2018) for a more detailed history of the proxy. Initially, the use of Fe speciation focussed on identifying controls on the formation of sedimentary pyrite (Fe_{py}), particularly the availability of reactive iron. This led to the development of the degree of pyritization (DOP) parameter (Berner 1970):

$$DOP = \frac{Fe_{py}}{Fe_{py}+HCl\ soluble\ Fe} \quad (1)$$

Subsequently, the DOP method was calibrated to distinguish aerobic, restricted and inhospitable bottom waters (Raiswell et al., 1988; Raiswell and Al-Biatty, 1989),

where Fe_{py} was determined via the chromium reduction method (Canfield *et al.* 1986), and a 1 minute boiling HCl extraction was used to define a 'reactive' Fe pool (Fe_R).

Further work on Fe minerals in modern marine sediments found that Fe-(oxyhydr)oxides are the dominant phases that react on early diagenetic timescales (Canfield, 1989), with such minerals having half-lives with respect to their sulphidization of the order of minutes to tens of days (Canfield et al., 1992; Poulton et al., 2004). However, while the boiling HCl extraction successfully extracts such minerals (Raiswell *et al*. 1994), it also extracts Fe from a variety of sheet-silicate minerals (termed Fe_{prs}; poorly reactive silicates), which are only reactive towards dissolved sulphide on a million-year timescale (Raiswell and Canfield, 1996). As a result, a sodium dithionite solution was developed (Canfield 1989, Raiswell *et al*. 1994) as a more suitable extractant of Fe (oxyhydr)oxide minerals (termed Fe_{ox}). Raiswell and Canfield (1998) then defined a 'highly reactive' Fe pool (Fe_{HR}) as the sum of Fe_{ox} and Fe_{py}.

Canfield et al. (1996) observed that enrichments in Fe_{HR}/Fe_T (normalisation to total Fe, Fe_T, is used to account for variable dilution by carbonate, organic matter or silica, as well as differences in grain size) commonly occur in sediments deposited beneath the euxinic water column of the Black Sea, due to the water column formation and settling of Fe sulphide minerals, which augments the terrestrial influx of Fe_{HR} minerals. Extensive further studies of modern and ancient marine settings demonstrated that under anoxic water column conditions, Fe_{HR}/Fe_T ratios commonly exceed 0.38, whereas values are generally below this for oxic depositional conditions (Raiswell and Canfield, 1998; Poulton and Raiswell, 2002; Canfield et al., 1996).

Under ferruginous conditions, sedimentary Fe_{HR} enrichments arise due to precipitation of non-sulphidized Fe minerals such as Fe (oxyhydr)oxides (e.g., (Ayres, 1972; Sun et al., 2015)), green rust and magnetite (Zegeye *et al*. 2012), Fe carbonates (e.g., (Klein and Beukes, 1989; Jiang and Tosca, 2019)), or potentially Fe silicates (e.g., (Rasmussen et al., 2015)). Recognising that magnetite and Fe carbonate minerals such as siderite were not extracted by existing techniques, Poulton and Canfield (2005) further refined the iron speciation methodology. This resulted in the development of a sequential extraction procedure to determine magnetite (Fe_{mag}) and iron-carbonate (Fe_{carb}) minerals, in addition to the previously identified Fe_{ox}, Fe_{py} and Fe_{prs} pools (with Fe_{HR} calculated as the sum of Fe_{carb}, Fe_{ox}, Fe_{mag} and Fe_{py}).

Based on observations from the Black Sea (Anderson and Raiswell, 2004), Poulton *et al*. (2004) developed the utility of Fe speciation further, by utilising the Fe_{py}/Fe_{HR} ratio to distinguish euxinic and ferruginous depositional conditions. In addition, noting that rapid deposition of terrigenous sediment and/or transfer of Fe_{HR} to Fe_{prs} under anoxic non-sulphidic conditions can both decrease depositional Fe_{HR}/Fe_T ratios (to potentially give a false oxic signal under anoxic depositional conditions), Poulton and Canfield (2011) revised the calibration boundaries. Thus, oxic depositional conditions are now commonly recognised by Fe_{HR}/Fe_T <0.22, ferruginous conditions are characterised by Fe_{HR}/Fe_T >0.38 and Fe_{py}/Fe_{HR} <0.7-0.8, and euxinic conditions are characterised by Fe_{HR}/Fe_T >0.38 and Fe_{py}/Fe_{HR} >0.7-0.8. When Fe_{HR}/Fe_T ratios are between 0.22-0.38, an 'equivocal' zone is recognised, where additional consideration is required to evaluate water column redox conditions. In particular, Fe_{prs} concentrations and Fe_{prs}/Fe_T ratios (Poulton *et al*. 2010, Doyle *et al*. 2019), and Fe/Al ratios (Lyons and Severmann *et al*. 2006, Clarkson *et al.* 2014) may be used to identify whether transfer of Fe_{HR} to Fe_{prs} has lowered initial depositional Fe_{HR} concentrations.

As a consequence of these developments, the iron speciation scheme of Poulton and Canfield (2005) has become widely used for evaluating paleoredox depositional conditions. However, while individual laboratories commonly use their own in-house standards as a procedural check, there is concern that discrepancies in operational procedures across different laboratories may be producing inconsistent results. Consequently, there is a clear requirement for a set of international reference materials. Here, we report the development of four reference materials for assessing ancient water column redox conditions via Fe speciation. This is based on the results of four independent laboratories, including the laboratories of the authors who developed and calibrated the Fe speciation technique that is now widely used (Poulton and Canfield 2005). We additionally present details of the methodology applied, and discuss operational issues related to the technique.

3.2 Experimental

Samples

Four marine shale samples (WHIT, KL133, KL134 and BHW) were selected to encompass a range of iron phase compositions, depositional settings and periods of Earth history. WHIT was collected from the Mulgrave Shale Member of the Whitby Mudstone Formation at Saltwick Bay, Whitby, UK (Benton and Taylor 1995, (Simms, 2004) The sample is early Jurassic (Toarcian; ~183 Ma) in age (Simms 2004), and is a fine-grained, laminated, organic carbon-rich mudstone thought to have been deposited in an anoxic water column (Kemp et al., 2005; Wignall et al., 2005). KL133 and KL134 were sampled from well-preserved drill core (borehole KL1/65) at the National Core Library, Donkerhoek, South Africa. These two Late Permian (Branch et al., 2007; Catuneanu et al., 2005) samples are from below and above the occurrence of the Upper Ecca microfloras of the Ecca and Beaufort groups (Linol et al., 2016; Chere et al., 2017). KL133 (1025 m depth in core KL1/65) is from just beneath the Upper Ecca microflora, and is comprised of grey-black silty shale (Linol et al., 2016). KL134 (104 m depth in core KL1/65) is a light-grey siltstone from above the microfloras (Linol et al., 2016).

While there is ongoing debate as to the absolute ages of the Ecca and Beaufort groups, the two samples were deposited at ~265 Ma (e.g., (McKay et al., 2015; Linol et al., 2016; Belica et al., 2017)). BHW is a partially silicified, dolomitic black shale of the Archean (~2.6 Ga) Black Reef Quartzite Formation, Transvaal Supergroup. The sample was taken from well-preserved drill core (62.5 m depth in core BHW-289) stored at the National Core Library, Donkerhoek, South Africa.

Sample preparation and storage

Post collection, weathered surfaces were removed and rocks were crushed at the University of Leeds using an agate TEMA pulverising mill, to obtain powder with the consistency of flour and without any larger isolated mineral grains. Initial attempts to sieve several of the samples were found to be problematic, due to coagulation of clay minerals during the procedure, which prevented adequate sieving and altered the nature of the sieved sediment. Thus, to ensure homogeneity of each entire bulk sample, powders were well-mixed via the repetitive use of a v-splitter, before decantation into

acid-clean jars containing ~100 g of rock powder. For longer term storage, samples are preserved under a nitrogen atmosphere at a constant temperature of -20ºC to prevent any possibility of sample oxidation.

Organic carbon analyses of the carbonate-free sample

Total organic carbon (TOC) was determined at the University of Leeds after acidification of the reference materials. Samples (n = 12 for each standard) of approximately 0.5 g were initially decarbonated with 10 mL of 20% v/v HCl for one hour. This was performed in 15 ml centrifuge tubes, which were left open to allow for CO_2 degassing. After centrifugation, the supernatant was decanted, and samples were then treated with a further 10 mL of 20% v/v HCl, followed by constant shaking at room temperature for 16 hours. Following this, the supernatant was decanted, and 10 mL of MilliQ water was added to the samples and agitated for 30 minutes. The samples were then repeatedly washed with MilliQ water until the supernatant reached pH > 4. The samples were then left to dry overnight, and TOC was measured using a LECO carbon-sulphur analyser, with LECO's medium-carbon soil used as reference material. The internal standard had a recovery of 101.03% TOC and a reproducibility (RSD) of 1.60%.

Major element analyses

Major element analyses were performed at the ICBM (University of Oldenburg) and the University of Leeds via Wavelength Dispersive X-Ray Fluorescence (Table 2). At ICBM, borate glass beads were produced by fusing 0.7 g of sample with 4.2 g of $Li_2B_4O_7$ following a peroxidation procedure with 1.0 g of $(NH_4)_2NO_3$ in a platinum crucible and measured using a Panalytical Axios max spectrometer. At the University of Leeds, the glass beads were created by fusing 0.4 g of sample with 4 g of flux (66% $Li_2B_4O_7$ + 34% $LiBO_2$) and 2 drops of Lithium Iodide solution (250g l^{-1}) in a platinum crucible, and measured using a Rigaku ZSX Primus II spectrometer. Calibration including line overlap correction and matrix correction was based on international reference samples (66; ICBM, 70; University of Leeds). Trueness was checked by international and in-house reference samples not included in the calibration with an error of, < 6 rel.% for ICBM and < 3 rel % for the University of Leeds, for major elements (except elements below quantitation limit).

Precision was measured at < 1 relative % for major elements. Major elements are reported as weight %.

Iron extractions

All iron extractions were conducted under oxic conditions using Analytical Reagent grade chemicals, and each analyst performed 8 replicates of each extraction. The sequential extractions and pyrite dissolutions were performed at four independent Fe speciation laboratories, including the Cohen Laboratory at the University of Leeds (3 different analysts), the NordCEE Laboratory at the University of Southern Denmark, the Sediment and Aqueous Geochemistry Laboratory at the University of Copenhagen and the Marine Geosystems Laboratory at the GEOMAR Helmholtz Centre for Ocean Research. The broad target phases for each extraction are reported in Table 3.1.

However, it should be noted that these are operationally defined extractions, and the Fe speciation technique for paleoredox analysis is predicated on the reactivity of different Fe pools towards dissolved sulphide, rather than the quantification of specific Fe-minerals, which is a common misconception. Thus, the precise minerals extracted in each step (and the extent of their dissolution) will vary dependent on mineral crystallinity (see Raiswell *et al.* 1994) and a host of other factors, including impurities within the structure (see Poulton *et al.* 2004). However, the Fe dissolved in each extraction can be considered to comprise an iron pool of similar reactivity towards dissolved sulphide, and it is this factor that has been calibrated in the use of Fe speciation as a paleoredox indicator.

Method	Target phases	Terminology
a) Na Acetate, pH 4.5, 48 h, 50ºC	Carbonate Fe; including siderite and ankerite	Fe_{carb}
b) Dithionite, 2 h	Ferric oxides; including ferrihydrite, hematite and goethite	Fe_{ox}
c) Oxalate, 6 h	Magnetite Fe	Fe_{mag}
d) Chromous chloride	Pyrite Fe	Fe_{py}
e) Boiling concentrated HCl	Reactive Fe; poorly reactive sheet-silicate Fe	Fe_R, Fe_{prs}
f) XRF	Total Fe; unreactive silicate Fe	Fe_T, Fe_U

Table 3.1. *Summary of iron speciation methods and their target phases. An unreactive Fe fraction (Fe_U) can be calculated as the difference between Fe_T and the sum of Fe_{carb} + Fe_{ox} + Fe_{mag} + Fe_{py} + Fe_{prs}.*

The sequential iron extractions (steps a – c; Table 3.1) were performed with a standard sample size of 60 ± 10 mg (accurately weighed), but tests were also performed using a sample size of up to 100 mg. Extraction solutions were prepared at room temperature, and the extractant volume for each step was 10 ml. During extractions, samples were constantly agitated in 15 ml centrifuge tubes as occasional shaking was found to result in incomplete extraction of the Fe phases. For step (a) at 50°C, samples were shaken either on a heated shaking table, or on a standard shaking table placed in an oven. Between extraction steps samples were centrifuged prior to decanting and analysis.

a) *Sodium acetate*: Samples were subjected to 10 ml of a 1 mol l^{-1} sodium acetate solution buffered with acetic acid (pH = 4.5) for 48 h, at a constant temperature of 50ºC. Carbonate-poor samples were degassed 1 h after the addition of sodium acetate, and again after 6 h. Carbonate-rich samples were degassed 1, 2, 6 and 24 h after sodium acetate addition. This first step (Fe_{carb}) primarily targets iron associated with carbonate phases (Table 3.1).

b) *Sodium dithionite*: The sample was then treated with 10 ml of a sodium dithionite solution (50 g l^{-1} sodium dithionite, 58.82 g l^{-1} tri-sodium citrate, 20 ml l^{-1} acetic acid) for 2 h. The sodium dithionite solution was always prepared immediately prior to use, to avoid oxidation of the solution and hence a lower extraction potential. This step (Fe_{ox}) primarily targets ferric oxide minerals (Table 3.1).

c) *Ammonium oxalate*: The final step of the sequential iron extraction targets mixed ferric/ferrous oxides, such as magnetite (Fe_{mag}). This was achieved with 10 ml of a 0.2 mol l^{-1} ammonium oxalate/0.17 mol l^{-1} oxalic acid solution, with a treatment time of 6 h.

d) *Hot chromous chloride distillation*: This method dissolves sulphide minerals, primarily comprising acid-volatile sulphides (AVS) and pyrite (Fe_{py}; Canfield et al., 1986).

The amount of sample required for this method depends on the amount of sulphide present. For the WHIT standard ~0.2 g was used for the extraction, for KL133 and KL134 ~2.5 g was used, and for BHW ~1.75 g was used. These sample weights ensure a sufficient amount of Ag_2S precipitation for later quantification, and at the same time avoid supersaturation of the $AgNO_3$ solution by hydrogen sulphide released from the samples. The samples were initially treated with near-boiling 50% v/v HCl (8 ml) under a nitrogen atmosphere to test for the presence of AVS (Canfield *et al.* 1986). However, no AVS was detected in any of the samples, and thus after addition of the HCl, 16 ml of chromous chloride was added. This solution was boiled for 1 h, also under a nitrogen atmosphere, and the released hydrogen sulphide was trapped (as Ag_2S) in a 1 mol $l^{-1}AgNO_3$ solution (with additional $AgNO_3$ added where appropriate to avoid saturation of the trap with sulphide). The Ag_2S precipitates were then filtered, dried and weighed, and the concentration of pyrite Fe was determined stoichiometrically. In one of the laboratories, Zn acetate instead of $AgNO_3$ was used to trap hydrogen sulphide and the analysis was done by spectrophotometry using the Cline reagent.

e) *Concentrated HCl*: To determine Fe_R, approximately 100 mg of sample was weighed into a glass test tube. Concentrated HCl (5 ml) was added and the sample was immediately gently heated for 60 seconds to bring to the boil.

The sample was then boiled more aggressively for a further 60 seconds (c.f. Berner, 1970; Raiswell et al., 1994). Samples were then immediately quenched with MilliQ water, and transferred quantitatively to 100 ml volumetric flasks and made up to volume. The difference between Fe_R and the sum of Fe_{carb} + Fe_{ox} + Fe_{mag} gives Fe_{prs}. Note, however, that this extraction may also be performed sequentially after steps a – c (Table 3.1), which gives a direct measurement of Fe_{prs} without the need to subtract Fe_{carb}, Fe_{ox} and Fe_{mag} (Poulton and Canfield, 2005).

Analysis of Fe solutions

Three commonly used techniques were compared for the analysis of the Fe solutions from steps a – c and e. Atomic absorption spectrometry (AAS) was the primary technique used by three of the laboratories. In this case, for the sequential extraction steps a – c, the supernatant was subjected to a 20 times dilution with MilliQ water prior to analysis relative to matrix matched standards. The same procedure was used for boiling HCl extractions, but with a 5 times dilution of the initial 100 ml solution. The fourth laboratory determined dissolved Fe via inductively coupled plasma optical emission spectroscopy (ICP-OES). Here, solutions were diluted fortyfold with 1% v/v HNO_3. The dilution acid contained 10 ppm yttrium as an internal standard, which was monitored to compensate for matrix-related signal fluctuation.

Finally, we tested the utility of the ferrozine method (Stookey, 1970). Here, we used the approach of Sperling et al. (2013), whereby 100 µl of extract was added to 4 ml of solution (prepared immediately prior to analysis) containing 12 g l^{-1} HEPES buffer, 0.2 g l^{-1} ferrozine reagent, and 10 g l^{-1} hydroxylamine hydrochloride (which reduces Fe(III) to Fe(II), to allow measurement by ferrozine). At the same time, a range of matrix-matched standards were prepared. For these standards, we compared the results of using both an Fe(III) stock solution (1000 ppm $Fe(NO3)_3$ in 0.5 mol l^{-1} HNO_3) and an Fe(II) stock solution (Mohr's salt, $(NH_4)_2Fe(SO_4)_2.6H_2O$). For the Fe_{carb} and Fe_{ox} extractions, similar results were obtained using both stock Fe solutions. However, for the Fe_{mag} extraction, a precipitate formed when using the Fe(II) stock solution, and thus all of our results are reported relative to standards prepared with the Fe(III) stock solution. Sperling et al. (2013) left samples overnight to allow colour development, followed by analysis by spectrophotometer.

To further test this technique, we performed regular repeat measurements of the solutions and standards (on a Thermo Scientific Genesys 6 spectrophotmeter) for up to 16 days after preparation.

3.3 Results and Discussion

Bulk geochemical characterisation

Replicate TOC analyses (n = 12) produced average values of 2.63 ± 0.03 wt% for WHIT, 0.09 ± 0.03 wt% for KL133, 0.85 ± 0.05 wt% for KL134, and 0.29 ± 0.03 wt% for BHW. Average major element analyses are shown in Table 3.2. A high degree of reproducibility is observed for all samples, and of particular significance, Fe_T concentrations show a relatively wide range across the four reference materials, from 1.62 to 5.03 wt% (Table 2).

ID	Si (wt%)	Ti (wt%)	Al (wt%)	Fe (wt%)	Mn (wt%)	Mg (wt%)	Ca (wt%)	Na (wt%)	K (wt%)	P (wt%)
WHIT	22.74 ± 0.24	0.553 ± 0.009	11.90 ± 0.16	4.54 ± 0.02	0.019 ± 0.001	1.10 ± 0.02	1.03 ± 0.02	0.378 ± 0.009	2.65 ± 0.02	0.070 ± 0.003
KL133	31.06 ± 0.19	0.371 ± 0.007	7.81 ± 0.03	3.19 ± 0.03	0.065 ± 0.001	1.44 ± 0.04	0.970 ± 0.016	1.18 ± 0.03	3.13 ± 0.04	0.083 ± 0.002
KL134	28.49 ± 0.83	0.385 ± 0.007	8.87 ± 0.25	5.03 ± 0.07	0.087 ± 0.002	1.00 ± 0.04	0.652 ± 0.008	1.60 ± 0.08	2.66 ± 0.04	0.092 ± 0.003
BHW	32.75 ± 0.33	0.236 ± 0.009	7.48 ± 0.06	1.62 ± 0.02	0.017 ± 0.001	1.03 ± 0.03	0.100 ± 0.010	0.065 ± 0.004	6.88 ± 0.09	0.018 ± 0.003

Table 3.2. *Average (± 1σ) major element concentrations of reference materials, measured by two independent XRF laboratories.*

Comparison of iron analyses in the extraction solutions by different techniques

A comparison of iron analyses by AAS, ICP-OES and spectrophotometer is presented in Table 3.3. The RSD for each analysis is generally within ~6%, with the exception of fractions with very low Fe concentrations where, as expected, RSDs are commonly higher. Nevertheless, despite these higher RSDs, the magnitude of the measured standard deviation is relatively small for the low Fe fractions (Table 3.3), and this degree of variability has little impact in terms of quantifying Fe_{HR}/Fe_T and

Fe_{py}/Fe_{HR} ratios (see below). The RSD for AAS analyses is often higher than for the other measurement techniques, which might reflect the fact that extractions of the solutions measured by AAS were performed by multiple users across three different laboratories, whereas extractions measured by ICP-OES and spectrophotometer were performed by one user in one laboratory.

ID	**Fe_{carb} (wt%)**	**Fe_{ox} (wt%)**	**Fe_{mag} (wt%)**
WHIT			
AAS	0.581 ± 0.033 (5.7)	0.063 ± 0.010 (15.9)	0.106 ± 0.012 (11.3)
ICP-OES	0.593 ± 0.009 (1.5)	0.058 ± 0.002 (3.5)	0.081 ± 0.002 (2.5)
Spec.	0.616 ± 0.008 (1.3)	0.084 ± 0.001 (1.6)	0.106 ± 0.003 (2.8)
KL133			
AAS	0.139 ± 0.006 (4.3)	0.046 ± 0.004 (8.7)	0.169 ± 0.011 (6.5)
ICP-OES	0.139 ± 0.004 (2.9)	0.046 ± 0.002 (4.3)	0.157 ± 0.010 (6.4)
Spec.	0.145 ± 0.002 (1.4)	0.049 ± 0.001 (2.0)	0.149 ± 0.003 (2.0)
KL134			
AAS	0.711 ± 0.041 (5.8)	0.095 ± 0.010 (10.5)	0.584 ± 0.028 (4.8)
ICP-OES	0.680 ± 0.020 (2.9)	0.088 ± 0.003 (3.4)	0.532 ± 0.016 (3.0)
Spec.	0.781 ± 0.005 (0.6)	0.110 ± 0.001 (0.9)	0.538 ± 0.012 (2.2)
BHW			
AAS	0.044 ± 0.006 (13.6)	0.016 ± 0.003 (18.8)	0.024 ± 0.002 (8.3)
ICP-OES	0.044 ± 0.002 (4.5)	0.018 ± 0.003 (16.7)	0.023 ± 0.005 (21.7)
Spec.	0.045 ± 0.001 (2.2)	0.015 ± 0.001 (6.7)	0.020 ± 0.001 (5.0)

Table 3.3. *Average concentrations (±1σ) of Fe in each sequential Fe extraction, as determined by AAS, ICP-OES and spectrophotometry. Spectrophotometry data are reported after 24 h for Fe_{carb} and Fe_{ox}, and after 168 h for Fe_{mag} (see text for further details). The RSD (%) for each analysis is given in parentheses.*

In general, there is good agreement (within error) between the measurements by AAS and ICP-OES for all extracted phases (Table 3.3), highlighting that both techniques are suitable for measuring the sequential Fe solutions, despite the potential for strong matrix effects. In addition, we found that the ferrozine technique generally produced comparable results for Fe_{carb} and Fe_{ox} (Table 3.3), and this was a consistent feature across the 11 days over which these analyses were performed (Figure 3.1). However, while there is reasonable agreement between both the Fe_{mag} AAS/ICP-OES

analyses and the spectrophotometric analyses after around 7 days of ferrozine reaction (Table 3.3), after 24 h of reaction (the current standard technique is to leave solutions overnight prior to analysis) only ~60-85% of the Fe_{mag} pool was measured by spectrophotometer (Figure 3.2). This suggests that the extracted Fe may be strongly complexed by the reagents in the oxalate extraction, such that considerable time is required for the reaction with ferrozine to proceed to completion. Furthermore, the average spectrophotometric Fe_{mag} results for KL133, KL134 and BHW were always lower than the average value determined by AAS, with a distinct decrease to even lower values after ~11 days. We thus conclude that the ferrozine spectrophotometric technique is not suitable for the measurement of Fe_{mag}.

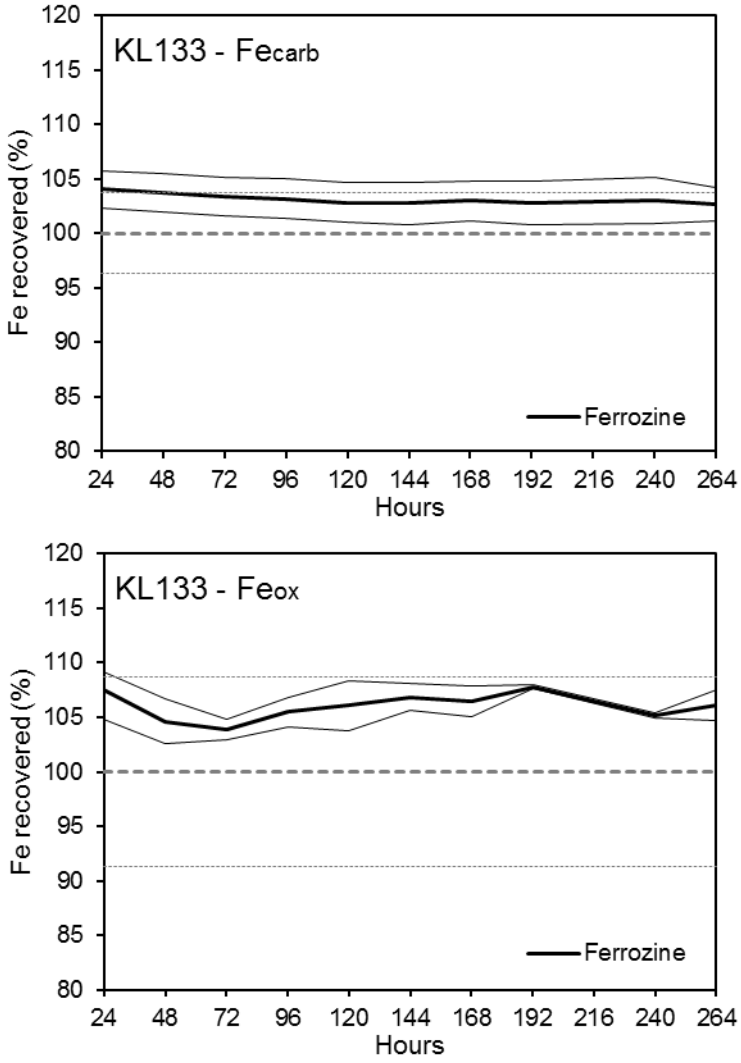

Figure 3.1. *Recovery of Fe for KL133 (solid line ±1σ) in the Fe_{carb} and Fe_{ox} fractions, as determined spectrophotometric ferrozine method, relative to the average combined value determined via AAS and ICP-OES (dashed line ±1σ).*

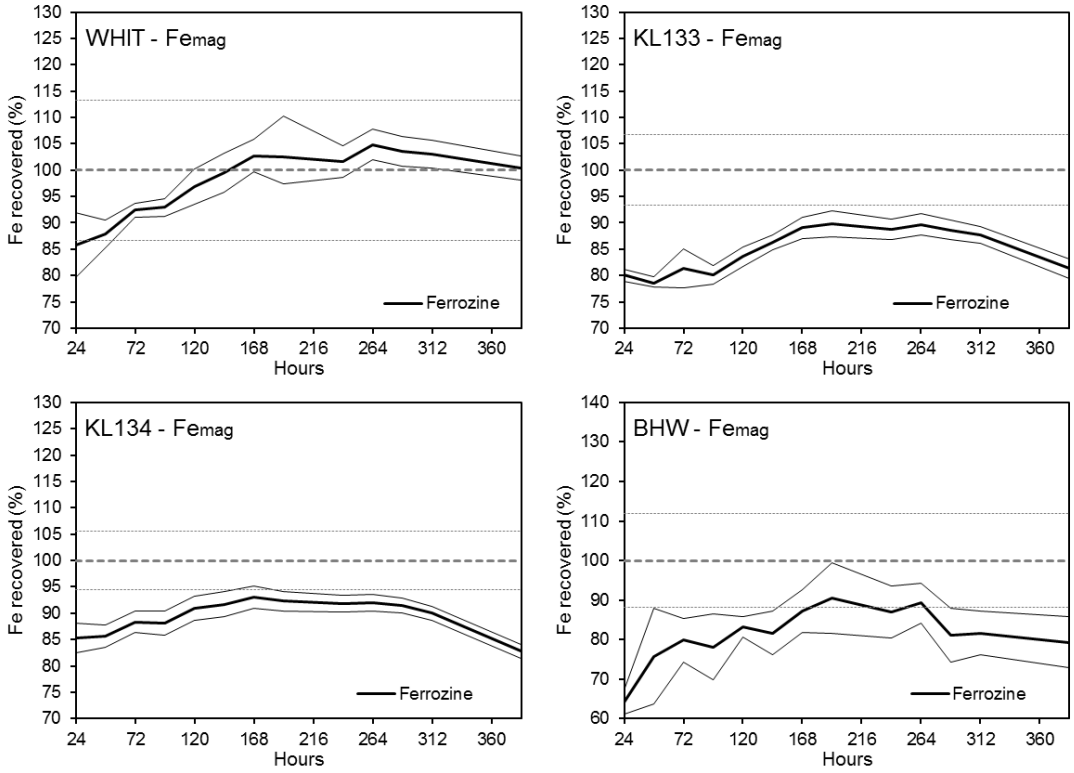

Figure 3.2. *Recovery of Fe_{mag} for the four reference materials (solid line ±1σ), as determined by the spectrophotometric ferrozine method, relative to the average combined value determined via AAS and ICP-OES (dashed line ±1σ).*

Effect of sample size on sequential extraction efficiency

During the course of our analyses, we found that the initial sample mass to extractant ratio may affect the quantity of Fe dissolved. To test this, we performed replicate extractions (n = 4 – 8) for all four reference materials using three initial sample masses: 50 mg, 70 mg, and 100 mg, with Fe analysed by ICP-OES. We found that lower contents were consistently obtained for Fe_{carb} as sample mass increased (Table 3.4). By contrast, the subsequent Fe_{ox} and Fe_{mag} extractions showed no consistent trends as sample masses increased, and thus the total amount of iron extracted during the three sequential phases decreased at higher sample masses (Table 3.4). We observed no consistent trend in the RSD of analyses over the range of sample masses used in our tests, even though in general, the relative standard deviation would be expected to increase at lower sample masses. Based on these considerations, we propose an optimal sample mass for the sequential extractions of 60 ± 10 mg for 10 ml of extractant.

ID	**Fe_{carb} (wt%)**	**Fe_{ox} (wt%)**	**Fe_{mag} (wt%)**	**Sum (wt%)**
WHIT				
50 mg	0.618 ± 0.003 (0.5)	0.056 ± 0.001 (1.8)	0.073 ± 0.001 (1.4)	0.748 ± 0.003 (0.4)
70 mg	0.593 ± 0.008 (1.3)	0.058 ± 0.002 (3.4)	0.078 ± 0.003 (3.9)	0.729 ± 0.010 (1.4)
100 mg	0.549 ± 0.008 (1.4)	0.056 ± 0.002 (3.6)	0.078 ± 0.003 (3.9)	0.683 ± 0.011 (1.6)
KL133				
50 mg	0.151 ± 0.005 (3.3)	0.048 ± 0.004 (8.3)	0.149 ± 0.001 (0.7)	0.348 ± 0.009 (2.6)
70 mg	0.137 ± 0.006 (4.4)	0.046 ± 0.002 (4.3)	0.155 ± 0.009 (5.8)	0.338 ± 0.012 (3.6)
100 mg	0.133 ± 0.005 (3.8)	0.045 ± 0.002 (4.4)	0.145 ± 0.009 (6.2)	0.323 ± 0.014 (4.3)
KL134				
50 mg	0.734 ± 0.026 (3.5)	0.091 ± 0.004 (4.4)	0.507 ± 0.012 (2.4)	1.332 ± 0.026 (2.0)
70 mg	0.689 ± 0.019 (2.8)	0.087 ± 0.003 (3.4)	0.512 ± 0.023 (4.5)	1.289 ± 0.016 (1.2)
100 mg	0.651 ± 0.009 (1.4)	0.088 ± 0.003 (3.4)	0.513 ± 0.012 (2.3)	1.251 ± 0.021 (1.7)
BHW				
50 mg	0.048 ± 0.003 (6.3)	0.018 ± 0.002 (11.1)	0.020 ± 0.002 (10.0)	0.087 ± 0.007 (8.0)
70 mg	0.044 ± 0.002 (4.5)	0.019 ± 0.003 (15.8)	0.021 ± 0.004 (19.0)	0.084 ± 0.007 (8.3)
100 mg	0.038 ± 0.001 (2.6)	0.015 ± 0.001 (6.7)	0.018 ± 0.005 (27.8)	0.071 ± 0.005 (7.0)

Table 3.4. *The effect of sample size on extraction efficiency. The sum of the three sequential extraction phases is also shown (Fe_{carb} + Fe_{ox} + Fe_{mag}). The RSD (%) for each analysis is given in parentheses.*

Development of iron speciation reference materials

We utilize the replicate extractions (as measured by AAS and ICP-OES) of the six users from four independent laboratories to determine the Fe speciation characteristics of the four reference materials (Table 3.5). Concentrations of Fe_{ox} are relatively low for all four samples, as might be expected for sediments that have experienced significant early diagenetic overprint, including dissimilatory iron reduction and pyrite formation, but the remaining Fe pools show considerable variability. In addition, average poorly reactive sheet silicate Fe concentrations (calculated as $Fe_{prs} = Fe_R - (Fe_{carb} + Fe_{ox} + Fe_{mag})$) are 0.219 wt% for WHIT, 1.399 wt% for KL133, 2.283 wt% for KL134, and 0.462 wt% for BHW. This gives Fe_{prs}/Fe_T ratios of 0.05 for WHIT, 0.44 for KL133, 0.45 for KL134, and 0.29 for BHW. The Fe_{prs}/Fe_T ratio for WHIT is low compared to the average ratio for Phanerozoic shales (0.39 ± 0.11; Raiswell et al., 2008), but the remaining samples fall close to this average.

ID	Fe_{carb} (wt%)	Fe_{ox} (wt%)	Fe_{mag} (wt%)	Fe_{py} (wt%)	Fe_R (wt%)	Fe_{HR}/Fe_T	Fe_{py}/Fe_{HR}
WHIT	0.583 ± 0.030	0.062 ± 0.009	0.103 ± 0.014	1.970 ± 0.087	0.967 ± 0.097	0.60 ± 0.02	0.73 ± 0.04
KL133	0.139 ± 0.005	0.046 ± 0.004	0.167 ± 0.011	0.011 ± 0.002	1.751 ± 0.121	0.11 ± 0.00	0.03 ± 0.01
KL134	0.705 ± 0.039	0.094 ± 0.009	0.578 ± 0.032	0.011 ± 0.002	3.660 ± 0.124	0.28 ± 0.01	0.01 ± 0.00
BHW	0.044 ± 0.005	0.017 ± 0.003	0.023 ± 0.003	0.068 ± 0.008	0.546 ± 0.077	0.09 ± 0.01	0.45 ± 0.06

Table 3.5. *Average concentrations (±1σ) of Fe in each fraction, and Fe_{HR}/Fe_T and Fe_{py}/Fe_{HR} ratios (±1σ) for each reference material.*

In Figure 3.3, we plot Fe_{HR}/Fe_T and Fe_{py}/Fe_{HR} ratios for each reference material (see Table 3.5), and we show the standard deviations that are obtained as a result of propagating the precision of measurements for each Fe pool through to the calculation of Fe speciation ratios. This demonstrates that the determination of Fe speciation ratios is highly reproducible, with the largest degree of variability occurring for the BHW Fe_{py}/Fe_{HR} ratio, which arises due to the low concentration of each Fe fraction in this sample (Table 3.5). The reference materials also document a range of redox conditions,

including oxic (KL133, BHW), equivocal (KL134) and anoxic (WHIT). Fe_{py}/Fe_{HR} ratios are only relevant as a water column redox indicator for samples that show clear evidence of deposition under anoxic water column conditions (Poulton and Canfield, 2011), and the anoxic WHIT sample plots close to the threshold for identifying euxinia. The remaining reference materials have variable Fe_{py}/Fe_{HR} ratios, which likely reflect different levels of sulphide production during diagenesis. Taken together, the variable speciation characteristics, combined with the wide range of concentrations evident across the Fe fractions, suggests that these four samples are ideal as international reference materials.

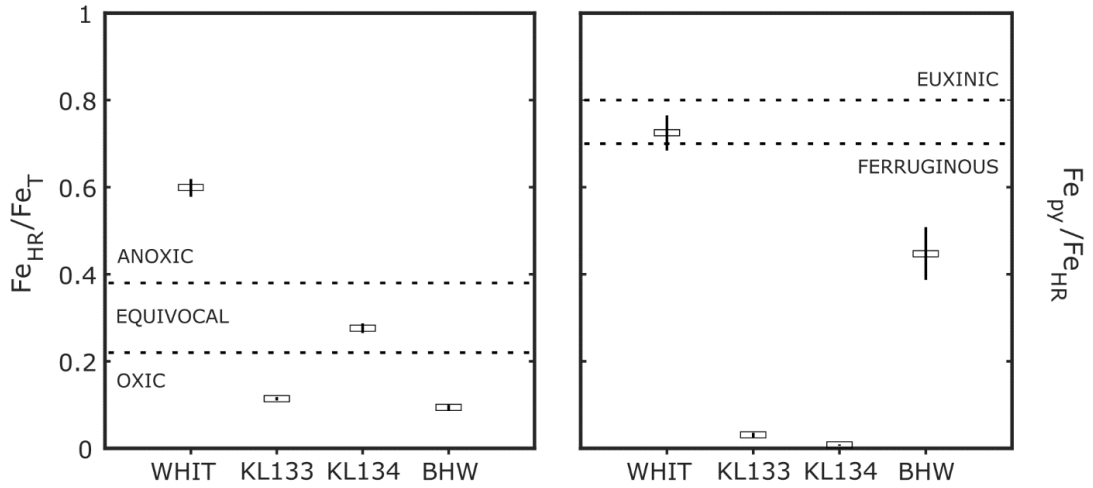

Figure 3.3. *Fe speciation characteristics of the reference materials. Error bars are calculated based on the propagation of standard deviations (1σ) determined for individual extractions.*

3.4 Conclusions

We have developed four reference materials that may be used by researchers conducting Fe speciation analyses of paleodepositional redox conditions. In the process of creating these reference materials, we have refined 'best practice' techniques for Fe speciation analyses, including detailed evaluation of the commonly employed techniques for determining Fe concentrations in extracted solutions. The amount of iron dissolved in each extraction step is sensitive to both sample agitation and sample size, and we recommend that extractions are performed on a sample size of 60 ± 10 mg for 10 ml of extractant. In addition, we recommend that the spectrophotometric determination of Fe_{mag} by ferrozine is discontinued due to the protracted completion time of the reaction.

The reference materials comprise a range of Fe fraction concentrations and document a range of depositional redox conditions. In addition, Fe concentrations and speciation ratios are generally highly reproducible, with a greater degree of uncertainty being limited to those fractions containing very low concentrations of Fe. These characteristics confirm the wide-ranging suitability of the samples as international reference materials. The samples are stored under controlled conditions, where oxygen, light and moisture are eliminated, making them suitable as long-term reference materials for the community.

4 Biogeochemical modelling

Biogeochemical box models have aided our understanding of modern and ancient Earth processes. The work from this PhD has focused on 'forwards' modelling, in which fluxes and reservoir sizes are determined by internal processes, rather than being inferred from datasets. This allows the model to test hypotheses about the drivers of system changes. I have focused on low complexity multi-box modelling which allows representation of different compartments within the ocean-atmosphere system (e.g. shelf, deep ocean, shallow open ocean) while also being capable of running for billions of years. A well-known early example of this kind of model is the 4 box atmosphere-ocean model of Sarmiento and Toggweiler (1984). This model was used to constrain atmospheric CO_2 levels in the Quaternary over glacial-interglacial timescales, by approximating primary production and thermohaline overturning.

The two seminal models of Van Cappellen and Ingall (1994) and Van Cappellen and Ingall (1996) contributed heavily to the ideas in this thesis. These models allowed for varying C:P ratios and other P burial fluxes in a simple one-box marine system, by using the geochemical data of Ingall et al. (1993) to aid in constraining the sedimentary C:P ratio depending on the dominant redox condition. Although the model treats the ocean and atmosphere as homogeneous, it demonstrates that positive feedbacks exist within the carbon, oxygen and phosphorus cycles which are capable of sustaining anoxia following an initial perturbation. For example, a pulse of weathered P into the system would cause decreasing marine oxygen concentrations due to increased respiration, leading to greater P recycling and availability, promoting primary production and further respiration, even though the continental supply of reactive P may return to normal. This idea was then taken further by their contribution in *1996*, with the inclusion of an atmospheric oxygen reservoir, leading to greater primary production increasing atmospheric oxygen concentrations, through increased organic carbon burial, therefore restricting the extent of deoxygenation through ocean-atmosphere interaction and downwelling.

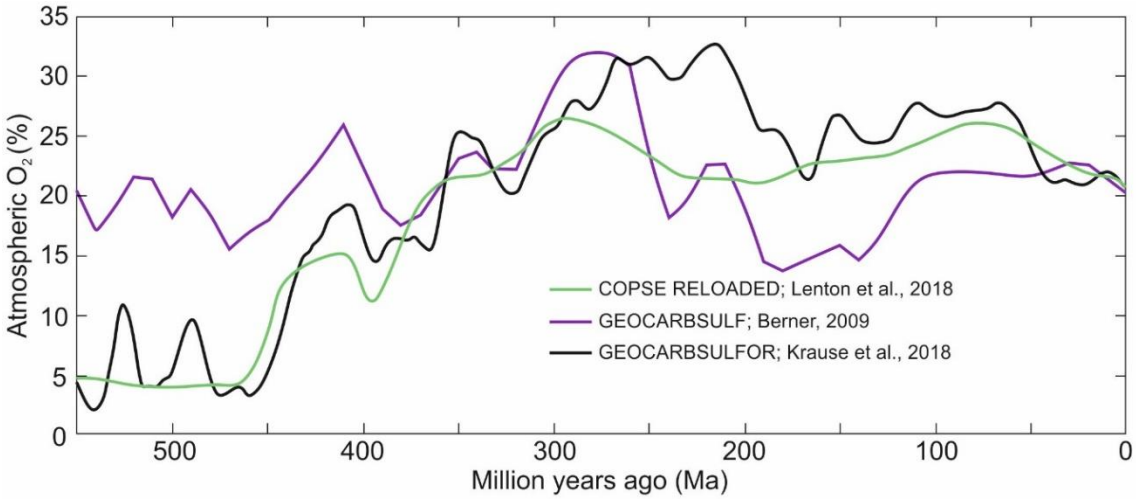

Figure 4.1. *Phanerozoic atmospheric O_2 reconstructions. Modified from Krause et al., 2018.*

Wallmann (2003) combined the three-box ocean structure of Sarmiento and Toggweiler (1984) with the phosphorus fluxes of Van Cappellen and Ingall (1994) and a simple nitrogen cycle. By applying this framework to glacial-interglacial conditions, Wallmann (2003) was able to demonstrate a change in the limiting nutrient depending on the presence of widespread glaciations. Interglacial periods would allow for efficient ocean-atmosphere interaction and weathering of nutrients into the ocean, leading to phosphate being the limiting nutrient, as opposed to nitrate under glaciated conditions. However, this model allowed for no changes in atmospheric or surface water oxygen reservoirs. This restriction means that only the deep ocean can vary with respect to oxygen concentration and the surface ocean always supplies ample oxygen via downwelling, possibly diminishing the full impact of deoxygenation.

The COPSE model (Bergman et al., 2004) employed a wider range of dependencies and fluxes in an attempt to constrain the key elemental cycles of the Phanerozoic (primarily from GEOCARB and Lenton and Watson, 2000a, b). The model, again within a one box framework, tested the theories of Phanerozoic Earth evolution. COPSE opposed the lineage of results from the GEOCARB models and initially predicted a third oxygenation event associated with the rise in land plants at around 400 Ma. This was due to increased terrestrially derived organic carbon burial, and plant-assisted weathering of phosphorus.

This model is still today widely used and has been adapted to include other elemental cycles and forcings to help match other lines of evidence throughout the rock record (e.g. Lenton et al. (2018)). This third Paleozoic oxygenation event is now supported by geochemical proxies (e.g. Dahl et al., 2010; Glasspool and Scott, 2010) and an adapted version of the GEOCARB model (Figure 4.1; Krause et al., 2018).

The work of Slomp and Van Cappellen (2007) combined a multi-box ocean with a total of four separate burial fluxes for phosphorus; organic bound P (P_{org}), iron associated P (P_{Fe}), authigenic P (P_{aut}) and fish debris (P_{bio}). Once again applied to relatively recent (Quaternary; (Slomp and Van Cappellen, 2007) and later Cretaceous conditions (Tsandev and Slomp, 2009), the model allowed for redox dependencies on all fluxes of P to the sediments based on simple relationships (See section 2.3.1 for more information). As with the Wallmann (2003) model, oxygen in the surface ocean was not allowed to vary in these models, and instead the parameter, Degree of Anoxia (*DOA*) was introduced. *DOA* was originally developed by Van Cappellen and Ingall (1994) in an attempt to constrain the percentage of sea floor that would be considered anoxic based on the oxygen concentrations of downwelling waters as well as expected oxygen utilization based on primary production.

Multi-box ocean modelling has also been employed for studies of the Precambrian. Reinhard et al. (2017) utilised the CANOPS model of Ozaki et al. (2011; 2013) (Ozaki and Tajika, 2013; Ozaki et al., 2011), proposing that an iron-trap functioned in the open ocean, where phosphorus is efficiently scavenged from the water column due to the high abundance of iron minerals oxidized at the surface in the ferruginous Proterozoic ocean. This process is implemented in the model by allowing a fraction of upwelled P from the deep ocean to be scavenged when the model deep ocean is anoxic, although it is not immediately clear why a similar process should not operate in an oxic ocean where there are hydrothermal sources of Fe^{2+}.

4.1 Model Development

The models of Slomp and Van Cappellen (2007); Tsandev et al. (2008); Tsandev and Slomp (2009) were extended in order to develop the model presented and published as part of Chapters 5 and 6. A summary of the sensitivity tests from the publication of Alcott et al. (2019) can also be found in Chapter 5, and the full model equations from Alcott et al. (2019) (Chapter 5) can be found in the Appendix.

The model comprises a four box ocean as shown in Figure 4.2. It includes the cycling of reactive forms of phosphorus, organic carbon and O_2. Initial reservoirs and steady state fluxes are estimated for the modern, pre-anthropogenic ocean system. The proximal zone (P) includes the coastal ocean directly influenced by river input including environments such as bays, estuaries, deltas and inland seas. The distal zone (D) includes open continental shelves where element recycling and upwelling are quantitatively more important than river input. The surface ocean box (S) includes the uppermost waters heavily influenced by atmosphere, and the final box is the deep ocean (DP), which does not exchange directly with the atmosphere. A hydrological cycle is included within the model to help parameterise soluble components that move via circulation. This cycle is assumed to have an input flux to the proximal zone via rivers and an output flux in the form of evaporation. Upwelling and downwelling fluxes are constrained by present day upwelling rates, thermohaline circulation and mass balance constraints. Equations 4.1 – 4.6 demonstrate the fluxes of dissolved species that are impacted by thermohaline circulation, where *X* is the chosen dissolved species (O_2 and soluble reactive phosphorus) and *circ* is the hydrological flux of water from and to respective boxes.

$$X_{PD} = circ_{PD} \cdot [X_D] \quad \text{(Equation 4.1)}$$

$$X_{DS} = circ_{DS} \cdot [X_D] \quad \text{(Equation 4.2)}$$

$$X_{SDP} = circ_{SDP} \cdot [X_s] \quad \text{(Equation 4.3)}$$

$$X_{DPD} = circ_{DPD} \cdot [X_{DP}] \quad \text{(Equation 4.4)}$$

$$X_{DDP} = circ_{DDP} \cdot [X_D] \quad \text{(Equation 4.5)}$$

$$X_{DPS} = circ_{DPS} \cdot [X_{DP}] \quad \text{(Equation 4.6)}$$

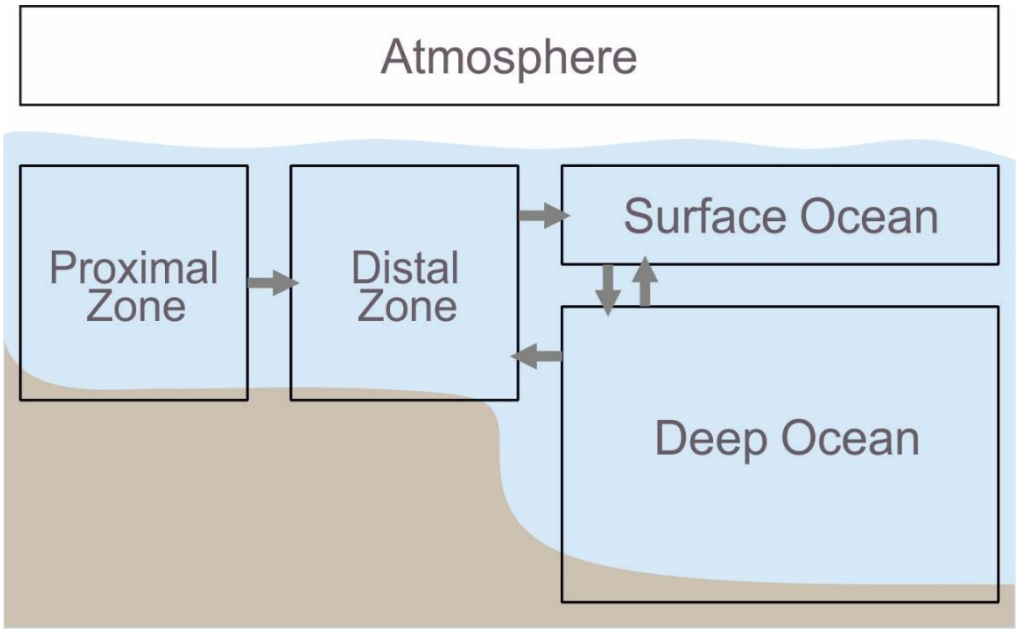

Figure 4.2. *Simple model schematic showing the four box ocean and atmosphere system. Arrow indicate ocean circulation fluxes. The oxygen reservoirs in contact with the atmosphere are assumed to be in equilibrium with the atmosphere and therefore are not shown as arrows on this figure. The ocean compartments of this model are the same geometrically as Slomp and Van Cappellen (2007).*

Carbon cycle

Particulate organic carbon is tracked within this model and is formed during primary production in the surface waters (proximal, distal and surface ocean zones). Terrestrial organic matter is assumed to be refractory and is not considered within this or any previous iterations of the model (Slomp and Van Cappellen, 2007; Tsandev et al., 2008; Tsandev and Slomp, 2009).

Primary Production

Primary production is considered to be phosphorus limited, for reasons outlined by Tyrell (1999) where phosphorus is considered the ultimate limiting nutrient, whilst nitrogen is considered to be the proximate limiting nutrient (discussed in more detail in section 1.3).

Primary production (*PP*) within the model is assumed to be in the form of oxygenic photosynthesis, producing both oxygen and organic matter. Anoxygenic photosynthesis would ultimately contribute to primary productivity, most notably in the Archean. It would not lead to oxygen production but would allow for a

consumption of oxidants in the water column, likely delaying oxygenation (Johnston et al., 2009; Hamilton et al., 2016). We utilise this model assuming that oxygenic photosynthesis has evolved and is well established. At present day, the contribution of anoxygenic primary production to total production is approximately 0.17% (Johnston et al., 2009). Due to the unknown contribution of anoxygenic photosynthesis moving back through time, we only include oxygenic production as it impacts all aspects of the model. We do acknowledge, however, that anoxygenic photosynthesis may have played a major role in regulating oxygen concentrations earlier in Earth history (e.g. Johnston et al., 2009). The organic matter contains both organic carbon and particulate organic phosphorus (POP). For the carbon cycle, primary production is considered to be linearly proportional to soluble reactive phosphorus concentrations (SRP).

$$PP = kPP \cdot \boldsymbol{P} \cdot RedCP \qquad \text{(Equation 4.7)}$$

Where $\boldsymbol{P}$ is the amount of phosphorus relative to present day, *RedCP* is the C:P ratio of primary organic matter (106; Redfield, 1958) and *kPP* is a proportionality constant to adjust for the present day primary production flux (Equation 4.7).

The Redfield ratio is assumed to be 106 throughout Earth history. As discussed in Section 1.3, the stoichiometry of organic matter is known to vary in the modern day due to a variety of factors. As it is still not known how this ratio varied though time (Planavsky et al., 2014) we use 106 as the best estimate available.

Export Production

Export production (*xp*) is considered to be a fraction of the newly produced organic carbon into the box each model time-step. The shelf boxes (Proximal and Distal) don't have any underlying boxes, so export production is treated as in Slomp and Van Cappellen (2007), where it can be exported laterally (from proximal to distal, distal to surface; e.g. Equation 4.8).

$$xp_{jk} = kxp_{jk} \cdot (xp_{ij} + PP_j) \qquad \text{(Equation 4.8)}$$

The generalised export production function in Equation 4.8 is the export from reservoir *j* to reservoir *k*, taking into account the exported production from other boxes (e.g. *i* to *j*) and the freshly produced organic matter in the respective box (PP_j). kxp_{jk} is a constant in order to adjust for present day export rates.

Remineralization

Organic carbon is also affected by remineralization, burial and transfer between ocean reservoirs but is not upwelled as it is assumed to only move laterally or sink within the ocean. Remineralization is considered to be proportional to the availability of organic carbon in the proximal, distal and surface ocean boxes (Slomp and Van Cappellen, 2007; Equation 4.9). Where $kcmin_j$ is the present day flux of remineralized organic carbon and $\boldsymbol{C_j}$ is the amount of organic carbon within the box (e.g. *j*) relative to present day.

$$POCmin_j = kcmin_j \cdot \boldsymbol{C_j} \qquad \text{(Equation 4.9)}$$

Remineralization of organic carbon in the deep ocean is constrained by the respiration of oxygen and is related by a ratio of 138 oxygen: 106 carbon, similar to Slomp and Van Cappellen (2007).

The formulation in Equation 4.9 allows for respiration to be of a form that includes both aerobic and anaerobic respiration in the productive proximal and distal regions. As for remineralisation and respiration in the deep ocean, we assume the amount of organic carbon that is ultimately buried is constrained by the rate of phosphorus release from organic matter (as described in Equation 4.25), which is only partly (25%) dependant on the concentration of oxygen in the deep ocean. These two methods attempt to alleviate the primary dependency on oxygen allowing for organic carbon consumption in an anoxic ocean.

Organic Carbon Burial

Organic carbon burial (*POCbur*) on the shelf is proportional to the newly produced and exported organic carbon within the respective box. In the deep ocean, in order to include a redox dependency on carbon burial, the organic carbon burial is derived from the redox sensitive organic phosphorus burial (Van Cappellen and Ingall, 1994). The proximal and distal box organic carbon burial fluxes are proportional to organic matter production.

The redox sensitive inclusion of organic carbon in the deep ocean is to attempt to constrain the increased potential for organic matter to be impacted by redox processes while sinking through the open ocean's much deeper water column.

Equations 4.10 - 4.13 show the differential equations for the four organic carbon reservoirs; Proximal (C_P), Distal (C_D), Surface Ocean (C_S) and Deep Ocean (C_{DP}). Organic carbon is introduced into the proximal zone via primary production and is removed via remineralization, organic carbon burial and export production to the distal zone. This export production is supplemented by primary production in the distal zone and is removed through burial, remineralization and export production to the surface ocean. Similarly, organic carbon in the surface ocean is removed via remineralisation and export production to the deep ocean. The primary source to the deep ocean is via the export from the surface ocean and is removed by respiration and burial.

Proximal Particulate Organic Carbon

$$\frac{dC_P}{dt} = PP_P - POCmin_P - POCbur_P - xp_{PD} \qquad \text{(Equation 4.10)}$$

Distal Particulate Organic Carbon

$$\frac{dC_D}{dt} = xp_{PD} + PP_D - POCbur_D - POCmin_D - xp_{DS} \qquad \text{(Equation 4.11)}$$

Surface Ocean Particulate Organic Carbon

$$\frac{dC_S}{dt} = xp_{DS} + PP_S - POCmin_S - xp_{SDP} \qquad \text{(Equation 4.12)}$$

Deep Ocean Particulate Organic Carbon

$$\frac{dC_{DP}}{dt} = xp_{SD} - RespPOC - POCbur_{DP} \qquad \text{(Equation 4.13)}$$

Oxygen cycle

In contrast to other biogeochemical box models, the oxygen cycle developed here allows for a variable atmosphere and upper surface ocean in addition to introducing a parameter to constrain oxygen in the bottom waters of the proximal and distal boxes. These changes are as follows.

Atmospheric Oxygen

Slomp and Van Cappellen (2007) primarily investigated biogeochemical impacts driven by ocean circulation, leading to the assumption that oxygen

concentrations in the reservoirs in contact with the atmosphere would remain at present day values. This relationship obviously wouldn't hold in more extreme or at least earlier periods in Earth history. In order to overcome this, we introduced an atmospheric reservoir, assuming that oxygen production associated with organic carbon burial (*POCbur*) enters the atmosphere and surface ocean box. There are two explicitly calculated oxygen reservoirs in the model, which are the atmosphere and deep ocean. The atmospheric O_2 balance is determined by burial of organic carbon versus consumption of O_2 through weathering or degassing, whereas deep ocean O_2 is calculated from downwelling versus respiration. To stay in accordance with the assumptions made by Slomp and Van Cappellen (2007), the upper most oxygen reservoirs in contact with the atmosphere scale with any change in the atmosphere relative to present day.

We calculate oxidative weathering (*AtmosW*) as the present day rate (*kAtmosW*; equal to present day organic carbon burial) being proportional to the square root of the atmospheric oxygen content relative to present day ($\boldsymbol{O_A}$), similar to the COPSE model (Bergman et al., 2004; Daines et al., 2017) but without the inclusion of a continental organic carbon reservoir, as shown in Equation 4.14.

$$AtmosW = kAtmosW \cdot (\sqrt{\boldsymbol{O_A}}) \qquad \text{(Equation 4.14)}$$

In addition to the oxidative weathering flux, we also include an inorganic reductant flux to represent earlier periods in Earth history. This reductant flux is constrained by approximations of reduced gas outgassing (Hayes and Waldbauer, 2006; Krissansen-Totten et al., 2018) and the availability and progressive release of hydrogen to space (Kharecha et al., 2005; Olson et al., 2013).

Aerobic Respiration

Present day rates of aerobic respiration (*OResp;* Equation 4.15) are based on the downwelling fluxes of oxygen and are calculated in order to provide a steady state. Aerobic respiration is then considered proportional to the availability of organic carbon and oxygen, where oxygen is formulated as a monod function. The monod function specifies that below the threshold of 0.1µM, aerobic respiration ceases to occur (Slomp and Van Cappellen, 2007).

$$OResp = kResp \cdot (\frac{\boldsymbol{C_{DP}}}{RedOC}) \cdot (\frac{O_{DP}}{(kmO_2 + O_{DP})}) \qquad \text{(Equation 4.15)}$$

Where $\boldsymbol{C_{DP}}$ is the amount of carbon available in the deep ocean relative to present day, *RedOC* is the ratio of oxygen to carbon in organic matter (138:106), O_{DP} is the oxygen content of the deep ocean and km_{O2} is the monod value of 0.1µM.

Extent of Anoxia

We use a parameter similar to *DOA*, termed f_{anoxic} (Equation 4.16; Watson et al., 2017) to allow for anoxic bottom waters on the shelf, whilst still retaining oxygenated upper surface ocean conditions.

$$f_{anoxic} = \frac{1}{1+\exp\left(-k_{anox}\left(k_U\left(\frac{P}{P_0}\right)-\left(\frac{O_2}{O_{20}}\right)\right)\right)} \quad \text{(Equation 4.16)}$$

Where f_{anoxic} is the relative fraction of the seafloor that is considered anoxic. k_{anox} is a constant to adjust to present day values, k_U represents the efficiency of nutrient utilization in upwelling regions and the two phosphorus and oxygen relationships are linear relationships to correct for present day (Watson et al., 2017). The relationship of phosphorus and oxygen abundance is used in an attempt to constrain the balance between organic carbon remineralisation and oxygen supply.

The differential equations for the oxygen cycle are shown below in Equations 4.17-4.21. As discussed, the oxygen concentration of the reservoirs in contact with the atmosphere are assumed to be proportional to the oxygen concentration in the atmosphere. In contrast, the deep ocean is supplied oxygen through open ocean downwelling with oxygen being removed via respiration and upwelling to the surface and distal boxes. Finally, the atmosphere oxygen reservoir is supplied by organic carbon burial and is consumed via oxidative weathering and reaction with reduced gases.

Proximal Oxygen

$$O_P = O_{P_0} \cdot \boldsymbol{O_A} \quad \text{(Equation 4.17)}$$

Distal Oxygen

$$O_D = O_{D_0} \cdot \boldsymbol{O_A} \quad \text{(Equation 4.18)}$$

Surface Ocean Oxygen

$$O_S = O_{S_0} \cdot \boldsymbol{O_A} \quad \text{(Equation 4.19)}$$

Deep Ocean Oxygen

$$\frac{dO_{DP}}{dt} = O_{SDP} - OResp - O_{DPS} - O_{DPD} \quad \text{(Equation 4.20)}$$

Atmospheric Oxygen

$$\frac{dO_A}{dt} = POCburT - AtmosW - genred \quad \text{(Equation 4.21)}$$

Phosphorus cycle

Phosphorus burial is redox dependant and can be buried in several forms. Three forms of P burial are considered within this model, P_{Fe}, P_{org} and P_{aut}. Phosphorus is inputted into the model by weathering (W_P; 9 x10^{10} mol P/yr at present day) and enters the proximal zone. Soluble reactive phosphorus is consumed via primary production (*PPP* for the phosphorus cycle) to form organic phosphorus, which itself can be remineralized back to reactive phosphorus (POP_{min}). These two fluxes are constrained by the organic carbon cycle with the consideration of the Redfield ratio (106:1) to adjust for the phosphorus cycle.

Iron bound phosphorus burial

The burial of P_{Fe} is considered linearly proportional to the concentration of oxygen, as more iron oxides can form with a greater availability of oxygen (for present day and reasonable iron concentrations) within the deep ocean (Slomp and Van Cappellen, 2007), or the f_{anoxic} parameter within the distal box (Similar to *DOA* in Tsandev and Slomp, 2009), as shown in Equations 4.22 - 4.24.

Proximal iron bound phosphorus burial

$$PFe_P = kFeP_P \cdot P_P \quad \text{(Equation 4.22)}$$

Distal iron bound phosphorus burial

$$PFe_D = kFeP_D \cdot P_D \cdot (1 - fanoxic_{dist}) \quad \text{(Equation 4.23)}$$

Deep iron bound phosphorus burial

$$PFe_{DP} = kFeP_{DP} \cdot [\boldsymbol{O_{DP}}] \quad \text{(Equation 4.24)}$$

Where constants (*kFeP*) are the present day values for iron bound phosphorus burial. An assumption of abundant iron being washed in from the continent is made, leading to the burial of phosphorus in the proximal zone being proportional to the concentration of SRP (Slomp and Van Cappellen, 2007).

Organic bound phosphorus burial

The burial of organic bound phosphorus is proportional to newly introduced particulate organic carbon (e.g. primary production, export production) as shown in Equations 4.25 - 4.27 following Slomp and Van Cappellen (2007).

Deep organic bound phosphorus burial

$$POPbur_{DP} = kPOPbur_{DP} \cdot \left(\frac{xp_{SDP}}{CP_{ratio}}\right) \cdot (0.75 + (0.25 \cdot [\boldsymbol{O_{DP}}])) \quad \text{(Equation 4.25)}$$

Proximal organic bound phosphorus burial

$$POPbur_{P} = kcbur_{P} \cdot \frac{PP_{P}}{CPratio_{proximal}} \quad \text{(Equation 4.26)}$$

Distal organic bound phosphorus burial

$$POPbur_{D} = kPOPbur_{D} \cdot \frac{PP_{D}+xp_{PD}}{CPratio_{distal}} \quad \text{(Equation 4.27)}$$

Where *xp* is the export production from the appropriate boxes to the box of deposition, *PP* is the primary production within the associated box and *CPratio* values are the calculated C:P ratios within the sediment, as described in Equation 4.28.

$$CPratio = \frac{(C{:}P)_{oxic}(C{:}P)_{anoxic}}{(1-DOA)(C{:}P)_{anoxic}+DOA(C{:}P)_{oxic}} \quad \text{(Equation 4.28)}$$

$C{:}P_{oxic}$ is the ratio of carbon to phosphorus in oxygenated sediments and is determined to be 200-250 to account for minor recycling from organic matter whilst $C{:}P_{anoxic}$ is the ratio of carbon to phosphorus in anoxic sediments based on Devonian laminated shales (Ingall et al., 1993) (typically 1100 or 4000; Slomp and Van Cappellen, 2007; Tsandev and Slomp, 2009). This upper value is used for all of Earth history as our current understanding of the primary C:P ratios of organic matter is not complete (see discussion above and within Section 1.3).

Authigenic phosphorus burial

The final burial term for reactive phosphorus is as an authigenic phase (e.g. CFA). We include an assumption, as in previous iterations of this model, that the burial of authigenic phases are redox dependant (Equation 4.29; Slomp and Van Cappellen, 2007; Tsandev and Slomp, 2009). This redox dependency is based on P release from P_{Fe} or P_{org} occurring under an anoxic water column which may occur in the water column or close to the sediment water interface, allowing a significant proportion to be recycled back to the water column (Slomp et al., 2002; Slomp and Van Cappellen, 2007). P_{aut} formation is considered to be linearly dependent on the rate of POP mineralization within the overlying ocean box (Slomp and Van Cappellen, 2007). A redox dependency on P_{aut} is also included in the distal zone, where it is linearly proportional to f_{anoxic} and the rate of respiration in the distal zone (as in Tsandev and Slomp (2009); Equation 4.31). Authigenic P burial in the proximal zone is not redox dependent and is related to the mineralized POP flux and the quantity of POP present at that time step in order to keep consistent with previous iterations of the model (Equation 4.29; Slomp and Van Cappellen, 2007).

Deep authigenic phosphorus burial

$$Paut_{DP} = kCaP_{DP} \cdot POPmin_{DP} \cdot (0.75 + (0.25 \cdot [\boldsymbol{O_{DP}}])) \qquad \text{(Equation 4.29)}$$

Proximal authigenic phosphorus burial

$$Paut_{P} = kpmin_{P} \cdot \boldsymbol{OP_{P}} \cdot kCaP_{P} \qquad \text{(Equation 4.30)}$$

Distal authigenic phosphorus burial

$$Paut_D = kCaP_D \cdot \boldsymbol{O_D} \cdot (1 - fanoxic_{dist}) \quad \text{(Equation 4.31)}$$

Where constants (*kCaP*) are used to adjust for present day values and POP_{min} is the mineralization flux of POP.

Although we include a redox dependency in the formation of P_{aut}, leading to increased P_{aut} formation under oxygenated conditions, it has been suggested that the inverse may also be true. Goldhammer et al. (2010) suggest that large sulfide-oxidising bacteria accumulate P and facilitate the conversion of phosphate to apatite more prominently under anoxic conditions by introducing phosphorus to pore waters. They further propose the possible expansion of OMZs at present and in the near future could restrict marine productivity due to this dynamic. Modern day OMZs however, typically show significant benthic phosphorus fluxes (e.g. Lomnitz et al. (2015)). In order to keep the model consistent with the original model of Slomp and Van Cappellen (2007) and its subsequent iterations, we continue to include the positive redox dependence as shown in the equations above but we conduct sensitivity tests as to how much of the authigenic pool is considered redox dependant (Chapter 5).

The differential equations for the phosphorus cycle are shown below in Equations 4.32 - 4.39. As soluble reactive phosphorus is bioavailable, it is consumed via primary production and introduced through remineralisation of organic matter and from rivers. In addition to this it is removed through adsorption to iron minerals and authigenic phases. Particulate organic phosphorus is assumed to only sink as part of organic matter so isn't influenced by circulation and is consumed by respiration and produced by primary production fluxes.

Proximal Soluble Reactive Phosphorus

$$\frac{dSRP_P}{dt} = W_P - PPP_P + POPmin_P - PFe_P - Pauth_P - SRP_{PD} \quad \text{(Equation 4.32)}$$

Distal Soluble Reactive Phosphorus

$$\frac{dSRP_D}{dt} = SRP_{PD} - PPP_D + POPmin_D - PFe_D - Pauth_D - SRP_{DS} + SRP_{DPD}$$

(Equation 4.33)

Surface Ocean Soluble Reactive Phosphorus

$$\frac{dSRP_S}{dt} = SRP_{DS} - PPP_S + POPmin_S - SRP_{SDP} + SRP_{DPS} \quad \text{(Equation 4.34)}$$

Deep Ocean Soluble Reactive Phosphorus

$$\frac{dSRP_{DP}}{dt} = SRP_{SDP} + POPmin_{DP} - PFe_P - Pauth_{DP} - SRP_{DPS} - SRP_{DPD}$$

(Equation 4.35)

Proximal Particulate Organic Phosphorus

$$\frac{dPOP_P}{dt} = PPP_P - POPmin_P - POPbur_P - POP_{PD} \quad \text{(Equation 4.36)}$$

Distal Particulate Organic Phosphorus

$$\frac{dPOP_D}{dt} = POP_{PD} + PPP_D - POPmin_D - POPbur_D - POP_{DS} \quad \text{(Equation 4.37)}$$

Surface Ocean Particulate Organic Phosphorus

$$\frac{dPOP_S}{dt} = POP_{DS} + PPP_S - POPmin_S - POP_{SDP} \quad \text{(Equation 4.38)}$$

Deep Ocean Particulate Organic Phosphorus

$$\frac{dPOP_{DP}}{dt} = POP_{SDP} - POPmin_{DP} - POPbur_{DP} \quad \text{(Equation 4.39)}$$

Chapter 5 Stepwise Earth oxygenation is an inherent property of global biogeochemical cycling

Preface

The contents of this chapter use the model developed in the previous chapter and are published as:

> Alcott, L. J., Mills, B. J. W. and Poulton, S. W. Stepwise Earth oxygenation is an inherent property of global biogeochemical cycling, *Science* **366**, pp.1333-1337 (2019)

This publication is presented as it is published. The model development section of the supplementary information is included as an appendix to this thesis, but is largely superseded by the previous chapter.

Article

Oxygenation of Earth's atmosphere and oceans occurred across three major steps during the Paleoproterozoic, Neoproterozoic, and Paleozoic Eras, with each increase having profound consequences for the biosphere. Biological or tectonic revolutions have been proposed to explain each of these stepwise increases in oxygen, but the principal driver of each event remains unclear. Here we show, using a theoretical model, that the observed oxygenation steps are a simple consequence of internal feedbacks within the long term biogeochemical cycles of carbon, oxygen and phosphorus, and there is no requirement for a specific 'stepwise' external forcing to explain the course of Earth surface oxygenation. We conclude that Earth's oxygenation events are entirely consistent with gradual oxygenation of the planetary surface following the evolution of oxygenic photosynthesis.

5.1 Main Text

Oxygenation of Earth's surface environment is thought to have occurred across three broad steps (Fig. 5.1). The 'Great Oxidation Event' (GOE) occurred around 2.4 - 2.2 billion years ago (Ga) and saw atmospheric oxygen rise from trace levels to greater than 10^{-5} PAL (Present Atmospheric Level) (Farquhar et al., 2000). The following ~1 billion years of the Proterozoic Eon likely sustained atmospheric oxygen levels of ~10^{-3} – 10^{-1} PAL (Planavsky et al., 2014b). Partial oxygenation of the surface ocean persisted throughout the Proterozoic (Hardisty et al., 2017), but deeper waters remained dominantly anoxic (Poulton and Canfield, 2011). The 'Neoproterozoic Oxygenation Event' (NOE) occurred between ~800 and 540 Ma, and is generally believed to have resulted in atmospheric oxygen levels of 0.1 - 0.5 PAL, as well as the first oxygenation of the deep ocean (Och and Shields-Zhou, 2012). However, there was considerable variability in the temporal and spatial extent of deep ocean oxygenation at this time, including the possibility of pulsed 'Oceanic Oxic Events' (Sahoo et al., 2016). Evidence for periodic deep water anoxia remains frequent up until the mid-Paleozoic, when a final major rise in atmospheric oxygen concentration occurred around 450 to 400 Ma (Krause et al., 2018). This 'Paleozoic Oxygenation Event' (POE) appears to have elevated atmospheric O_2 to present day levels, and established a dominantly oxygenated deep ocean, which persisted throughout the Mesozoic and Cenozoic Eras.

These major oxygenation steps are intertwined with the evolution of progressively more complex lifeforms. The first eukaryotes evolved either following the GOE, or during the run-up to the event when O_2 began to rise (Butterfield, 2015), while the NOE is coincident with major eukaryote diversification and the evolution of the first animals (Brocks et al., 2017), followed by the 'Cambrian Explosion' where animals began to dominate marine ecosystems. The POE is accompanied by a major increase in animal body size, more diverse and specialized predators, and the evolution of vascular land plants (Krause et al., 2018). However, determining causality between rises in marine and atmospheric O_2 levels and the evolution of the biosphere is complex, and there is considerable debate over the role of oxygen in driving biological evolution versus the role of life in 'bioengineering' oxygen to higher levels (Meyer et al., 2016; Lenton et al., 2014).

Tectonic evolution has also been considered a potential driver of the stepwise transitions in Earth surface oxygenation. Changes to plate tectonics have been linked to the GOE through, for example, a change in the fraction of subaerial volcanism or the composition of the crust (Lee et al., 2016; Kump and Barley, 2007). Some, but not all, supercontinent formation times correspond to oxygenation events (Campbell and Allen, 2008), as do emplacement times of some Large Igneous Provinces (LIPs), which are proposed to have driven ocean oxygenation through delivery of the limiting nutrient, phosphate (Horton, 2015).

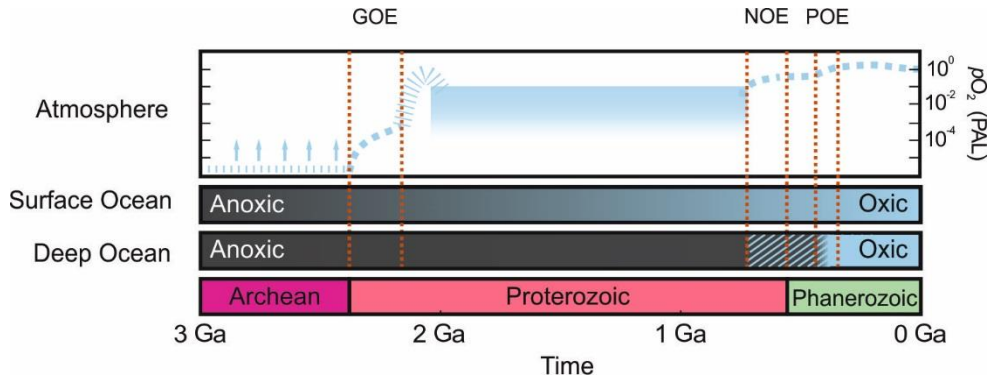

Figure 5.1. *Redox history of the Earth. Atmospheric O2 based on Lyons et al., 2014. GOE – Great Oxidation Event, NOE – Neoproterozoic Oxygenation Event, POE – Paleozoic Oxygenation Event. Ga – Billion Years. Crosshatch indicates variable deep ocean redox between the start of the NOE and the POE. See text for summary and references.*

However, the geologically-rapid yet ultimately rare nature of Earth's oxygenation events does not clearly correspond to either tectonic or evolutionary processes. For example, mantle dynamics and the supercontinent cycle are unlikely to produce large-scale changes on timescales of the order of less than ~100 Myr, whilst LIP emplacements are far more common than major rises in O_2. Looking to biological innovations, the timescale between the origination of a domain or kingdom of life and its rise to global ecological dominance may also be 100's of Myrs (e.g. Eukarya (Knoll et al., 2016)). Furthermore, the oscillations in ocean redox apparent during the NOE are difficult to explain via a sequence of tectonic or biological 'switches' acting on the system (e.g.Lenton and Daines, 2018).

It is therefore possible that Earth's stepwise oxygenation was not the product of individual trigger events and may instead be explained by some inherent property of global biogeochemical feedbacks. This hypothesis has wide implications for the evolution of life on Earth and other planets, and there have therefore been a number of attempts to explain the known 'stepwise' oxygen trajectory as a feature of Earth's internal dynamics: for example, it has been shown that atmospheric feedbacks might promote the GOE (Goldblatt et al., 2006; Claire et al., 2006). However, no study has provided a sound theoretical basis that can explain the trajectory and timings of marine and atmospheric oxygenation over Earth history without relying either on external 'trigger events' or on arbitrary switches within the model itself (such as assuming a transition to greater nutrient availability when O_2 crosses a threshold (Laakso and Schrag, 2017; Laakso and Schrag, 2014).

Here we identify a set of feedbacks that exist between the global phosphorus, carbon and oxygen cycles, which are capable of driving rapid shifts in ocean and atmospheric O_2 levels without requiring any 'stepwise' change in either tectonics or the evolution of the biosphere. These feedbacks reproduce the observed 3-step oxygenation pattern when driven solely by a gradual shift from reducing to oxidizing surface conditions over time.

Phosphorus (P) is generally considered the ultimate limiting nutrient for marine productivity over geological timescales (Tyrrell, 1999), and P bioavailability exerts a key control on the long-term rate of O_2 production through oxygenic photosynthesis and organic carbon burial. In the modern ocean, bioavailable phosphorus is fixed in the sediments via three primary pathways. Organic-bound P (P_{org}) is buried with sinking organic matter, iron-bound P (P_{Fe}) forms as P is adsorbed or co-precipitated with iron (oxyhydr)oxide minerals, and authigenic P (P_{aut}) is primarily formed within the sediment via 'sink switching' of these phases to carbonate fluorapatite and/or vivianite (Krom and Berner, 1981; Ruttenberg and Berner, 1993; Jilbert and Slomp, 2013).

The phase partitioning of sedimentary phosphorus is largely controlled by redox conditions in the water column and sediments. Phosphorus may be preferentially released from organic matter during remineralization under anoxic conditions, leading to elevated C_{org}:P_{org} ratios within the sediment (Van Cappellen and Ingall, 1994),

increased recycling of P back to the water column, and reduced formation of authigenic carbonate fluorapatite (Slomp et al., 2002; Tsandev and Slomp, 2009). The availability of iron (oxyhydr)oxides is also typically considered to diminish in an anoxic system which limits burial of P_{Fe} (Krom and Berner, 1981), although this dynamic becomes more complex when considering the prevalence of low sulphate, ferruginous (anoxic Fe-rich) oceanic conditions throughout large parts of Earth history (Poulton and Canfield, 2011), whereby Fe minerals may trap a proportion of the P delivered to the sediment (Reinhard et al., 2017).

Assuming that bottom-water anoxia leads to an overall enhancement of sedimentary P regeneration, two important feedback mechanisms arise that affect global biogeochemistry, with each operating over a different timescale. Firstly, a 'short-term' positive feedback mechanism (self-promoting) operates, whereby the spread of ocean anoxia results in increased phosphorus availability in the water column. This stimulates primary productivity and fuels respiration, thus further increasing phosphorus availability (Van Cappellen and Ingall, 1994). These eutrophic conditions rapidly deplete water column oxygen and in turn increase the rate of spread of anoxia. Secondly, a geologically-paced negative feedback mechanism (self-inhibiting) operates on the combined C-O-P cycles, whereby the burial of organic carbon in marine sediments leads to oxygenation of the atmosphere. This increase in pO_2 drives higher rates of oxidative weathering of ancient sedimentary organic C (Daines et al., 2017), and ventilates the ocean, acting to stabilize O_2 both by reducing the rate of organic carbon burial and by increasing the consumption of oxygen on land.

Theoretical models have previously linked the above feedbacks to the geologically-rapid onset of Cretaceous Ocean Anoxic Events (OAEs), and to their delayed termination via increasing atmospheric O_2 (Tsandev and Slomp, 2009). It has also been shown that under an increased continental weathering input of phosphorus, self-sustaining oscillations between oxic and anoxic oceanic states might occur (Handoh and Lenton, 2003). We hypothesize here that the above feedbacks are in fact sufficient to explain the stepwise oxygenation of Earth's atmosphere and oceans, including apparent cyclic ocean oxygenation/deoxygenation events during the Neoproterozoic and early Phanerozoic (Sahoo et al., 2016), which are followed by the transition to a sustained oxic deep ocean.

Firstly, the GOE can occur when the weathering of organic carbon becomes the principal long-term oxygen sink. This can be achieved once the rate of photosynthetic oxygen production outpaces the consumption of oxygen via reaction with reduced gases and reduced seawater species. Secondly, cyclic oxygenation events in the NOE would be a likely consequence of the combined positive and negative feedbacks between ocean oxygenation and sedimentary P recycling, whereby a small shift towards a more oxygenated planetary surface results in gradual oxygenation of oceanic bottom waters. This would limit P regeneration from sediments, reducing short-term productivity and oxygen demand, and thus further increasing dissolved oxygen concentrations. This positive feedback could oxygenate ocean basins, but only temporarily, as reduced P availability for primary productivity then leads to less O_2 production over geologic timescales, thus reducing atmospheric O_2, which eventually leads to a return to marine anoxia. Finally, a combination of the two mechanisms outlined above can result in sustained oceanic oxygenation. In this case, a sufficiently large increase in surface redox potential, coupled with a greater contribution of oxidative weathering to overall O_2 regulation, allows deep ocean oxygenation to be maintained.

We test our hypothesis by building upon a well-established conceptual model of marine biogeochemistry (Tsandev and Slomp, 2009; Slomp and Van Cappellen, 2007; Tsandev et al., 2008). The model tracks the global cycles of phosphorus, carbon and oxygen within a 4-box ocean system representing shelf, open-ocean and deep water environments (Fig. 5.2). We add to the model an atmospheric oxygen reservoir, a global geological oxygen cycle, oxidative weathering of organic carbon, and an open-ocean scavenging flux of P by upwelled Fe, basing these on other previous models (Reinhard et al., 2017; Daines et al., 2017).

Phosphorus-dependent primary productivity occurs in all surface ocean boxes, and redox-dependent burial of P is included in all boxes in contact with the sediments. This is in contrast to Sarmiento and Toggweiler (1984) who assume zero phosphorus concentrations in the low latitude ocean, as these oceans are relatively nutrient depleted. More recent studies have shown that the nutrient depletion is partially driven by intense primary production, at odds with their initial assumption. As in previous versions of the model, sedimentary inventories are not calculated explicitly, and regeneration of P from sediments is addressed via the net P burial terms,

which follow previous model derivations (Tsandev and Slomp, 2009; Slomp and Van Cappellen, 2007). Deep ocean dissolved oxygen concentration is calculated explicitly, as is the oxygen content of the atmosphere. Following previous model versions, the oxygen content of the ocean boxes in contact with the atmosphere is represented by a 'degree of anoxia' parameter, which we term f_{anoxic} and which represents the balance between O_2 diffusion from the atmosphere and oxygen utilization (Slomp and Van Cappellen, 2007). An optional scavenging flux of phosphorus sorption to upwelling iron particles (Reinhard et al., 2017) is implemented in order to test the effects of additional phosphorus draw-down in a ferruginous (iron-rich) ocean – a state which may have persisted throughout much of Earth history (Poulton and Canfield, 2011).

The scavenging flux directly follows previous models (Reinhard et al., 2017), operating at oxygen concentrations below 1 μM and removing 25% of P that is upwelled into the open ocean. Full model equations are shown in the Supplementary Information. As well as testing different limits on the scavenging flux, we also ran sensitivity tests to vary the degree of redox dependency of the P_{org} and P_{aut} burial terms (following previous versions of this model).

Figure 5.3 shows steady state responses of the baseline model to variable fluxes of reduced gas to the surface system, representing overall changes in net surface redox over Earth history. All other parameters remain at their present day values, and processes vary only via internal feedbacks. The redox dependence of the P_{org} and P_{aut} burial fluxes were varied and are shown as different lines. The model runs with stronger redox dependencies (40% for P_{aut}, 25% for P_{org}) responded first to oxygenation (left-most lines in Fig. 3), and weaker dependencies (35% for P_{aut}, 25% for P_{org} and 10% for both P_{aut} and P_{org}) plot to the right of these. Under a very high reductant flux (left side of x-axis in Fig. 3), as proposed for the Archean ($>>1 \times 10^{13}$ mol O_2 equivalent reductant input (Kharecha et al., 2005; Krissansen-Totton et al., 2018), O_2 production is overwhelmed and atmospheric O_2 is stable at around 10^{-5} PAL, consistent with the maximum concentrations of pre-GOE conditions (Pavlov and Kasting, 2002). Here, the O_2 balance is primarily maintained by reaction of O_2 with reduced gases (Daines et al., 2017). All surface and deep ocean boxes are anoxic due to the low O_2 supply. A 'Great Oxidation Event' occurs in the model when consumption of atmospheric oxygen via reduced gases is reduced to a value lower than the total oxygen source from organic C burial (at $\sim 1.5 \times 10^{13}$ mol O_2 equivalent).

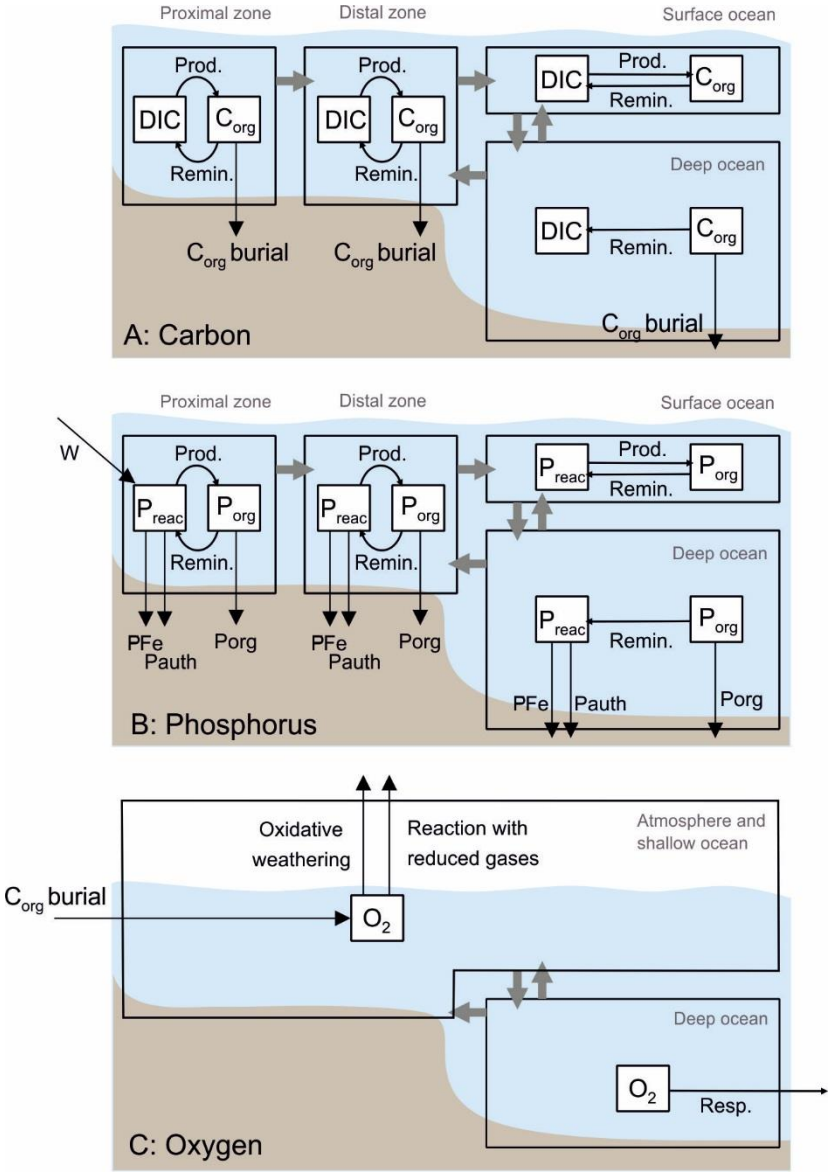

Figure 5.2. *Ocean and atmosphere box model. Clear boxes show hydrospheric reservoirs and grey arrows denote mixing between them. White boxes show chemical reservoirs and black arrows denote biogeochemical fluxes. (A) Carbon cycle: C exists as dissolved inorganic carbon (DIC) or organic carbon (C_{org}). (B) Phosphorus cycle: P exists as soluble reactive phosphorus (P_{reac}) and particulate organic phosphorus (P_{org}). (C) Oxygen cycle. Single oxygen reservoir encompasses all ocean boxes that exchange with the atmosphere. See text for full description, and methods and SI for equations.*

We find that atmospheric O_2 rises by several orders of magnitude to ~0.06 – 0.25 PAL, broadly consistent with several estimates for the mid-Proterozoic (0.01 – 0.1 PAL; Catling and Claire (2005)), and the O_2 balance is primarily controlled by oxidative weathering (Daines et al., 2017). Deep ocean oxygen concentration also rises to around 1% of the modern value, whilst the proximal and distal shelf environments remain anoxic, as O_2 diffusion from the atmosphere is not sufficient to outweigh oxygen demand.

Under a further decrease in reductant input, shelf environments undergo rapid oxygenation events. Here, gradually rising atmospheric oxygen concentrations cause a step-change in water column redox due to the positive feedback between bottom-water oxygen concentration and net P burial. Gradual ventilation of shelf bottom waters results in greater net removal of P, reducing overall O_2 demand and promoting further oxygenation. As the input of reduced gas declines, this transition happens first in the proximal shelf, and then in the distal shelf environment, as the latter is more strongly buffered against oxygenation due to upwelling of P from anoxic deeper waters. Finally, as reductant input declines further, the deep ocean becomes fully-oxygenated (reductant input of $< 0.5 \times 10^{13}$ mol O_2 equivalent). The positive feedback between dissolved O_2 concentration and net P burial again causes a rapid transition. In our model, the deep ocean is oxygenated when atmospheric O_2 reaches 0.7-0.8 PAL, which is consistent with values reported in other studies (Sperling et al., 2015).

Figure 5.3c demonstrates the degree of sedimentary P recycling in the model (shown as C_{org}/P_{org}). These changing ratios reflect the positive feedbacks between bottom-water redox and P recycling. This P recycling is dependent only on the extent of bottom water anoxia and thus the model predicts a significant degree of recycling prior to the 'GOE'. However, under global ferruginous conditions in the early Archean, P may have been more effectively trapped in the sediment (Reinhard et al., 2017) (See SI for a test of this). Nevertheless, this would ultimately help to stabilize O_2 at low levels by reducing surface ocean productivity.

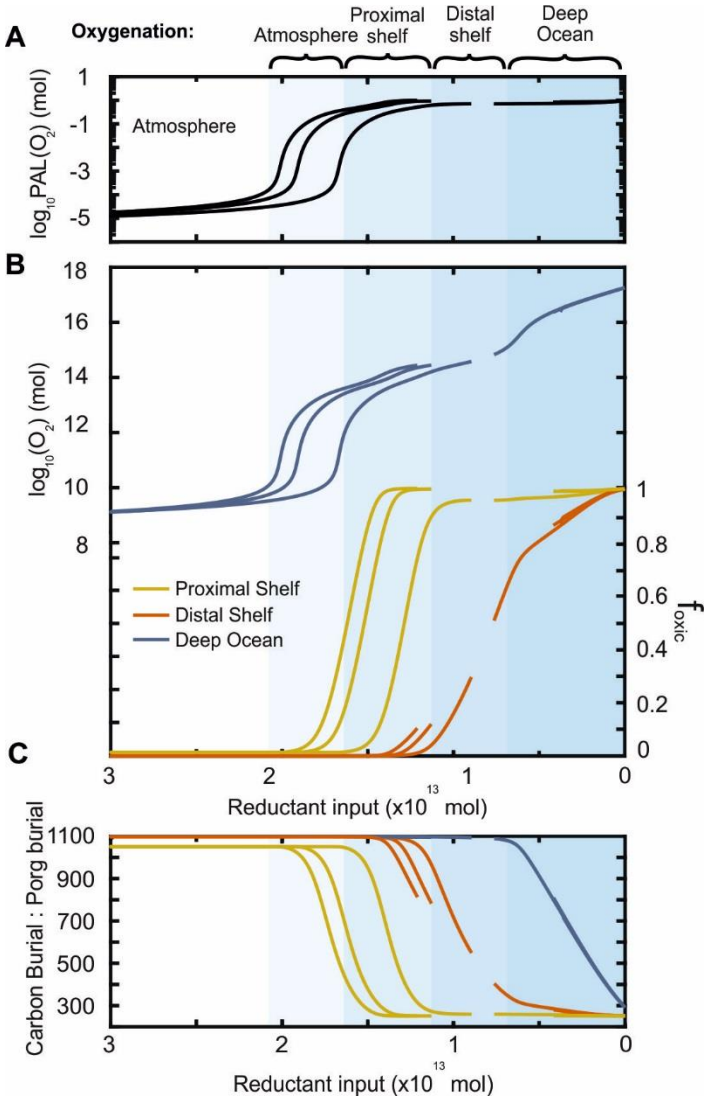

Figure 5.3. *Model stable solutions with respect to overall surface redox state. The model is run to steady state for changes to the reduced gas input rate. (A) Atmospheric O_2 reservoir. (B) Deep ocean O_2 reservoir (mol) and shelf 'oxic fraction' of seafloor (f_{oxic}). (C) Molar carbon and phosphorus burial ratio in sediments. Three lines for each zone represent different choices of redox dependence for P burial fluxes (see text). Breaks in solid lines indicate periods where no stable solution exists, in these parameter spaces the model produces an oscillating solution.*

The oxygenation of the distal shelf environment has the potential for oscillatory behaviour ('limit cycles'), denoted by the break in steady state lines in Fig. 5.3. Here, the oxygenation of the entire shelf environment results in a large reduction in overall organic carbon burial rates (as the shelves are the major locus of C_{org} burial). Over geological timescales, this reduction in carbon burial sufficiently reduces the O_2 content of the atmosphere to return the shelves to anoxia. Figure 5.4 shows this cyclic response of the model under reductant inputs of 1 and 2.5×10^{13} mol O_2 equivalent yr^{-1}. The cyclic regime includes temporary oxygenation of both the distal shelf and the deep ocean, as the rapid oxygenation event results in increased supply of oxic water via down-welling. These Ocean Oxygenation Events (OOEs) last between 2 – 5 Myrs for the range of redox dependencies tested in the model, and occur on approximate 5 – 20 Myr timescales.

Our model demonstrates that gradual oxygenation of Earth's surface over time results in distinct oxygenation events. This occurs because in our model the atmosphere, continental shelves, and deep ocean act as distinct 'compartments' of the Earth system (Broecker and Peng, 1982; Wallmann, 2003), which are controlled by local, rather than global feedbacks (Bjerrum et al., 2016). Firstly, a 'Great Oxidation' of the atmosphere occurs, followed by oxygenation of nearshore shelf environments, and then distal shelf environments. This oxygenation of the whole shelf is manifest as an oscillating solution, which would likely lead to a series of Ocean Oxygenation Events. Finally, the deep ocean becomes resiliently oxygenated. This sequence of events tracks the apparent oxygenation history of the Earth as recorded by multiple redox proxies, including cycling between oxic and anoxic deep ocean states during the Neoproterozoic and early Paleozoic (Sahoo et al., 2016).

Our model of course neglects some potentially-stabilizing negative feedbacks, such as the climate-silicate weathering link, although models that do include these processes still exhibit rapid shifts in marine anoxia (e.g. Lenton et al., (2018)).

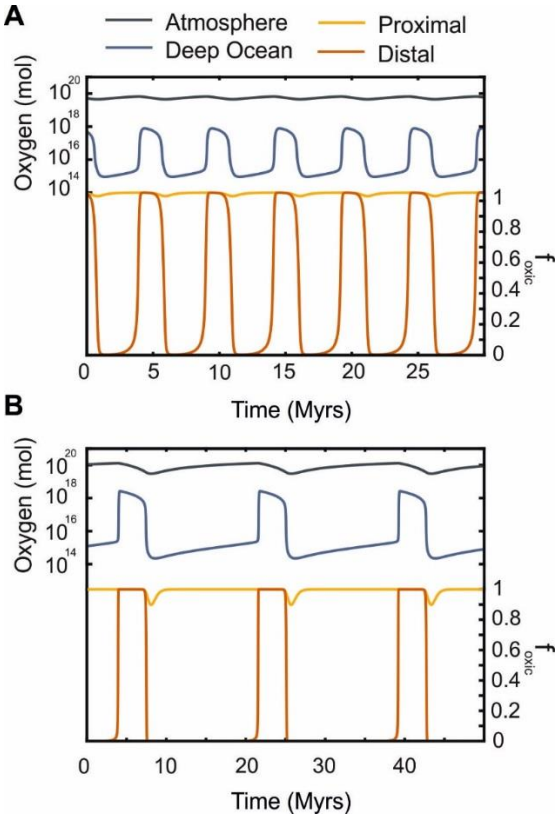

Figure 5.4. *Oscillating redox solutions. Transient model responses, demonstrating limit cycles of frequency ~5-20 Myrs. (A) Conservative redox dependency for deep ocean P burial terms (50% - P_{aut}, 25% - P_{org}) with 1 × 10^{13} moles of oxygen consumption. (B) Stronger redox dependencies following Tsandev and Slomp, 2009 (90% - P_{aut}, 50% - P_{org}) with 2.5 × 10^{13} moles of oxygen consumption.*

In Fig. 5.5 we examine the potential for our model to recreate Earth's oxygenation history by performing transient model simulations under a continuous decline in reductant input constrained by mantle thermal evolution (Hayes and Waldbauer, 2006). In light of the potential for high Archean reductant availability and outgassing, and considering the relatively high rate of O_2 production in our model, we test starting fluxes of 4.5 × 10^{13} mol O_2 equivalent yr^{-1} at 4 Ga (Krissansen-Totton et al., 2018; Hayes and Waldbauer, 2006). With or without the inclusion of open water P scavenging, the model is able to recreate the broad observed pattern of atmospheric and oceanic oxygenation over Earth history. This includes a 'Great Oxidation' of the atmosphere at around 2.5-2 Ga, and unstable oxygenation of the deeper ocean starting at around 1 Ga, which continues until permanent oxygenation of the deep ocean is established at around 0.7 – 0.4 Ga.

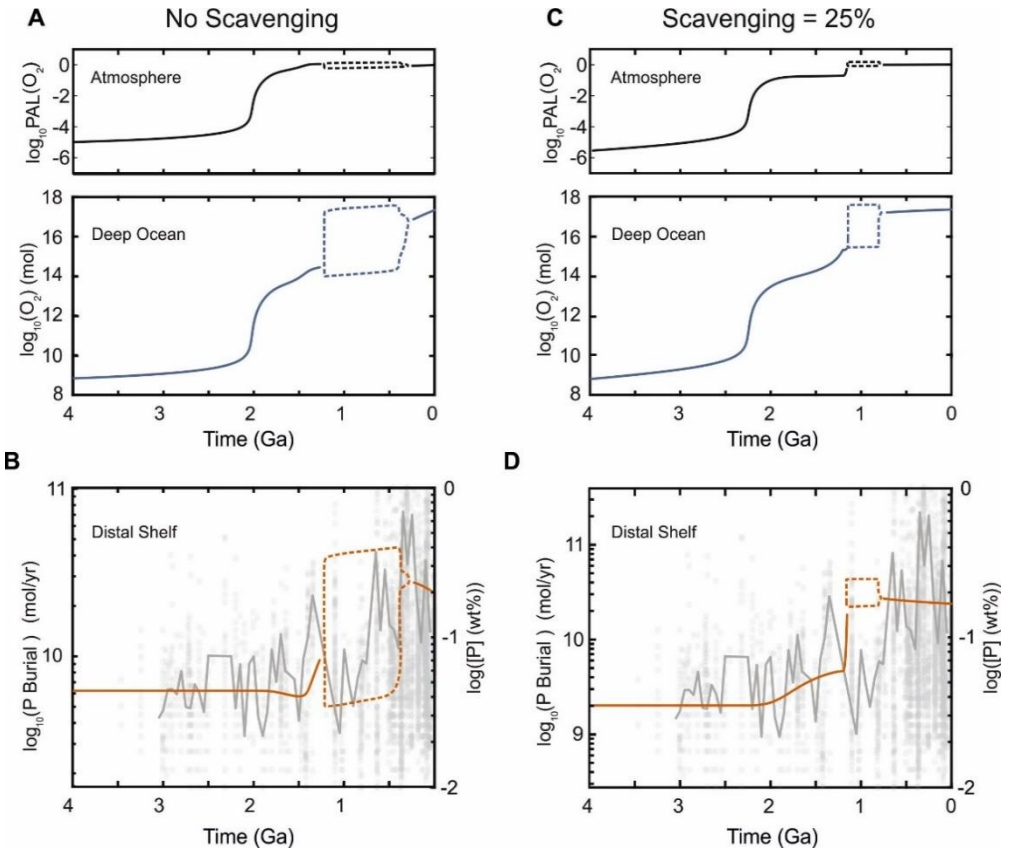

Figure 5.5. *Possible O_2 evolution over Earth history. Model is run for 4 Gyrs subject to a decrease in reductant input – illustrative of a gradual shift in net redox, and demonstrating possible evolution of surface O2 levels. Dotted boxes represent the boundaries of limit cycles in the solution. (A, C) Atmosphere and deep ocean O2 abundances. (B, D) Total shelf P burial rates (red, left axis) compared to phosphorus abundance in marine shales (Reinhard et al., 2017; right axis). Grey line shows 50 Myr binned moving average through compilation data. (A, B) No iron-bound scavenging and redox dependencies of 50% - P_{aut}, 25% - P_{org} following Slomp and Van Cappellen (2007) with a starting O_2 consumption via reductants of 45 × 10^{12} mol/yr and a linear decrease. (C, D) Iron-bound scavenging included with a maximum rate of 5 × 10^{10} mol P/yr. Stronger redox dependencies, following Tsandev and Slomp, (2009) (90% - P_{aut}, 50% - P_{org}). Starting O_2 consumption via reductants was 45 × 10^{12} mol/yr and an exponential decrease.*

We compare our model results with a compilation of phosphorus concentrations from marine shales (Reinhard et al., 2017) (Fig. 5.5). The data show an approximate four-fold increase in P weight percent between the Precambrian and Phanerozoic baselines, and this corresponds to an increase in P burial rate in the model shelf environment between the 'Proterozoic' and 'oxygenated ocean' states. Our model does not calculate sediment phosphorus weight percentages, but does produce an upwards baseline shift in shelf sedimentary phosphorus burial rate, which is qualitatively consistent with the data. This increase in P burial is much greater when open ocean scavenging is included, as the shutdown of scavenging upon deep ocean oxygenation results in significantly more P remaining in the system, in exactly the manner described by Reinhard et al. (2017). Interestingly, we also note a 2-4 fold increase in shelf P burial rates when the model does not include open-ocean scavenging. This occurs simply because more P is trapped in the sediments when the shelves become oxygenated.

It is important to note that the reductant-driven oxygenation of the surface system that we analyze here, although plausible, is only one way in which to drive gradual net surface redox changes over time. Others include the long-term build-up of organic carbon in the crust (Lee et al., 2016, Hayes and Waldbauer, 2006), the escape of hydrogen to space (Catling et al., 2001) or a gradually increasing supply of phosphorus to the ocean. Net redox changes driven by continual removal of hydrogen or C_{org} from Earth's surface should operate in a similar way to the addition of reduced gases that we explore here. Interestingly, in these model runs, under a fixed present-day rate of riverine phosphate delivery and no scavenging flux, the model predicts a declining inventory of ocean P and declining rates of productivity and carbon burial over Earth history, as sedimentary P recycling is curtailed (see Figure 5.9 for full details). When scavenging is considered, the P inventory and overall C_{org} burial rates are broadly static through early Earth history and increase slightly when the deep ocean is oxygenated. Both model outputs reproduce the increasing P concentrations in shales through time (Reinhard et al., 2017), and although we cannot produce a $\delta^{13}C$ record with this model (as it lacks an inorganic carbon cycle), it would likely be consistent with the geological record; firstly because the model can produce either an increase or decrease in C_{org} burial, and secondly because ocean $\delta^{13}C$ is buffered by the adjustment of oxidative weathering rates at low O_2 (Daines et al., 2017), and by higher rates of

inorganic carbon degassing and deposition on the Early Earth (Shields and Mills, 2017). Nevertheless, although phosphorus input over Earth history is highly uncertain (Mills et al., 2014a) it is quite commonly assumed that the P inventory, along with productivity and carbon burial rates, have increased substantially over time. Thus, in the SI we re-run our model under a varying riverine P input and show that the stepwise oxygenation events are indeed reproducible when Earth's gradual redox shift is driven by a steady increase in P supply to the oceans.

We demonstrate here that relationships between the global phosphorus, carbon and oxygen cycles are fundamental to understanding the oxygenation history of the Earth. Our model confirms that observed 'oxygenation events' through Earth history may be driven by well-defined internal system feedbacks between these cycles, without the requirement for extensive external forcings. The results of this analysis are wide-reaching. It appears that oxygenation of the Earth's surface did not require any biological advances beyond simple photosynthetic cyanobacteria, and was simply a matter of time, which drastically increases the possibility of high-O_2 worlds existing elsewhere.

5.2 Supplementary Text

Steady-state model outputs with respect varying P input

In the main text we explore the model response to varying net surface redox by inputting reductant. The flux of reductant from the mantle has varied substantially over Earth history and undoubtedly plays some role in oxygenating the Earth, however it is also important to test our model response to different mechanisms of long-term oxygenation, specifically a long-term gradual increase in phosphorus input to the ocean. Model steady-state responses to varying riverine P input display the same overall pattern to those shown in the manuscript figure 5.3 (in which reductant input is varied). Increasing P input results in oxygenation of the atmosphere, followed by oxygenation events on the shelves, and finally in the deep ocean. The key difference between this plot and that shown in the manuscript is the slightly oxygenated shelf environments prior to the "GOE". This situation is created because very low P availability limits O_2 consumption in these areas. We think it is likely that both P input and changes to reductant input drove Earth's O_2 evolution, so such low values for P availability are probably unrealistic (indeed, substantial rates of silicate weathering may be required to balance the early Earth's carbon cycle under high mantle degassing rates (Mills et al., 2014a)).

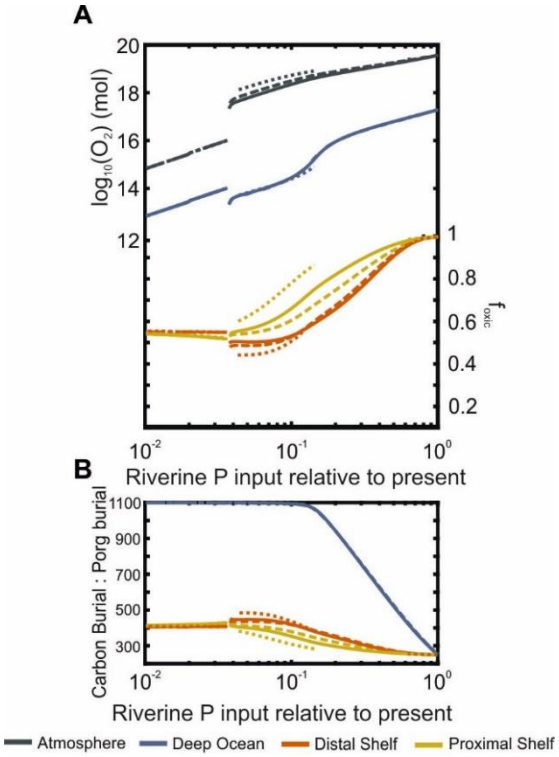

Figure 5.6. *Steady state responses with varying riverine P input relative to present. The f_{oxic} parameter is used to quantify the percentage of anoxic sea floor and is quantified by 1- f_{anoxic}, as described in the model (f_{anoxic} = 0.0025 present day; Watson et al., 2017). Varying redox dependencies on P_{org} and P_{aut} burial are shown for values used in previous models of Slomp and Van Cappellen, 2007 (10% - P_{aut} and 10% - P_{org}) (solid line). Greater redox dependencies are also tested (25% - P_{aut} and 50% - P_{org}, dashed line; 90% - P_{aut} and 50% - P_{org}, dotted line). Regions in which lines do not continue indicate unstable model outputs.*

Phosphorus scavenging in iron-rich oceans

The model on which we base our analysis was originally designed for Phanerozoic time. While the model considers ocean anoxia and its effects on the cycling of phosphorus, it does not consider the additional controls on P cycling in a ferruginous ocean (i.e. anoxic, low-sulphate and iron-rich). Under these conditions, which likely persisted for large parts of the Precambrian, it has been proposed that P would be effectively scavenged and removed from the ocean via formation of both ferrous and ferric iron compounds (e.g. Reinhard et al. 2017). Quantifying these mechanisms over deep time is an outstanding puzzle, and models are currently very poorly-constrained. But it is important to test whether the current formulation of P scavenging would effect the conclusions of this work.

In order to test the robustness of our model results we included the scavenging function used in the modelling study of Reinhard et al., (2017). As in their model, we quantify the scavenging flux by allowing a fraction of open ocean upwelled P to be buried immediately in the deep ocean sediments when deep ocean oxygen concentration is below 1µM. This results in an extremely powerful flux which can quickly deplete all ocean P, and we test various upper limits on the P burial via this mechanism. Broadly, consideration of P scavenging in an iron rich ocean does not alter the conclusions of our study. Addition of the scavenging flux alters the timings of the oxygenation events in the model by changing the relationship between overall surface redox and P cycling, but does not act to remove any of the positive feedbacks that cause the oxygenation transitions in our model. Indeed, the proposed shut-down of scavenging adds further positive feedback to the model and widens the parameter space for oscillating solutions.

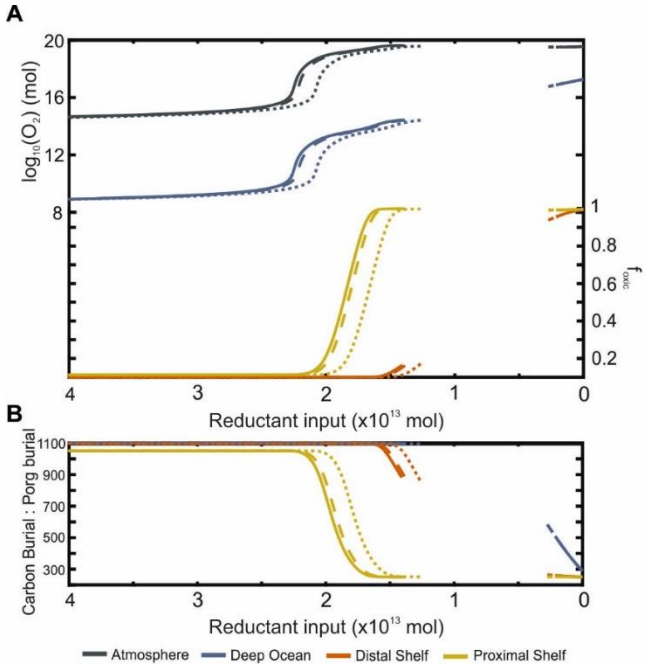

Figure 5.7. *Steady state responses with varying reduced gas concentrations with the inclusion of the scavenging flux. (A) The f_{oxic} parameter is used to quantify the percentage of anoxic sea floor and is quantified by 1- f_{anoxic}, as described in the model (f_{anoxic} = 0.0025 present day; Watson et al., 2017). Redox dependencies are set to values from Slomp and Van Cappellen (2007), where 50% of P_{aut} and 25% of P_{org} are redox dependent. (B) Carbon and phosphorus burial ratio in sediments. Breaks in solid lines indicate periods where no stable solution exists, in these parameter spaces the model produces an oscillating solution. (No scavenging, solid line; maximum value of 1 x 10^9mol P/yr, dashed line; maximum value of 5 x 10^9mol P/yr, dotted line).*

Transient model run with estimated values of reductant.

An estimated flux of reductant into the model atmosphere over time is required to produce Figure 5.5. We estimate the initial flux at 4 Ga from Hayes and Waldbauer (2006) and Krissansen-Totten et al. (2018). We test both a linear and exponential decrease in the model. The linear decrease corresponds better to continental growth and change in subaerial/submarine degassing, while the exponential decrease corresponds better to mantle cooling and direct injection. This flux is highly uncertain and curves between the two shown could be used to produce very realistic timings of oxygenation in Figure 5.5, but we aim to avoid over-fitting and simply show results under one or other of these curves in the manuscript as a demonstration of Earth's oxygenation history.

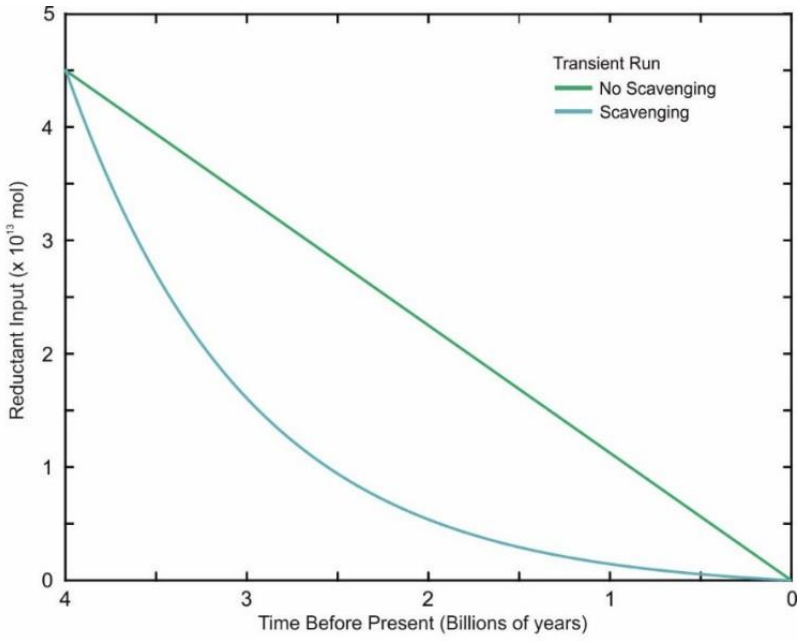

Figure 5.8. *Estimated flux of O_2 consumption via reductant input. Green line follows the linear decreasing trend through time, used for the transient run that did not included scavenging in Figure 5. Blue line follows an approximately exponential decrease used for the transient run that did included scavenging in Figure 5.5.*

Reactive phosphorus abundance, primary productivity and carbon burial for different model scenarios.

Figure 5.9 shows the SRP abundance, organic carbon burial and primary productivity for the three model scenarios explored in this work (#1: reductant-driven no scavenging (A-C), #2: reductant-driven with scavenging (D-F) and #3: phosphorus input driven (G-I)). Each model scenario has already been shown to be consistent with stepwise oxygenation, but each shows a distinctly different pattern in phosphate abundance, productivity and carbon burial. In #1, riverine P input is fixed, and P concentration is controlled solely by sedimentary burial and recycling. As recycling is more prominent under low O_2, the P concentration, productivity and burial all decrease as the reductant input declines and O_2 rises. In #2, the addition of the Fe-scavenging flux under an anoxic deep ocean results in the removal of significant amounts of SRP when the deep ocean becomes anoxic. In this scenario the SRP concentration, productivity and burial all increase as the deep ocean becomes oxygenated. Finally, in #3, reductant input is fixed and the riverine P input is varied. SRP is now controlled both by riverine input rates and recycling rates, with the former dominating the latter. Here, SRP abundance, and productivity and carbon burial all increase as P input increases.

Overall, we show here that stepwise oxygenation can occur in this model under either an increasing, static, or decreasing P inventory and C burial over Earth history.

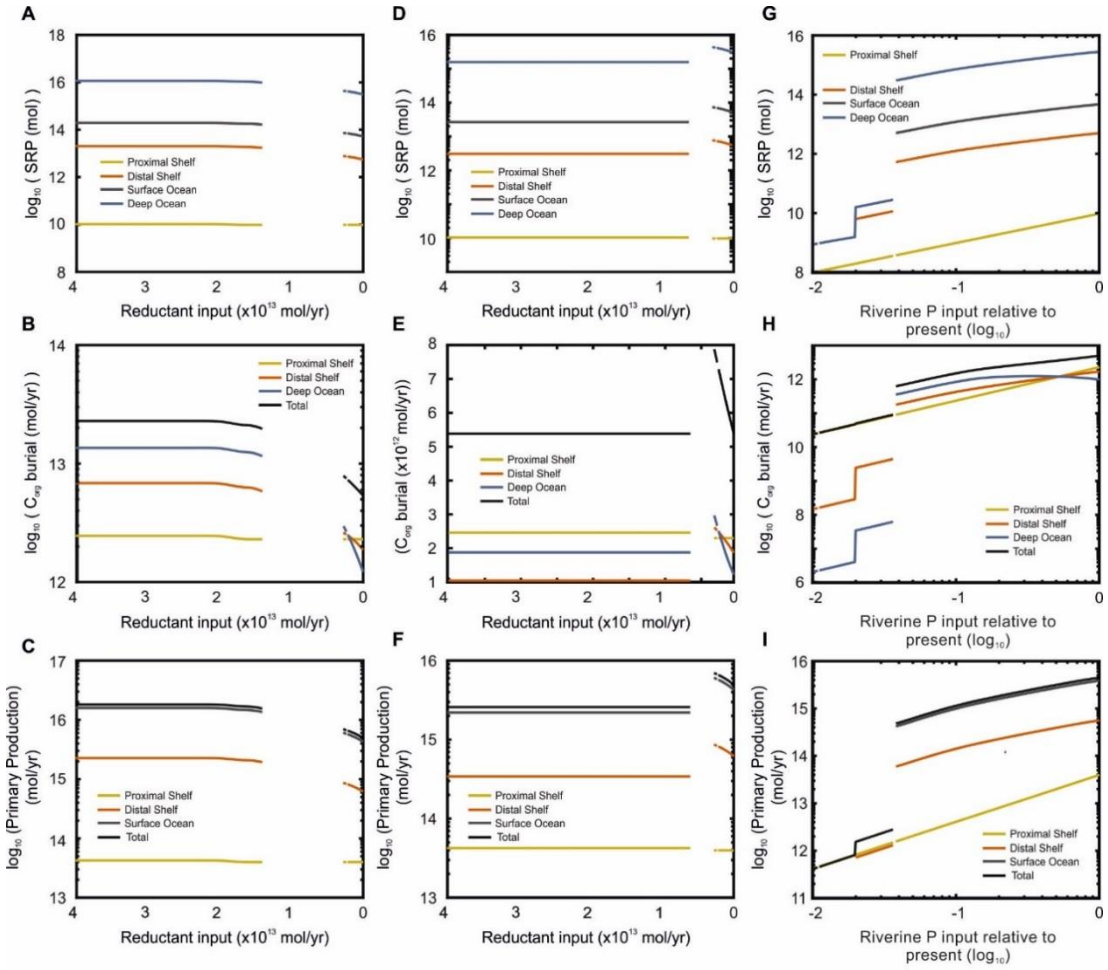

Figure 5.9. *(A, D, G) Soluble Reactive Phosphorus (mol) for all ocean reservoirs. (B, E, H) Total C_{org} burial for all ocean-sediment fluxes (molyr^{-1}). (C, F, I) Primary production flux of organic carbon for respective ocean reservoirs (molyr-1). Panels A, B and C show results in accordance with Figure 3, panels D, E and F show results in accordance with Figure S2 (scavenging included) G, H and I show results with varying riverine P input. (A, B, C) No iron-bound scavenging was used and redox dependencies of 50% - P_{aut}, 25% - P_{org} following Slomp and Van Cappellen (2007). (D, E, F) Iron bound scavenging of 25% of upwelled P (maximum value of 5 x 10^{10}) with redox dependencies following Slomp and Van Cappellen (2007) (50% - P_{aut} and 25% - P_{org}). (G, H, I) Steady state responses with varying riverine P input relative to present with redox dependencies following Slomp and Van Cappellen (2007) (50% - P_{aut} and 25% - P_{org}). Regions where the lines do not continue represent unstable solutions.*

Chapter 6 The rise of phosphorus recycling facilitated Earth's Great Oxidation Event

Preface

The contents of this chapter has been submitted as:

Alcott, L. J., Mills, B. J. W., Bekker, A. and Poulton, S. W. The rise of phosphorus recycling paved the way for the Great Oxidation Event. (*submitted*).

The manuscript is reproduced here in full.

Article

The rise of atmospheric oxygen during the Great Oxidation Event (GOE) ~2.4 billion years ago (Ga) was a defining transition in the evolution of global biogeochemical cycles and life on Earth (Canfield, 2005; Zerkle et al., 2017). There is, however, abundant evidence for mild oxidative continental weathering and the development of ocean oxygen oases several hundred million years prior to the GOE (Anbar et al., 2007; Kendall et al., 2010; Ostrander et al., 2019; Ossa Ossa et al., 2019). The GOE thus represents a threshold, whereby primary productivity and O_2 production overwhelmed the input of reduced species that consume O_2 (Goldblatt et al., 2006; Claire et al., 2006; Kump and Barley, 2007), and its timing is assumed to be related to a balance between the riverine input of the major limiting nutrient, phosphate (Greber et al., 2017), and the dynamics of the solid Earth (Lee et al., 2016). However, the sequence of events that ultimately facilitated persistent atmospheric oxygenation remains elusive. Here, we report novel geochemical analyses of ~2.65 to 2.43 Ga drill core samples from the Transvaal Supergroup, South Africa, which document an early rise of sedimentary phosphorus recycling as dissolved sulfide became more abundant in the ocean system, which itself was a progressive response to the onset of oxidative continental weathering. Biogeochemical modelling of the C-O-P cycles, based on our data, shows that the evolution of phosphorus recycling was a critical step change in biogeochemical cycling that likely supported Earth's first persistent rise in atmospheric oxygen.

6.1 Main Text

The evolution of oxygenic photosynthesis resulted in the first development of locally oxygenated surface waters in continental margin settings during the late Archean (Anbar et al., 2007; Kendall et al., 2010). These "oxygen oases" apparently became more expansive between ~2.9 and ~2.5 Ga (Ossa Ossa et al., 2019; Ostrander et al., 2019), prior to the start of the GOE at ~2.4 Ga. This progressive surface ocean oxygenation occurred against a backdrop of persistently anoxic, ferruginous (iron-rich) deep-ocean conditions (Poulton and Canfield, 2011), but enhanced oxidative continental weathering also increased the delivery of sulfate to the ocean system, thus increasing the production of dissolved sulfide (Canfield, 2005). In addition to an expansion of sulfidic pore waters, this led to spatially and temporally restricted episodes of ocean euxinia (sulfidic water-column conditions) in some Neoarchean continental margin settings (Reinhard et al., 2009; Kendall et al., 2010; Scott et al., 2011).

These progressive changes in ocean and sediment redox conditions prior to the GOE would be expected to exert a major control on the bioavailability of phosphorus (Poulton, 2017). Phosphorus (P) is generally considered to have been the major limiting nutrient throughout Earth history (Tyrrell, 1999), but was likely scarce during the Archean due to extensive drawdown and fixation in association with iron minerals under widespread ferruginous conditions (Bjerrum and Canfield, 2002; Reinhard et al., 2017; Ossa Ossa et al., 2019). This "iron-trap" is thought to have limited primary productivity and organic carbon burial, such that the global sinks for oxygen (continental weathering and oxidation of reduced hydrothermal inputs) exceeded its production, maintaining an anoxic atmosphere (Canfield, 2005; Reinhard et al., 2017). However, the rise of sulfidic environments would have limited this drawdown and fixation of P in association with reactive Fe minerals, due to the transformation of such minerals to pyrite, to which P does not significantly adsorb (Krom and Berner, 1981). In addition, organic-bound P is preferentially released from organic matter (C_{org}) during anaerobic remineralisation, particularly during the production of sulfide by sulfate-reducers, which drives to high C_{org}/P_{org} ratios relative to the Redfield Ratio (Ingall et al., 1993; Ingall and Jahnke, 1994).

These processes result in the release of bioavailable P, either directly to the water column under euxinic conditions or to pore waters in sulfidic sediments, although a proportion of the P released to pore waters may undergo "sink switching" to authigenic phases such as carbonate fluorapatite (Ruttenberg and Berner, 1993) or vivianite (Xiong et al., 2019; Dijkstra et al., 2014). Nevertheless, this P release would ultimately drive further surface ocean primary productivity and carbon burial, hence increasing O_2 production (Van Cappellen and Ingall, 1994). However, the rise of P recycling has not previously been considered in relation to either the GOE or the gradual oxygenation of Earth's surface during the late Archean. Instead, studies of early Earth oxygenation have tended to focus on the weathering input of phosphate, or on mechanisms that directly consume or produce free O_2, such as the nature of the hydrothermal influx, oxidation of reduced gases, or escape of hydrogen to space (Catling et al., 2001; Kump and Barley, 2007; Lee et al., 2016; Greber et al., 2017). Given the >10 fold increase in sedimentary P release that commonly occurs under anoxic, sulfidic conditions (Van Cappellen and Ingall, 1994), the impact of P recycling has the potential to overwhelm other Earth system controls on oxygenation (Alcott et al., 2019).

To investigate the role of anaerobic P recycling as sulfide became more abundant in the ocean system prior to the GOE, we analysed four cores through the ~2.65 to 2.43 Ga Campbellrand and overlying Koegas subgroups, South Africa (Fig. 6.1; see Supplementary Information for full details on the geologic setting and all data). Existing (Kendall et al., 2010; Zerkle et al., 2012a) and new geochemical data (see Methods) for the older part of the stratigraphic succession from the GKF01 (proximal) and GKP01 (distal) drill cores demonstrate a complex redox history across the continental shelf-slope transect (Fig. 1). Samples from below the ~2650 Ma Lokammona Formation show evidence of deposition under fluctuating oxic (Fe_{HR}/Fe_T <0.22; Fe/Al <0.66) to ferruginous (Fe_{HR}/Fe_T >0.22; Fe/Al >0.66; Fe_{py}/Fe_{HR} <0.7) bottom waters. However, as with most of the older Archean shales, Fe_{py}/Fe_{HR} ratios are relatively high, including some samples deposited under oxic water-column conditions, demonstrating that pore waters were sulfidic during early diagenesis (Hardisty et al., 2018). This redox condition can be thought of as an intermediate between three distinct end members (oxic, euxinic and low-TOC ferruginous conditions). The determining factors to allow for this sliding scale include oxygen and

sulfate/sulfide availability but also TOC which is required to reduce both sulfate and ferric iron. Clear TOC and pyrite concentration differences can be seen between the earlier (GKF01 and GKP01) and the later (GTF01 and GEC01) suggesting both may have played a role in the differing redox states. The Lokammona and Monteville formations also show evidence for deposition beneath oxic bottom waters, but some samples have higher Fe_{HR}/Fe_T (>0.38) and Fe_{py}/Fe_{HR} (>0.7) ratios, potentially indicating euxinic depositional conditions.

However, pyrite textures in these samples are more consistent with intense sulfide production during very early diagenesis beneath a ferruginous water column (see Supplementary Information), which was likely stimulated by a higher rate of organic matter burial (Fig. 6.1A, B).

The lower and upper Nauga formations contain intervals deposited beneath partially oxic surface waters, based on Fe speciation and trace metal systematics (Kendall et al., 2010), but other horizons in these units with elevated Fe_{HR}/Fe_T (>0.38) and low Fe_{py}/Fe_{HR} (<0.7) suggest redox fluctuations between oxic and ferruginous conditions. The lower part of the Klein Naute Formation dominantly shows evidence of anoxic deposition (elevated Fe_{HR}/Fe_T and/or high Fe/Al), with some intervals of high Fe_{py}/Fe_{HR} (>0.7) suggesting the development of water-column euxinia, which is supported by pyrite textures in these samples (see Supplementary Information). The overlying Kuruman Iron Formation documents an extensive interval of iron formation deposition, which persisted during deposition of most of the overlying sediments in the GTF01 and GEC01 cores. Here, the iron mineralogy is characterised by high concentrations of Fe-rich silicates, giving relatively low Fe_{HR}/Fe_T ratios (Fig. 6.1). However, elevated Fe/Al and low Fe_{py}/Fe_{HR} ratios support persistent deposition under anoxic, ferruginous conditions.

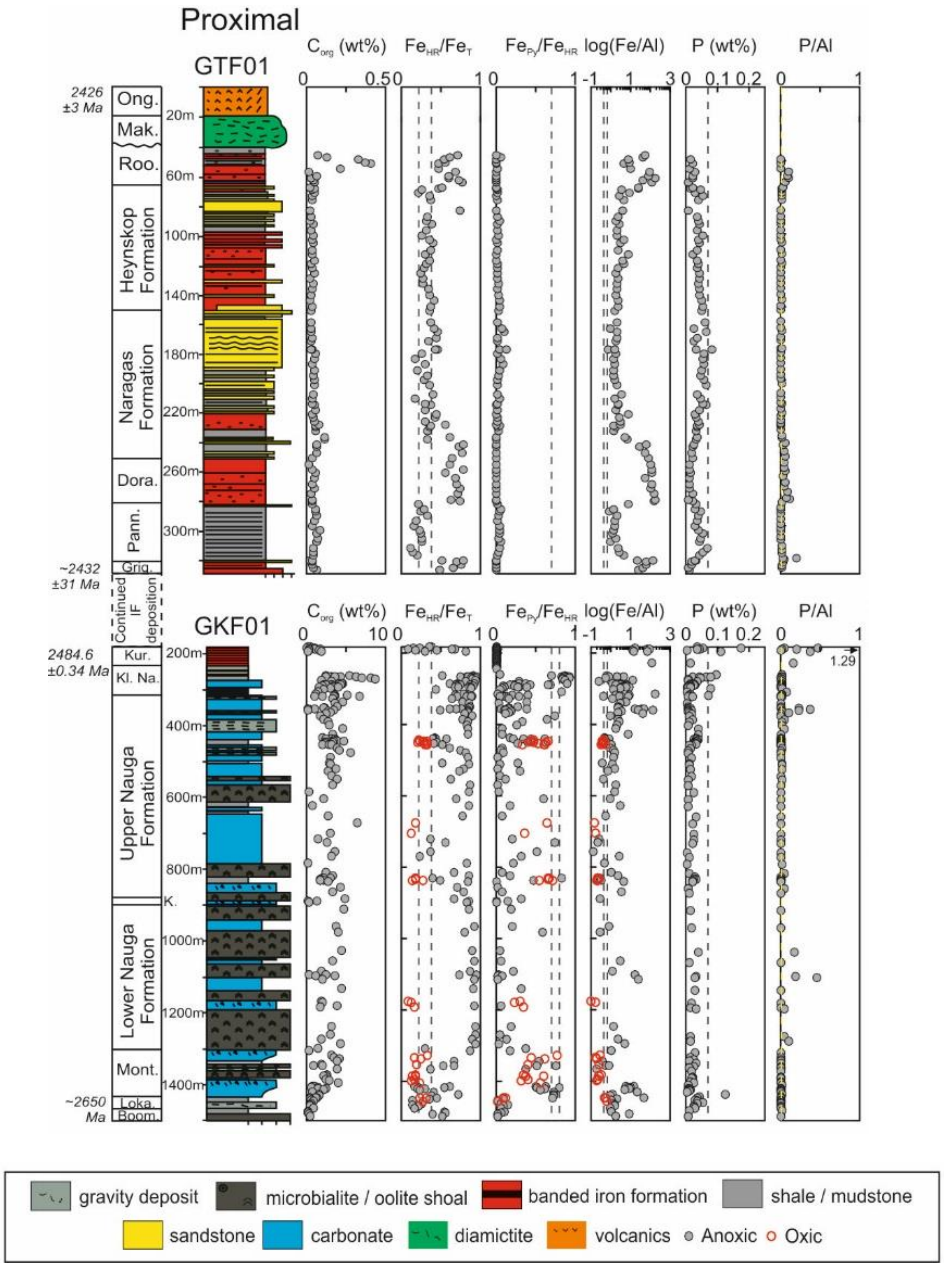

Figure 6.1A. *Stratigraphy and geochemistry of the studied drill cores (Schröder et al., 2011; Schröder, 2006; Gumsley et al., 2017; Trendall et al., 1990; Lantink et al., 2019; Gutzmer and Beukes, 1998). Grainsize divisions are mudstone, siltstone, sandstone, and breccia for the two Koegas Subgroup drill cores, and mudstone, sandstone, and boundstone for the two Campbellrand Subgroup drill cores. Dashed lines on the* Fe_{HR}/Fe_T *plots represent the defined boundaries for identifying oxic and anoxic deposition, with equivocal samples falling between these lines. Dashed line on* Fe_{Py}/Fe_{HR} *plots distinguishes euxinic from ferruginous deposition for grey circles (representing samples clearly deposited from an anoxic water-column), whereas red open circles likely represent deposition under oxic conditions, and hence* Fe_{py}/Fe_{HR} *ratios for these samples reflect production of sulphide during early diagenesis.*

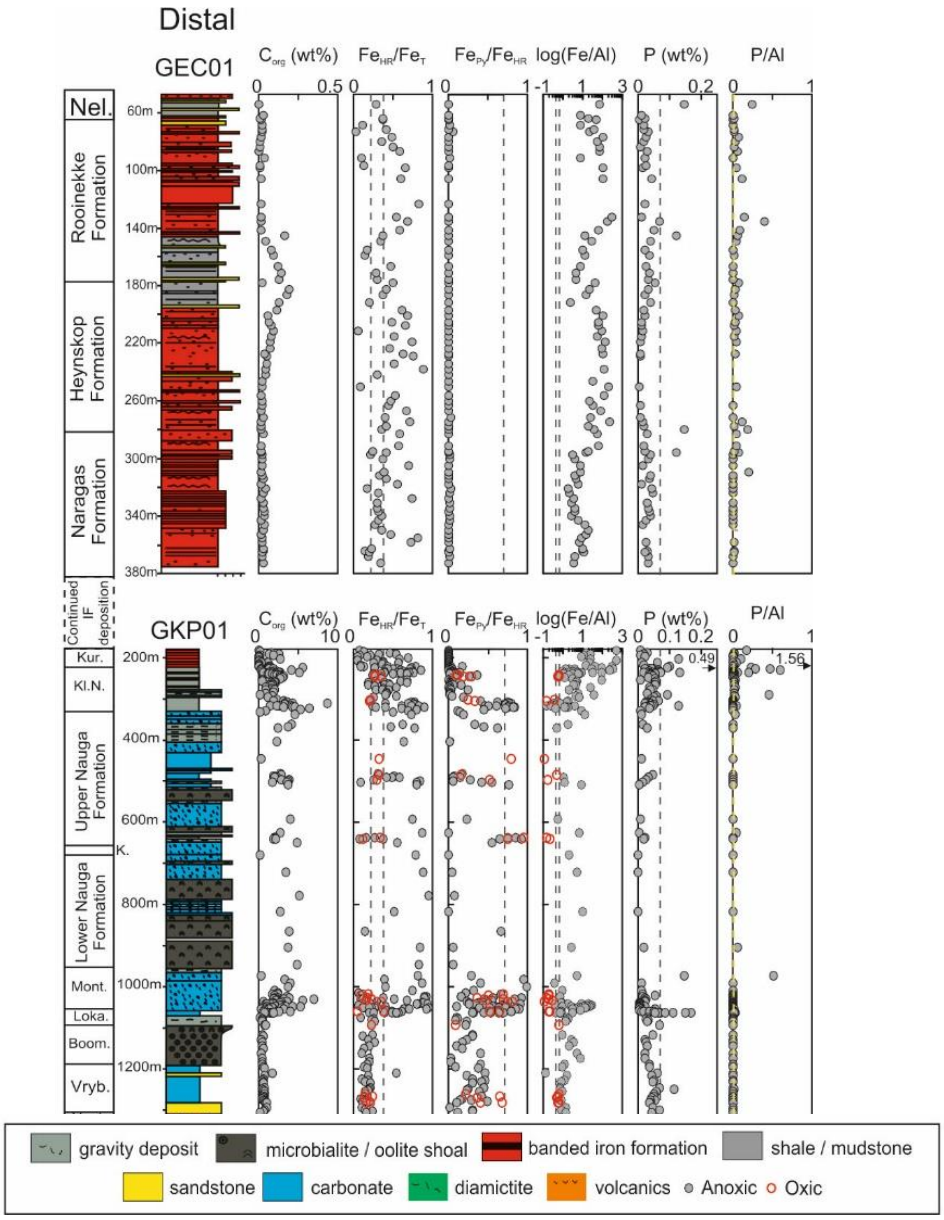

Figure 6.1B. *continued. Dashed lines on Fe/Al plots represent the normal range for oxic deposition. Dashed lines on the P and P/Al plots represent the average shale. Fe/Al and P/Al ratios are reported as wt%/wt%. Ong. – Ongeluk Formation; Mak. – Makganyene Formation; Roo. – Rooinekke Formation; Dore. – Doredale Formation; Pann. – Pannetjie Formation; Griq. – Griquatown Iron Formation; Nel. – Nelani Formation; Kur. – Kuruman Iron Formation; Kl. Na. – Klein Naute Formation; K. – Kamden Member; Mont. – Monteville Formation; Loka. – Lokamonna Formation; Boom. – Boompaas Formation; Vryb. – Vryburg Formation; Vent. – Ventersdorp Group.*

Phosphorus concentrations are generally below the average shale value throughout the succession, although normalisation to Al suggests that the majority of samples are similar to average shale (Fig. 6.1). There are exceptions, however, and the high P concentrations that occur in the Monteville and Klein Naute formations (drill cores GKF01 and GKP01) are likely due to elevated organic content in these samples. Notably, high P concentrations and P/Al ratios also occur in the Kuruman Iron Formation, which contrasts with the generally much lower P content of the overlying iron formations of the Koegas Subgroup (GTF01 and GEC01 drill cores; Fig. 6.1).

To evaluate the potential for phosphorus recycling we determined the phase portioning of P via a novel, recently developed (Thompson et al., 2019) extraction scheme (Fig. 6.2).

All data for the two drill cores (GKP01 and GKF01) that represent the older part of the succession have C_{org}/P_{org} ratios that are highly elevated, relative to both the Redfield Ratio of 106:1, and the predicted ratio of ~300:1 for organic matter buried under the P-limited conditions inferred for the early Precambrian (Reinhard et al., 2017). This suggests extensive preferential release of P during anaerobic organic matter remineralisation (Ingall et al., 1993). To evaluate whether this P was recycled to the water column or fixed as authigenic phases in the sediment, we define a reactive P pool (P_{reac}), which in addition to P_{org}, includes the phases that may sequester dissolved P (e.g., authigenic P, $P_{aut,}$ and iron-bound P, P_{Fe}). With the exception of some ferruginous shale and iron formation samples (where in addition to the organic P sink, drawdown would also have occurred in association with Fe minerals, giving low initial C_{org}/P_{reac} ratios), most samples continue to plot well above the Redfield Ratio, demonstrating extensive recycling of P back to the water column (Ingall and Jahnke, 1994). This recycling is evident in all euxinic and oxic samples, and a large proportion of ferruginous samples (Fig. 6.2A), highlighting that reducing conditions close to the sediment-water interface, and particularly the development of sulfidic porewaters, likely exerted the primary control on P recycling. As seen in the sedimentary logs, some portions of the older sections are relatively carbonate rich. To try to ensure lithology does not play a major role in some of our interpretations, we investigate the progressive redox changes as opposed to strict water column conditions, in addition to ensuring any carbonate rich samples satisfy conditions in which iron speciation can be utilised (Clarkson et al., 2014). The extent of sulfidation of iron minerals allows the

P_{Fe} sink to become diminished via the formation of pyrite demonstrating that appreciable Fe_{py}/Fe_{HR} ratios correspond to elevated C_{org}:P_{reac} ratios (Figure 6.2B). This also provides support for the importance of the sulfur cycle in preferential recycling of P_{org} with respect to C_{org} as high C_{org}:P_{org} ratios also fit this trend. Several samples that indicate intense ferruginous bottom water conditions (as defined by iron speciation) also plot above the Redfield ratio but are also found to have vanishingly low total phosphorus concentrations (Figure 6.2C). This suggests that phosphorus speciation can be applied to these ancient sediments effectively where sufficient phosphorus is present (in a similar sense to a minimum of 0.5 wt% iron being required for trustworthy iron speciation data). Further investigation and analyses should be undertaken in order to formally define this lower limit. Alternatively, the preservation potential of organic carbon has been proposed to be heightened with the presence of abundant iron oxides (e.g. Lalonde et al., 2012). Whether or not the remaining components of the initial organic matter (e.g. P_{org}) are also preserved is yet to be seen but could explain the elevated C_{org} concentrations under intense ferruginous conditions whilst containing limited organic phosphorus (which would be expected to be recycled). Statistical analyses were attempted to distinguish separate C:P ratio ranges and upper and lower interquartile ranges. Due to the harsh boundary conditions of the redox definitions (e.g. <0.7 Fe_{py}/Fe_{HR}), the ranges displayed significant overlap as ferruginous conditions with elevated pyrite formation (e.g. 0.69 = Fe_{py}/Fe_{HR}) can display significant P recycling. This additional consideration is in line with our hypothesis of sulfide production at or near the sediment-water interface and not within a euxinic water column.

The overlying interval of ~2.48 to 2.43 Ga iron formation (Fig. 6.1) records a secular event driven by the emplacement of Large Igneous Provinces (LIPs) and an exceptionally high submarine hydrothermal flux (Bekker et al., 2013a; Gumsley et al., 2017; Bekker et al., 2013b). High concentrations of P are apparent during the earliest stages of the Kuruman Iron Formation deposition (Fig. 6.1), supporting extensive P drawdown in association with Fe minerals from a water column that was initially enriched in recycled P. Subsequently, generally muted P concentrations (drill cores GTF01 and GEC01) reflect the maintenance of decreased water-column P concentrations during a prolonged period of iron formation deposition. Indeed, a significant proportion of samples have C_{org}/P_{reac} ratios that fall below the Redfield

Ratio (Fig. 2D), consistent with drawdown of P in association with Fe minerals. However, some samples (particularly shales) have C_{org}/P_{org} and C_{org}/P_{reac} ratios that fall above the Redfield Ratio (and above the predicted ratio of ~300:1 for organic matter buried under P-limited conditions), likely reflecting significant P recycling back to the water column during early diagenetic Fe-mineral transformation.

Furthermore, while P recycling and organic carbon burial was clearly less extensive when BIFs were deposited, the riverine input of P was likely high due to enhanced chemical weathering in association with LIP emplacement at this time (Gumsley et al., 2017), and thus water-column P concentrations may locally have remained relatively high. This is supported by an array of samples that have C_{org}/P_{org} ratios close to the Redfield Ratio (Fig. 2B), suggesting that water-column conditions were not strongly or persistently oligotrophic during BIF deposition.

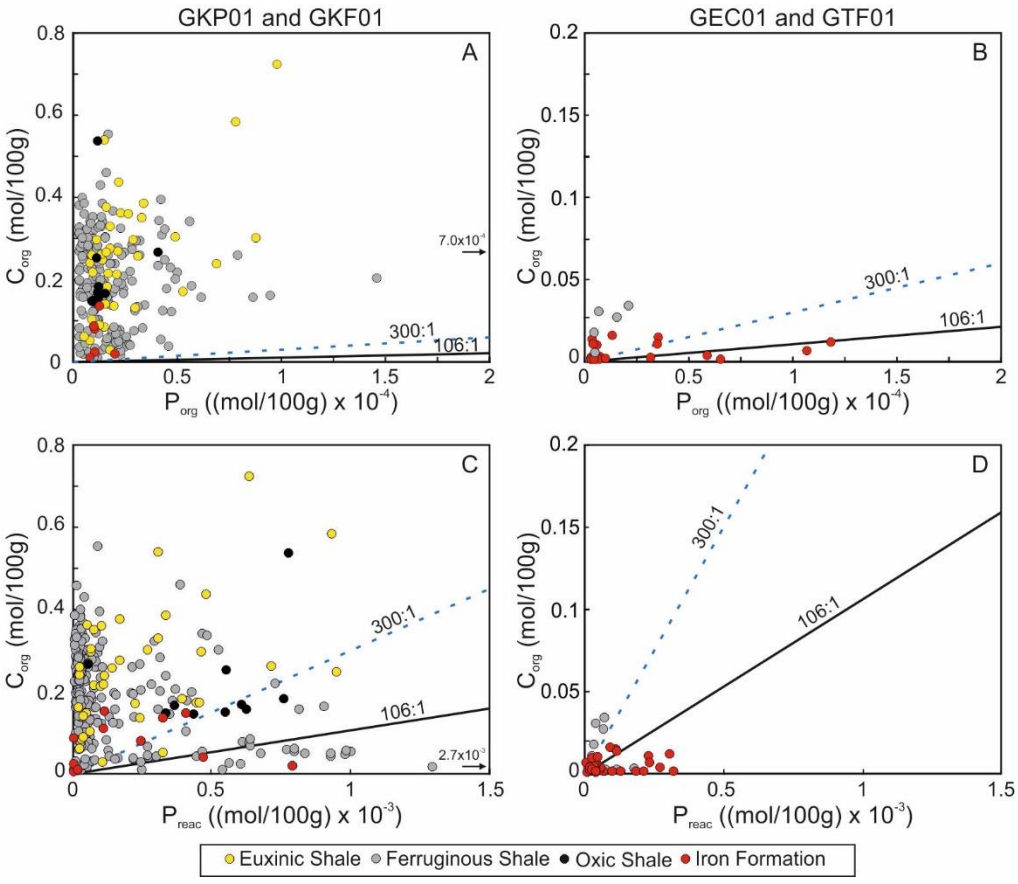

Figure 6.2.A *Relationships between organic carbon and different phosphorus pools. (A) C_{org}:P_{org} for the Ghaap Group drill cores (GKF01 and GKP01); (B) C_{org}:P_{org} for the Koegas Subgroup drill cores (GTF01 and GEC01); (C) C_{org}:P_{reac} for the Ghaap*

Group drill cores; (D) C_{org}:P_{reac} for the Koegas Subgroup drill cores. Dashed lines represent the Redfield Ratio (106:1) and the inferred C_{org}/P_{org} ratio for the early Precambrian sediments deposited under highly oligotrophic P-limited conditions (300:1(Reinhard et al., 2017)).

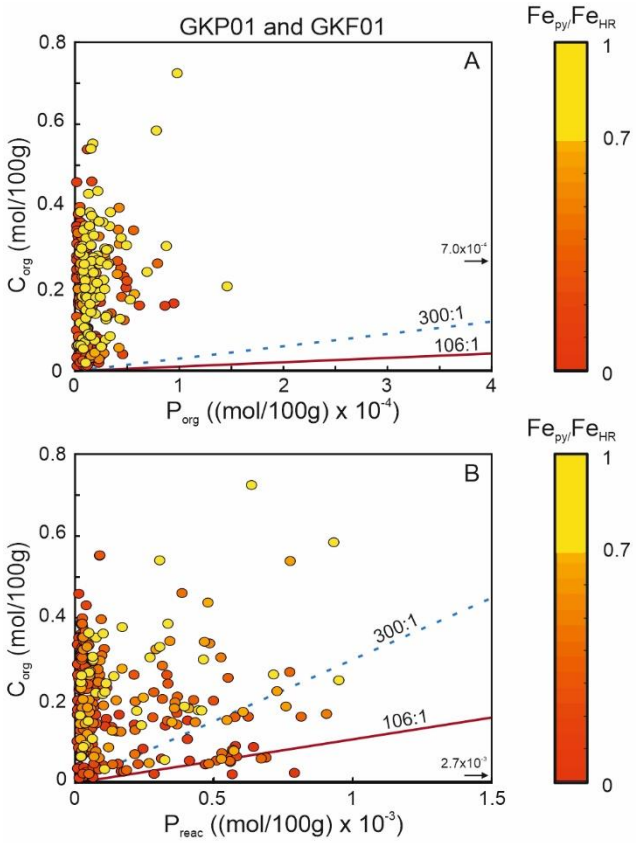

Figure 6.2.B *Relationships between organic carbon and different phosphorus pools. (A) C_{org}:P_{org} for the Ghaap Group drill cores (GKF01 and GKP01); (B) C_{org}:$P_{reac.}$ Colour of data describes the Fe_{py}/Fe_{HR} ratio of the studied sample. Dashed lines represent the Redfield Ratio (106:1) and the inferred C_{org}/P_{org} ratio for the early Precambrian sediments deposited under highly oligotrophic P-limited conditions (300:1(Reinhard et al., 2017)).*

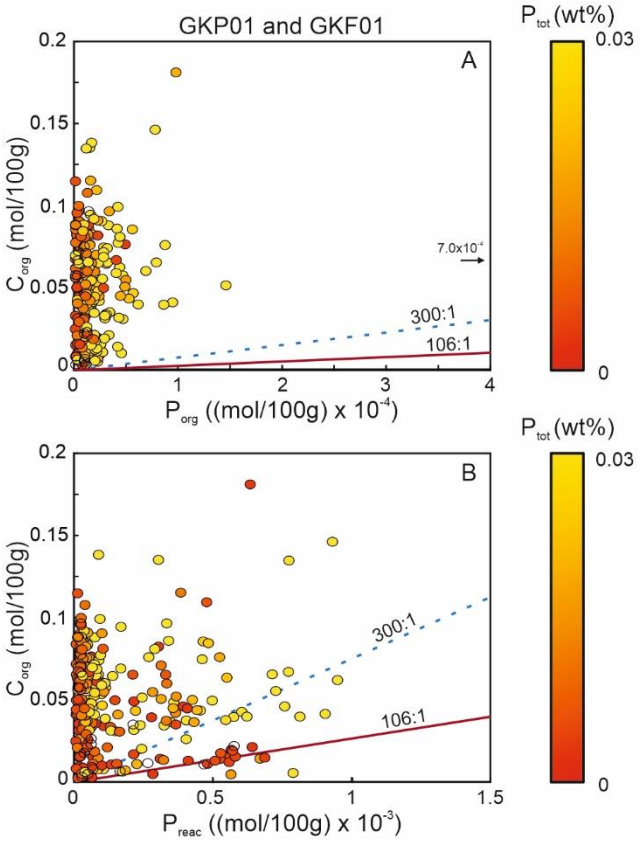

Figure 6.2.C *Relationships between organic carbon and different phosphorus pools. (A)* C_{org}*:*P_{org} *for the Ghaap Group drill cores (GKF01 and GKP01); (B)* C_{org}*:*$P_{reac.}$ *Colour of data describes the total P concentration of the studied sample. Dashed lines represent the Redfield Ratio (106:1) and the inferred* C_{org}*/*P_{org} *ratio for the early Precambrian sediments deposited under highly oligotrophic P-limited conditions (300:1(Reinhard et al., 2017)).*

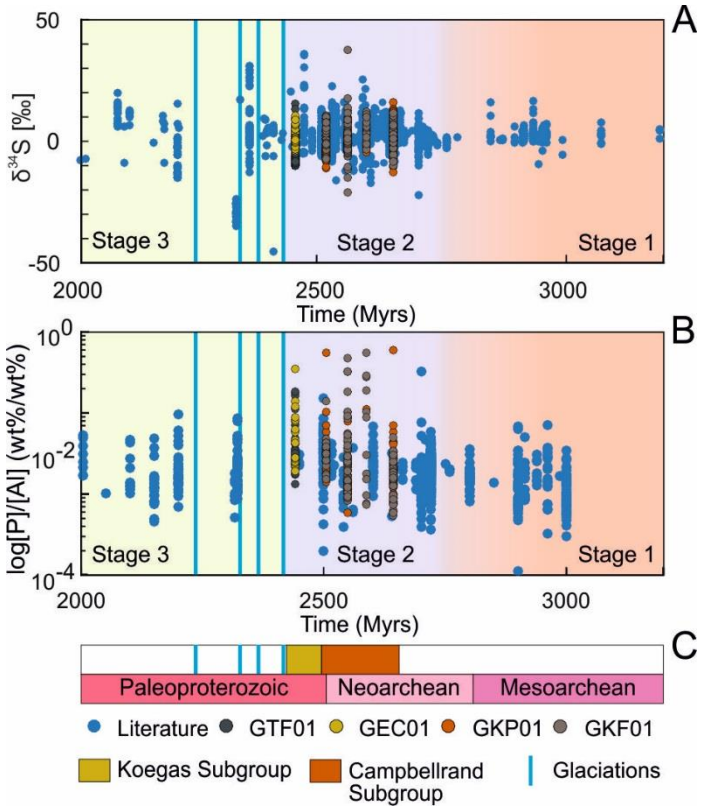

Figure 6.3. *Long-term trends in the phosphorus content and the sulphur isotope composition of marine sediments, highlighting Stages 1 to 3 in the progressive oxygenation of the early Earth. Stage 1: approximately 3.2 – 2.7 Ga; Stage 2: approximately 2.7 – 2.43 Ga. Stage 3: approximately 2.43 to 2.0 Ga. (A) Whole-rock $\delta^{34}S$ compilation, including data for the GKF01 and GKP01 drill cores, which demonstrates a progressively increasing range in $\delta^{34}S$ data through the three stages (Havig et al., 2017). The Koegas Subgroup sulfur isotope data is from Johnson et al., 2013(Johnson et al., 2013). (B) An expanded dataset showing published P/Al ratios (Reinhard et al., 2017) and P/Al ratios for the GTF01, GEC01, GKF01, and GKP01 drill cores (see Supplementary Information).*

The overlying interval of ~2.48 to 2.43 Ga iron formation (Fig. 6.1) records a secular event driven by the emplacement of Large Igneous Provinces (LIPs) and an exceptionally high submarine hydrothermal flux (Bekker et al., 2013a; Gumsley et al., 2017; Bekker et al., 2013b). High concentrations of P are apparent during the earliest stages of the Kuruman Iron Formation deposition (Fig. 6.1), supporting extensive P drawdown in association with Fe minerals from a water column that was initially enriched in recycled P. Subsequently, generally muted P concentrations (drill cores GTF01 and GEC01) reflect the maintenance of decreased water-column P concentrations during a prolonged period of iron formation deposition. Indeed, a significant proportion of samples have C_{org}/P_{reac} ratios that fall below the Redfield Ratio (Fig. 6.2D), consistent with drawdown of P in association with Fe minerals. However, some samples (particularly shales) have C_{org}/P_{org} and C_{org}/P_{reac} ratios that fall above the Redfield Ratio (and above the predicted ratio of ~300:1 for organic matter buried under P-limited conditions), likely reflecting significant P recycling back to the water column during early diagenetic Fe-mineral transformation. Furthermore, while P recycling and organic carbon burial was clearly less extensive when BIFs were deposited, the riverine input of P was likely high due to enhanced chemical weathering in association with LIP emplacement at this time (Gumsley et al., 2017), and thus water-column P concentrations may locally have remained relatively high. This is supported by an array of samples that have C_{org}/P_{org} ratios close to the Redfield Ratio (Fig. 6.2B), suggesting that water-column conditions were not strongly or persistently oligotrophic during BIF deposition.

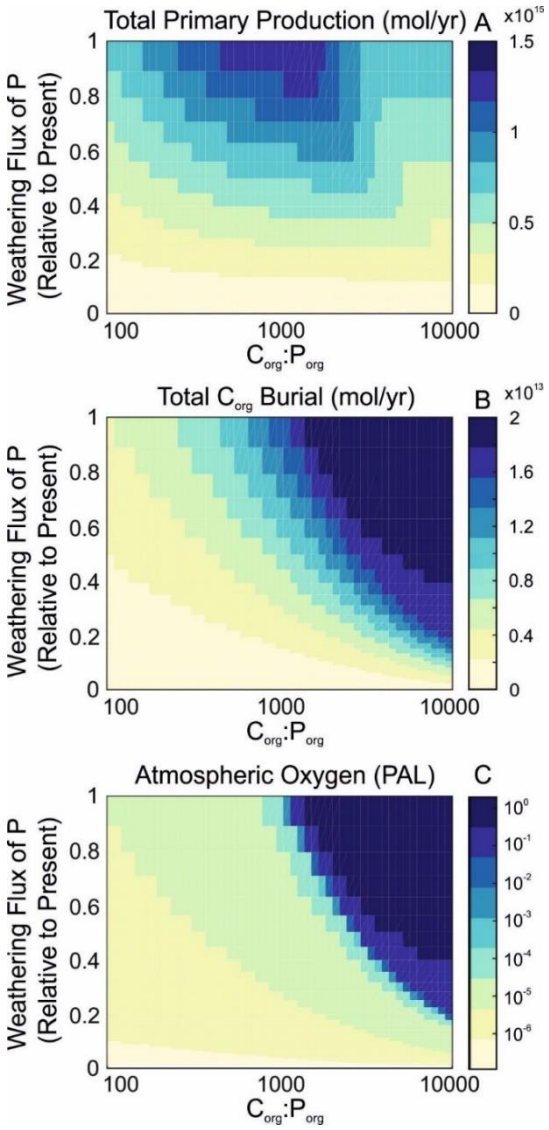

Figure 6.4. *Steady-state model solutions for a fixed reduced gas flux. (A) Total primary organic carbon production (moles C/year). (B) Total organic carbon burial (moles C/year). (C) Atmospheric oxygen concentration in PAL units.* C_{org}/P_{org} *ratios for Phanerozoic shales commonly exceed several thousand (Ingall et al., 1993), consistent with the average value of ~5000 ± 3000 for shales in the GKP01 and GKF01 drill cores.*

We note that the Transvaal Supergroup contains an unconformity at the top of the Koegas Subgroup beneath the oldest glacial diamictite (Makganyene Formation) of the GOE (Fig. 6.1). Therefore, the behaviour of the P cycle immediately prior to the onset of the GOE is unclear. Thus, to provide global context, we also consider the longer-term pyrite sulphur isotope record (Fig. 6.3A), which demonstrates a clear and consistent increase in the range of $\delta^{34}S$ values from the Mesoarchean (which we define as Stage 1 in Earth's early oxygenation history) through the more expansive, but still localized, continental margin oxygenation of the Neoarchean (which we term Stage 2). This likely represents a gradual increase in seawater sulfate concentration driven by oxidative continental weathering (Canfield, 2005), thus leading to an increase in sulfide availability in the ocean system. More extensive anaerobic recycling of P from Stage 1 to Stage 2 would be a natural consequence of this increase in sulfide availability, and, consistent with this, the longer-term P record (Fig. 3B) documents elevated P content at times in Stage 2 when P was drawn down and fixed in the sediment (e.g., during some shorter-term intervals of iron-formation deposition).

Our data imply that long-term oxygenation in the run up to the GOE may have been promoted by increased recycling of P from the sediments. This mechanism would have operated in addition to any changes in weathering-related input of P (i.e., via the emergence of appreciable subaerial landmasses (Bindeman et al., 2018), a secular increase in the continental phosphorus inventory (Greber et al., 2017; Cox et al., 2018), or the emplacement of LIPs (Gumsley et al., 2017)). To evaluate how changes to P recycling versus P input may have influenced planetary oxygenation we utilise a modified biogeochemical model of the C-O-P cycles (Alcott et al., 2019) (see Methods). We run the model to steady state under changes in both the continental P weathering input and the sedimentary P recycling rate, while keeping the global rate of reductant input fixed at a level inferred for the Paleoproterozoic (Kharecha et al., 2005; Olson et al., 2013). We find that both recycling and changes to the continental weathering influx of P can cause substantial changes to the atmospheric O_2 reservoir (Fig. 6.4). Assuming elevated sedimentary molar C:P ratios, as measured in the majority of our ferruginous and euxinic shale samples (~5000 ± 3000), the GOE transition could have occurred with only a moderate enhancement in continental weathering rates, at around 0.3 times the present-day P input rate, which is similar to recent calculations for apatite weathering on the early Earth (Hao et al., 2020).

When sedimentary molar C:P ratios are instead assumed to be ~300, the GOE transition requires a much larger, and highly unlikely (Hao et al., 2020), P input rate of around 2-3 times the present day. Thus, when considering a simplified version of the Earth system with phosphorus limited production, our model suggests that extensive phosphorus recycling is necessary to raise O_2 to post-GOE values. It appears that the rise of sedimentary P recycling was a necessary, prerequisite factor in paving the way for the GOE on Earth.

Reconstructions of the bioavailability of P, based on both the shale and iron formation records, have suggested that concentrations were persistently very low throughout the Archean, thus maintaining organic carbon burial and oxygen production at a low level (Bjerrum and Canfield, 2002; Reinhard et al., 2017). By contrast, we demonstrate here that the rise of sulfide in the ocean system, which was initiated by the onset of mild oxidative continental weathering, led to progressively enhanced anaerobic recycling of P, thus initiating a positive productivity feedback. This may have been the tipping point leading to an intermediate oxygenation state in the Earth System, characterised by more pervasive oxygenation of continental margin settings during the Neoarchean, but with the atmosphere being maintained in an anoxic state. Subsequently, extensive phosphorus recycling, possibly combined with a general increase in the continental weathering P influx (Bindeman et al., 2018; Gumsley et al., 2017), may have facilitated rates of oxygen production, resulting in the first persistent oxygenation of the atmosphere.

In extension to the behaviour of phosphorus in the run up to the GOE, the other commonly invoked limiting nutrient, nitrogen, can also be investigated with the phosphorus data. It is currently understood that the behaviour of the nitrogen cycle must have been drastically different from the present day under both anoxic ferruginous and euxinic conditions (e.g. Boyle et al., 2013; Mettam et al., 2019). Ferruginous conditions have been better explored, with the primary fixed nitrogen source thought to be ammonium as oxygen is not abundant enough to sustain an aerobic nitrogen cycle with appreciable concentrations of nitrate and nitrite (e.g. Michiels et al.,2017). In contrast, the behaviour of nitrogen under euxinic conditions requires diminished nitrate availability as it would outcompete sulfate reducers for the available organic carbon. Therefore, in order to promote productivity and oxygenation during these sulfide productive intervals in our dataset, the behaviour of the nitrogen

cycle must have also changed. Firstly, as we demonstrate that a benthic flux of phosphorus does not necessarily require water column euxinia but only sulfidic pore waters, the competition of nitrate and sulfate will not necessarily be occurring in the water column. Also, as this quantitative sulfide production is taking place within the sediment, we would not expect any enhanced trace metal drawdown in association with free H_2S to the extent of limitation on nitrogen fixation (Anbar and Knoll, 2002; Zerkle et al., 2006).

Although these cores have not been directly studied for nitrogen isotopes, a coeval shallower core from the same basin has been explored (BH-1 / Sacha core) (Mettam et al., 2019). Nitrogen isotopes of ~ 0 ‰ throughout this BH-1 core suggests appreciable nitrogen fixation or the complete utilization of remineralised ammonium with an isotopic composition of ~0 ‰ (Mettam et al., 2019). The limited evidence for nitrification/denitrification in these cores allows for the establishment of euxinic conditions at greater depths supporting the initial hypothesis of ammonium allowing for H_2S build up put forward by Boyle et al. (2013). Mettam et al. (2019) propose that upwelling of phosphorus rich deep waters stimulated primary productivity and an enhanced flux of organic matter that was subsequently remineralised, promoting ammonium availability. The work presented here provides a hypothesis on how these phosphorus rich waters formed and this study, alongside coeval nitrogen isotopes, offers a more conprehensive view into how nutrients behave in the anoxic ocean in the lead up to the GOE.

6.2 Supplementary Information

Geological and stratigraphic context

The Kaapvaal craton covers more than 10^6 km^2 with a general trend of older to younger successions from east to west, with the most ancient terranes being formed at ~3.6 Ga (James and Fouch, 2002). Continued cratonic development is viewed as being driven by a period of continental growth (starting at *c.* 3.1 Ga) until the final craton stabilization at approximately 2.6 Ga (James and Fouch, 2002). This period led to extensive development of depositional basins, including the two Neoarchean – Paleoproterozoic structural sub-basins considered in this study, the Transvaal and Griqualand West sub-basins (Moore et al., 2001). Both structural sub-basins preserve the Transvaal Supergroup, and were parts of a single depositional basin.

The Griqualand West sub-basin preserves the Ghaap Group (Figure 6.5), which correlates to the Chuniespoort Group of the Transvaal sub-basin (Moore et al., 2001). The Ghaap Group is considered to have undergone minimal metamorphism (sub-greenschist facies) and contains four subgroups (Kendall et al., 2013). The oldest, the Schmidtsdrif Subgroup, unconformably overlies the Ventersdorp Supergroup and contains tidal sandstones overlain by shallow-marine carbonates. The uppermost Schmidtsdrif Subgroup includes the Lokamonna Formation with deeper-water siliciclastic mudstones (Schröder, 2006). The Campbellrand Subgroup is dated at ~2.6 – 2.5 Ga (Altermann and Nelson, 1998; Sumner and Grotzinger, 2004) and records the development of an extensive carbonate platform, which was ultimately drowned to allow deposition of the Asbestos Hills Subgroup iron formations (Kendall et al., 2013). A switch from chemical sedimentation to siliciclastic-chemical deposition defines the transition from the Griquatown Iron Formation of the Asbestos Hills Subgroup to the Koegas Subgroup, which consists of several transgressive-regressive cycles deposited in a delta-submarine fan depositional setting (Schröder et al., 2011). This study primarily focuses on the Campbellrand, Asbestos Hills, and Koegas subgroups. We briefly describe the stratigraphy and sedimentology of these three subgroups here, with a more extensive review provided by Schröder et al. (2006; 2011 (Schröder et al., 2011)) (Figure 6.6).

The carbonate platform of the Campbellrand Subgroup includes the Monteville, Nauga, and Klein Naute formations. The Monteville Formation consists of metre-scale parasequences starting with slope dolostones, and progressing grades into dolograinstones and microbialites(Schröder, 2006). Underlying the Monteville Formation, the Lokamonna Formation is dated at ~2650 Ma (Gutzmer and Beukes, 1998) and consists of mixed shallow-marine carbonate-siliciclastics (Schröder, 2006). The Nauga Formation has been informally divided into lower and upper units. The lower Nauga Formation was also deposited on a slope and contains both microbialites and reworked carbonate lithologies. The upper and lower Nauga formations are separated by the Kamden Member. The upper unit was also deposited in a slope setting with a deepening and/or higher input of fine-grained detrital material (Schröder, 2006). The Klein Naute Formation contains massive and laminated siliciclastic mudstone with abundant diagenetic pyrite and chert nodules (Schröder, 2006), and is dated at ~2549 ± 7 Ma (Altermann and Nelson, 1998).

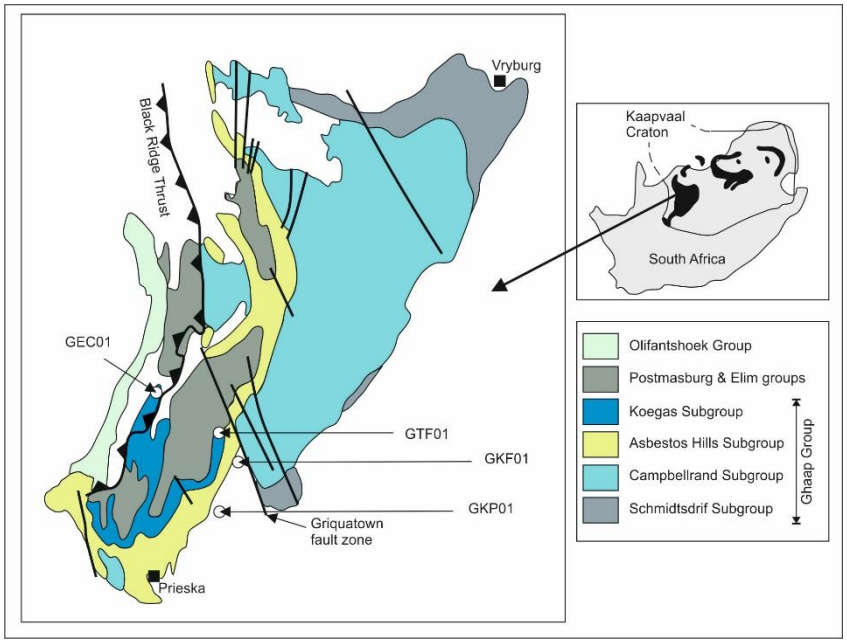

Figure 6.5. *Geological map of the Griqualand West sub-basin. Location of the four studied drill cores indicated by white dots. Inset map shows outcrop area of both the Griqualand West and Transvaal sub-basins, in addition to a generalised stratigraphy of the Ghaap Group.*

The Asbestos Hills Subgroup (~2.45 Ga (Trendall et al., 1990; Pickard, 2003)) conformably overlies the Campbellrand Subgroup and primarily includes iron formation and chert sediments (<1,000 m thick (Beukes, 1984)). The initial drowning of the Campbellrand carbonate platform led to deposition of banded iron formation and chert sediments of the Kuruman Iron Formation, leading into the granular iron formation of the Griquatown Iron Formation (Beukes, 1984). The Kuruman Iron Formation includes magnetite BIF and sideritic chert, and records persistent BIF deposition (Schröder, 2006) at 2,484.6 ± 0.34 Ma (Lantink et al., 2019). Following the Kuruman Iron Formation, the Griquatown Iron Formation consists of banded and granular iron formation sediments deposited in a relatively shallow-marine environment with storm and wave influence (Beukes, 1984). The Griquatown Iron Formation is dated at ~2432 ± 31 Ma (Trendall et al., 1990).

The Koegas Subgroup comprises intercalated siliciclastic and chemically precipitated iron-rich sediments (Schröder et al., 2011) and is older than the overlying Ongeluk Formation volcanics (2426 ± 3 Ma (Gumsley et al., 2017)). At the base of the Koegas Subgroup, the Pannetjie Formation contains an upward-coarsening mudstone to greywacke succession that is terminated by the Doradale Iron Formation, which marks the transition back to chemical precipitates (Schröder et al., 2011). Continued shallowing from the Doradale Iron Formation defines the transition to the Naragas Formation, with a greater proportion of sandstone towards the northeast as opposed to mudstone in the SW (Beukes, 1978). The third depositional cycle comprises the Heynskop Formation, which includes iron-rich lithologies, shallowing towards coarser siliciclastic units upsection (Schröder et al., 2011). The overlying Rooinekke Formation predominantly comprises banded iron formation and stromatolitic bioherms (Schröder et al., 2011). The Nelani Formation is only developed in the distal drill core sampled here (GEC01). The Koegas Subgroup contains modest manganese concentrations, the genesis of which has been linked to the development of oxygen oases (Kurzweil et al., 2016). The Makganyene Formation overlies the Koegas Subgroup and represents the oldest of the low-latitude glaciations associated with the Great Oxidation Event (Gumsley et al., 2017). The contact between the Makganyene Formation and Koegas Subgroup is considered to be erosional, but the missing period of time has recently been reduced by up to 200 Myrs (Gumsley et al., 2017).

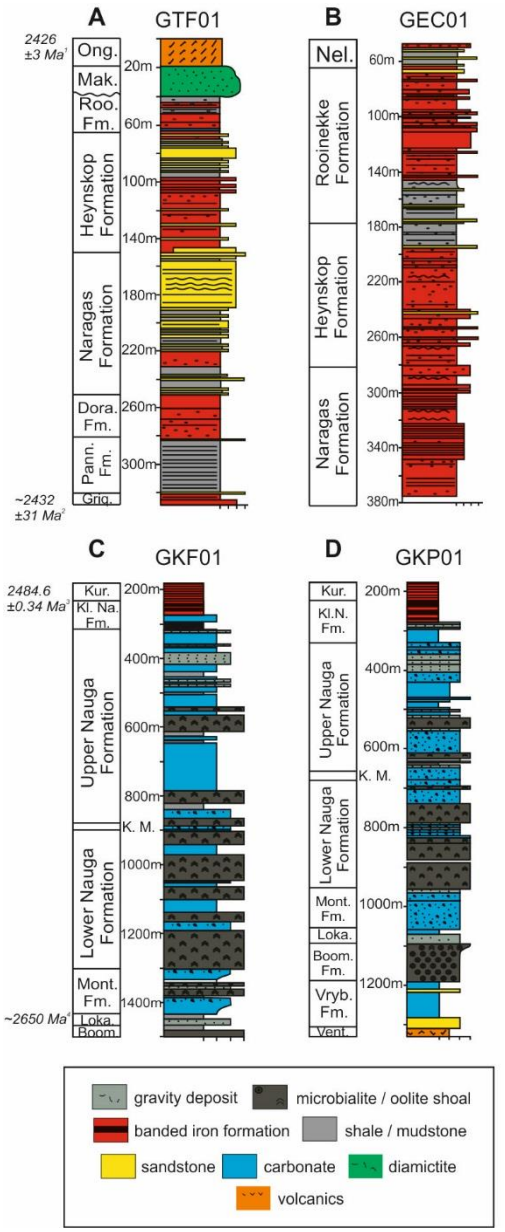

Figure 6.6. *Stratigraphic columns of the four studied drill cores (Schröder et al., 2006(Schröder, 2006); 2011(Schröder et al., 2011)). (A) GTF01 drill core. (B) GEC01 drill core. (C) GKF01 drill core. (D) GKP01 drill core. Abbreviations for formations: Ong. – Ongeluk Formation; Mak. – Makganyene Formation; Roo. – Rooinekke Formation; Dora. – Doredale Formation; Pann. – Pannetjie Formation; Griq. – Griquatown Iron Formation; Nel. – Nelani Formation; Dwyka. – Dwyka Formation; Kur. – Kuruman Iron Formation; Kl. Na. – Klein Naute Formation; K. – Kamden Member; Mont. – Monteville Formation; Loka. – Lokamonna Formation; Boom. – Boompaas Formation; Vryb. – Vryburg Formation; Vent. – Ventersdorp Group. Age constraints are from (1) Gumsley et al., 2017(Gumsley et al., 2017); (2) Trendall et al., 1990(Trendall et al., 1990); (3) Lantink et al., 2019(Lantink et al., 2019); (4) Gutzmer and Beukes, 1998(Gutzmer and Beukes, 1998).*

Samples and methods

Samples were taken from four well-preserved drill cores stored at the National Core Library in Donkerhoek, South Africa (Figure 6.6). The GKF01 and GKP01 drill cores represent proximal and distal sections of the Campbellrand-Malmani carbonate platform, respectively. Correlation between these two drill cores is primarily based on sequence stratigraphy, volcanic horizons, and similar lithologies (Schröder, 2006). The GTF01 and GEC01 drill cores also represent respectively more proximal and distal sections for the uppermost Asbestos Hills and Koegas subgroups (Schröder et al., 2011).

Iron speciation analysis was conducted via the well-established sequential extraction procedure of Poulton and Canfield (2005), with pyrite Fe (Fe_{Py}) quantified gravimetrically via chromous chloride distillation (Canfield et al., 1986). Solutions from the sequential extracts were analysed via AAS, and replicate extractions gave RSDs of <5% for all Fe phases. Total element concentrations (Fe, P, and Al) were determined on ashed samples via an HF-$HClO_4$-HNO_3 extraction, with HBO_3 used to ensure full solubilisation of Al. Solutions were analysed by ICP-OES with >98% recovery for all elements and RSDs of <5%. For organic carbon content, samples were treated with 50% vol/vol HCl prior to total organic carbon analysis using a LECO C/S analyser.

A highly reactive fraction (Fe_{HR}) is extracted from four operationally defined sedimentary phases; carbonate-associated iron (Fe_{Carb}), ferric oxides (Fe_{Ox}), mixed-valence iron oxides (principally magnetite (Fe_{Mag})), and pyrite-associated Fe (Fe_{py}). The ratio of this summed highly reactive fraction to total Fe concentration (Fe_T) is used to determine bottom-water redox conditions, whereby ratios < 0.22 are typically considered oxic, and ratios >0.38 define anoxic conditions (Poulton and Canfield, 2011). Intermediate values (0.22-0.38) are considered equivocal and require further investigation (see below). Further information on the redox state of the water column can be achieved via consideration of the ratio of Fe_{py} to Fe_{HR} for clearly anoxic samples (i.e., Fe_{HR}/Fe_T >0.38), in which Fe_{py}/Fe_{HR} ratios >0.7-0.8 identify euxinic conditions and ratios <0.7 identify ferruginous water-column conditions. The relatively high concentrations of siderite and pyrite present in the samples suggests minimal post-depositional oxidation, as would be expected with deep drill-core samples.

Equivocal Fe_{HR}/Fe_T ratios may occur due to either rapid sedimentation (which may mask the anoxic water-column conditions and limit deposition of minerals included in the Fe_{HR} pool such that enrichments are not evident in the sediment), or due to potential conversion of highly reactive iron to Fe-rich sheet silicates, which is a common process in ferruginous settings characterised by minimal sulphate reduction (e.g., (Poulton et al., 2010; Cumming et al., 2013; Doyle et al., 2018)). Fe_T/Al ratios can be used to address the latter case of diagenetic transfer of Fe_{HR} to Fe_{PRS}, since this metric is not affected by phase speciation, and ratios >0.66 are considered to provide a robust indication of anoxic water-column deposition (Clarkson et al., 2014). In order to discriminate between ferruginous shale and iron formation samples, we take the classic definition of iron formation, and assign a minimum value of 20 wt% Fe to identify iron formation samples. However, we stress that this distinction does not affect any of our interpretations or conclusions.

We utilised a revised P speciation technique (originally developed by Ruttenberg, 1992) for application to ancient rocks (Figure 6.7 (Thompson et al., 2019)). The sequential method targets 5 operationally defined phosphorus pools. These pools include ferric oxide-bound phosphorus (P_{Fe1} and P_{Fe2}), authigenic carbonate fluorapatite (CFA) associated P (P_{aut}), crystalline apatite-associated P (P_{cryst}), magnetite-associated P (P_{mag}), and organic-bound P (P_{org}). Here, for simplicity, we combine P_{Fe1}, P_{Fe2}, and P_{mag} to give the total P pool associated with Fe-oxide minerals (P_{Fe}). Phosphorus concentrations were generally determined spectrophotometrically on a Spectonic GENESYS^{TM} 6 at 880 nm, using the molybdate-blue method (Strickland and Parsons, 1972). However, the chemicals in the P_{Fe} (CDB and CDA; see Figure S3) and P_{mag} (ammonium oxalate) solutions interfere with colour development, and hence these solutions were analysed with ICP-OES (for specific details of ICP-OES configuration see Thompson et al., 2019).

On average, the summed sequential P extractions recovered 94% of the total P measured by bulk digest. Replicate analyses gave an RSD of ~10% for P_{aut} and P_{cryst} in addition to P_{mag} and P_{org} both providing a RSD of <13%. P_{Fe} was at very low concentration in our samples (close to the limit of detection), but the RSD for such analyses is generally ~3% when P_{Fe} is present above trace concentrations (Thompson et al., 2019), and the very low concentrations of P_{Fe} in our samples do not affect the interpretation of our P speciation data (see the main text).

For the calculation of the average C_{org}:P_{org} ratios (see the main text) we only utilised P_{org} data for samples, which were above the limit of quantification (9.90 ppm).

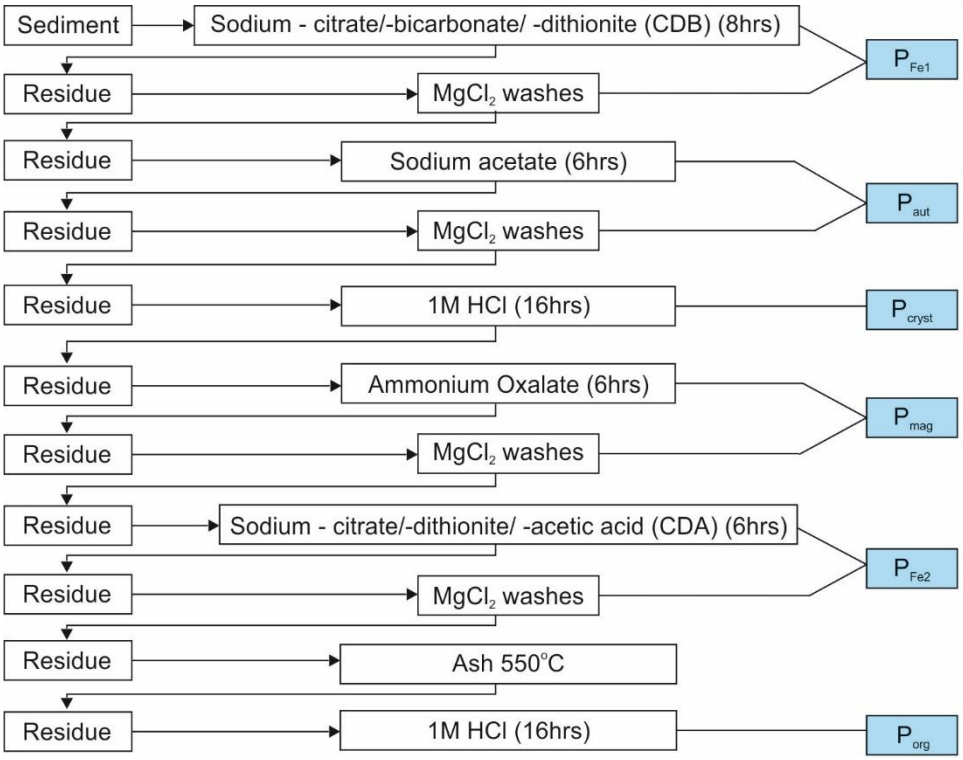

Figure 6.7. *Sequential extraction procedure for phosphorus (Thompson et al., 2019).*

Biogeochemical modelling

We utilise a modified 5 box ocean-atmosphere biogeochemical model for C-O-P cycling over Earth history (Alcott et al., 2019) to examine the response to altering P weathering and varying C_{org}:P_{org} ratios of buried material. The model was originally devised by Slomp and Van Cappellen (2007), and later modified by Tsandev et al. (2008), Tsandev and Slomp (2009), and Alcott et al. (2019). The full model equations are presented in Alcott et al. (2019), and are briefly summarised here. The 4 ocean boxes represent regions of the proximal and distal coastal shelf along with the surface and deep oceans. These marine boxes consider organic carbon, organic phosphorus, soluble phosphorus, and oxygen. A fifth box represents the atmosphere, where only oxygen is considered. The model includes productivity, remineralization, and burial of organic carbon, and 3 separate phosphorus phases. The redox-dependent P burial phases considered in the model consist of P_{org}, iron-oxide bound P_{Fe}, and authigenic P_{aut}.

In this paper we modify the original model of Alcott et al. (2019) in order to accommodate the results from this dataset: we considered values for the maximum C_{org}:P_{org} burial ratio under anoxic conditions to be between 100 and 10,000. We also varied the input of P from continental weathering from 1 to 100% of the present-day flux. We plot steady states with respect to both P input and C:P ratio for a fixed amount of oxygen consumption via reductant input following the values used in Alcott et al. (2019) for ~2.4 Ga (1.5×10^{13} mol yr^{-1}). All model equations are listed below and are fully summarised in Alcott et al. (2019), to which we direct the reader for further discussion of the model. The model schematic is shown in Figure 6.8.

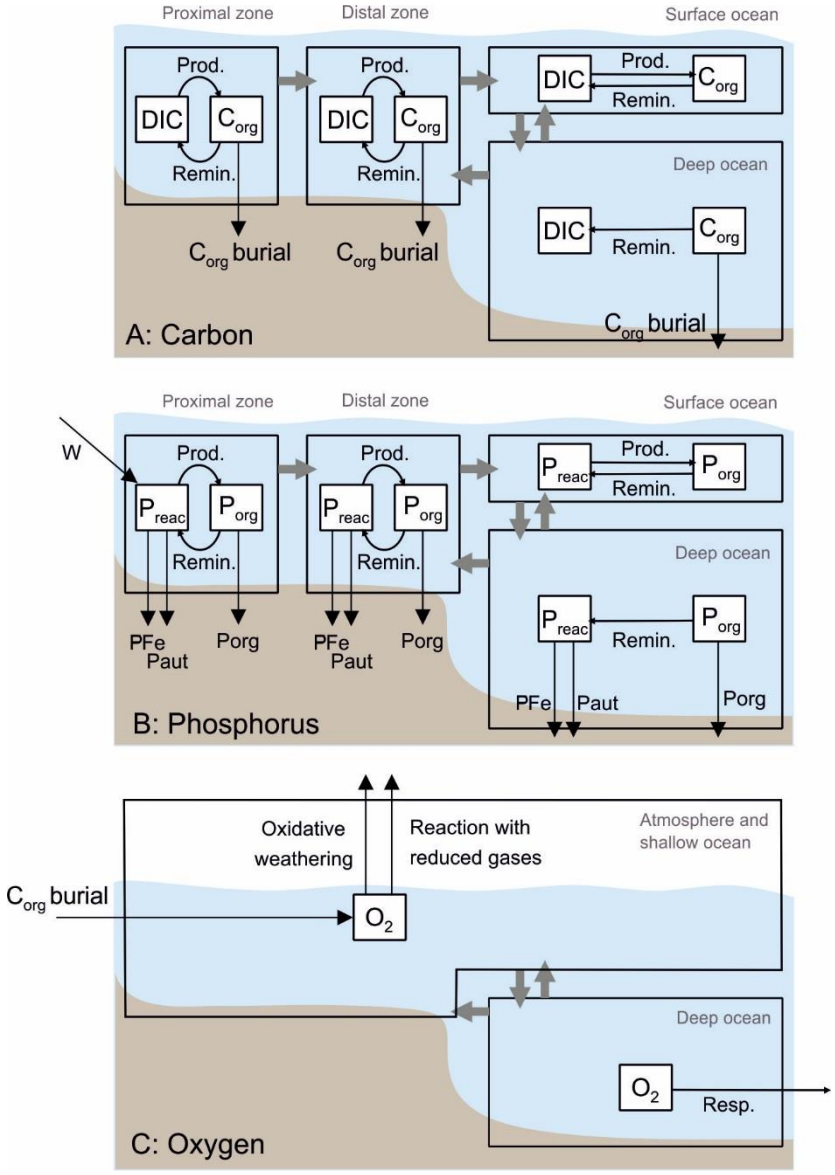

Figure 6.8. *Ocean and atmosphere box model. Clear boxes show hydrospheric reservoirs and grey arrows denote mixing between them. White boxes show chemical reservoirs and black arrows denote biogeochemical fluxes. (A) Carbon cycle: C exists as dissolved inorganic carbon (DIC) or organic carbon (C_{org}). (B) Phosphorus cycle: P exists as soluble reactive phosphorus (P_{reac}) and particulate organic phosphorus (P_{org}). (C) Oxygen cycle. Single oxygen reservoir encompasses all ocean boxes that exchange with the atmosphere. See text for full description, and methods and SI for equations.*

P Speciation

Consideration of possible late-stage diagenetic P phase alteration is required when applying P speciation to ancient sedimentary rocks (Creveling et al., 2014; Thompson et al., 2019). The main issue that might affect interpretation of P speciation data (which utilises two P pools: P_{org} and P_{reac}; see the main text) is the potential for recrystallization of carbonate fluorapatite (P_{aut}) to more crystalline apatite (P_{cryst}). Although P_{cryst} does constitute a significant proportion in some of our samples (~66% on average for the GKF01 and GKP01 drill cores), we note that there is no correlation between P_{aut} and P_{cryst} (Figure 6.9) and particularly high P_{cryst}/Al ratios only tend to occur at euxinic to ferruginous transitions, as shown by excursions in the P_{cryst}/Al ratio (Figure 6.10). Therefore, while a portion of the authigenic phase may have been recrystallized, it does not detract from our overall interpretation and would only support our hypothesis of greater fixation of P within the sediment during ferruginous conditions, as more P would be included within our P_{reac} phase (shifting a minor proportion of the ferruginous data in Figure 6.2 of the main text, to below or, at least, more towards the Redfield Ratio of 106:1). We can also demonstrate recycling of P from the sediment based on the ratio of C_{org}:P_{total} (P_{total}; total P by bulk digest) (Figure 6.11). The GKF01 and GKP01 drill cores demonstrate P recycling based on C_{org}:P_{reac} and C_{org}:P_{org} ratios (see the main text), but they even have several samples that plot above the Redfield Ratio with the inclusion of all the P phases. By contrast, samples of the Koegas Subgroup from the GTF01 and GEC01 drill cores exclusively plot below the Redfield ratio with the inclusion of the additional P phases (primarily P_{cryst}). This overall trend further supports recycling of P from the sediment under sulfidic porewater/euxinic water-column conditions regardless of the extent of conversion of P_{aut} to P_{cryst}.

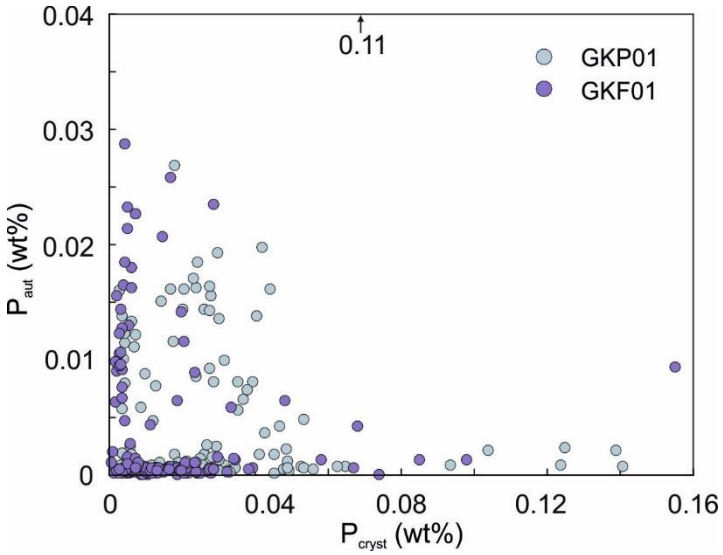

Figure 6.9. *P_{cryst} vs. P_{aut} plot for all samples analyzed for P speciation from the GKP01 and GKF01 drill cores.*

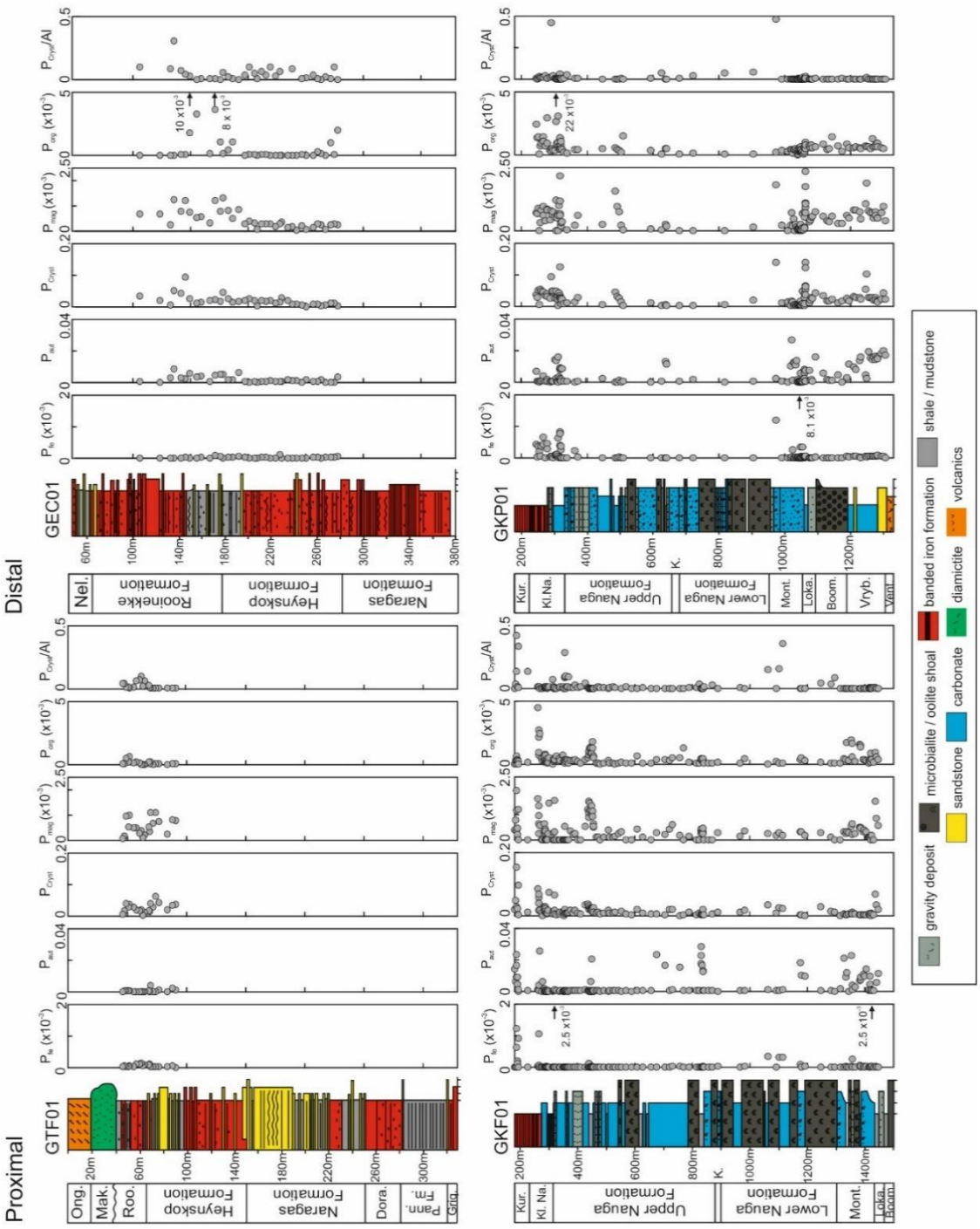

Figure 6.10. *P speciation data for drill-core samples (wt%). (A) Proximal GTF01 drill core. (B) Distal GEC01 drill core. (C) Proximal GKF01 drill core. (D) Distal GKP01 drill core.* P_{Fe} *(Fe-associated P),* P_{aut} *(authigenic P),* P_{Cryst} *(highly crystalline P),* P_{mag} *(magnetite-associated P) and* P_{org} *(organic-associated P). Abbreviations for formations: Ong. – Ongeluk Formation; Mak. – Makganyene Formation; Roo. – Rooinekke Formation; Dora. – Doredale Formation; Pann. – Pannetjie Formation; Griq. – Griquatown Iron Formation; Nel. – Nelani Formation; Dwyka. – Dwyka Formation; Kur. – Kuruman Iron Formation; Kl. Na. – Klein Naute Formation; K. – Kamden Member; Mont. – Monteville Formation; Loka. – Lokamonna Formation; Boom. – Boompaas Formation; Vryb. – Vryburg Formation; Vent. – Ventersdorp Group.*

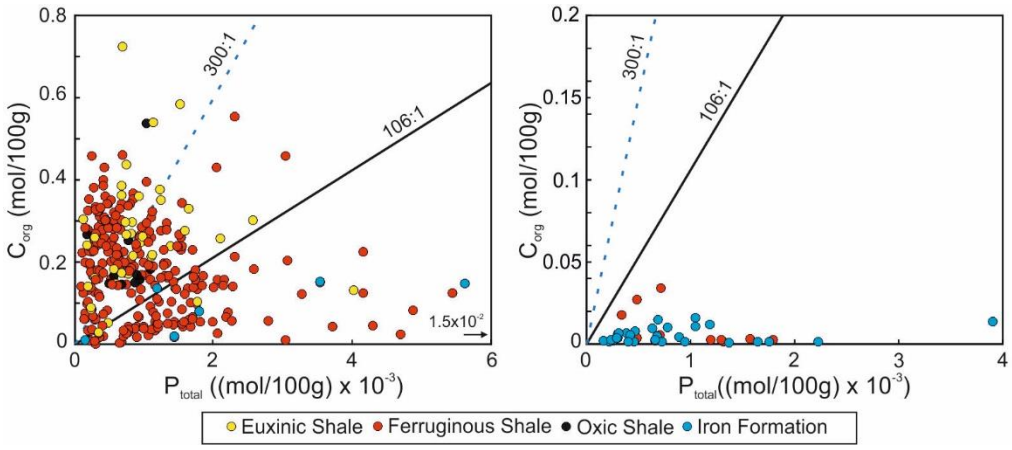

Figure 6.11. *Relationship between organic carbon and total phosphorus. (A) Corg/Ptotal for the Ghaap Group drill cores (GKF01 and GKP01); (B) C_{org}/P_{total} for the Koegas Subgroup drill cores (GTF01 and GEC01). Solid line represents the Redfield Ratio (106:1), and the dashed line represents the inferred C_{org}/P_{org} ratio for the early Precambrian sediments deposited under highly oligotrophic, P-limited conditions (Reinhard et al., 2017).*

Distinguishing between sulphidic porewaters and euxinic water-column conditions

As discussed in the main text, two horizons in the succession have elevated Fe_{HR}/Fe_T and Fe_{py}/Fe_{HR} ratios that might suggest euxinic water-column conditions. However, such a signal may also be generated during intense sulphide production in pore waters close to the sediment-water interface beneath a ferruginous water column. To address this possibility we consider the morphology of pyrite in the two horizons. In the case of the older Monteville Formation samples, reflected light microscopy shows abundant evidence for wavy layers, rip up clasts and nodules, and poorly disseminated coarser-grained euhedral pyrite (Figure 6.12). These features are not typical of textures commonly found when iron sulphide formation is dominantly instigated in a euxinic water column, where instead, fine-grained dispersed pyrite tends to dominate (Wignall and Newton, 1998). We thus suggest that the high Fe_{HR}/Fe_T and Fe_{py}/Fe_{HR} ratios evident for these samples most likely reflect intense diagenetic pyrite formation close to the sediment-water interface beneath a dominantly ferruginous water column. By contrast, pyrite in the younger Klein Naute Formation consists of fine, well-disseminated pyrite, with only occasional larger euhedral grains likely formed during diagenesis. Indeed, the pyrite morphology of these samples has been suggested to dominantly comprise relic framboids (Farquhar et al., 2013), and their small size and limited size range is more consistent with morphologies found in sediments deposited under an euxinic water column (Wignall and Newton, 1998).

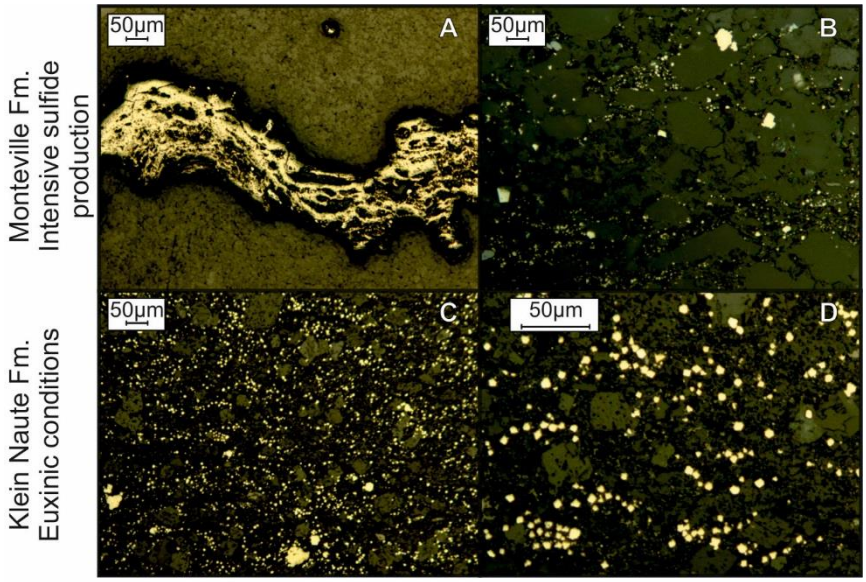

Figure 6.12. *Images of pyrite morphologies within the two stratigraphic intervals with elevated Fe_{py}/Fe_{HR} ratios. A, B - layered and nodular pyrite of the Monteville Formation. C, D - disseminated and euhedral pyrite of the Klein Naute Formation.*

Model results with elevated weathering fluxes

The phosphorus input flux to the ocean at 2.5 Ga has been estimated based on weathering kinetics and continental emergence times (Hao et al., 2020). The central estimates show negligible weathering in the Early Archean, rising to a flux within ~0.4 to ~1.2 times the present day, but with a maximum error up to ~3 times present day. In the manuscript we test the central estimates of this flux in a biogeochemical model, and here we extend the estimates up to 3x present (Figure 6.13). It is possible to see that when no P recycling is considered (maximum primary C_{org}:P_{org} of ~300) (Reinhard et al., 2016), the absolute maximum (and unlikely) weathering fluxes are required in order to provide oxygenation on the scale of the GOE, supporting our interpretation of phosphorus recycling facilitating planetary oxygenation.

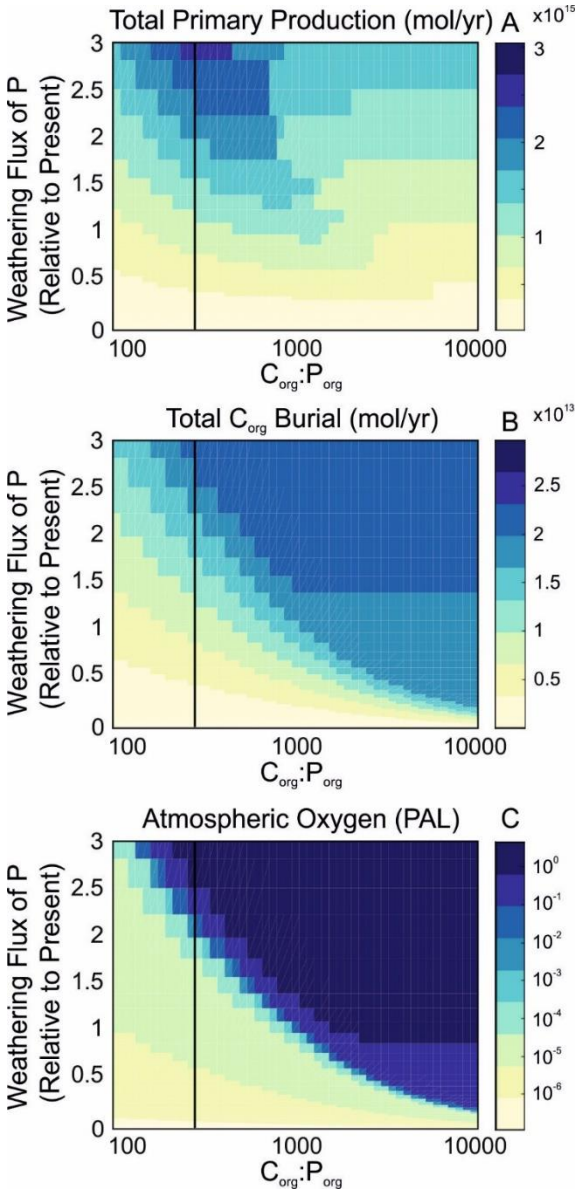

Figure 6.13. *Steady-state model solutions for a fixed reduced gas flux of 15 x 10^{12} (O_2 equivalents yr^{-1}). (A) Total primary production (mol C yr^{-1}). (B) Total organic carbon burial (mol C yr^{-1}). (C) Atmospheric oxygen concentration relative to Present Atmospheric Level (PAL).*

Table 6.4 Analytical data including major element concentrations, iron speciation, C_{org}, and P phases. ND = not determined. BD = below detection (0.95 ppm).

GTF01 - Proximal Koegas Subgroup drill core									
Depth(m)	Al (wt%)	Fe_T (wt%)	Fe_{HR}/Fe_T	Fe_{Py}/Fe_{HR}	Fe_T/Al	C_{org} (wt%)	P_T (ppm)	P_{reac} (ppm)	P_{org} (ppm)
328.45	0.97	24.39	0.48	0.00	25.03	0.065	115	ND	ND
327.50	0.63	26.75	0.66	0.00	42.19	0.047	78	ND	ND
325.10	0.56	32.81	0.75	0.00	58.90	0.037	167	ND	ND
323.00	0.38	24.69	0.69	0.00	65.29	0.039	182	ND	ND
322.45	0.16	21.13	0.78	0.00	129.25	0.022	336	ND	ND
321.90	1.19	25.57	0.52	0.00	21.49	0.035	285	ND	ND
318.95	4.05	19.15	0.20	0.01	4.72	0.044	431	ND	ND
316.30	5.45	14.77	0.14	0.03	2.71	0.043	533	ND	ND
313.60	5.63	13.37	0.12	0.04	2.37	0.041	665	ND	ND
309.75	6.24	6.06	0.25	0.06	0.97	0.065	437	ND	ND
307.30	6.08	10.93	0.26	0.03	1.80	0.074	464	ND	ND
304.05	6.44	8.12	0.24	0.04	1.26	0.066	526	ND	ND
301.45	5.97	8.54	0.23	0.04	1.43	0.084	388	ND	ND
298.40	6.83	10.31	0.16	0.04	1.51	0.040	304	ND	ND
295.30	6.30	10.23	0.19	0.02	1.63	0.049	379	ND	ND
291.85	5.61	11.14	0.32	0.03	1.99	0.067	382	ND	ND
289.00	7.13	5.91	0.24	0.05	0.83	0.056	451	ND	ND
287.30	5.52	7.63	0.28	0.05	1.38	0.057	280	ND	ND
284.00	2.88	21.40	0.21	0.01	7.43	0.036	339	ND	ND
281.80	0.17	26.21	0.74	0.00	156.07	0.036	202	ND	ND
280.70	0.12	21.56	0.63	0.00	173.75	0.040	87	ND	ND
276.90	0.23	34.57	0.72	0.00	150.52	0.032	204	ND	ND
273.30	0.31	31.17	0.74	0.00	100.78	0.052	122	ND	ND
269.95	0.20	24.16	0.70	0.00	118.35	0.036	113	ND	ND
266.05	0.51	28.62	0.68	0.00	56.01	0.050	125	ND	ND
262.60	0.27	32.57	0.56	0.00	119.75	0.055	150	ND	ND
260.10	0.25	31.12	0.78	0.00	125.08	0.038	118	ND	ND
256.80	0.27	28.03	0.62	0.00	103.09	0.017	110	ND	ND
252.55	0.34	26.20	0.64	0.00	76.19	0.036	204	ND	ND
248.80	0.38	21.27	0.77	0.00	55.63	0.065	188	ND	ND
244.80	0.80	22.97	0.73	0.00	28.59	0.068	228	ND	ND
242.90	0.40	24.83	0.79	0.01	61.48	0.067	250	ND	ND
240.00	2.56	16.74	0.33	0.01	6.53	0.114	313	ND	ND
238.00	3.37	17.76	0.61	0.01	5.27	0.113	345	ND	ND
234.00	5.53	7.72	0.33	0.03	1.40	0.060	320	ND	ND
231.00	5.67	10.78	0.35	0.02	1.90	0.056	357	ND	ND
230.25	4.96	7.06	0.37	0.04	1.42	0.061	356	ND	ND
229.40	4.69	13.88	0.56	0.00	2.96	0.080	427	ND	ND
227.60	4.80	14.89	0.30	0.01	3.10	0.052	387	ND	ND
225.00	4.55	11.91	0.43	0.01	2.62	0.044	322	ND	ND
222.90	2.12	16.09	0.44	0.00	7.59	0.037	281	ND	ND
219.60	6.11	10.81	0.31	0.02	1.77	0.060	437	ND	ND
216.45	6.13	15.27	0.38	0.01	2.49	0.053	649	ND	ND
215.50	6.62	14.97	0.30	0.02	2.26	0.037	554	ND	ND
212.15	6.94	10.68	0.17	0.04	1.54	0.035	465	ND	ND
209.20	4.16	13.96	0.40	0.01	3.36	0.041	369	ND	ND
202.85	6.70	14.52	0.36	0.01	2.17	0.054	657	ND	ND
199.10	6.79	11.32	0.28	0.02	1.67	0.052	564	ND	ND

196.30	6.51	9.33	0.33	0.03	1.43	0.047	466	ND	ND
193.00	7.00	9.94	0.21	0.04	1.42	0.050	512	ND	ND
188.40	6.37	10.01	0.30	0.08	1.57	0.037	575	ND	ND
184.50	7.59	10.10	0.18	0.05	1.33	0.049	540	ND	ND
181.20	7.25	13.86	0.26	0.02	1.91	0.058	558	ND	ND
178.50	5.48	3.86	0.46	0.05	0.70	0.038	339	ND	ND
178.10	5.81	9.76	0.43	0.13	1.68	0.033	816	ND	ND
172.50	5.65	10.87	0.35	0.01	1.92	0.031	270	ND	ND
170.30	4.57	9.82	0.45	0.02	2.15	0.036	362	ND	ND
166.00	4.55	9.53	0.46	0.10	2.09	0.028	654	ND	ND
164.00	3.95	3.86	0.41	0.08	0.98	0.033	238	ND	ND
159.90	6.79	14.35	0.38	0.02	2.11	0.031	615	ND	ND
151.90	5.71	9.52	0.36	0.03	1.67	0.032	503	ND	ND
148.90	5.79	13.28	0.37	0.04	2.30	0.040	528	ND	ND
144.60	4.89	11.34	0.41	0.05	2.32	0.025	509	ND	ND
141.15	5.53	10.67	0.36	0.02	1.93	0.031	441	ND	ND
137.30	6.25	12.77	0.35	0.01	2.04	0.040	432	ND	ND
133.90	5.39	11.01	0.28	0.03	2.04	0.045	413	ND	ND
129.65	6.17	14.27	0.27	0.02	2.31	0.024	443	ND	ND
126.65	5.91	10.95	0.24	0.02	1.85	0.051	430	ND	ND
122.80	5.53	13.76	0.29	0.02	2.49	0.039	355	ND	ND
120.05	3.63	16.65	0.32	0.02	4.59	0.033	401	ND	ND
117.60	4.42	18.55	0.36	0.01	4.20	0.052	379	ND	ND
113.50	2.19	17.11	0.30	0.00	7.83	0.035	229	ND	ND
110.90	5.01	11.43	0.37	0.02	2.28	0.034	353	ND	ND
106.00	4.15	13.39	0.40	0.01	3.22	0.043	424	ND	ND
103.35	4.31	18.54	0.36	0.01	4.30	0.039	410	ND	ND
100.60	5.89	13.01	0.26	0.03	2.21	0.043	542	ND	ND
97.45	5.75	12.55	0.31	0.02	2.18	0.033	367	ND	ND
93.20	5.10	14.09	0.38	0.02	2.76	0.042	421	ND	ND
91.00	5.72	10.28	0.32	0.04	1.80	0.021	406	22	1
88.20	5.57	13.45	0.34	0.02	2.42	0.031	369	36	1
83.50	2.51	10.32	0.74	0.01	4.11	0.025	80	5	BD
76.80	4.11	19.61	0.38	0.01	4.77	0.035	401	23	1
73.60	5.77	16.40	0.36	0.01	2.84	0.034	556	16	1
71.35	2.50	21.43	0.22	0.01	8.58	0.050	274	10	BD
69.45	4.82	16.37	0.26	0.01	3.39	0.035	485	55	2
68.50	0.85	20.45	0.48	0.00	24.18	0.048	150	7	BD
68.10	0.71	17.91	0.51	0.01	25.16	0.022	203	12	2
64.85	0.17	20.60	0.78	0.00	123.11	0.048	91	6	ND
63.00	0.21	8.30	0.73	0.00	40.46	0.043	ND	4	BD
62.00	0.20	33.49	0.61	0.00	167.04	0.030	203	8	ND
60.15	0.24	18.55	0.60	0.00	77.36	0.064	219	9	1
57.25	0.29	26.47	0.69	0.00	92.13	0.015	293	12	2
55.00	1.66	16.68	0.46	0.01	10.03	0.214	105	10	1
52.00	3.63	16.80	0.47	0.00	4.63	0.408	222	22	7
51.05	2.19	18.41	0.56	0.00	8.41	0.369	ND	12	2
49.15	2.36	18.81	0.55	0.00	7.96	0.325	150	20	5
47.50	0.43	17.60	0.62	0.06	40.70	0.130	ND	8	1
46.00	0.14	7.70	0.71	0.01	55.50	0.072	ND	3	BD

GEC01 - Distal Koegas Subgroup drill core

Depth(m)	Al (wt%)	Fe_T (wt%)	Fe_{HR}/Fe_T	Fe_{Py}/Fe_{HR}	Fe_T/Al	C_{org} (wt%)	P_T (ppm)	P_{reac} (ppm)	P_{org} (ppm)
372.60	4.38	15.70	0.35	0.00	3.58	0.033	343	ND	ND
368.50	4.43	18.15	0.18	0.02	4.10	0.024	335	ND	ND
364.20	2.75	26.18	0.14	0.01	9.53	0.027	274	ND	ND
365.55	2.30	27.64	0.20	0.00	12.04	0.020	224	ND	ND
362.70	2.19	23.30	0.23	0.02	10.65	0.030	ND	ND	ND
358.70	2.16	13.81	0.73	0.00	6.40	0.025	242	ND	ND
355.30	1.38	12.26	0.81	0.01	8.91	0.024	ND	ND	ND
352.70	1.17	18.47	0.47	0.00	15.78	0.015	ND	ND	ND
349.80	1.56	30.54	0.36	0.00	19.59	0.031	ND	ND	ND
345.90	1.73	21.71	0.27	0.00	12.54	0.035	ND	ND	ND
343.20	3.35	19.61	0.32	0.01	5.85	0.013	259	ND	ND
340.20	5.98	16.26	0.36	0.01	2.72	0.037	383	ND	ND
337.15	4.59	19.24	0.32	0.01	4.19	0.037	377	ND	ND
334.50	4.64	19.09	0.30	0.01	4.11	0.027	311	ND	ND
330.70	5.39	14.54	0.30	0.02	2.70	0.032	300	ND	ND
327.75	3.15	10.74	0.74	0.01	3.41	0.014	ND	ND	ND
324.40	6.53	13.28	0.32	0.02	2.03	0.029	461	ND	ND
321.25	7.04	12.61	0.17	0.03	1.79	0.047	435	ND	ND
318.00	2.90	16.20	0.56	0.00	5.58	0.017	122	ND	ND
314.50	4.02	18.14	0.42	0.01	4.52	0.028	350	ND	ND
312.00	4.44	18.68	0.32	0.01	4.21	0.022	399	ND	ND
309.30	2.68	21.21	0.38	0.01	7.92	0.019	5350	ND	ND
305.00	2.21	16.19	0.69	0.00	7.32	0.024	152	ND	ND
300.65	4.73	19.59	0.38	0.01	4.14	0.021	334	ND	ND
297.75	5.00	15.65	0.22	0.02	3.13	0.025	413	ND	ND
296.30	1.83	25.97	0.42	0.00	14.22	0.016	1221	ND	ND
295.50	1.27	23.49	0.25	0.00	18.45	0.016	212	ND	ND
291.55	0.50	30.00	0.57	0.00	59.98	0.018	200	ND	ND
282.90	0.63	34.40	0.59	0.00	54.39	0.033	306	ND	ND
280.00	0.79	30.05	0.36	0.00	37.88	0.017	1477	ND	ND
277.45	1.69	31.09	0.42	0.00	18.44	0.018	179	57	20
274.90	0.12	26.06	0.71	0.00	219.06	0.016	140	5	1
271.50	1.13	26.61	0.40	0.03	23.48	0.032	80	15	10
267.40	0.31	24.05	0.67	0.00	78.47	0.013	ND	3	BD
263.60	1.22	38.80	0.44	0.00	31.76	0.021	66	21	1
260.55	1.14	25.89	0.48	0.00	22.70	0.022	ND	13	3
256.50	0.23	27.65	0.53	0.00	118.95	0.015	ND	9	BD
250.00	0.11	22.09	0.08	0.00	206.25	0.025	49	17	BD
246.20	0.68	21.25	1.06	0.00	31.03	0.022	ND	6	BD
242.10	ND	36.30	0.30	0.00	ND	0.043	ND	14	BD
238.40	0.11	12.94	0.88	0.00	116.75	0.044	ND	12	BD
234.10	ND	23.65	0.52	0.00	ND	0.049	ND	18	ND
229.30	ND	21.94	0.76	0.00	ND	0.048	93	10	BD
227.20	0.25	26.93	0.63	0.00	106.03	0.035	74	12	BD
224.00	0.35	31.41	0.45	0.00	89.58	0.074	ND	8	BD
219.30	0.21	26.90	0.74	0.00	130.51	0.073	94	13	BD
215.50	0.52	29.23	0.51	0.00	55.77	0.081	117	11	1
211.25	0.31	27.69	0.07	0.01	88.87	0.093	144	8	1
208.00	0.42	27.94	0.65	0.00	65.78	0.080	95	2	BD
205.20	0.39	25.62	0.48	0.00	66.09	0.069	129	11	1
201.20	0.26	27.60	0.68	0.00	105.34	0.061	209	7	1
197.25	0.54	25.61	0.61	0.00	47.57	0.118	194	8	BD

191.50	6.20	14.80	0.20	0.01	2.39	0.128	395	154	80
186.70	1.32	20.52	0.37	0.00	15.55	0.175	212	35	11
182.60	1.27	26.62	0.42	0.00	20.88	0.190	323	28	4
178.10	0.76	33.85	0.50	0.00	44.74	0.020	543	65	2
175.85	4.53	19.54	0.30	0.00	4.31	0.129	323	72	11
170.95	4.28	20.50	0.29	0.00	4.79	0.140	367	95	37
166.70	3.36	25.47	0.48	0.00	7.58	0.125	242	14	2
159.40	2.10	28.67	0.14	0.00	13.64	0.097	356	150	105
155.10	2.93	29.84	0.17	0.01	10.20	0.079	237	73	33
149.30	0.99	27.21	0.34	0.00	27.53	0.042	392	84	18
145.30	2.04	26.71	0.38	0.00	13.10	0.162	1209	36	1
141.55	0.59	36.96	0.58	0.00	62.36	0.018	509	41	1
135.20	0.17	32.03	0.69	0.00	187.83	0.015	689	100	BD
132.35	0.08	25.17	0.55	0.00	302.20	0.016	125	31	BD
123.00	ND	38.95	0.82	0.00	ND	0.018	225	10	BD
105.60	0.35	36.65	0.61	0.00	105.86	0.013	425	12	BD
98.50	0.33	34.53	0.66	0.00	104.21	0.005	154	ND	ND
96.80	ND	22.79	0.13	ND	ND	0.006	249	ND	ND
91.45	2.78	21.99	0.10	0.01	7.92	0.036	205	ND	ND
87.05	0.50	35.12	0.59	0.00	69.75	0.004	293	ND	ND
84.00	0.43	28.76	0.49	0.00	67.15	0.009	80	ND	ND
79.95	0.68	35.87	0.36	0.00	52.72	0.006	173	ND	ND
77.15	0.32	34.78	0.48	0.00	108.67	0.015	243	ND	ND
72.90	1.60	33.36	0.03	0.05	20.87	0.025	333	ND	ND
71.60	0.88	32.87	0.41	0.00	37.56	0.021	185	ND	ND
69.00	3.13	23.57	0.11	0.01	7.53	0.024	201	ND	ND
64.90	0.61	31.28	0.38	0.00	51.27	0.017	53	ND	ND
64.00	1.55	29.66	0.37	0.00	19.13	0.011	232	ND	ND
62.00	2.10	15.67	1.36	0.00	7.47	0.031	110	ND	ND
54.00	0.59	39.37	0.29	0.00	67.06	ND	1465	ND	ND

GKF01 - Proximal Campbellrand Subgroup drill core

Depth(m)	Al (wt%)	Fe_T (wt%)	Fe_{HR}/Fe_T	Fe_{Py}/Fe_{HR}	Fe_T/Al	C_{org} (wt%)	P_T (ppm)	P_{reac} (ppm)	P_{org} (ppm)
183.50	ND	34.99	0.40	0.00	ND	0.500	ND	145	ND
183.80	0.03	31.28	0.38	0.00	1256.09	0.120	348	ND	ND
184.40	ND	21.75	0.16	0.00	ND	0.080	ND	ND	ND
186.30	1.42	25.51	0.24	0.00	18.01	0.960	553	75	3
187.60	0.37	23.57	0.72	0.02	68.23	1.790	1742	125	ND
188.60	ND	19.43	0.68	0.00	ND	1.040	ND	ND	6
189.60	0.21	15.99	0.09	0.00	88.95	0.250	441	245	6
192.30	1.82	24.79	0.19	0.00	12.88	1.640	366	100	4
193.00	ND	11.78	0.47	0.00	ND	0.300	ND	ND	3
195.05	0.75	11.35	0.32	0.00	14.84	0.130	46	5	2
196.70	0.29	17.76	0.85	0.00	75.71	1.840	1092	35	ND
198.42	ND	13.36	1.04	0.00	ND	1.333	ND	ND	ND
200.11	ND	12.37	1.34	0.00	ND	1.500	ND	ND	ND
201.81	ND	11.38	1.69	0.00	ND	1.667	ND	ND	ND
203.50	ND	10.39	2.10	0.00	ND	1.834	ND	ND	ND
205.20	ND	9.40	2.60	0.00	ND	2.001	ND	ND	ND
206.89	ND	8.41	3.22	0.00	ND	2.168	ND	ND	ND
208.59	ND	7.42	4.00	0.00	ND	2.335	ND	ND	ND
210.28	ND	6.43	5.02	0.00	ND	2.502	ND	ND	ND
211.98	ND	5.44	6.41	0.00	ND	2.669	ND	ND	ND
213.67	ND	4.45	8.43	0.00	ND	2.836	ND	ND	ND

215.37	ND	3.46	11.59	0.00	ND	3.003	ND	ND	ND
217.06	ND	2.47	17.29	0.00	ND	3.170	ND	ND	ND
218.76	ND	1.48	30.60	0.00	ND	3.337	ND	ND	ND
220.45	ND	0.49	97.23	0.00	ND	3.504	ND	ND	ND
228.93	0.08	ND	ND	ND	ND	ND	136	7	2
264.00	7.08	4.86	0.54	0.69	0.65	2.460	948	76	45
264.40	ND	4.01	0.95	0.87	ND	5.400	ND	ND	ND
265.00	ND	6.31	0.96	0.91	ND	6.340	ND	ND	ND
265.10	2.65	13.33	0.87	0.89	4.53	4.360	210	15	7
265.20	4.13	9.90	0.79	0.88	2.19	3.090	647	43	10
265.40	3.83	8.61	0.99	0.93	2.12	2.880	424	34	21
265.50	5.66	5.19	0.92	0.83	0.88	3.640	792	83	27
265.70	ND	2.26	0.88	0.86	ND	2.500	ND	ND	ND
268.30	ND	2.94	0.99	0.92	ND	8.140	ND	ND	ND
269.10	6.21	3.67	0.93	0.84	0.57	7.020	469	288	24
274.10	ND	2.74	0.95	0.85	ND	8.640	ND	ND	ND
277.00	0.84	12.13	0.99	0.87	13.61	1.940	89	5	4
280.20	1.30	0.30	0.85	0.29	0.25	3.130	83	66	2
284.00	3.70	13.17	0.64	0.90	3.25	4.530	377	52	5
286.10	1.90	3.56	0.75	0.28	1.79	4.110	207	10	3
286.50	2.61	3.64	0.97	0.37	1.31	4.410	261	11	6
287.30	0.85	4.32	0.75	0.22	4.76	3.130	131	3	2
287.90	1.65	5.90	0.73	0.68	3.31	3.200	294	13	8
289.10	1.71	5.62	0.92	0.43	3.05	2.150	196	11	7
290.00	2.74	5.21	0.78	0.17	1.76	4.240	258	8	3
290.20	1.26	9.21	0.91	0.66	6.80	2.410	159	9	3
291.00	0.82	5.10	0.75	0.09	5.67	1.960	103	3	1
292.00	0.70	5.30	0.95	0.22	6.98	3.440	104	3	1
293.60	1.86	7.37	0.90	0.39	3.69	1.530	86	9	3
293.90	1.26	6.34	0.92	0.29	4.68	3.660	116	6	5
294.70	0.58	5.69	0.71	0.27	9.09	3.360	57	11	3
295.50	0.89	5.63	0.75	0.10	5.81	4.020	91	3	1
296.80	1.77	6.24	0.93	0.07	3.20	3.000	164	12	2
300.60	5.35	7.72	0.45	0.05	1.34	2.190	800	21	5
309.10	ND	ND	ND	0.82	ND	1.440	ND	ND	ND
314.00	0.07	13.43	0.83	0.01	183.56	1.180	54	2	BD
317.50	1.08	10.50	0.90	0.41	8.83	3.570	142	7	2
318.50	2.96	5.99	0.71	0.19	1.84	5.170	130	12	4
319.50	7.20	3.51	0.87	0.29	0.45	6.640	712	27	5
320.30	2.21	6.62	0.93	0.14	2.69	3.620	172	14	3
321.30	1.67	6.49	0.93	0.10	3.55	3.370	167	5	ND
322.30	2.12	5.91	0.74	0.07	2.57	1.990	79	4	ND
322.40	0.80	6.49	0.92	0.04	7.52	1.090	ND	19	4
327.80	5.34	7.48	0.68	0.15	1.27	3.360	202	13	7
337.20	0.63	4.13	0.82	0.39	6.10	4.630	ND	8	4
341.20	1.01	3.40	0.89	0.03	2.95	3.600	ND	10	3
350.20	0.80	2.08	0.92	0.27	2.51	3.920	56	10	7
352.40	0.82	2.36	0.90	0.15	2.72	2.310	65	7	2
354.80	0.80	1.88	0.90	0.17	2.23	2.110	72	3	1
356.00	0.06	2.42	0.80	0.15	38.37	0.990	143	4	1
357.20	0.17	3.20	0.73	0.05	17.97	0.140	ND	9	4
357.90	0.07	3.38	0.64	0.38	50.47	0.220	ND	15	3
358.40	0.02	2.94	0.51	0.10	144.96	0.100	71	5	ND
358.70	0.08	2.08	0.89	0.11	24.63	3.400	186	8	2

361.80	0.42	1.49	0.89	0.19	3.35	2.710	77	12	4
367.40	0.72	1.97	0.88	0.16	2.51	3.020	89	4	3
368.80	0.12	5.45	0.84	0.11	41.64	2.380	123	3	1
377.30	2.71	2.91	0.93	0.74	1.01	1.770	181	15	3
384.50	1.60	3.86	0.82	0.64	2.27	2.170	99	14	3
392.10	0.57	1.61	0.88	0.32	2.87	2.710	217	13	4
400.60	0.90	1.87	0.87	0.25	2.05	2.900	101	11	3
411.70	0.54	1.02	0.88	0.07	1.91	4.580	84	8	1
426.50	0.77	5.90	0.89	0.07	7.28	3.330	382	22	3
438.40	6.07	3.19	0.44	0.18	0.49	1.960	414	23	5
439.70	9.16	5.15	0.60	0.45	0.56	3.130	339	27	10
440.15	8.33	4.49	0.46	0.35	0.51	3.110	288	24	7
441.20	7.66	6.26	0.42	0.21	0.79	2.500	251	23	7
441.80	10.58	5.23	0.41	0.62	0.49	3.550	409	28	10
444.00	12.52	5.26	0.23	0.47	0.40	3.700	340	30	13
445.20	13.22	4.77	0.34	0.66	0.36	3.880	347	90	14
446.10	13.07	4.87	0.24	0.45	0.37	4.760	321	29	13
447.50	11.88	5.49	0.30	0.42	0.45	3.430	297	23	9
448.50	12.43	5.31	0.21	0.47	0.42	3.290	330	26	9
449.90	8.84	5.27	0.47	0.40	0.60	2.290	264	19	7
451.20	10.78	4.66	0.29	0.63	0.43	2.650	287	225	8
452.30	8.95	5.24	0.42	0.27	0.57	2.820	274	31	13
453.60	9.58	3.86	0.34	0.53	0.39	2.230	251	31	18
455.50	5.86	6.37	0.54	0.61	1.07	2.030	318	16	6
456.20	8.36	4.90	0.34	0.33	0.57	2.860	165	14	6
457.10	10.43	3.65	0.32	0.61	0.34	3.110	173	16	5
467.60	1.46	1.38	0.64	0.08	0.91	3.930	107	7	1
474.10	0.68	0.88	0.78	0.06	1.34	4.100	147	8	1
480.30	0.84	1.27	0.86	0.09	1.55	5.510	76	4	BD
492.50	1.11	1.60	0.88	0.02	1.37	2.960	95	6	1
507.10	5.57	2.28	0.54	0.28	0.39	2.820	187	10	3
510.90	0.96	1.12	0.90	0.05	1.22	2.950	118	7	1
523.40	0.67	1.13	0.82	0.02	1.65	3.730	110	6	1
530.80	1.22	0.91	0.76	0.31	0.78	2.690	146	8	BD
544.40	ND	ND	ND	0.04	ND	3.190	ND	ND	1
554.10	4.81	2.02	0.66	0.11	0.44	3.840	174	8	2
569.20	0.38	0.71	0.91	0.02	1.82	3.240	78	5	1
588.90	0.94	1.35	0.89	0.03	1.55	0.380	64	3	1
608.60	5.66	5.02	0.73	0.59	0.91	2.130	239	17	6
628.70	1.21	3.58	0.90	0.17	3.14	0.710	89	6	1
657.80	1.64	0.91	0.82	0.07	0.60	2.750	86	7	1
676.80	12.35	1.65	0.19	0.64	0.15	6.470	321	240	4
705.15	9.68	1.54	0.12	0.36	0.17	3.040	236	171	4
720.30	6.57	1.67	0.39	0.20	0.26	1.500	250	17	3
729.70	7.36	1.56	0.59	0.74	0.23	2.600	260	23	5
756.80	9.69	1.18	0.38	0.52	0.13	3.640	208	163	5
770.60	1.51	4.07	0.25	0.32	2.78	3.200	54	17	13
789.90	1.44	0.63	0.87	0.22	0.46	0.230	128	9	2
815.30	0.34	0.34	0.70	0.08	1.10	2.400	46	5	1
822.60	0.25	0.53	0.90	0.17	2.27	3.360	120	8	1
829.50	9.78	2.65	0.41	0.83	0.28	2.970	293	294	4
830.80	11.99	2.65	0.18	0.67	0.23	2.040	278	187	4
832.10	12.38	2.66	0.19	0.66	0.22	2.200	337	235	4
834.60	11.81	2.88	0.18	0.65	0.25	1.800	268	169	3

835.60	11.91	2.48	0.29	0.72	0.22	2.090	225	137	4
837.20	10.74	2.07	0.15	0.54	0.20	1.740	207	134	3
838.50	6.31	2.00	0.52	0.47	0.32	1.750	228	13	4
841.80	0.13	0.56	0.88	0.00	4.75	2.760	ND	5	BD
855.80	ND	0.62	0.74	0.01	ND	4.240	ND	ND	BD
870.10	0.22	0.77	0.83	0.08	3.71	3.230	93	5	BD
888.30	4.61	1.41	0.70	0.32	0.29	4.790	128	8	1
895.80	ND	3.94	0.90	0.14	ND	0.220	ND	ND	ND
896.40	ND	ND	ND	0.00	ND	1.260	ND	ND	ND
896.90	ND	11.32	0.87	0.00	ND	0.350	ND	ND	ND
917.90	ND	0.58	0.90	0.19	ND	4.780	ND	ND	ND
966.40	1.41	1.28	0.97	0.20	0.86	3.710	133	8	1
982.00	4.21	1.25	0.84	0.59	0.29	3.950	198	13	4
1032.80	ND	0.90	0.93	0.04	ND	4.390	ND	ND	ND
1064.50	0.23	0.77	0.97	0.06	3.13	3.340	410	21	BD
1092.30	2.73	3.39	0.92	0.21	1.19	1.930	103	12	2
1101.40	ND	5.02	0.99	0.03	ND	2.440	ND	ND	ND
1102.60	0.17	3.05	0.78	0.04	17.62	0.280	329	12	1
1104.00	ND	ND	ND	0.01	ND	1.190	ND	ND	ND
1104.20	ND	ND	ND	0.08	ND	3.560	ND	ND	ND
1115.30	0.06	1.76	0.97	0.01	25.76	2.030	298	17	1
1141.80	ND	1.68	0.95	0.31	ND	4.380	ND	ND	ND
1176.50	13.87	1.57	0.09	0.29	0.11	1.900	290	193	4
1179.20	11.55	2.09	0.13	0.24	0.17	2.010	174	113	5
1188.20	ND	1.25	0.96	0.06	ND	3.850	ND	ND	ND
1192.90	10.41	0.98	0.17	0.35	0.09	1.780	152	103	3
1245.70	0.64	1.00	0.99	0.19	1.43	3.100	320	10	1
1270.70	ND	0.85	0.98	0.05	ND	3.010	ND	ND	ND
1281.90	0.40	0.96	0.94	0.14	2.26	1.930	161	9	1
1294.70	0.15	0.86	0.99	0.03	5.36	4.220	160	4	BD
1308.90	ND	3.81	0.31	0.38	ND	1.480	ND	ND	ND
1315.30	0.73	0.74	0.92	0.17	1.04	0.370	ND	21	1
1326.80	10.73	3.00	0.35	0.77	0.27	3.140	301	221	4
1334.10	12.43	2.29	0.17	0.44	0.18	3.400	148	97	4
1336.10	12.02	2.43	0.27	0.62	0.21	4.100	245	144	17
1344.30	6.86	2.75	0.70	0.54	0.40	3.870	106	9	3
1353.30	10.87	2.71	0.20	0.40	0.25	1.900	336	252	19
1354.90	7.92	4.77	0.55	0.76	0.58	2.070	239	69	16
1356.20	3.22	2.74	0.70	0.51	0.83	0.880	125	23	6
1366.80	10.69	2.09	0.39	0.38	0.19	3.890	101	32	2
1381.20	11.98	3.97	0.19	0.34	0.32	2.620	189	88	15
1384.40	12.98	3.37	0.15	0.37	0.26	2.420	209	97	15
1386.50	12.53	3.01	0.19	0.60	0.24	2.150	215	111	14
1395.40	12.49	2.84	0.17	0.41	0.22	2.490	179	114	3
1396.90	13.01	2.58	0.13	0.31	0.20	2.870	137	104	4
1404.60	13.71	1.30	0.25	0.56	0.10	4.050	239	150	3
1413.60	0.85	5.05	0.64	0.62	6.03	0.740	91	7	1
1416.10	1.22	18.46	0.18	0.51	14.88	1.010	77	15	4
1417.70	1.50	14.31	0.23	0.51	9.54	1.460	106	51	3
1418.30	1.92	15.16	0.58	0.80	7.79	0.630	147	100	2
1420.80	1.35	11.46	0.31	0.62	8.60	1.390	111	14	1
1422.10	2.26	25.78	0.21	0.61	9.16	2.380	66	46	9
1425.00	2.85	14.80	0.25	0.56	5.36	2.140	108	12	3
1430.70	0.56	11.54	0.43	0.73	20.88	0.730	46	7	2

1436.30	6.90	8.93	0.75	0.73	1.24	1.570	1242	1097	9
1439.10	7.85	7.39	0.40	0.73	0.91	1.650	449	74	6
1445.20	7.96	3.86	0.24	0.09	0.49	1.240	375	125	4
1445.40	0.23	10.25	0.47	0.71	46.56	0.430	ND	ND	ND
1448.20	7.49	3.93	0.33	0.11	0.53	1.120	337	ND	ND
1451.30	5.55	10.40	0.37	0.09	2.00	0.510	277	ND	ND
1454.30	7.43	7.97	0.14	0.01	1.08	0.650	357	ND	ND
1456.70	7.22	4.46	0.28	0.02	0.62	0.810	526	ND	ND
1462.30	6.96	9.10	0.27	0.06	1.26	0.590	364	ND	ND
1465.50	5.43	9.19	0.15	0.15	1.65	0.450	261	ND	ND
1469.90	5.25	8.92	0.23	0.09	1.63	0.520	238	ND	ND
1474.70	7.29	6.59	0.17	0.06	0.90	0.810	287	ND	ND
1484.40	0.99	1.02	0.58	0.10	1.06	0.220	107	ND	ND
1488.80	ND	0.84	0.59	0.05	ND	0.170	ND	ND	ND
1493.30	0.14	1.09	0.42	0.02	8.22	0.250	ND	ND	ND
1497.50	0.63	5.86	0.54	0.02	1.88	0.410	60	ND	ND

GKP01 - Distal Campbellrand Subgroup drill core

Depth(m)	Al (wt%)	Fe_T (wt%)	Fe_{HR}/Fe_T	Fe_{Py}/Fe_{HR}	Fe_T/Al	C_{org} (wt%)	P_T (ppm)	P_{reac} (ppm)	P_{org} (ppm)
183.10	0.05	25.10	0.07	0.00	504.60	0.020	91	ND	ND
186.60	ND	25.97	0.13	0.00	ND	0.100	ND	ND	ND
188.80	1.95	29.66	0.47	0.00	14.32	1.610	293	ND	ND
190.00	ND	27.84	0.56	0.00	ND	1.300	ND	ND	ND
190.80	1.34	33.22	0.33	0.00	23.79	2.630	188	ND	ND
193.10	ND	25.39	0.21	0.00	ND	1.850	ND	ND	ND
193.70	2.19	28.42	0.07	0.00	11.93	0.110	88	ND	ND
197.20	ND	28.24	0.18	0.00	ND	0.030	ND	ND	ND
198.00	2.62	25.52	0.05	0.00	9.03	0.060	209	ND	ND
199.30	ND	25.50	0.71	0.00	ND	0.030	ND	ND	ND
204.00	1.33	33.56	0.60	0.00	24.37	2.690	1285	ND	ND
205.50	ND	51.99	0.29	0.00	ND	0.040	ND	ND	ND
205.60	0.05	26.58	0.05	0.00	526.59	0.020	ND	ND	ND
208.40	ND	34.59	0.39	0.00	ND	0.020	ND	ND	ND
210.90	1.33	31.32	0.59	0.00	22.62	0.660	615	ND	ND
212.00	ND	31.60	0.38	0.00	ND	1.150	ND	ND	ND
213.50	ND	32.17	0.26	0.00	ND	0.310	103	ND	ND
214.90	ND	35.53	0.38	0.00	ND	0.020	ND	ND	ND
219.50	1.82	29.05	0.09	0.00	14.84	0.040	199	ND	ND
220.90	ND	36.41	0.45	0.00	ND	0.050	ND	ND	ND
221.00	0.07	14.73	0.13	0.18	40.55	0.070	ND	ND	ND
221.90	ND	24.96	0.09	0.03	ND	1.240	ND	ND	ND
222.60	0.06	17.29	0.81	0.00	287.43	1.460	1012	ND	ND
223.00	ND	27.80	0.28	0.00	ND	1.380	ND	ND	ND
223.55	0.42	36.37	0.75	0.02	90.44	5.510	937	ND	ND
226.10	1.04	30.28	0.57	0.02	29.46	0.300	4874	ND	ND
226.50	5.73	12.37	0.41	0.02	2.20	1.650	501	ND	ND
227.10	4.58	18.91	0.52	0.05	4.26	1.320	368	ND	ND
227.40	0.08	23.58	0.75	0.00	354.73	0.250	214	ND	ND
228.30	6.81	9.53	0.45	0.05	1.40	1.840	438	ND	ND
230.00	0.11	22.98	0.88	0.00	227.96	0.320	635	ND	ND
231.00	ND	10.73	0.62	0.03	ND	4.120	ND	ND	ND
232.00	5.46	18.90	0.40	0.04	3.54	0.420	356	ND	ND
233.90	7.55	7.61	0.65	0.04	1.00	2.280	348	ND	ND
234.50	4.80	21.97	0.77	0.05	4.47	1.880	635	ND	ND

235.10	3.23	29.23	0.70	0.09	9.11	1.290	288	ND	ND
236.10	6.55	8.59	0.57	0.15	1.30	5.160	631	ND	ND
236.70	0.29	25.75	0.78	0.08	94.53	1.720	191	ND	ND
237.05	6.40	13.65	0.40	0.04	2.10	2.750	471	ND	ND
237.10	0.67	21.13	0.73	0.01	34.00	0.540	1329	ND	ND
237.50	3.76	20.38	0.61	0.05	5.35	2.560	713	ND	ND
238.30	3.74	25.38	0.70	0.08	6.67	1.200	539	ND	ND
238.50	5.15	15.48	0.52	0.03	3.00	1.260	430	ND	ND
239.50	7.57	8.81	0.28	0.04	1.13	2.000	402	ND	ND
239.70	3.14	18.42	0.70	0.01	5.85	1.720	357	ND	ND
240.20	7.62	8.57	0.26	0.04	1.11	2.130	445	ND	ND
240.50	7.45	8.55	0.36	0.02	1.12	2.180	536	ND	ND
241.50	5.73	11.51	0.24	0.36	1.97	2.010	417	ND	ND
242.60	8.03	5.28	0.28	0.10	0.64	2.360	394	ND	ND
243.60	8.02	5.12	0.27	0.12	0.62	2.760	397	ND	ND
244.98	7.99	4.72	0.36	0.29	0.60	2.860	478	ND	ND
245.60	7.83	4.97	0.27	0.18	0.61	2.850	459	ND	ND
246.20	7.54	5.63	0.28	0.26	0.72	3.130	473	102	25
248.00	6.99	8.93	0.37	0.09	1.24	2.990	329	27	14
249.80	4.66	15.43	0.36	0.04	3.05	2.750	522	35	15
255.50	0.30	26.72	0.70	0.00	92.79	0.440	76	6	1
257.90	ND	14.10	0.62	0.04	ND	0.510	ND	ND	ND
258.20	3.33	16.57	0.29	0.03	4.90	2.000	570	18	8
260.00	ND	14.26	0.69	0.02	ND	2.140	ND	ND	ND
260.90	3.09	14.08	0.41	0.11	4.64	1.620	547	33	10
261.20	ND	10.60	0.19	0.05	ND	1.950	ND	ND	ND
262.60	ND	10.22	0.46	0.03	ND	1.720	ND	ND	ND
264.80	2.99	13.95	0.19	0.15	4.57	1.470	490	46	15
266.00	ND	12.42	0.40	0.03	ND	1.810	ND	ND	ND
267.20	3.16	12.46	0.48	0.06	3.73	1.670	530	66	11
269.90	ND	12.39	0.28	0.01	ND	1.530	ND	ND	ND
271.60	1.05	27.67	0.56	0.01	26.19	0.930	347	15	7
274.70	ND	10.73	0.39	0.01	ND	1.530	ND	ND	ND
276.80	4.02	9.17	0.46	0.02	2.22	1.600	452	41	10
277.00	ND	21.30	0.29	0.24	ND	0.910	ND	ND	ND
277.50	3.64	8.40	0.37	0.03	2.19	1.960	384	49	29
283.80	ND	13.18	0.42	0.01	ND	1.810	ND	ND	ND
286.00	2.03	13.07	0.42	0.01	6.13	0.840	281	11	4
291.20	0.20	7.35	0.41	0.02	35.05	0.120	938	20	3
292.50	2.47	12.12	0.56	0.05	4.61	1.710	566	17	5
297.50	1.75	12.04	0.26	0.18	6.63	1.230	514	16	4
301.80	5.27	2.11	0.22	0.25	0.38	2.370	408	154	4
303.90	8.74	1.50	0.20	0.33	0.16	1.890	663	178	27
306.10	4.88	10.11	0.22	0.40	1.88	3.210	466	239	216
307.00	4.40	7.69	0.76	0.62	1.60	3.530	320	20	9
309.00	5.48	3.19	0.79	0.75	0.55	3.570	255	20	9
310.20	5.00	3.76	0.78	0.79	0.70	4.220	383	24	10
311.20	7.16	2.61	0.71	0.71	0.34	3.230	250	17	7
312.50	5.64	4.56	0.41	0.76	0.74	8.700	213	197	30
315.00	6.71	1.77	0.80	0.71	0.25	3.310	488	52	5
316.10	8.70	1.34	0.63	0.60	0.15	4.120	475	106	13
317.10	6.91	2.62	0.85	0.76	0.36	2.560	339	31	7
317.80	2.70	10.88	0.25	0.46	3.79	1.510	1286	67	13
318.00	5.21	1.41	0.75	0.50	0.26	2.320	394	112	4

319.10	4.91	9.57	0.42	0.83	1.85	4.340	285	31	8
320.00	4.65	6.76	0.28	0.75	1.41	4.630	207	104	11
321.10	3.08	3.77	0.92	0.81	1.16	3.200	228	16	5
321.90	6.05	2.64	0.63	0.72	0.41	6.490	349	94	5
324.70	ND	3.77	0.82	0.44	ND	5.320	ND	ND	ND
328.30	0.70	6.02	0.72	0.12	8.41	0.880	62	7	2
332.70	ND	1.88	0.52	0.14	ND	0.140	ND	ND	ND
337.00	0.37	5.32	0.75	0.19	13.24	4.640	125	7	2
361.90	1.81	3.51	0.65	0.33	1.77	4.100	145	12	4
369.10	ND	5.09	0.49	0.45	ND	3.770	ND	ND	ND
371.00	5.22	2.56	0.80	0.61	0.47	2.390	307	16	5
403.00	ND	2.08	0.66	0.02	ND	2.300	ND	ND	ND
445.60	9.64	1.19	0.34	0.79	0.11	0.360	103	33	5
482.80	ND	5.40	0.32	0.18	ND	2.790	ND	ND	ND
484.95	10.37	5.57	0.33	0.16	0.48	2.860	457	23	6
486.70	ND	9.27	0.53	0.08	ND	1.930	ND	ND	ND
490.00	9.44	11.11	0.50	0.14	1.04	2.300	328	17	4
490.70	ND	9.89	0.60	0.07	ND	2.060	ND	ND	ND
491.95	ND	8.56	0.42	0.05	ND	2.050	ND	ND	ND
495.90	12.31	2.43	0.31	0.51	0.18	2.920	272	26	4
497.20	ND	2.77	0.26	0.27	ND	3.900	ND	ND	ND
499.40	ND	1.73	0.87	0.06	ND	3.730	ND	ND	ND
503.50	2.09	3.08	0.83	0.42	1.29	3.640	140	8	2
503.90	ND	20.53	0.08	0.54	ND	1.750	ND	ND	ND
509.10	1.12	2.03	0.83	0.76	8.78	3.660	38	20	15
592.90	1.78	1.16	0.77	0.23	0.59	3.940	93	8	4
624.50	0.08	0.75	0.90	0.00	6.71	2.680	32	6	1
637.10	ND	2.05	0.27	0.75	ND	2.000	ND	ND	ND
637.80	ND	1.88	0.16	0.84	ND	2.040	ND	ND	ND
638.40	11.51	2.08	0.34	0.94	0.16	2.080	208	141	5
639.20	ND	2.56	0.38	0.91	ND	2.010	ND	ND	ND
640.00	ND	1.64	0.08	0.64	ND	1.850	ND	ND	ND
640.60	6.99	1.80	0.12	0.75	0.23	2.200	173	122	5
649.20	ND	2.73	0.57	0.54	ND	4.800	ND	ND	ND
679.50	0.31	0.80	0.82	0.00	2.17	0.130	ND	10	1
722.10	0.14	0.86	0.92	0.05	5.41	3.460	ND	19	1
779.60	ND	0.99	0.98	0.07	ND	5.120	ND	ND	ND
816.70	0.09	1.02	0.53	0.00	10.07	2.690	ND	4	BD
864.70	ND	1.29	0.15	0.65	ND	3.840	ND	ND	ND
905.60	0.33	1.05	0.86	0.06	2.77	3.780	182	7	1
946.50	ND	0.93	0.86	0.06	ND	4.870	ND	ND	ND
972.00	0.29	1.57	0.84	0.28	5.12	0.290	1452	54	2
982.00	ND	1.77	0.39	0.93	ND	3.270	ND	ND	ND
992.10	3.71	1.59	0.89	0.39	0.38	4.000	113	15	4
999.90	ND	0.93	0.42	0.99	ND	3.780	ND	ND	ND
1010.10	3.69	3.87	0.77	0.31	0.94	2.080	124	7	3
1016.30	ND	2.03	0.06	0.22	ND	2.400	ND	ND	ND
1017.70	11.53	2.53	0.19	0.69	0.20	1.740	166	108	5
1019.30	ND	2.39	0.12	0.65	ND	2.410	ND	ND	ND
1020.05	13.63	2.48	0.09	0.50	0.19	1.980	528	280	4
1024.05	ND	1.82	0.95	0.16	ND	3.630	ND	ND	ND
1024.90	3.02	2.18	0.92	0.16	0.75	3.630	136	17	1
1026.20	ND	1.98	0.93	0.55	ND	3.910	ND	ND	ND
1027.70	ND	3.55	0.38	0.91	ND	2.080	ND	ND	ND

1028.30	14.11	1.83	0.17	0.36	0.15	2.390	219	132	4
1028.90	ND	2.16	0.15	0.68	ND	2.290	ND	ND	ND
1029.00	12.81	2.03	0.23	0.68	0.19	2.140	241	127	4
1029.70	ND	4.58	0.09	0.46	ND	1.880	ND	ND	ND
1029.90	ND	2.18	0.53	0.82	ND	6.980	ND	ND	ND
1030.80	ND	2.79	0.12	0.45	ND	3.220	ND	ND	ND
1032.80	11.38	3.04	0.16	0.47	0.28	5.530	214	119	5
1033.60	ND	2.79	0.69	0.55	ND	2.220	ND	ND	ND
1035.90	14.02	1.62	0.35	0.80	0.12	3.580	225	143	3
1035.90	ND	1.47	0.31	0.75	ND	2.870	ND	ND	ND
1036.80	ND	6.96	0.19	0.24	ND	0.650	ND	ND	ND
1038.30	ND	1.46	0.90	0.37	ND	1.940	ND	ND	ND
1039.20	1.33	1.26	0.90	0.26	0.93	1.570	57	19	BD
1040.20	1.97	1.51	0.92	0.42	0.79	2.740	62	6	2
1041.20	4.92	1.75	0.85	0.35	0.37	1.890	90	5	2
1041.60	0.67	1.39	0.83	0.25	1.94	1.500	37	6	1
1042.30	1.38	10.07	0.21	0.51	8.25	0.820	80	9	3
1043.00	1.31	24.39	0.97	0.90	19.58	1.010	72	9	5
1044.60	0.83	21.64	0.14	0.43	27.13	2.860	60	8	5
1046.20	0.89	21.03	0.05	0.68	24.89	2.740	82	7	3
1046.60	0.81	16.68	0.18	0.10	20.97	3.400	45	6	2
1047.20	2.48	5.25	0.42	0.59	2.53	2.160	200	8	2
1048.20	2.36	27.68	0.30	0.73	11.88	1.070	72	11	4
1048.30	8.08	6.97	0.19	0.71	0.89	5.250	230	148	7
1049.50	1.21	18.33	0.17	0.56	15.97	4.230	60	9	4
1050.40	0.99	6.71	0.27	0.52	7.68	0.910	45	8	2
1050.90	1.05	7.89	0.99	0.86	7.72	2.910	53	7	2
1051.30	2.59	20.01	0.14	0.65	8.16	1.240	56	6	3
1051.50	3.44	16.41	0.12	0.39	5.31	1.680	72	8	4
1051.90	0.92	12.38	0.23	0.63	15.14	1.690	29	5	ND
1052.10	1.62	18.94	0.20	0.71	12.54	1.700	57	11	5
1052.70	2.20	10.65	0.96	0.88	4.86	3.110	89	7	3
1054.10	3.41	10.76	0.66	0.82	3.25	1.250	544	19	3
1054.20	ND	2.32	0.73	0.85	ND	0.350	ND	ND	ND
1056.10	0.81	5.43	0.41	0.63	7.69	0.730	39	21	1
1059.10	11.20	2.03	0.05	0.64	0.19	0.540	124	83	2
1059.20	8.58	1.74	0.38	0.51	0.22	2.350	190	67	7
1060.10	7.33	5.87	0.62	0.79	0.80	2.630	345	33	3
1061.00	7.26	5.50	0.50	0.79	0.88	3.950	507	94	6
1062.00	7.30	5.04	0.59	0.67	0.71	1.490	1682	41	9
1062.30	7.16	4.52	0.54	0.69	0.71	1.800	1091	ND	ND
1062.90	5.18	14.81	0.20	0.63	3.19	1.000	1510	37	10
1063.40	6.82	4.07	0.50	0.31	0.64	1.700	703	24	5
1063.50	7.01	5.46	0.56	0.44	0.83	1.710	660	21	5
1064.10	8.86	3.53	0.25	0.30	0.42	1.880	538	87	5
1064.20	7.95	4.65	0.40	0.53	0.70	0.690	861	27	8
1074.20	8.60	11.03	0.09	0.10	1.54	0.220	278	88	7
1077.20	6.05	9.58	0.26	0.12	1.78	0.450	267	23	6
1080.50	6.59	8.43	0.22	0.09	1.48	0.430	340	29	8
1084.70	6.71	8.81	0.27	0.23	1.48	0.520	304	21	6
1091.80	ND	5.52	0.23	0.22	ND	0.720	ND	ND	ND
1092.50	8.20	4.72	0.23	0.09	0.60	0.930	683	176	7
1115.60	8.01	6.68	0.25	0.30	0.95	0.510	482	70	8
1121.10	ND	8.29	0.12	0.31	ND	0.660	ND	ND	ND

1129.20	4.29	10.42	0.18	0.23	2.80	0.350	236	27	4
1136.00	4.34	12.95	0.27	0.18	3.45	0.430	238	20	5
1143.70	6.61	11.19	0.20	0.10	2.03	0.470	304	31	14
1150.80	ND	12.24	0.14	0.17	ND	0.570	ND	ND	ND
1162.80	3.51	14.52	0.10	0.40	4.90	0.330	230	57	7
1173.30	3.02	18.46	0.21	0.03	7.51	0.410	214	10	3
1182.20	ND	13.66	0.20	0.04	ND	0.480	ND	ND	ND
1189.80	8.31	7.79	0.18	0.39	1.22	0.500	369	42	9
1194.20	8.83	6.43	0.13	0.09	0.89	0.610	369	128	6
1199.20	ND	7.32	0.17	0.37	ND	0.680	ND	ND	ND
1209.60	9.55	1.04	0.56	0.45	0.14	1.670	619	114	6
1214.30	7.42	9.39	0.18	0.23	1.55	0.670	441	96	7
1224.30	ND	4.55	0.10	0.30	ND	0.620	ND	ND	ND
1228.50	8.22	8.15	0.18	0.46	1.17	0.520	514	149	6
1229.60	7.41	5.29	0.15	0.42	0.88	0.600	476	173	5
1235.20	ND	5.02	0.21	0.31	ND	0.540	ND	ND	ND
1244.60	8.19	5.26	0.22	0.45	0.78	0.800	675	67	7
1247.45	8.13	5.24	0.20	0.24	0.76	0.520	1148	48	7
1251.70	ND	4.04	0.18	0.23	ND	0.560	ND	ND	ND
1255.10	9.78	7.47	0.14	0.38	0.90	0.670	559	208	7
1261.10	9.06	4.77	0.15	0.22	0.61	0.710	507	169	5
1265.50	ND	4.18	0.13	0.41	ND	0.670	ND	ND	ND
1267.90	8.59	4.27	0.24	0.64	0.56	0.660	487	163	13
1270.10	8.21	3.67	0.14	0.36	0.52	0.570	437	173	6
1272.60	ND	4.15	0.09	0.17	ND	0.420	ND	ND	ND
1275.80	9.82	6.03	0.14	0.15	0.74	0.730	524	180	8
1277.00	9.69	6.59	0.12	0.29	0.82	0.610	414	158	7
1280.10	ND	6.01	0.20	0.49	ND	0.700	ND	ND	ND
1281.60	10.34	5.85	0.22	0.67	0.64	0.900	413	177	9
1281.85	9.90	4.73	0.16	0.40	0.57	0.830	363	164	6
1282.70	ND	5.44	0.12	0.10	ND	1.020	ND	ND	ND
1293.60	9.94	13.54	0.10	0.01	1.49	1.010	479	199	6
1300.90	12.50	8.52	0.15	0.30	0.79	0.700	698	213	5
1302.45	ND	13.08	0.24	0.30	ND	0.530	ND	ND	ND
1306.60	5.12	6.47	0.15	0.11	1.50	0.210	441	175	ND

Chapter 7 Nutrient feedbacks on oxygenation at the heart of the Great Oxidation Event

Preface

The contents of this chapter are written as a manuscript to be submitted:

Alcott, L. J., Mills, B. J. W. and Poulton, S. W. Nutrient feedbacks on oxygenation at the heart of the Great Oxidation Event. (*in prep*)

It is presented here as written for submission:

Article

The first appreciable rise in atmospheric oxygen is defined both temporally and in magnitude by the loss of mass independent fractionation of sulfur (MIF-S). This 'Great Oxidation Event' (GOE) has been recently redefined as non-unidirectional, which calls for a re-assessment of its feedbacks and drivers. The canonical source of oxygen to achieve the GOE is from photosynthesis, which over geological timescales is limited by the bioavailability of phosphorus. Alongside the oscillatory rise of oxygen, oceanic redox conditions fluctuated between ferruginous, oxic and euxinic bottom waters, which greatly impacted the availability of phosphorus. Here, we investigate the behaviour of phosphorus following deglaciation of a snowball Earth event and across oscillations in oceanic and atmospheric redox. The Rooihoogte and Timeball Hill formations, deposited at ~2.31 Ga, clearly demonstrate P recycling from the sediment under euxinic conditions in the aftermath of deglaciation, with progressively more effective burial and retention of P under the ferruginous and oxic bottom water conditions that subsequently developed. This highlights elevated phosphorus availability following deglaciation which stimulated oxygen production and resulted in the loss of MIF-S as atmospheric oxygen rose. However, this oxygen production ultimately hindered the sedimentary recycling of phosphorus, leading to a return to anoxic oceanic conditions.

This return to ferruginous conditions with limited sulfide production during the interglacial period continued to restrict phosphorus availability. This suggests that the behaviour of phosphorus provided a self-limiting feedback on the rise of oxygen.

7.1 Main Text

The Great Oxidation Event (GOE) was a defining moment in Earth history with respect to both the redox state of the oceans and the evolution of life, as atmospheric oxygen levels rose above 10^{-5} PAL (Present Atmospheric Level; Pavlov and Kasting, 2002). This quantitative threshold is commonly constrained in both magnitude and timing by the loss of mass-independent fractionation of sulfur isotopes (MIF-S, Farquhar et al., 2000). Prior to this event at ~2.4-2.3 Ga, sporadic increases in the oceanic concentrations of sulfate and sulfide were driven by "whiffs" of oxygen, as oxidative weathering of sulfides became more prevalent whilst the MIF-S signal remained (Anbar et al., 2007; Reinhard et al., 2009). The continued fluctuations (and overall positive trajectory; Fakharee et al. (2018)) of atmospheric oxygen finally overcame the 10^{-5} PAL threshold, leading to intermittent loss of the MIF-S signature at ~2.3 Ga (Gumsley et al., 2017; Poulton, in prep). Recent work has demonstrated the interplay between the prominent snowball Earth glaciations alongside the oscillatory nature of the GOE, with oxygenation peaking during the interglacial intervals (Gumsley et al., 2017). Oceans maintained their predominantly ferruginous redox state across the GOE (anoxic and Fe^{2+} rich; Poulton and Canfield, 2011). However, the influx of sulfate from the continents led to the development of spatially and temporally restricted euxinic (anoxic and sulfidic) conditions on productive margins across the globe (Reinhard et al., 2009; Scott et al., 2008; Kendall et al., 2010; Zerkle et al., 2012). The impact of the increased sulfate and sulfide concentrations has been explored with respect to both oxygenation history and nutrient availability (Fakharee et al., 2019) (Alcott et al., in prep/ Chapter 6).

Phosphorus is commonly considered the geologically paced ultimate limiting nutrient (Tyrell, 1999) for primary producers and is thought to have been fundamental in driving and priming the GOE (e.g. Cox et al., 2018; Alcott et al., in prep/ Chapter 5), whilst being heavily influenced by the redox state of the oceans (e.g. (Bjerrum and Canfield, 2002; Guilbaud et al., 2020)(Alcott et al., in prep/ Chapter 5). Ferruginous conditions are commonly linked to extensive drawdown and fixation of P associated with iron mineral deposition (P_{Fe}, Bjerrum and Canfield, 2002). However, sulfate and organic carbon availability can diminish this iron trap through the production of H_2S (Krom and Berner, 1980; Slomp et al., 2002) (Alcott et al., in prep/ Chapter 5).

This H_2S can then drive P recycling via the reductive dissolution of iron (oxyhydr)oxides and subsequent phosphorus release from sulfidic sediments (or in a euxinic water column; Krom and Berner, 1980; Slomp et al., 2002). The benthic flux of P is also promoted by the preferential release of organic-bound P (P_{org}) relative to organic carbon (C_{org}) during anaerobic remineralisation, particularly by sulfate-reducers, leading to high C_{org}/P_{org} ratios relative to the Redfield Ratio (Ingall et al., 1993; Ingall and Jahnke, 1994). Release of bioavailable P to the water column can stimulate productivity leading to a net increase in oxygen production (Van Cappellen and Ingall, 1994; Slomp et al., 2002) (Alcott et al., in prep/ Chapter 5). When initially released into sedimentary pore waters, phosphorus concentrations have the potential to approach saturation, leading to 'sink-switching' to authigenic phases (P_{aut}) such as carbonate fluorapatite (Ruttenberg and Berner, 1993; März et al., 2018) or vivianite (Slomp et al., 2013; März et al., 2018; Xiong et al., 2019).

To investigate the role of P in the oscillatory nature of the GOE, we focus on the Rooihoogte and Timeball Hill formations, South Africa, which demonstrate ocean-atmosphere redox fluctuations (Zerkle et al., 2017; Poulton, in prep). Tuffs from the lower Timeball Hill give an age of 2.31 ± 0.009 Gyr based on U-Pb zircon dating (Rasmussen et al., 2013), which now constrains the Rooihoogte formation to have been deposited immediately after a snowball Earth glaciation associated with the GOE (Gumsley et al., 2017). This glaciation is thought to have been the 3rd of 4 global snowball event (Gumsley et al., 2017). This 3rd glaciation is now thought to be correlated with the Gowganda Formation of the Huronian Basin, North America and is "missing" from the correlative Australian sections (Gumsley et al., 2017). The onset of a persistent aerobic nitrogen cycle is attributed to these formations, fuelled by appreciable oxygen concentrations within the water column in addition to ample upwelled nutrient availability (Zerkle et al., 2017).

Previous work has proposed the irreversible rise of oxygen to exist within the lower Timeball Hill formation, with studies suggesting the permanent loss of MIF-S (Luo et al., 2016). However, this has recently been found not to be the case (Poulton, in prep). A MIF-S signature is still recorded within the Rooihoogte formation, however it is lost alongside variable redox bottom water conditions approaching the Rooihoogte upper boundary (Poulton, in prep; Fig 7.1; 7.2). Other work has highlighted periodic disappearances of the MIF-S signature and attributed it to oxidative weathering of pre-

initial MIF-S loss crustal material (e.g. Lyons et al., 2014; Phillipot et al., 2018). This "crustal memory effect" has been interpreted to have occurred within sediments aged from ~2.45 Ga to beyond 2.31 Ga in Australia (Phillipot et al., 2018). A proposed asynchronous loss of the MIF-S signal calls for the current paradigm of an irreversible GOE occurring at ~2.31 Ga to be re-evaluated. Correlative sections in North America, Fennoscandia and other southern African basins have also been investigated with respect to the timing of the loss of MIF-S (Guo et al., 2009; Cui et al., 2018). The Huronian succession of North America contains a small but resolvable MIF-S signal throughout, but due to the preservation of the material it has been proposed to have occurred via homogenization by regional metamorphism, sulfur recycling or dilution of MIF-S by magmatic fluids (Cui et al., 2018). Fennoscandia has recently been studied and the initial loss of MIF-S seems to have occurred prior to the first glaciation (Warke et al., 2020). However, as discussed by the authors, extensive regional unconformities complicates correlations of the snowball Earth events. The Duitschland Formation of an equivalent basin in South Africa also documents the loss of MIF-S and, based on updated correlations (Bekker et al. in prep), documents oscillatory increases in oxygen may have occurred in sediment older than those studied here. As discussed in Poulton (in prep), at the base of the Timeball Hill formation the MIF-S signal returns with up to four successive fluctuations in atmospheric oxygen concentrations throughout the formations deposition, with the successive loss and gain of the MIF-S signature. This oscillatory nature further complicates the correlation of the "definitive loss of MIF-S" as earlier intervals proposing the loss of MIF-S (e.g. Warke et al., 2020) may just be an earlier atmospheric oxygen oscillation.

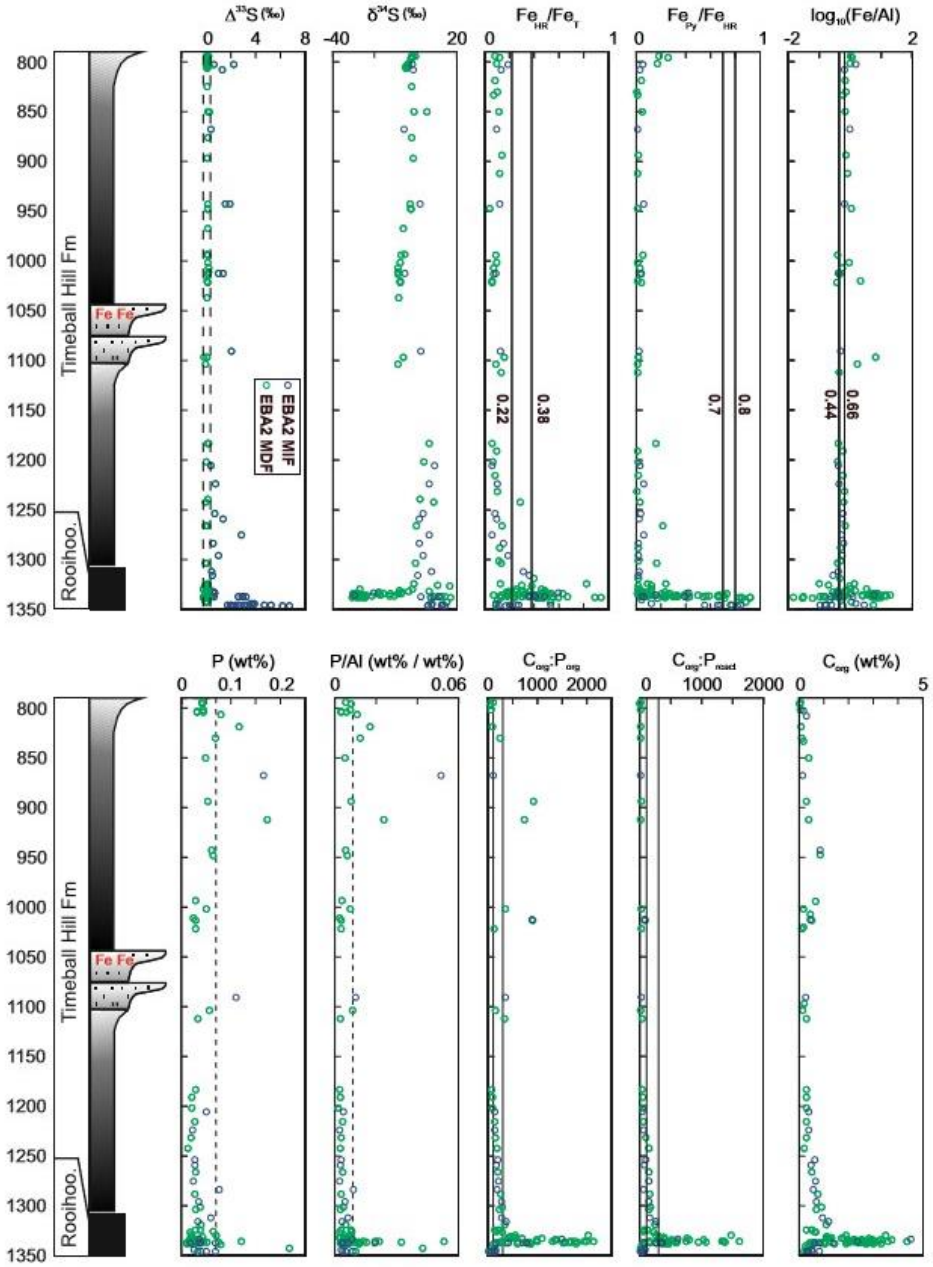

Figure 7.1. *Stratigraphy and geochemistry of the EBA-2 drill core. $\Delta^{33}S$ and $\delta^{34}S$ and iron speciation data from Poulton (in prep). Dashed lines on the Fe_{HR}/Fe_T plots represent the defined boundaries for identifying oxic and anoxic deposition, with equivocal samples falling between these lines. Dashed line on Fe_{Py}/Fe_{HR} plots distinguishes euxinic from ferruginous deposition when other iron proxies suggest anoxic deposition. Dashed lines on Fe_T/Al plots represent the normal range for oxic deposition (wt%/wt%). Dashed lines represent the Redfield Ratio (106:1), and the inferred $C_{org}:P_{org}$ ratio for the early Precambrian sediments deposited under highly oligotrophic P-limited conditions (300:1; Reinhard et al., 2017).*

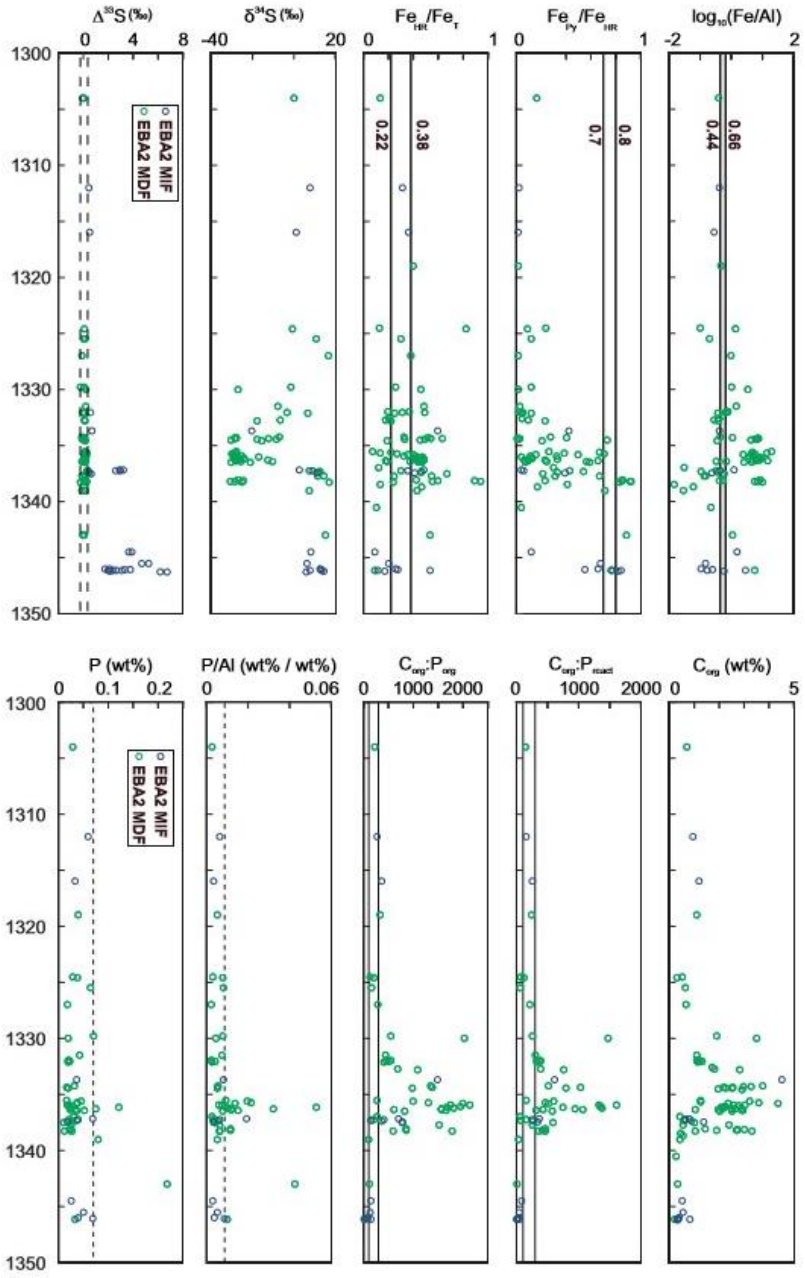

Figure 7.2. *Geochemistry of Rooihoogte-Timeball Hill formation boundary as seen in EBA-2 drill core. $\Delta^{33}S$ and $\delta^{34}S$ and iron speciation data from Poulton (in prep). Dashed lines on the Fe_{HR}/Fe_T plots represent the defined boundaries for identifying oxic and anoxic deposition, with equivocal samples falling between these lines. Dashed line on Fe_{Py}/Fe_{HR} plots distinguishes euxinic from ferruginous deposition when other iron proxies suggest anoxic deposition. Dashed lines on Fe_T/Al plots represent the normal range for oxic deposition (wt%/wt%). Dashed lines represent the Redfield Ratio (106:1), and the inferred $C_{org}:P_{org}$ ratio for the early Precambrian sediments deposited under highly oligotrophic P-limited conditions (300:1; Reinhard et al., 2017).*

The ocean redox chemistry broadly matches the atmospheric O_2 behaviour (Figure 7.1; 7.2). The Rooihoogte formation displays initially intermittent ferruginous conditions (Fe_{HR}/Fe_T >0.22; Fe/Al >0.66; Fe_{py}/Fe_{HR} <0.7) under a predominantly anoxic atmosphere. The upper Rooihoogte and the base of the Timeball Hill formations suggest predominantly euxinic bottom waters (Fe_{HR}/Fe_T >0.22; Fe/Al >0.66; Fe_{py}/Fe_{HR} >0.7) whilst the atmosphere demonstrates oxygen concentrations above 10^{-5} PAL. The Lower Timeball Hill formation displays a variable atmospheric signature along with the introduction of firstly ferruginous conditions followed by oxygenated bottom waters (Fe_{HR}/Fe_T <0.38; Fe/Al <0.66) accompanying a shallowing of the water column (Coetzee, 2001). The remainder of the Timeball Hill formation (<1150m depth) suggests anoxic ferruginous conditions due to the elevated Fe/Al ratios with significant transformation of Fe_{HR} to poorly reactive silicates (Fe_{PRS}; See Supplementary Information) alongside the several fluctuations in atmospheric oxygen.

Throughout the succession, phosphorus concentrations are typically low, apart for a few notable samples which are also elevated above average shale values when normalised to Al. Significantly elevated P concentrations and P/Al ratios are found within the Rooihoogte formation and typically align with transitions to either ferruginous or oxic conditions, as P would be extensively drawn down and retained under ferruginous or oxic conditions in contrast to euxinic conditions (Alcott et al. in prep/ Chapter 6).

With these variable redox conditions, the behaviour of P can also be investigated based on partitioning of various phases as determined by phosphorus speciation (Figure 7.1; 7.2; 7.3). To assess whether phosphorus is recycled from the sediment to the water column, we define a reactive P pool (P_{reac}) that may sequester dissolved P (P_{org}, P_{aut}, P_{Fe}). Once euxinic conditions became more prominent in the Rooihoogte formation, the C:P ratios become elevated, demonstrating recycling from organic matter (C_{org}:P_{org} >106) and the sediment (C_{org}:P_{reac} >106) (Figure 7.3). This recycling is also seen within samples that indicate ferruginous conditions in the upper Rooihoogte formation, as seen in Figure 3. These ferruginous samples of the Rooihoogte formation suggest active microbial sulfate reduction based on the elevated Fe_{Py}/Fe_{HR} ratios, but not to the extent to develop euxinic bottom waters (Figure 7.1; 7.2). As the overlying bottom waters became progressively more ferruginous and ultimately oxic, the ratios pass below 300:1 (possible C_{org}:P_{org} ratio of primary organic matter under P limited

conditions; Reinhard et al., 2017) and 106:1. In contrast to greater nitrate availability in the lower Timeball Hill formation (Zerkle et al., 2017; Luo et al., 2018), the elevated P_{Fe} concentrations and reduced P_{org} recycling suggests greater P retention under ferruginous and oxic conditions (See Supplementary Information).

The remainder of the Timeball Hill formation, which is predominantly anoxic within the ocean and with variable oxygen in the atmosphere, indicates some recycling of P from organic matter into the pore waters. The corresponding low C_{org}:P_{reac} ratios, however, suggest that the P was trapped within the sediment and efficiently underwent 'sink-switching' to P_{aut} likely via P_{Fe} (See Supplementary Information).

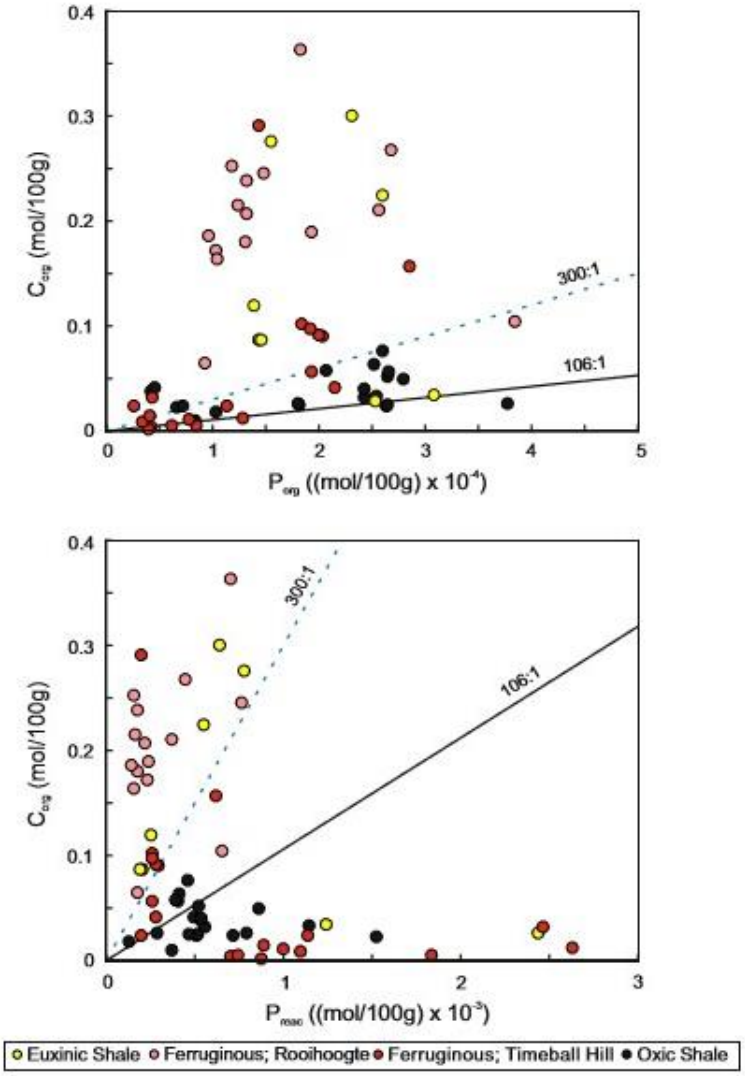

Figure 7.3. *Relationships between organic carbon and different phosphorus pools. (A) C_{org}:P_{org}; (B) C_{org}:P_{reac}. Dashed lines represent the Redfield Ratio (106:1) and the inferred C_{org}:P_{org} ratio for the early Precambrian sediments deposited under highly oligotrophic P-limited conditions (300:1; Reinhard et al., 2017).*

This dataset illustrates the expected course of events recorded by iron and phosphorus speciation that follow deglaciation of a snowball Earth event (Figure 7.4). During deglaciation, weathering rates would have increased leading to the enhanced delivery of nutrients such as phosphorus (e.g. (Hoffman et al., 1998; Planavsky et al., 2010b; Canfield et al., 2007)).

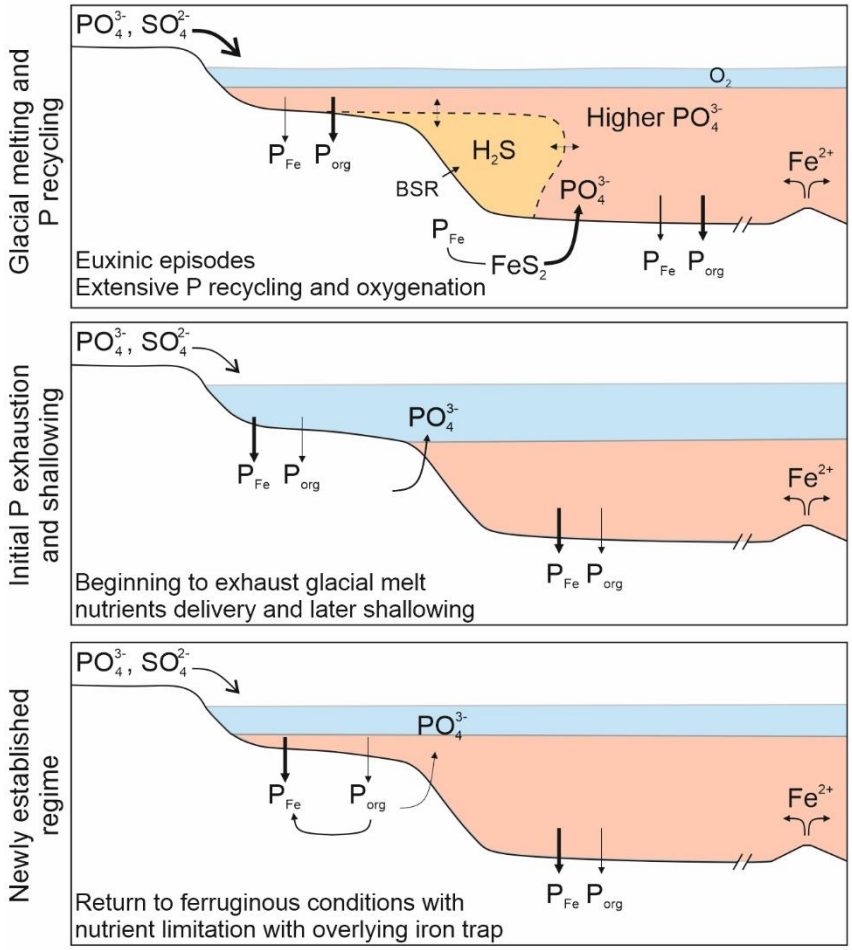

Figure 7.4. *Illustration demonstrating the self-limiting feedback between the oxygen and phosphorus cycles following deglaciation.*

This increased phosphorus availability would have driven primary production supplying organic carbon to fuel microbial sulfate reduction (MSR), allowing for pyrite formation and diminishing the P_{Fe} trap as seen by the elevated C_{org}:P_{reac} ratios. This is what is depicted in the upper Rooihoogte formation, with elevated Fe_{py}/Fe_{HR} ratios suggesting extensive sulfide production. Coupled with this, highly negative $\delta^{34}S$ values suggest pyrite formation under less sulfate limiting conditions proposing both increased nutrient supply and recycling in addition to an increased sulfate concentration. The interpretation of increased sulfate availability must be considered cautiously, as with variable atmospheric oxygen and oxidative weathering, the isotopic signature of sulfur delivered to the oceans may have also been different to present day.

As demonstrated by iron speciation, bottom waters across the formation boundary became ferruginous contemporaneous with a decrease in C_{org}:P_{reac} ratios, indicating a weakening of the benthic flux of P. As sustained oxygenated conditions became

established, P recycling from the sediment continued to be restricted in addition to C_{org}:P_{org} ratios suggesting little to no recycling from organic matter.

The remainder of the Timeball Hill formation (<1150 m) returns to ferruginous conditions (supported by elevated Fe/Al ratios) suggesting that the continued and commonly considered uni-directional rise in oxygen is unfounded in both the atmosphere and ocean (Poulton, in prep). Under these later ferruginous conditions, P was recycled from organic matter but not from the sediment. The main mechanism for retaining this pore water P, would have either been via the formation of authigenic minerals such as calcium fluorapatite (CFA) (e.g. Ruttenberg and Berner, 1993) or trapping of upward migrating P by freshly deposited iron minerals (e.g. Bjerrum and Canfield, 2002). Phosphorus speciation suggests the relinquished P is sequestered as authigenic phases, however late stage diagenesis may have allowed for 'sink-switching' from iron bound to authigenic bound phases.

The nitrogen cycle has been extensively explored throughout the core studied here through the use of nitrogen isotopes (Zerkle et al., 2017; Luo et al., 2018). The limited bioavailability of nitrogen in the periodically euxinic portion (Rooihoogte Formation) of the core is supported by the presence of euxinia as nitrate would have been the preferential oxidant for organic matter (Boyle et al., 2013). Nitrogen isotopes then support an increase in bioavailable nitrate coincident with the transition to more oxygenated conditions in the Timeball Hill Formation (Zerkle et al., 2017). This increase in bioavailable nitrogen is thought to have been fuelled by elevated nitrification driven by newly available marine oxidants (Zerkle et al., 2017). The upper Timeball Hill Formation suggests diazotrophy responding to an exhausted nitrogen pool defining the first widespread nitrogen famine in the Palaeoproterozoic rock record (Luo et al., 2018). As discussed, this step change in nutrient behaviour is also found within the phosphorus record, with P retention under the oxygenated conditions of the lower Timeball Hill Formation and recycling being restricted due to the presence of an overlying iron trap in the upper Timeball Hill Formation. The variable P/Al ratios in this upper interval may suggest a fluctuating P reservoir. This minimal and restricted P recycling seems, according to the nitrogen isotope record, to have been sufficient to allow for appreciable diazotrophy. It may have been possible for colimitation of both nitrogen and phosphorus to produce the variable atmospheric and ocean redox conditions. Aluminium concentrations are relatively stable throughout the Timeball

Hill Formation suggesting, tentatively, no significant changes in weathered nutrient input.

This dataset demonstrates the impact of deglaciation on the behaviour of phosphorus within the context of the oscillatory rise of oxygen across the GOE. As glacial melt waters brought appreciable nutrients and sulfate from the freshly oxidized continents, euxinia induced extensive phosphorus recycling. Elevated P concentrations derived both from deglaciation and recycling promoted oxygenation as seen by the correlated loss of the MIF-S signal and euxinia. As this riverine supply was eventually exhausted, phosphorus recycling from the sediment halted due to the lack of organic carbon and sulfate availability for MSR and oxygen production, decreasing ocean and atmosphere oxygen concentrations. As the burial and retention of phosphorus under oxygenated conditions set in, primary production (and associated oxygen production) becomes limited leading to persistent ferruginous conditions for the remainder of the studied section. This series of feedbacks explains the apparent oscillatory rise of oxygen across the GOE in between the glaciations.

7.2 Supplementary Information

Geological and stratigraphic context

The EBA-2 drill core passes through low grade metamorphic sedimentary deposits of late Neoarchean-Palaeoproterozoic age. This succession in the Transvaal sub-basin is correlated with the Griquland West basin, also in South Africa (Moore et al., 2001). Within the Transvaal sub-basin, the Transvaal Supergroup preserves sediments aged between approximately 2.65 – 2.05 Ga and contains the Chuniespoort and Pretoria groups (Moore et al., 2001). The studied formations, the Rooihoogte and Timeball Hill formations, are within the Pretoria group (Moore et al., 2001). Beneath the Rooihoogte formation, a mid-Transvaal unconformity is correlatable across other Paleoproterozoic successions within South Africa and is often associated with the formation and persistence of a Snowball Earth event (Eriksson et al., 1995; Gumsley et al., 2017).

The Pretoria group as a whole is dominated by alternating mudstone and sandstone units within minor conglomerate and volcanic units (Catuneanu and Eriksson, 1999). This interaction is interpreted as alluvial and marine sedimentation (Catuneanu and Eriksson, 1999).

The shales of the Rooihoogte formation are thought to have been relatively proximal to the coastline as part of a fan-delta open to the ocean (Catuneanu and Eriksson, 2002; Bekker et al., 2004). The Timeball Hill formation is however clearly dominated by marine sedimentation with small sandstone deposits suggesting brief intervals of regression allowing for deltaic deposits (Catuneanu and Eriksson, 2002). The Timeball Hill formation consists of two shale members. The lower shale member includes interbedded mudstone, siltstone and fine-grained sandstones, with coarser units being interpreted as delta-fed turbidite deposits (Eriksson and Reczko, 1998). In contrast, the upper shale member is interpreted to include more characteristic black shale deposition (Catuneanu and Eriksson, 1999). This overall pattern of sedimentation is thought to have occurred due to progressive rifting providing accommodation for sedimentation (Catuneanu and Eriksson, 1999).

At the base of the Rooihoogte formation, there is a basal glacial diamictite signifying the presence of Snowball Earth formation (Gumsley et al.,2017). The shared boundary of the two studied formations has often been noted as a possible transitionary period

for the loss of the mass independent fractionation of sulfur signal at ~2.32 Ga (Bekker et al., 2004; Luo et al., 2016; Gumsley et al., 2017).

P phase alteration

Late-stage P phase alteration has been identified as a key factor to consider when utilising phosphorus speciation for ancient sediments (Creveling et al., 2014; Thompson et al., 2019). The main concern is the transfer from P_{aut} to P_{cryst} via potential recrystallization of carbonate fluorapatite. We note that on the strongest correlation between the two phases is within the upper Timeball Hill formation. This correlation would only lead to a decrease in the C_{org}:P_{reac} ratios when including the contribution of P_{cryst}. As we suggest that there is limited to no recycling in this part of the core, this conversion does not detrimentally impact our interpretation.

The period of proposed recycling during the Rooihoogte formation must also be scrutinised as to its primary origin, as the inclusion of the P_{cryst} phase would lead to lower values going against our interpretation. However, the C_{org}:P_{tot} ratio also above 106:1 and 300:1 suggesting that recycling is still occurring regardless of the extent of phase conversion.

Fe phase alteration

As explored in Poulton (*in prep*), the redox interpretation of the EBA-2 core is relatively complex due to transformation of highly reactive iron phases to poorly reactive sheet silicates (Figure 7.5; 7.6). This phenomena has been explored extensively in past uses of iron speciation (e.g. Cumming et al. (2013); Doyle et al., 2018). We use the ratio of the highly reactive and poorly reactive iron phases to the total iron concentration and compare it to the average Phanerozoic shale to try and constrain the extent of conversion. As it is possible to see, some samples demonstrate significant transformation meaning that this must be taken into account with the traditional iron speciation ratios. Based on this, the majority of the upper Timeball Hill can be seen to be enriched in the sheet silicates allowing for the interpretation of anoxic bottom waters as the Fe_{HR}/Fe_T ratio should be higher than in Figure 1. The lower Timeball Hill on the other hand, allows for the original Fe_{HR}/Fe_T ratio to be used as no significant enrichment is found allowing for oxic conditions to be interpreted.

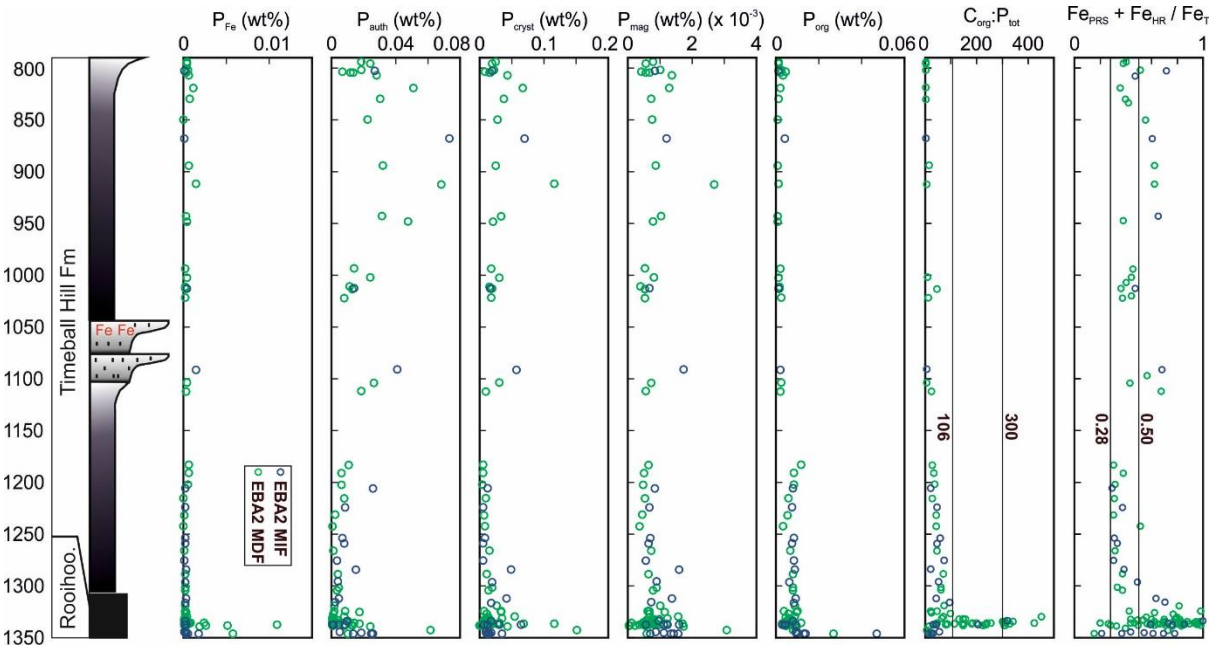

Figure 7.5. *P speciation data and (Fe_{PRS} + Fe_{HR})/Fe_T ratios.*

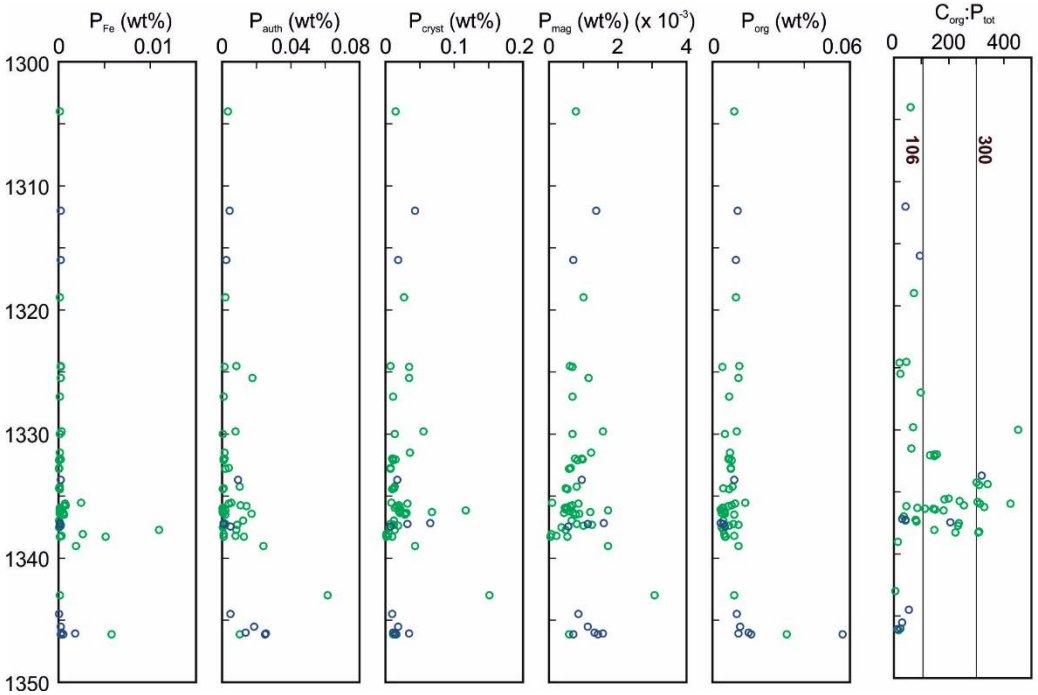

Figure 7.6. *Rooihoogte-Timeball Hill formation boundary P speciation data*

Table 7.1 Analytical data including data for major element concentrations, iron speciation, C_{org} and P phases. ND = not determined.

EBA-2 – Rooihoogte – Timeball Hill Formations

Depth(m)	Al (wt%)	Fe_T (wt%)	Fe_{HR}/Fe_T	Fe_{Py}/Fe_{HR}	Fe_T/Al	Fe_{PRS} (wt%)	C_{org} (wt%)	P_T (ppm)	P_{reac} (ppm)	P_{org} (ppm)
794	7.52	7.89	0.09	0.18	1.05	2.49	0.050	408.6	211.2	12.9
795.5	5.45	6.33	0.12	0.25	1.16	1.63	0.020	419.8	262.9	12.1
802	5.95	5.90	0.10	0.17	0.99	2.44	0.060	441.6	223.4	26.3
802.7	ND	ND	ND	ND	ND	ND	ND	ND	293.6	13.8
802.7	4.52	6.84	0.19	0.05	1.51	3.60	0.170	ND	ND	ND
803.5	ND	ND	ND	ND	ND	ND	ND	317.1	117.6	45.6
804.1	ND	ND	ND	ND	ND	ND	ND	436.7	164.9	20.0
804.5	ND	ND	ND	ND	ND	ND	ND	311.5	144.6	20.5
806.8	ND	ND	ND	ND	ND	ND	ND	802.9	331.5	33.5
808	6.98	4.47	0.13	0.03	0.64	1.50	0.300	ND	ND	ND
819	6.77	4.70	0.08	0.04	0.69	1.29	0.070	1167.7	550.8	19.1
830	5.61	4.05	0.10	0.01	0.72	1.18	0.100	689.0	327.7	10.5
833.5	8.34	4.74	0.07	0.01	0.57	1.65	0.190	ND	ND	ND
849.8	ND	ND	ND	ND	ND	ND	ND	481.0	237.3	5.7
850	6.94	4.90	0.12	0.05	0.71	2.12	0.400	ND	ND	ND
868	3.24	3.11	0.10	0.01	0.96	1.58	0.150	1658.2	788.5	39.8
894	6.81	4.94	0.14	0.01	0.73	2.37	0.290	530.9	341.9	8.2
912	7.24	5.80	0.12	0.01	0.80	2.89	0.380	1730.5	738.5	13.4
943	10.37	6.68	0.12	0.06	0.64	3.50	0.860	ND	ND	ND
943.1	ND	ND	ND	ND	ND	ND	ND	613.7	333.9	7.1
947.5	7.63	8.54	0.04	0.01	1.12	2.89	0.860	ND	ND	ND
948.3	ND	ND	ND	ND	ND	ND	ND	644.4	498.7	9.0
993.7	ND	ND	ND	ND	ND	ND	ND	293.2	168.8	20.1
994	8.56	3.45	0.09	0.06	0.40	1.26	0.660	ND	ND	ND
1002	6.81	6.28	0.10	0.01	0.92	2.16	0.170	506.5	267.2	12.5
1007	10.27	5.64	0.07	0.03	0.55	1.87	0.460	ND	ND	ND
1011	ND	ND	ND	ND	ND	ND	ND	248.1	133.6	14.8
1012.5	11.61	4.78	0.09	0.04	0.41	1.81	0.450	ND	161.2	13.1
1013	9.49	4.32	0.07	0.04	0.45	1.26	0.500	290.8	148.0	14.2
1020	11.10	24.43	0.06	0.01	2.20	9.27	0.180	ND	ND	ND
1022	9.06	3.36	0.06	0.04	0.37	1.05	0.120	286.8	111.7	25.7
1091	11.13	5.47	0.13	0.02	0.49	2.99	0.280	1102.3	457.9	20.4
1097	3.95	26.09	0.16	0.01	6.61	10.62	0.200	ND	ND	ND
1104	6.60	11.11	0.09	0.01	1.68	3.76	0.140	570.8	299.4	24.1
1112	12.54	5.60	0.14	0.01	0.45	3.02	0.290	330.1	213.7	22.2
1183	13.26	5.40	0.06	0.16	0.41	1.30	0.310	287.7	237.4	116.7
1191	7.69	4.47	0.09	0.01	0.58	1.28	0.290	217.3	152.5	81.4
1202	12.90	5.12	0.07	0.01	0.40	1.26	0.300	210.5	154.1	81.9
1205.5	12.11	4.93	0.06	0.03	0.41	1.15	0.400	500.9	343.9	78.6
1215.5	7.44	4.33	0.08	0.02	0.58	0.98	0.300	278.1	139.2	56.1
1224	9.81	4.32	0.10	0.06	0.44	1.17	0.390	219.2	167.2	75.2
1231.5	5.97	3.92	0.10	0.00	0.66	0.79	0.310	190.2	85.4	55.9
1242.5	4.73	2.98	0.29	0.03	0.63	0.66	0.220	133.6	39.0	32.1
1253.5	9.05	5.26	0.08	0.03	0.58	1.20	0.630	276.8	155.6	82.0
1259	9.60	5.18	0.09	0.02	0.54	1.24	0.480	269.3	160.1	75.2
1266	7.66	5.40	0.14	0.21	0.71	0.94	0.500	281.2	84.8	66.5
1275.5	10.15	5.39	0.06	0.06	0.53	1.29	0.680	239.7	121.5	82.2
1284	8.52	5.36	0.15	0.02	0.63	1.24	0.590	759.0	257.6	86.5

1288.3	9.14	4.45	0.12	0.02	0.49	1.11	0.760	279.7	123.1	77.8
1296	7.17	4.03	0.19	0.01	0.56	1.22	0.690	352.4	116.4	64.0
1301.5	9.48	4.63	0.12	0.02	0.49	0.99	0.920	384.6	137.5	80.6
1304	10.88	4.25	0.14	0.17	0.39	1.00	0.690	294.5	120.8	79.1
1312	9.15	3.84	0.31	0.02	0.42	1.23	0.950	592.1	152.1	92.0
1316	9.62	2.67	0.36	0.02	0.28	0.90	1.200	327.3	115.4	85.1
1319	7.36	3.33	0.40	0.02	0.45	1.39	1.110	389.7	114.8	86.8
1324.5	9.99	1.03	0.13	0.24	0.10	0.30	0.510	285.8	190.5	98.4
1324.6	4.84	6.50	0.82	0.09	1.34	1.00	0.290	382.4	58.5	35.1
1325.5	7.98	1.59	0.30	0.12	0.20	0.51	0.630	646.9	283.4	95.3
1327	7.65	7.23	0.38	0.01	0.95	2.77	0.680	179.2	77.9	59.7
1329.8	8.91	9.34	0.25	0.12	1.05	2.81	1.890	703.0	186.4	88.2
1330	4.38	14.86	0.46	0.01	3.40	4.99	3.490	199.7	59.0	44.3
1331.5	5.75	8.27	0.48	0.03	1.44	2.51	1.090	433.4	88.3	62.8
1331.98	8.68	6.87	0.19	0.02	0.79	1.69	1.100	195.0	83.5	62.0
1332.01	8.81	6.32	0.37	0.03	0.72	2.60	1.230	204.3	78.6	56.9
1332.04	5.68	3.72	0.31	0.04	0.66	1.42	1.300	ND	ND	ND
1332.07	5.32	4.00	0.49	0.05	0.75	1.32	1.170	227.3	78.1	59.3
1332.1	7.73	2.79	0.25	0.12	0.36	0.96	1.140	199.1	87.9	70.4
1332.6	8.78	3.58	0.20	0.05	0.41	1.03	1.720	ND	ND	ND
1332.7	7.25	2.06	0.18	0.10	0.28	0.74	1.820	ND	115.0	67.9
1332.8	8.53	3.16	0.22	0.23	0.37	0.96	2.810	ND	92.2	66.6
1333.7	4.54	1.86	0.59	0.42	0.41	0.75	4.510	365.3	182.5	78.4
1334.2	5.76	2.50	0.32	0.27	0.43	0.94	3.740	320.4	184.0	71.5
1334.3	3.65	3.96	0.52	0.40	1.08	1.82	3.300	ND	ND	ND
1334.36	3.22	22.57	0.63	0.03	7.01	7.11	2.170	164.8	52.6	40.5
1334.39	3.11	23.95	0.54	0.01	7.70	7.94	2.540	ND	ND	ND
1334.43	3.69	22.64	0.49	0.01	6.13	7.50	2.500	ND	ND	ND
1334.46	3.61	22.49	0.33	0.01	6.24	8.23	2.270	189.3	71.3	59.6
1334.5	3.51	15.20	0.45	0.73	4.33	2.59	1.950	ND	ND	ND
1334.6	6.70	2.29	0.19	0.21	0.34	ND	2.920	ND	ND	ND
1335.54	1.77	34.71	0.07	0.26	19.66	4.35	1.250	162.5	195.1	119.0
1335.6	2.30	10.66	0.22	0.67	4.65	2.61	3.220	454.7	134.2	83.0
1335.66	2.19	30.73	0.13	0.38	14.02	1.95	1.250	ND	ND	ND
1335.72	1.80	8.06	0.27	0.71	4.47	1.34	3.600	386.6	192.4	71.4
1335.78	2.66	6.52	0.36	0.50	2.45	1.61	4.360	368.4	210.9	56.4
1335.84	3.13	18.34	0.40	0.16	5.86	5.99	2.370	ND	ND	ND
1335.93	2.47	11.94	0.41	0.12	4.84	5.21	3.030	183.8	47.0	36.6
1335.97	3.64	18.10	0.32	0.32	4.97	6.74	2.590	213.1	48.6	38.2
1336.03	4.07	15.37	0.47	0.04	3.78	4.78	2.790	ND	ND	ND
1336.09	2.55	21.31	0.46	0.13	8.35	7.92	2.240	226.2	41.6	29.7
1336.14	2.28	20.84	0.43	0.13	9.13	10.51	2.070	1207.0	69.0	31.9
1336.19	2.37	16.77	0.41	0.10	7.08	8.09	2.190	ND	ND	ND
1336.23	2.17	13.78	0.49	0.33	6.34	4.63	2.870	225.3	51.9	40.9
1336.27	2.31	18.84	0.44	0.06	8.16	8.46	2.490	746.0	66.2	40.9
1336.29	2.59	12.04	0.48	0.23	4.65	3.76	2.650	ND	ND	ND
1336.33	2.96	18.21	0.47	0.10	6.15	8.97	1.970	352.6	46.0	32.4
1336.35	1.99	29.34	0.18	0.66	14.78	2.47	1.050	238.8	61.0	44.4
1336.39	5.50	1.87	0.19	0.25	0.34	0.71	2.930	ND	ND	ND
1336.44	3.36	2.29	0.38	0.57	0.68	0.62	2.950	511.4	228.7	45.7
1336.47	1.93	8.84	0.44	0.07	4.57	3.35	2.010	ND	ND	ND
1336.5	4.67	11.62	0.47	0.59	2.49	2.34	2.530	361.9	110.5	79.3
1337	11.56	0.36	0.12	0.30	0.03	ND	0.410	303.8	169.3	38.5
1337.2	3.52	4.25	0.48	0.04	1.21	1.19	0.780	683.1	53.7	28.7

1337.24	6.15	2.71	0.35	0.06	0.44	0.65	0.640	397.1	64.2	40.1
1337.27	6.71	2.16	0.30	0.43	0.32	0.63	0.630	207.6	104.1	75.3
1337.32	8.50	0.89	0.47	0.54	0.11	0.52	0.570	359.5	194.1	93.6
1337.38	4.97	1.88	0.46	0.33	0.38	0.72	0.870	272.7	82.4	60.8
1337.43	5.23	1.26	0.41	0.39	0.24	0.56	1.370	173.3	99.1	45.6
1337.5	2.95	1.68	0.67	0.22	0.57	0.48	1.010	110.3	42.8	33.6
1337.7	4.16	0.56	0.54	0.67	0.14	0.24	2.390	262.8	235.8	40.5
1337.7	8.34	1.25	0.24	0.31	0.15	0.47	0.560	ND	ND	ND
1338.07	2.16	18.37	0.42	0.85	8.50	1.30	1.430	248.4	76.2	43.0
1338.1	1.37	0.56	0.59	0.23	0.41	0.24	2.720	ND	ND	ND
1338.13	4.91	2.72	0.89	0.85	0.55	0.77	3.010	ND	ND	ND
1338.17	1.94	13.42	0.55	0.92	6.90	2.03	2.700	223.6	164.1	80.5
1338.2	1.85	10.69	0.94	0.92	5.79	1.25	1.910	ND	ND	ND
1338.24	ND	ND	ND	ND	ND	ND	3.310	279.2	232.3	47.8
1338.3	1.87	18.15	0.24	0.83	9.71	0.82	1.050	120.3	56.5	45.2
1338.5	14.73	0.22	0.13	0.41	0.02	0.04	0.440	ND	ND	ND
1338.7	8.55	0.53	0.47	0.17	0.06	0.15	0.560	ND	ND	ND
1339	15.61	0.46	0.43	0.71	0.03	0.19	0.410	795.7	372.8	95.3
1340.5	9.70	2.21	0.11	0.04	0.23	0.64	0.260	ND	ND	ND
1343	5.13	5.50	0.53	0.89	1.07	1.07	0.340	2177.5	723.8	78.3
1344.5	8.73	13.03	0.09	0.12	1.49	4.50	0.530	254.3	149.4	89.7
1345.5	9.29	1.40	0.20	0.67	0.15	0.47	0.560	498.9	300.7	101.8
1346	10.77	1.14	0.26	0.66	0.11	0.40	0.390	398.3	284.2	131.8
1346.1	7.92	2.00	0.27	0.55	0.25	0.84	0.320	685.0	383.9	94.9
1346.16	11.94	1.95	0.53	0.84	0.16	0.48	0.810	ND	406.8	140.2
1346.2	9.45	5.46	0.17	0.82	0.58	1.07	0.340	ND	ND	ND

Chapter 8 Conclusions

8.1 Summary

8.1.1 Earth's oxygen history

Through the application of a biogeochemical model, the results of Chapter 5 have proposed a feasible method for oxygenation of the Earth that does not rely on specific tectonic or biological trigger events. In the model that has been developed as part of this thesis (Alcott et al., 2019), the feedbacks within the carbon, oxygen and phosphorus cycle can themselves induce these oxygen steps in response to a gradual oxygenation of the Earth's surface. A 'Great Oxidation' of the atmosphere can be driven by the transition from reduced gas regulation to regulation by oxidative weathering of organic carbon as proposed by Daines et al. (2017). Further progressive oxygenation then leads to a change in the behaviour of the phosphorus cycle resulting in less P regeneration and rapid redox changes on the continental shelves: when the shelf becomes oxygenated, competing feedbacks allow for an unstable oscillatory period that are comparable to oceanic oxygenation events found within the Neoproterozoic (Sahoo et al., 2016). Finally, following progressive oxygenation of the upper ocean, the downwelling fluxes eventually sustain a fully oxygenated deep ocean.

This study suggests that the evolution of progressively more complex life, beyond cyanobacteria, or a major tectonic event were not required in order to produce the Earth's stepwise major oxygenation events. Leading to the proposal of the Earth's oxygen history being facilitated by the inherent interplay between biogeochemical cycles.

8.1.2 A driver for the Great Oxidation Event

The application of iron and phosphorus speciation on core material from prior to the GOE, has added to the understanding of the behaviour of the ultimate limiting nutrient, phosphorus, and its role in initial planetary oxygenation.

Sections from the Campbellrand platform and Koegas subgroup (~2.65 to 2.43 Ga) demonstrate predominantly ferruginous conditions with intermittent periods of euxinia. These two differing redox conditions display drastically different phosphorus speciation records indicating a benthic flux of phosphorus under euxinic conditions.

Phosphorus recycling is defined by the interpreted preferential remineralisation of phosphorus with respect to carbon from both organic matter and the sediment based on the C:P ratios of reactive P phases. This benthic flux supports a phosphorus enriched flux of upwelling water into shallower portions of the basin in order to promote nearer shore production as determined by nitrogen isotopes (Mettam et al., 2019). The overlying Koegas subgroup however demonstrates persistent ferruginous conditions with BIF deposition. These later cores suggest very little recycling with phosphorus being drawn down and retained within the sediment due to the greater abundance of iron rich (>20 wt%) and banded iron formation deposition.

Using the biogeochemical model of Chapter 5 it is possible to see that recycling of phosphorus can facilitate planetary oxygenation under reasonable weathering fluxes of phosphorus to the oceans. This recycling was ultimately driven by increases in ocean sulfate concentrations from the oxidative weathering of sulfides on the continents, leading to a potential positive feedback within the system, in addition to the feedbacks documented in Chapter 5.

8.1.3 Phosphorus dynamics during the Great Oxidation Event

The association between nutrient availability and sulfur dynamics is taken further with the $\Delta^{33}S$ record. Unpublished work (Poulton, *in prep*) proposes that the Rooihoogte-Timeball Hill formations demonstrate an oscillatory rise in atmospheric oxygen as the MIF-S fluctuates.

The oscillations take place across the interglacial following a snowball Earth deglaciation. This is recorded within the iron and phosphorus records, with euxinia being coeval with phosphorus recycling following deglaciation, as expected with the elevated weathering fluxes promoting productivity, supplying sulfate reducers.

However, further up the core, iron speciation suggests ferruginous and oxic conditions throughout the lower Timeball Hill formation. This, as demonstrated in Chapter 6, leads to greater phosphorus draw down and retention in the sediment, with limiting preferential recycling from organic matter or iron minerals.

The upper Timeball Hill exhibits a return to anoxic conditions, alongside an oscillatory atmospheric redox signal as shown by the $\Delta^{33}S$ record. This ferruginous interval however, displays recycling from organic matter but overall retention within

the sediment, most likely by iron minerals that have ultimately undergone sink switching to authigenic phases. Proposed extensive diazotrophy responding to an exhausted nitrogen pool in this interval requires sufficient phosphorus availability in contrast to the initial interpretation of the P speciation record. The variable P/Al ratios in this upper interval may indicate a fluctuating P reservoir. It may be possible for colimitation of both nitrogen and phosphorus to produce the variable atmospheric and ocean redox conditions.

The overall trend revealed by phosphorus speciation following deglaciation, suggests a self-limiting feedback on the rise of oxygen, with the expanding oxygenated conditions, stifling the benthic flux of phosphorus, hindering primary production and organic carbon burial.

Overall this thesis highlights the importance of phosphorus' role in the oxygenation of the planet. The rise of phosphorus recycling likely facilitated the first initial rise in atmospheric oxygen and then controlled its behaviour throughout the Proterozoic by providing a negative feedback on oxygenation via phosphorus sequestration. As is seen during the GOE, and later in the Neoproterozoic, phosphorus recycling effectively shuts down as the water column becomes sufficiently oxygenated, driving unstable redox conditions during these transitions.

8.2 Future Work

The model presented in Chapter 4 and 5 can potentially be coupled to an inorganic carbon cycle model. Providing the ability to predict both carbon isotopes in addition to temperature on geological timescales. Employing this model to a variety of scenarios, initially for testing against rich geochemical data such as OAEs. It could have the same versatility as the COPSE model commonly used to test global scale events (e.g. Bergman et al., 2004) but with the addition of a partitioned 4 box ocean-atmosphere system to provide global and localised context.

A key limiter to P recycling within and from the sediment is the concentration of sulfate and thus sulfide in the water column and pore waters. This has been shown throughout this thesis both before and during the GOE. The Lomagundi event is often considered a period of extensive organic carbon burial, primary production and

nutrient availability, initiating an oxygen overshoot (Bekker and Holland, 2012). Previous studies have suggested an expansion and following contraction of the sulfate reservoir across the Lomagundi event (Planavsky et al., 2012; Ossa Ossa et al., 2018; Ouyang et al., 2020). It would seem plausible that the increase in sulfate, if accompanied by euxinia, would lead to an elevated flux of P from the sediment leading to enhanced primary production and maintaining the Lomagundi event. The availability of shale material across this interval is rare as stratigraphic correlation is based on carbonate carbon isotopes of carbonate platforms. However, sections demonstrating the closing moments of the Lomagundi event (e.g. El Albani et al., 2010) could be studied using some of the methods in this thesis, e.g. phosphorus speciation.

The relative importance of sulfate on the behaviour of other biogeochemical cycles throughout Earth history can also be investigated. As shown in present day studies, the SMTZ is likely important with regards to the ultimate burial of P on geological timescales (e.g. Liu et al., 2018; März et al., 2018; Xiong et al., 2019). However, during the Archean and prior to the GOE, the concentration of sulfate is significantly lower, leading to questions about the depth or even presence of the SMTZ. Would iron oxidation of methane become a major process in the globally ferruginous ocean? And would the suppression of methane in addition to oxidation of methane by oxygen lead to global scale glaciations? These questions have been briefly explored in modern settings and within a modelling framework, however applications to Proterozoic studies seem to be limited (Catling et al., 2007; Sturm et al., 2019; Crowe et al., 2011; Lambrecht et al., 2020). A first test in the relative importance of iron oxidation of methane would be to implement its role in more biogeochemical models that consider methane. Following this, a more direct approach to find more modern day Archean analogues or traditional modern day settings to test its importance, or lack thereof, can be crucial in determining a numerical relationship. Taking these relationships back through time in the form of an Earth system model might help us better address questions such as the faint young sun paradox.

This thesis has also shown that the phosphorus cycle is a key consideration in the path to a habitable planet. On local and shorter timescales, the proximate limiting

nutrient, nitrogen may play a key role in limiting or promoting productivity. Coupled investigations of phosphorus speciation and nitrogen isotopes may provide insight into this delicate balance. The balance of these two nutrients has been investigated via modelling studies on glacial-interglacial timescales (Wallmann, 2003). As discussed in Chapter 4, Wallmann (2003) determined that during interglacial periods, phosphate would be the limiting nutrient, as opposed to nitrate under glaciated conditions. These limitations can be investigated with respect to Snowball Earth events. It has been proposed that during the Marinoan snowball Earth event, the surface ocean was connected to an oxygenated atmosphere (Johnson et al., 2017). With these two end members in mind, one with complete ocean-atmosphere separation and one in which interaction is fully allowed, the relative access of diazotrophs to the “endless” supply of atmospheric nitrogen can be investigated. One way to do this would be implementing a simple (or complex) nitrogen cycle into a biogeochemical model that includes at least the carbon, oxygen and phosphorus cycles and parameterising the extent or relative efficiency nitrogen fixation can occur.

References

Alcott, L.J., Mills, B.J.W. and Poulton, S.W. 2019. Stepwise Earth oxygenation is an inherent property of global biogeochemical cycling. *Science.* **366**(6471), pp.1333-1337.

Algeo, T.J. and Ingall, E. 2007. Sedimentary Corg: P ratios, paleocean ventilation, and Phanerozoic atmospheric pO2. *Palaeogeography, Palaeoclimatology, Palaeoecology.* **256**, pp.130-155.

Altermann, W. and Nelson, D.R. 1998. Sedimentation rates, basin analysis and regional correlations of three Neoarchaean and Palaeoproterozoic sub-basins of the Kaapvaal craton as inferred from precise U-Pb zircon ages from volcaniclastic sediments. *Sedimentary Geology.* **120**, pp.225-256.

Anbar, A. D. and Knoll, A. H. 2002. Proterozoic ocean chemistry and evolution: a bioinorganic bridge? *Science* **297**, pp. 1137-1142

Anbar, A.D., Duan, Y., Lyons, T.W., Arnold, G.L., Kendall, B., Creaser, R.A., Kaufman, A.J., Gordon, G.W., Scott, C., Garvin, J. and Buick, R. 2007. A Whiff of Oxygen Before the Great Oxidation Event? *Science.* **317**(5846), pp.1903-1906.

Andersen, M.B., Romaniello, S.J., Vance, D., Little, S.H., Herdman, R. and Lyons, T.W. 2014. A modern framework for the interpretation of 238U/235U in studies of ancient ocean redox. *Earth and Planetary Science Letters.* **400**, pp.184-194.

Anderson, T.F. and Raiswell, R. 2004. Sources and mechanisms for the enrichment of highly reactive iron in euxinic Black Sea sediments. *American Journal of Science.* **304**(3), pp.203-233.

Arning, E.T., Birgel, D., Brunner, B. and Peckmann, J. 2009. Bacterial formation of phosphatic laminites off Peru. *Geobiology.* **7**(3).

Arnold, G.L., Anbar, A.D., Barling, J. and Lyons, T.W. 2004. Molybdenum Isotope Evidence for Widespread Anoxia in Mid-Proterozoic Oceans. *Science.* **304**(5667), pp.87-90.

Asael, D., Rouxel, O., Poulton, S.W., Lyons, T.W. and Bekker, A. 2018. Molybdenum record from black shales indicates oscillating atmospheric oxygen levels in the early Paleoproterozoic. *American Journal of Science.* **318**(3), pp.275-299.

Aspila, K.I., Agemian, H. and Chau, A.S.Y. 1976. A semi-automated method for the determination of inorganic, organic and total phosphate in sediments. *Analyst.* (1200).

Ayres, D.E. 1972. Genesis of iron-bearing minerals in banded iron formation mesobands in the Dales Gorge Member, Hamersley Group, Western Australia. *Economic Geology.*

Bau, M. and Koschinsky, A. 2009. Oxidative scavenging of cerium on hydrous Fe oxide: Evidence fromthe distribution of rare earth elements and yttrium betweenFe oxides and Mn oxides in hydrogenetic ferromanganese crusts. *Geochemical Journal.* **43**, pp.37-47.

Bekker, A. 2015. Great Oxygenation Event. pp.1009-1017.

Bekker, A. and Holland, H.D. 2012. Oxygen overshoot and recovery during the early Paleoproterozoic. *Earth and Planetary Science Letters.* **317-318**, pp.295-304.

Bekker, A., Holland, H.D., Wang, P.L., Rumble, D., Stein, H.J., Hannah, J.L., Coetzee, L.L. and Beukes, N.J. 2004. Dating the rise of atmospheric oxygen. *Nature.* **427**.

Bekker, A., Kasting, J. and Anbar, A. 2013a. Evolution of the atmosphere and ocean through time. *Chemical Geology.* **362**, pp.1-2.

Bekker, A., Planavsky, N.J., Krapez, B., Rasmussen, B., Hofmann, A., Slack, J.F., Rouxel, O.J. and Konhauser, K.O. 2013b. Iron Formations: Their Origins and Implications for Ancient Seawater Chemistry. *Treatise on Geochemistry.* **9**, pp.561-628.

Bekker, A., Slack, J.F., Planavsky, N.J., Krapez, B., Hofmann, A., Konhauser, K.O. and Rouxel, O.J. 2010. Iron formation: the sedimentary product of a complex interplay

among mantle, tectonic, oceanic, and biospheric processes. *Economic Geology.* **105**(3), pp.467-508.

Belica, M.E., Tohver, E., Poyatos-More, M., Flint, S.S., Parra-Avila, L.A., Lanci, L., Denyszyn, S. and Pisarevsky, S.A. 2017. Refining the chronostratigraphy of the Karoo Basin, South Africa:magnetostratigraphic constraints support an early Permian agefor the Ecca Group. *Geophysical Journal International.* **211**, pp.1354-1374.

Benitez-Nelson, C. 2000. The biogeochemical cycling of phosphorus in marine systems. *Earth-Science Reviews.* **51**, pp.109-135.

Bergman, N.M., Lenton, T.M. and Watson, A.J. 2004. COPSE: A new model of biogeochemical cycling over Phanerozoic time. *American Journal of Science.* **304**, pp.397-437.

Berner, R.A. 1970. Sedimentary Pyrite Formation. *American Journal of Science.* **268**, pp.1-23.

Berner, R.A., Ruttenberg, K.C., Ingall, E. and Rao, J. 1993. The Nature of Phosphorus Burial in Modern Marine Sediments. *Interactions of C, N, P and S Biogeochemical Cycles and Global Change.* pp.365-378.

Betts, H.C., Puttick, M.N., Clark, J.W., Williams, T.A., Donoghue, P.C.J. and Pisani, D. 2018. Integrated genomic and fossil evidence illuminates life's early evolution and eukaryote origin. *Nature Ecol Evol.* **2**(10), pp.1556-1562.

Beukes, N.J. 1978. *Die karbonaatgesteentes en ysterformasies van die Ghaap-Groep van die Transvaal-Supergroep in Noord-Kaapland*. thesis, Rand Afrikaans University.

Beukes, N.J. 1984. Sedimentology of the Kuruman and Griquatown Iron-formations, Transvaal Supergroup, Griqualand West, South Africa *Precambrian Research.* **24**, pp.47-84.

Bindeman, I.N., Zakharov, D.O., Palandri, J., Greber, N.D., Dauphas, N., Retallack, G.J., Hofmann, A., Lackey, J.S. and Bekker, A. 2018. Rapid emergence of subaerial landmasses and onset of a modern hydrologic cycle 2.5 billion years ago. *Nature.* **557**(7706), pp.545-548.

Bjerrum, C.J. and Canfield, D.E. 2002. Ocean productivity before about 1.9 Gyr ago limited by phosphorus adsorption onto iron oxides. *Nature.* **417**, pp.159-162.

Bjerrum, C.J., Canfield, D.E. and Dahl, T.W. 2016. Chasing Neoproterozoic Atmospheric Oxygen Ghosts. In: *American Geophysical Union, Fall Meeting 2016*.

Borch, T. and Fendorf, S. 2007. Phosphate interactions with iron (hydr) oxides: Mineralization pathways and phosphorus retention upon bioreduction. *Developments in Earth and Environmental Sciences.*

Boyle, R. A., Clark, J. R., Poulton, S. W., Shields-Zhou, G., Canfield, D. E. and Lenton, T. M. 2013. Nitogen cycle feedbacks as a control on euxinia in the mid-Proterozoic ocean. *Nature Comm.*

Branch, T., Ritter, O., Weckman, U., Scachsenhofer, R. and Schilling, F. 2007. The Whitehill Formation- a high conductivity marker horizon in the KarooBasin. *South African Journal of Geology.* **110**, pp.465-476.

Brasier, M.D. and Lindsay, J.F. 1998. A billion years of environmental stability and the emergence of eukaryotes: new data from northern Australia. *Geology.* **26**(6), pp.555-558.

Brock, J. and Schulz-Vogt, H.N. 2011. Sulfide induces phosphate release from polyphosphate in cultures of a marine Beggiatoa strain. *ISME J.* **5**(3), pp.497-506.

Brocks, J.J., Jarrett, A.J.M., Sirantoine, E., Hallmann, C., Hoshino, Y. and Liyanage, T. 2017. The rise of algae in the Cryogenian oceans and the emergence of animals. *Nature.* **548**, pp.578-581.

Broecker, W.S. and Peng, T.H. 1982. *Tracers in the Sea.* New York: Eldigio Press.

Brumsack, H.J. 2006. The trace metal content of recent organic carbon-rich sediments: implications for Cretaceous black shale formation. *Palaeogeography, Palaeoclimatology, Palaeoecology.* **232**, pp.344-361.

Buick, R. 2008. When did oxygenic photosynthesis evolve? *Philosophical Transcations B.* **363**(1504).

Burnett, W.C. 1977. Geochemistry and origin of phosphorite deposits from off Peru and Chile. *Geol. Soc. Am. Bull.* **88**, pp.813-823.

Busigny, V., Lebeau, O., Ader, M., Krapez, B. and Bekker, A. 2013. Nitrogen cycle in the Late Archean ferruginous ocean. *Chemical Geology.* **362**. pp. 115-130.

Butterfield, N.J. 2015. Early evolution of the Eukaryota. *Palaeontology.* **58**, pp.5-17.

Butterfield, N.J. 2018. Oxygen, animals and aquatic bioturbation: An updated account. *Geobiology.* **16**, pp.3-16.

Cairns-Smith, A.G. 1978. Precambrian solution photochemistry, inverse segregation, and banded iron formations. *Nature.* **276**, pp.807-808.

Campbell, I.H. and Allen, C.M. 2008. Formation of supercontinents linked to increases in atmospheric oxygen. *Nature Geoscience.* **1**(8), pp.554-558.

Canfield, D.E. 1989. Reactive iron in marine sediments. *Geochimica et Cosmochimica Acta.* **53**(3), pp.619-632.

Canfield, D.E. 1998. A new model for Proterozoic ocean chemistry. *Nature.* **396**.

Canfield, D.E. 2005. THE EARLY HISTORY OF ATMOSPHERIC OXYGEN: Homage to Robert M. Garrels. *Annual Review of Earth and Planetary Sciences.* **33**(1), pp.1-36.

Canfield, D.E. 2006. Early anaerobic metabolisms. *Philos Trans R Soc Lond B Biol Sci.* **361**(1474), pp.1819-1834.

Canfield, D.E., Lyons, T.W. and Raiswell, R. 1996. A model for iron deposition to euxinic Black Sea sediments. *American Journal of Science.* **296**, pp.818-834.

Canfield, D.E., Poulton, S.W. and Narbonne, G.M. 2007. Late-Neoproterozoic Deep-Ocean Oxygenation and the Rise of Animal Life. *Science.* **315**(5808), pp.92-95.

Canfield, D. E. and Thamdrup, B. 2009. Towards a consistent classification scheme for geochemical environments, or, why we wish the term 'suboxic' would go away. *Geobiology* **7**(4)

Canfield, D.E., Raiswell, R. and Bottrell, S.H. 1992. The reactivity of sedimentary iron minerals toward sulfide. *American Journal of Science.* **292**(9).

Canfield, D.E., Raiswell, R., Westrich, J.T., Reaves, C.M. and Berner, R.A. 1986. The use of chromium reduction in the analysis of reduced inorganic sulfur in sediments and shales. *Chemical Geology.* **54**, pp.149-155.

Canfield, D.E., Stewart, F.J., Thamdrup, B., De Brabandere, L., Dalsgaard, T., Delong, E.F., Revsbech, N.P. and Ulloa, O. 2010. A cryptic sulfur cycle in oxygen-minimum-zone waters off the Chilean coast. *Science.* **330**.

Canfield, D.E. and Teske, A. 1996. Late Proterozoic rise in atmospheric oxygen concentration inferred from phylogenetic and sulphur-isotope studies. *Nature.* **382**, pp.127-132.

Casciotti, K L. 2016. Nitrogen and oxygen isotopic studies of the marine nitrogen cycle. *Annu. Rev. Mar. Sci*. **8**, pp.379-407

Catling, D.C. and Claire, M.W. 2005. How Earth's atmosphere evolved to an oxic state: a status report. *Earth and Planetary Science Letters.* **237**, pp.1-20.

Catling, D.C., Claire, M.W. and Zahnle, K.J. 2007. Anaerobic methanotrophy and the rise of atmospheric oxygen. *Philos Trans A Math Phys Eng Sci.* **365**(1856), pp.1867-1888.

Catling, D.C., Zahnle, K.J. and McKay, C.P. 2001. Biogenic Methane, Hydrogen Escape, and the Irreversible Oxidation of Early Earth. *Science.* **293**(5531), pp.839-843.

Catuneanu, O. and Eriksson, P.G. 1999. The sequence stratigraphic concept and the Precambrian rockrecord: an example from the 2.7–2.1 Ga TransvaalSupergroup, Kaapvaal craton. *Precambrian Research.* **97**, pp.215-251.

Catuneanu, O., Wopfner, H., Eriksson, P.G., Carincross, B., Rubidge, B.S., Smith, R.M.H. and Hancox, J.P. 2005. The Karoo Basins of south-central Africa. *Journal of African Earth Sciences.* **43**(1-3), pp.211-253.

Cawood, P.A., Hawkesworth, C.J. and Dhuime, B. 2013. The continental record and the generation of continental crust. *GSA Bulletin.* **125**.

Cawood, P.A., Hawkesworth, C.J., Pisarevsky, S.A., Dhuime, B., Capitanio, F.A. and Nebel, O. 2018. Geological archive of the onset of plate tectonics. *Philosophical Transactions of the Royal Society A.*

Chere, N., Linol, B., De Wit, M.J. and Schulz, H.M. 2017. Lateral and temporal variations of black shales across the southern Karoo Basin - Implications for shale gas exploration. *South African Journal of Geology.* **120**(4).

Chi-Fru, E., Rodriguez, N.P., Partin, C.A., Lalonde, S., Andersson, P., Weiss, D.J., El Albani, A., Rodushkin, I. and Konhauser, K.O. 2016. Cu isotopes in marine black shales record the Great Oxidation Event. *PNAS.* **113**(18), pp.4941-4946.

Claire, M.W., Catling, D.C. and Zahnle, K.J. 2006. Biogeochemical modelling of the rise in atmospheric oxygen. *Geobiology.* **4**(4), pp.239-269.

Clarkson, M.O., Poulton, S.W., Guilbaud, R. and Wood, R.A. 2014. Assessing the utility of Fe/Al and Fe-speciation to record water column redox conditions in carbonate-rich sediments. *Chemical Geology*. **382**, pp.111-122.

Cline, J. D. and Kaplan, I. R. 1975. Isotopic fractionation of dissolved nitrate during denitrification in the eastern tropical North Pacific Ocean. *Mar. Chem.*, **3**, pp. 271-299

Cloud, P. 1973. Paleoecological Significance of the Banded Iron-Formation. *Economic Geology*. **68**(7), pp.1135-1143.

Cloud, P.E. 1965. Significance of Gunflint (Precambrian) microflora—pho-tosynthetic oxygen may have had important local effects before becominga major atmospheric gas. *Science*. **148**, pp.27-35.

Coetzee, L. L. 2001. Genetic stratigraphic of the Paleoproterozoic Pretoria Group in the Western Transvaal, MSc Thesis, Rand Afrikaans University, 212 pp.

Condie, K.C. 2011. The supercontinent cycle. *Earth as an Evolving System.* New York: Academic Press New York.

Cosmidis, J., Benzerara, K., Morin, G., Busigny, V., Lebeau, O., Jezequel, D., Noel, V., Dublet, G. and Othmane, G. 2014. Biomineralization of iron-phosphates in the water column of LakePavin (Massif Central, France). *Geochimica et Cosmochimica Acta.* **126**, pp.78-96.

Cox, G.M., Lyons, T.W., Mitchell, R.N., Hasterok, D. and Gard, M. 2018. Linking the rise of atmospheric oxygen to growth in the continental phosphorus inventory. *Earth and Planetary Science Letters.* **489**, pp.28-36.

Creveling, J.R., Johnston, D.T., Poulton, S.W., Kotrc, B., Marz, C., Schrag, D.P. and Knoll, A.H. 2014. Phosphorus sources for phosphatic Cambrian carbonates. *Geological Society of America Bulletin.* **126**(1-2), pp.145-163.

Crockford, P.W., Kunzmann, M., Bekker, A., Hayles, J., Bao, H., Halverson, G.P., Peng, Y., Bui, T.H., Cox, G.M., Gibson, T.M., Wörndle, S., Rainbird, R., Lepland, A., Swanson-Hysell, N.L., Master, S., Sreenivas, B., Kuznetsov, A., Krupenik, V. and Wing, B.A. 2019. Claypool continued: Extending the isotopic record of sedimentary sulfate. *Chemical Geology.* **513**, pp.200-225.

Crowe, S.A., Døssing, L.N., Beukes, N.J., Bau, M., Kruger, S.J., Frei, R. and Canfield, D.E. 2013. Atmospheric oxygenation three billion years ago. *Nature.* **501**, pp.535-538.

Crowe, S.A., Jones, C., Katsev, S., Magen, C., O'Neill, A.H., Sturm, A., Canfield, D.E., Haffner, G.D., Mucci, A., Sundby, B. and Fowle, D.A. 2008. Photoferrotrophs thrive in an Archean Ocean analogue. *PNAS.* **105**(41), pp.15938-15943.

Crowe, S.A., Katsev, S., Leslie, K., Strum, A., Magen, C., Nomosatryo, S., Pack, M.A., Kessler, J.D., Reeburgh, W.S., Roberts, J.A., Gonzalez, L., Douglas, G., Mucci, A., Sundby, B. and Fowle, D.A. 2011. The methane cycle in ferruginous Lake Matano. *Geobiology.* **9**, pp.61-78.

Crowe, S. A., Paris, G., Katsev, S., Jones, C., Kim, S., Zerkle, A. L., Nomosatryo, S., Fowle, D. A., Adkins, J. F., Sessions, A. L., Farquhar, J. and Canfield, D. E. 2014. Sulfate was a trace constituent of Archean seawater. *Science*. **346**(6210)

Cui, H., Jouki, K., Spicuzz, M. J., Fournelle, J. H., Ishida, A., Brown, P. E. and Valley, J. W. 2018. Searching for the Great Oxidation Event in North America: A Reappraisal of

the Huronian Supergroup by SIMS Sulfur Four-Isotope Analysis. *Astrobiology*, **18**(5)

Cumming, V.M., Poulton, S.W., Rooney, A.D. and Selby, D. 2013. Anoxia in the terrestrial environment during the late Mesoproterozoic. *Geology.* **41**(5), pp.583-586.

Dahl, T.W., Hammarlund, E.U., Anbar, A.D., Bond, D.P., Gill, B.C., Gordon, G.W., Knoll, A.H., Nielsen, A.T., Schovsbo, N.H. and Canfield, D.E. 2010. Devonian rise in atmospheric oxygen correlated to the radiations of terrestrial plants and large predatory fish. *Proc Natl Acad Sci U S A.* **107**(42), pp.17911-17915.

Daines, S.J., Mills, B.J.W. and Lenton, T.M. 2017. Atmospheric oxygen regulation at low Proterozoic levels by incomplete oxidative weathering of sedimentary organic carbon. *Nature Communications.* **8**.

Danielson, A., Moller, P. and Dulski, P. 1992. The europium anomalies in banded iron formations and the thermal history of the oceanic crust. *Chemical Geology.* **97**(1-2), pp.89-100.

Daye, M., Klepax-Ceraj, V., Pajusalu, M., Rowland, S., Farrell-Sherman, A., Beukes, N.J., Tamura, N., Fournier, G. and Bosak, T. 2019. Light-driven anaerobic microbial oxidation of manganese. *Nature.* **576**, pp.311-314.

De Baar, H.J.W., Bacon, M.P., Brewer, P.G. and Bruland, K.W. 1985. Rare earth elements in the Pacific and Atlantic Oceans. *Geochimica et Cosmochimica Acta.* **49**, pp.1943-1959.

Des Marais, D.J., Strauss, H., Summons, R.E. and Hayes, J.M. 1992. Carbon isotope evidence for the stepwise oxidation of the Proterozoic environment. *Nature.* **359**.

Deutsch, C. and Weber, T. 2012. Nutrient Ratios as a Tracer and Driver of Ocean Biogeochemistry. *Annual Review of Marine Science.* **4**, pp.113-141.

Devries, T. and Deutsch, C. 2014. Large-scale variations in the stoichiometry ofmarine organic matter respiration. *Nature Geoscience.* **7**, pp.890-894.

Diamond, C. W., Planavsky, N. J., Wang, C. and Lyons, T. W. 2018. What the ~1.4 Ga Xiamaling Formation can and cannot tell us about the mid-Proterozoic ocean. *Geobiology*, **16**, pp.219-236

Dijkstra, N., Kraal, P., Kuypers, M.M., Schnetger, B. and Slomp, C.P. 2014. Are iron-phosphate minerals a sink for phosphorus in anoxic Black Sea sediments? *PLoS One.* **9**(7), pe101139.

Dodd, M.S., Papineau, D., Grenne, T., Slack, J.F., Rittner, M., Pirajno, F., O'Neil, J. and Little, C.T.S. 2017. Evidence for early life in Earth's oldest hydrothermal vent precipitates. *Nature.* **543**, pp.60-64.

Doyle, K.A., Poulton, S.W., Newton, R.J., Podkovyrov, V.N. and Bekker, A. 2018. Shallow water anoxia in the Mesoproterozoic ocean: Evidence from the Bashkir Meganticlinorium, Southern Urals. *Precambrian Research.* **317**, pp.196-210.

Egger, M., Jilbert, T., Behrends, T., Rivard, C. and Slomp, C.P. 2015. Vivianite is a major sink for phosphorus in methanogenic coastal surface sediments. *Geochimica et Cosmochimica Acta.* **169**, pp.217-235.

Eguchi, J., Seales, J. and Dasgupta, R. 2019. Great Oxidation and Lomagundi Events Linked by Deep Cycling and Enhanced Degassing of Carbon. *Nature Geoscience.*

Eickmann, B., Hofmann, A., Wille, M., Bui, T.H., Wing, B.A. and Schoenberg, R. 2018. Isotopic evidence for oxygenated Mesoarchaean shallow oceans. *Nature Geoscience.* **11**(2), pp.133-138.

El Albani et al. 2010. Large colonial organisms with coordinated growth in oxygenated environments 2.1 Gyr ago. *Nature* **466**, pp. 100-104

El Albani et al. 2019. Organism motility in an oxygenated shallow-marine environment 2.1 billion years ago. *PNAS*, pp.3431-3436

Eriksson, P.G. and Cheney, E.S. 1992. Evidence for the transition to an oxygen-rich atmosphere during the evolution of red beds in the lower proterozoic sequences of southern Africa. *Precambrian Research.* **54**(2-4), pp.257-269.

Eriksson, P.G., Hattingh, P.J. and Altermann, W. 1995. An overview of the geology of the Transvaal Sequence and Bushveld Complex, South Africa. *Mineralium Deposita.* **30**, pp.98-111.

Evans, N.P., Beukes, N.J. and Kirschvink, J.L. 1997. Low-latitude glaciation in the Palaeoproterozoic era. *Nature.* **386**.

Fakharee, M., Crowe, S.A. and Katsev, S. 2018. Sedimentary sulfur isotopes and Neoarchean ocean oxygenation. *Science Advances.* **4**.

Fakharee, M., Hancisse, O., Canfield, D.E., Crowe, S.A. and Katsev, S. 2019. Proterozoic seawater sulfate scarcity and the evolution of ocean–atmosphere chemistry. *Natrue Geoscience.* **12**.

Farquhar, J. 2000. Atmospheric Influence of Earth's Earliest Sulfur Cycle. *Science.* **289**(5480), pp.756-758.

Farquhar, J., Bao, H. and Thiemens, M. 2000. Atmospheric Influence of Earth's Earliest Sulfur Cycle. *Science.* **289**(5480), pp.756-758.

Farquhar, J., Cliff, J., Zerkle, A.L., Kamyshny, A., Poulton, S.W., Claire, M.W., Adams, D. and Harms, B. 2013. Pathways for Neoarchean pyrite formation constrained by mass-independent sulfur isotopes. *PNAS.* **110**(44), pp.17638-17643.

Farquhar, J. and Wing, B.A. 2003. Multiple sulfur isotopes and the evolution of the atmosphere. *Earth and Planetary Science Letters.* **213**, pp.1-13.

Feulner, G. 2012. The faint young sun problem. *Reviews of Geophysics.*

Filippelli, G. M. and Delaney, M. L. Phosphorus geochemistry of Equatorial Pacific sediments. *Geochimica et Cosmochimica Acta*. **60**(9), pp.1479-1495

Fischer, W.W. 2008. Biogeochemistry: Life before the rise of oxygen. Nature. **455**, p7216.

Frei, R., Gaucher, C., Poulton, S.W. and Canfield, D.E. 2009. Fluctuations in Precambrian atmospheric oxygenation recorded by chromium isotopes. *Nature.* **461**(7261), pp.250-253.

Froelich, P.N., Bender, M.L. and Luedtke, N.A. 1982. The Marine Phosphorus Cycle. *American Journal of Science.* **282**, pp.474-511.

Fung, I.Y., Meyn, S.K., Tegen, I., Doney, S.C., John, J.G. and Bishop, J.K.B. 2000. Iron supply and demand in the upper ocean. *Global Biogeochemical Cycles.* **14**, pp.281-296.

Gächter, R., Meyer, J.S. and Mares, A. 1988. Contribution of bacteria to release and fixation of phosphorus in lake sediments. *Limnol. Oceanogr.* **33**(6/2).

Gao, Y. and Mucci, A. 2003. Individual and competitive adsorption of phosphate and arsenate on goethite in artificial seawater. *Chemical Geology.* **199**(1), pp.91-109.

Garcia-Picel, F., Lombard, J., Soule, T., Dunaj, S., Wu, S.H. and Wojciechowski, M.F. 2019. Timing the Evolutionary Advent of Cyanobacteria and the Later Great Oxidation Event Using Gene Phylogenies of a Sunscreen. *American Society for Microbiology.*

Garvin, J., Buick, R., Anbar, A. D., Arnold, G. L. and Kaufman, A. J. 2009. Isotopic evidence for an aerobic nitrogen cycle in the latest Archean. *Science*. **323**, pp. 1045-1048

Geider, R. and La Roche, J. 2002. Redfield revisited: variability of C:N:P in marine microalgae and its biochemical basis. *European Journal of Phycology.* **37**(1).

German, C.R. and Elderfield, H. 1990. Application of the Ce anomaly as a paleoredox indicator: The ground rules. *Paleoceanography.*

Gilbert, F., Hulth, S., Grossi, V. and Aller, R. C. 2016. Redox oscillation and benthic nitrogen mineralization within burrowed sediments: An experimental simulation at low frequency. *Journal of Experimental Marine Biology and Ecology*. **482**, pp. 75-84

Gilleaudeau, G.J., Romaniello, S.J., Luo, G., Kaufman, A.J., Zhang, F., Klaebe, R.M., Kah, L.C., Azmy, K., Bartley, J.K., Zheng, W., Knoll, A.H. and Anbar, A.D. 2019. Uranium isotope evidence for limited euxinia in mid-Proterozoic oceans. *Earth and Planetary Science Letters.* **521**, pp.150-157.

Gilleaudeau, G. J., Sahoo, S. K., Ostrander, C. M., Owens, J. D., Poulton, S. W., Lyons, T. W. and Anbar, A. D. 2020. Molybdenum isotope and trace metal signals in an iron-

rich Mesoproterozoic ocean: A snapshot from the Vindhyan Basin, India. *Precambrian Research*, **343**.

Glasspool, I.J. and Scott, A.C. 2010. Phanerozoic atmospheric oxygenconcentrations reconstructed from sedimentary charcoal. *Natrue Geoscience.* **3**, pp.627-630.

Godfrey, L. V. and Glass, J. B. 2011. The geochemical record of the ancient nitrogen cycle, nitrogen isotopes, and metal cofactors. *Methods Enzymol.* **486**, pp. 483-506

Godfrey, L. V. and Falkowski, P. G. 2009. The cycling and redox state of nitrogen in the Archean ocean. *Nature Geoscience*. **2**. pp. 725-729

Goldblatt, C., Lenton, T.M. and Watson, A.J. 2006. Bistability of atmospheric oxygen and the Great Oxidation. *Nature.* **443**(7112), pp.683-686.

Goldhammer, T., Bruchert, V., Ferdelman, T.G. and Zabel, M. 2010. Microbial sequestration of phosphorus in anoxic upwelling sediments. *Nature Geoscience.* **3**, pp.557-561.

Gough, D.O. 1981. Solar interior structure and luminosity variations. *Sol. Phys.* **74**(1), pp.21-34.

Granger, J., Sigman, D. M., Lehmann, M. F. and Tortell, P. D. 2008. Nitrogen and oxygen isotope fractionation during dissimilatory nitrate reduction by denitrifying bacteria. *Limnol. Oceanogr.* **53**(6), pp. 2533-2545.

Greber, N.D., Dauphas, N., Bekker, A., Ptáček, M.P., Bindeman, I.N. and Hofmann, A. 2017. Titanium isotopic evidence for felsic crust and plate tectonics 3.5 billion years ago. *Science.* **357**(6357), pp.1271-1274.

Gruber, N. and Deutsch, C. A. Redfield's evolving legacy. 2014 *Nature Geoscience*. **7**, pp.853-855

Guilbaud, R., Poulton, S.W., Thompson, J., Husband, K.F., Zhu, M., Zhou, Y., Shields, G.A. and Lenton, T.M. 2020. Phosphorus-limited conditions in the early Neoproterozoic ocean maintained low levels of atmospheric oxygen. *Nature Geoscience.*

Gumsley, A.P., Chamberlain, K.R., Bleeker, W., Söderlund, U., de Kock, M.O., Larsson, E.R. and Bekker, A. 2017. Timing and tempo of the Great Oxidation Event. *PNAS.* **114**, pp.1811-1816.

Guo, Q., Strauss, H., Kaufman, A.J., Schroder, S., Gutzmer, J., Wing, B., Baker, M.A., Bekker, A., Jin, Q., Kim, S.-T., and Farquhar, J. (2009) Reconstructing Earth's surface oxidation across the Archean–Proterozoic transition. *Geology* **37**, pp. 399–402.

Gutzmer, J. and Beukes, N.J. 1998. High-grade manganese res in the Kalahari Manganese Field: Characterisation and dating of ore-forming events. *Final Technical Report.*

Habicht, K.S., Gade, M., Thamdrup, B., Berg, P. and Canfield, D.E. 2002. Calibration of sulfate levels in the archean ocean. *Science.* **298**(5602).

Halevy, I. 2013. Production, preservation, and biological processing of mass-independent sulfur isotope fractionation in the Archean surface environment. *PNAS.* **110**(44), pp.17644-17649.

Hamilton, T. L., Bryant, D. A. and Macalady, J. L. 2016. The Role of Biology in Planetary Evolution: Cyanobacterial Primary Production in Low-Oxygen Proterozoic Oceans. *Environ. Microbiol.*

Handoh, I.C. and Lenton, T.M. 2003. Periodic mid-Cretaceous oceanic anoxic events linked by oscillations of the phosphorus and oxygen biogeochemical cycles. *Global Biogeochemical Cycles.* **17**, p1092.

Hao, J., Knoll, A.H., Huang, F., Hazen, R.M. and Daniel, I. 2020. Cycling phosphorus on the Archean Earth: Part I. Continental weathering and riverine transport of phosphorus. *Geochimica et Cosmochimica Acta.* **273**, pp.70-84.

Harada, M., Tajika, E. and Sekine, Y. 2015. Transition to an oxygen-rich atmosphere with an extensive overshoot triggered by the Paleoproterozoic snowball Earth. *Earth and Planetary Science Letters.* **419**, pp.178-186.

Hardisty, D.S., Lu, Z., Bekker, A., Diamond, C.W., Gill, B.C., Jiang, G., Kah, L.C., Knoll, A.H., Loyd, S.J., Osburn, M.R., Planavsky, N.J., Wang, C., Zhou, X. and Lyons, T.W. 2017. Perspectives on Proterozoic surface ocean redox from iodine contents in ancient and recent carbonate. *Earth and Planetary Science Letters.* **463**, pp.159-170.

Hardisty, D.S., Lyons, T.W., Riedinger, N., Isson, T.T., Owens, J.D., Aller, R.C., Rye, D.M., Planavsky, N.J., Reinhard, C.T., Gill, B.C., Masterson, A.L., Asael, D. and Johnston, D.T. 2018. An evaluation of sedimentary molybdenum and iron as proxies for pore fluid paleoredox conditions. *American Journal of Science.* **318**, pp.527-556.

Harrison, W.G. 1986. Respiration and its size-dependence in microplankton populations from surface waters of the Canadian Arctic. *Polar Biology.* **6**, pp.145-152.

Havig, J.R., Hamilton, T.L., Bachan, A. and Kump, L.R. 2017. Sulfur and carbon isotopic evidence for metabolic pathway evolution and a four-stepped Earth system progression across the Archean and Paleoproterozoic. *Earth-Science Reviews.* **174**, pp.1-21.

Hayes, J.M. and Waldbauer, J.R. 2006. The carbon cycle and assocaited redox process through time. *Philos Trans R Soc.* **361**, pp.931-950.

He, T., Zhu, M., Mills, B.J.W., Wynn, P.M., Zhuravlev, A.Y., Tostevin, R., Pogge von Strandmann, P.A.E., Yang, A., Poulton, S.W. and Shields, G.A. 2019. Possible links between extreme oxygen perturbations and the Cambrian radiation of animals. *Nat Geosci.* **12**(6), pp.468-474.

Ho, S. 2008. The molecular clock and estimating species divergence. *Nature Education.* **1**(1).

Hodgskiss, M.S.W., Crockford, P.W., Peng, Y., Wing, B.A. and Horner, T.J. 2019. A productivity collapse to end Earth's Great Oxidation. *PNAS.* **116**(35), pp.17207-17212.

Hoffman, P.F., Kaufman, A., Halverson, G.P. and Schrag, D.P. 1998. A Neoproterozoic Snowball Earth. *Science.* **281**, pp.1342-1346.

Hoffman, P. F. 2013. The Great Oxidation and a Siderian snowball Earth: MIF-S based correlation of Paleoproterozoic glacial epochs. *Chemical Geology.* **362**(20), pp. 143-156

Holland, H.D. 1984. The chemical evolution of the atmosphere and oceans. Princeton, NJ: Princeton University Press.

Holland, H.D. 2002. Volcanic gases, black smokers, and the Great Oxidation Event. *Geochimica et Cosmochimica Acta.* **66**(21), pp.3811-3826.

Homoky, W.B., Severmann, Mills, R.A., Statham, P.J. and Fones, G.R. 2009. Pore-fluid Fe isotopes reflect the extent of benthic Fe redox recycling: Evidence from continental shelf and deep-sea sediments. *Geology.* **37**(8), pp.751-754.

Horton, F. 2015. Did phosphorus derived from the weathering of large igneous provinces fertilize the Neoproterozoic ocean? *Geochemistry, Geophysics, Geosystems.* **16**(6), pp.1723-1738.

Ingall, E. and Jahnke, R. 1994. Evidence for enhanced phosphorus regeneration from marine sediments overlain by oxygen depleted waters. *Geochimica et Cosmochimica Acta.* **58**(11).

Ingall, E.D., Bustin, R.M. and Van Cappellen, P. 1993. Influence of water column anoxia on the bruial and preservation of carbon and phosphorus in marine shales. *Geochimica et Cosmochimica Acta.* **57**, pp.303-316.

Izon, G., Zerkle, A.L., Zhelezinskaia, I., Farquhar, J., Newton, R.J., Poulton, S.W., Eigenbrode, J.L. and Claire, M.W. 2015. Multiple oscillations in Neoarchaean atmospheric chemistry. *Earth and Planetary Science Letters.* **431**, pp.264-273.

Jacobson, J.W. 1988. Isotopic constraints on crustal growth and recycling. *Earth and Planetary Science Letters.* **90**(3), pp.315-329.

James, D.E. and Fouch, M.J. 2002. Formation and evolution of Archaean cratons: Insights from southern Africa. *Geological Society of London Special Publications.* **199**(1), pp.1-26.

Javaux, E. J. and Lepot, K. 2017. The Paleoproterozoic fossil record: Implications for the evolution of the biosphere during Earth's middle-age. *Earth-Science Reviews.*

Jiang, C.Z. and Tosca, N.J. 2019. Fe (II)-carbonate precipitation kinetics and the chemistry of anoxic ferruginous seawater. *Earth and Planetary Science Letters.*

Jilbert, T. and Slomp, C.P. 2013. Iron and manganese shuttles control the formation of authigenic phosphorus minerals in the euxinic basins of the Baltic Sea. *Geochimica et Cosmochimica Acta.* **107**, pp.155-169.

Johnson, J.E., Gerpheide, A., Lamb, M.P. and Fischer, W.W. 2014. O2constraints from Paleoproterozoic detrital pyrite and uraninite. *Geological Society of America Bulletin.* **126**(5-6), pp.813-830.

Johnson, J.E., Muhling, J.R., Cosmidis, J., Rasmussen, B. and Templeton, A.S. 2018. Low-Fe(III) Greenalite Was a Primary Mineral From Neoarchean Oceans. *Geophysical Research Letters.* **45**(7).

Johnson, J.E., Webb, S.M., Thomas, K., Ono, S., Kirschvink, J.L. and Fischer, W.W. 2013. Manganese-oxidizing photosynthesis before the rise of cyanobacteria. *PNAS.* **110**(28).

Johnson, B. W., Poulton, S. W. and Goldblatt, C. 2017. Marine oxygen production and open water supported an active nitrogen cycle during the Marinoan Snowball Earth. *Nature Communications*. **6**(1316)

Johnston, D. T., Wolfe-Simon, F., Pearson, A. and Knoll, A. H. 2009. Anoxygenic photosynthesis modulated Proterozoic oxygen and sustained Earth's middle age. *PNAS*. **106**(40)

Johnston, D.T. 2011. Multiple sulfur isotopes and the evolution of Earth's surface sulfur cycle. *Earth Science Reviews.* **106**(1), pp.161-183.

Jones, C., Nomosatryo, S., Crowe, S.A., Bjerrum, C.J. and Canfield, D.E. 2015. Iron oxides, divalent cations, silica, and the early earth phosphorus crisis. *Geology.* **43**(2), pp.135-138.

Kanakidou, M., Duce, R.A., Prospero, J.M., Baker, A.R., Benitez-Nelson, C., Dentener, F.J., Hunter, K.A., Liss, P.S., Mahowald, N., Okin, G.S., Sarin, M., Tsigaridis, K., Uematsu, M., Zamora, L.M. and Zhu, T. 2012. Atmospheric fluxes of organic N and P to the global ocean. *Global Biogeochemical Cycles.* **26**(3).

Karhu, J. and Holland, H.D. 1996. Carbon isotopes and the rise of atmopsheric oxygen. *Geology.* **24**, pp.867-870.

Kartal, B., Kuypers, M. M. M., Lavik, G., Schalk, J. 2007. Anammox bacteria disguised as denitrifiers: nitrate reduction to dinitrogen gas via nitrite and ammonium. *Environmental Microbiology* **9**(3).

Kasting, J.F. 1987. Theoretical constraints on oxygen and carbondioxide concentrations in the Precambrian atmosphere. *Precambrian Research.* **34**, pp.205-229.

Kasting, J.F. 2006. "Ups and downs of ancient oxygen". *Nature.* **443**(643).

Kasting, J.F., Liu, S.C. and Donahue, T.M. 1979. Oxygen levels in the prebiological atmosphere. *Journal of Geophysical Research: Oceans.* **84**(C6).

Kemp, D.B., Coe, A.L., Cohen, A.S. and Schwark, L. 2005. Astronomical pacing of methane release in the Early Jurassic period. *Nature.* **437**, pp.396-399.

Kendall, B., Brenneck, G.A., Weyer, S. and Anbar, A.D. 2013. Uranium isotope fractionation suggests oxidative uranium mobilization at 2.50 Ga. *Chemical Geology.* **362**, pp.105-114.

Kendall, B., Creaser, R.A., Reinhard, C.T., Lyons, T.W. and Anbar, A.D. 2015. Transient episodes of mild environmental oxygenation and oxidative continental weathering during the later Archean. *Science Advances.* **1**(10).

Kendall, B., Reinhard, C.T., Lyons, T.W., Kaufman, A.J., Poulton, S.W. and Anbar, A.D. 2010. Pervasive oxygenation along late Archaean ocean margins. *Nature Geoscience.* **3**(9), pp.647-652.

Kharecha, P., Kasting, J.F. and Siefert, J. 2005. A coupled atmosphere-ecosystem model of the early Archean Earth. *Geobiology.* **3**, pp.53-76.

Kipp, M. A., Stueken, E. E., Bekker, A. and Buick, R. 2017. Selenium isotopes record extensive marine suboxia during the Great Oxidation Event. *Proc. Natl. Acad. Sci. USA*, **114**, pp.875-880

Klein, C. and Beukes, N.J. 1989. Geochemistry and sedimentology of a facies transition from limestone to iron-formation deposition in the early Proterozoic Transvaal Supergroup, South Africa. *Economic Geology.*

Knoll, A.H., Bergmann, K.D. and Strauss, J.V. 2016. Life: the first two billion years. *Philosophical Transactions of the Royal Society B: Biological Sciences.* **371**(1707).

Konhauser, K.O., Hamade, T., Raiswell, R., Morris, R.C., Farris, G.F., Southam, G. and Canfield, D.E. 2002. Could bacteria have formed the Precambrian banded iron formations? *Geology.* **30**(12), p1079.

Konhauser, K.O., Lalonde, S.V., Amskold, L. and Holland, H.D. 2007. Was there really an Archean phosphate crisis? *Science.* **315**(5816), p1234.

Kopp, R.E., Kirschvink, J.L., Hilburn, I.A. and Nash, C.Z. 2005. The Paleoproterozoic snowball Earth: a climate disaster triggered by the evolution of oxygenic photosynthesis. *Proc Natl Acad Sci U S A.* **102**(32), pp.11131-11136.

Koroleff, G. 1976. Methods of seawater analysis. p317.

Kraal, P., Slomp, C.P., Forster, A. and Kuypers, M.M.M. 2010. Phosphorus cycling from the margin to abyssal depths in the proto-Atlantic during oceanic anoxic event 2. *Palaeogeography, Palaeoclimatology, Palaeoecology.* **295**(1-2), pp.42-54.

Krause, A.J., Mills, B.J.W., Zhang, S., Planavsky, N.J., Lenton, T.M. and Poulton, S.W. 2018. Stepwise oxygenation of the Paleozoic atmosphere. *Nature Communications.* **9**(1), p4081.

Krissansen-Totton, J., Arney, G.N. and Catling, D.C. 2018. Constraining the climate and ocean pH of the early Earth with a geological carbon cycle model. *PNAS.* **115**, pp.4105-4110.

Krom, M.D. and Berner, R.A. 1980. Adsorption of phosphate in anoxic marine sediments. *Limnology and Oceanography.* **25**(5).

Krom, M.D. and Berner, R.A. 1981. The diagenesis of phosphorus in a nearshore marine sediment. *Geochimica et Cosmochimica Acta.* **45**, pp.207-216.

Kump, L.R. and Barley, M.E. 2007. Increased subaerial volcanism and the rise of atmospheric oxygen 2.5[thinsp]billion years ago. *Nature.* **448**(7157), pp.1033-1036.

Kurzweil, F., Wille, M., Gantert, N., Beukes, N.J. and Schoenberg, R. 2016. Manganese oxide shuttling in pre-GOE oceans – evidence from molybdenum and iron isotopes. *Earth and Planetary Science Letters.* **452**, pp.69-78.

Kuznetsov, I., Neumann, T. and Burchard, H. 2008. Model study on the ecosystem impact of a variable C:N:P ratio for cyanobacteria in the Baltic Proper. *Ecological Modelling.* **219**(1-2), pp.107-114.

Laakso, T.A. and Schrag, D.P. 2014. Regulation of atmospheric oxygen during the Proterozoic. *Earth and Planetary Science Letters.* **388**, pp.81-91.

Laakso, T.A. and Schrag, D.P. 2017. A theory of atmospheric oxygen. *Geobiology.* **15**, pp.366-384.

Lalonde, K., Mucci, A., Ouellet, A. and Gelinas, Y. 2012. Preservation of organic matter in sediments promoted by iron. *Nature*, **483**(7388), pp. 198-200.

Lambrecht, N., Katsev, S., Wittkop, C., Hall, S.J., Sheik, C.S., Picard, A., Fakharee, M. and Swanner, E.D. 2020. Biogeochemical and physical controls on methane fluxes from two ferruginous meromictic lakes. *Geobiology.* **18**(1).

Lantink, M.L., Davies, J.H.F.L., Mason, P.R.D., Schaltegger, U. and Hilfen, F.J. 2019. Climate control on banded iron formations linked to orbital eccentricity. *Nature Geoscience.* **12**(5), pp.369-374.

Lawrence, M.G., Greig, A., Collerson, K.D. and Kamber, B.S. 2006. Rare earth element and yttrium variability in South East Queensland waterways. *Aquatic Geochemistry.* **12**, pp.39-72.

Lee, C.-T.A., Yeung, L.Y., McKenzie, N.R., Yokoyama, Y., Ozaki, K. and Lenardic, A. 2016. Two-step rise of atmospheric oxygen linked to the growth of continents. *Nature Geoscience.* **9**(6), pp.417-424.

Lenton, T.M., Boyle, R.A., Poulton, S.W., Shields-Zhou, G.A. and Butterfield, N.J. 2014. Co-evolution of eukaryotes and ocean oxygenation in the Neoproterozoic era. *Nature Geoscience.* **7**, pp.257-265.

Lenton, T.M., Dahl, T.W., Daines, S.J., Mills, B.J.W., Ozaki, K., Saltzman, M.R. and Porada. 2016. Earliest land plants created modern levels of atmospheric oxygen. *PNAS.* **113**(35), pp.9704-9709.

Lenton, T.M. and Daines, S.J. 2018. The effects of marine eukaryote evolution on phosphorus, carbon and oxygen cycling across the Proterozoic–Phanerozoic transition. *Emerging Topics in Life Sciences.* **2**(2), pp.267-278.

Lenton, T.M., Daines, S.J. and Mills, B.J.W. 2018. COPSE reloaded: An improved model of biogeochemical cycling over Phanerozoic time. *Earth-Science Reviews.* **178**, pp.1-28.

Li, Z., Zhang, L., Xue, C., Zheng, M., Zhu, M., Robbins, L.J., Slack, J.F., Planavsky, N.J. and Konhauser, K.O. 2018. Earth's youngest banded iron formation implies ferruginous conditions in the Early Cambrian ocean. *Scientific Reports.* **8**(9970).

Li, S., Junkin, W. D., Gaschnig, R. M., Ash, R. D., Piccoli, P. M., Candela, P. A. and Rudnick, R. L. 2019. Molybdenum contents of sulfides in ancient glacial diamictites: Implications for molybdenum delivery to the oceans prior to the Great Oxidation Event. *Geochimica et Cosmochimica Acta*. **278**, pp.30-50

Linol, B., Chere, N., Muedi, T., Nengovhela, V. and de Wit, M.J. 2016. Deep Borehole Lithostratigraphy and Basin Structure of the Southern Karoo Basin Re-Visited. pp.3-16.

Liu, P., Harman, C.E., Kasting, J.F., Hu, Y. and Wang, J. 2019. Can organic haze and O2 plumes explain patterns of sulfur mass-independent fractionation during the Archean? *Earth and Planetary Science Letters.* **526**.

Lomnitz, U., Sommer, S., Dale, A.W., Loscher, C.R., Noffke, A., Wallmann, K. and Hensen, C. 2015. Benthic phosphorus cycling in the Peruvian oxygen minimum zone. *Biogeosciences.* **13**(5), pp.1367-1386.

Luo, G., Ono, S., Beukes, N.J., Wang, D.T., Xie, S. and Summons, R.E. 2016. Rapid oxygenation of Earth's atmosphere 2.33 billion years ago. *Science Advances.* **2**(5).

Luo, G., Ono, S., Hunag, J., Li, C., Robinson, A., Xie, S., Algeo, T. J. 2015. Decline in oceanic sulfate levels during the Mesoproterozoic. *Precambrian Research*.

Lyons, T.W., Reinhard, C.T. and Planavsky, N.J. 2014a. The rise of oxygen in Earth's early ocean and atmosphere. *Nature.* **506**(7488), pp.307-315.

Lyons, T.W., Reinhard, C.T. and Planavsky, N.J. 2014b. The rise of oxygen in Earth/'s early ocean and atmosphere. *Nature.* **506**(7488), pp.307-315.

Lyons, T.W. and Severmann, S. 2006. A critical look at iron paleoredox proxies: New insights from modern euxinic marine basins. *Geochimica et Cosmochimica Acta.* **70**(23), pp.5698-5722.

Maruyama, S., Santosh, M. and Azuma, S. 2018. Initiation of plate tectonics in the Hadean: Eclogitization triggered by the ABEL Bombardment. *Geoscience Frontiers.* **9**(4).

März, C., Poulton, S.W., Beckmann, B., Küster, K., Wagner, T. and Kasten, S. 2008. Redox sensitivity of P cycling during marine black shale formation: Dynamics of sulfidic and anoxic, non-sulfidic bottom waters. *Geochimica et Cosmochimica Acta.* **72**(15), pp.3703-3717.

März, C., Poulton, S.W., Wagner, T., Schnetger, B. and Brumsack, H.J. 2014. Phosphorus burial and diagenesis in the central Bering Sea (Bowers Ridge, IODP Site U1341): Perspectives on the marine P cycle. *Chemical Geology.* **363**, pp.270-282.

März, C., Riedinger, N., Sena, C. and Kasten, S. 2018. Phosphorus dynamics around the sulphate-methane transition in continentalmargin sediments: Authigenic apatite and Fe(II) phosphates. *Marine Geology.* **404**, pp.84-96.

McKay, M.P., Weislogel, A.L., Fildani, A., Brunt, R.L., Hodgson, D.M. and Flint, S.S. 2015. U-PB zircon tuff geochronology from the Karoo Basin, South Africa: implications of zircon recycling on stratigraphic age controls. *Internation Geology Review.* **57**(4), pp.393-410.

Melezhik, V.A., Fallick, A.E., Hanski, E.J., Kump, L.R., Lepland, A., Prave, A.R. and Strauss, H. 2005. Emergence of the aerobic biosphere during the Archean-Proterozoic transition: Challenges of future research. *Geosciences.*

Mettam, C., Zerkle, A. L., Claire, M. W., Prave, A. R., Poulton, S. W. and Junium, C. K. 2019. Anaerobic nitrogen cycling on a Neoarchean ocean margin. *Earth and Planetary Science Letters.* **527**, 115800

Meyer, K.M., Ridgwell, A. and Payne, J.L. 2016. The influence of the biological pump on ocean chemistry: implications for long-term trends in marine redox chemistry, the global carbon cycle, and marine animal ecosystems. *Geobiology.* **14**, pp.207-219.

Michiels, C. C., Darchambeau, F., Rolan, F., Morana, C., Lliros, M., Garcia-Armisen, T., Thamdrup, B., Borges, A., Canfield, D. E., Servais, P., Descy, J. and Crowe, S. A. 2017. Iron-dependent nitrogen cycling in a ferruginous lake and the nutrient status of Proterozoic oceans. *Nat. Geo.*

Mills, B., Lenton, T.M. and Watson, A.J. 2014a. Proterozoic oxygen rise linked to shifting balance between seafloor and terrestrial weathering. *Proc Natl Acad Sci U S A.* **111**(25), pp.9073-9078.

Mills, D., B., Ward, L.M., Jones, C., Sweeten, B., Forth, M., Treusch, A.H. and Canfield, D.E. 2014b. Oxygen requirements of the earliest animals. *PNAS.*

Moore, J.M., Tsikos, H. and Polteau, S. 2001. Deconstructing the Transvaal Supergroup, South Africa: implications for Palaeoproterozoic palaeoclimate models. *Journal of African Earth Sciences.* **33**.

Moreno, A.R. and Martiny, A.C. 2018. Ecological Stoichiometry of Ocean Plankton. *Annual Review of Marine Science.* **10**, pp.43-69.

Mort, H.P., Adatte, T., Föllmi, K.B., Keller, G., Steinmann, P., Matera, V., Berner, Z. and Stüben, D. 2007. Phosphorus and the roles of productivity and nutrient recycling during oceanic anoxic event 2. *Geology.* **35**(6), p483.

Mulholland, M. R., and M. W. Lomas. 2008. Nitrogen uptake and assimilation, pp. 303–384. In D. G. Capone, D. A. Bronk, M. R. Mulholland, and E. J. Carpenter [eds.], Nitrogen in the marine environment. Academic Press.

Naafs, B. D. A., Monteiro, F. M., Pearson, A., Higgins, M. B., Pancost, R. D. and Ridgwell, A. 2019. Fundamentally different global marine nitrogen cycling in response to severe ocean deoxygenation. *PNAS.* **116**(50)

Nisbet, E.G. and Fowler, C.M.R. 1999. Archaean metabolic evolution of microbial mats. *Proceedings of the Royal Society B.*

Nutman, A.P., Bennett, V.C., Friend, C.R.L., Van Kranendonk, M.J. and Chivas, A.R. 2016. Rapid emergence of life shown by discovery of 3,700-million-year-old microbial structures. *Nature.* **537**, pp.535-538.

Och, L. and Shields-Zhou, G. 2012. The Neoproterozoic oxygenation event: Environmental pertubations and biogeochemical cycling. *Earth-Science Reviews.* **110**, pp.26-57.

Olson, S.L., Kump, L.R. and Kasting, J.F. 2013. Quantifying the areal extent and dissolved oxygen concentrations of Archean oxygen oases. *Chemical Geology.* **362**, pp.35-43.

Olson, S. L., Reinhard, C. T. and Lyons, T. W. 2016. Limited role for methane in the mid-Proterozoic greenhouse. *PNAS.*

Olson, S.L., Ostrander, C.M., Gregory, D.D., Roy, M., Anbar, A.D. and Lyons, T.W. 2019. Volcanically modulated pyrite burial and ocean–atmosphere oxidation. *Earth and Planetary Science Letters.* **506**, pp.417-427.

Ono, S. 2017. Photochemistry of Sulfur Dioxide and the Origin of Mass-Independent Isotope Fractionation in Earth's Atmosphere. *Annual Review of Earth and Planetary Sciences.* **45**, pp.301-329.

Ossa Ossa, F., Hofmann, A., Spangenberg, J.E., Poulton, S.W., Stüeken, E.E., Schoenberg, R., Eickmann, B., Wille, M., Butler, M. and Bekker, A. 2019. Limited oxygen production in the Mesoarchean ocean. *PNAS.* **116**(14), pp.6647-6652.

Ossa Ossa, F., Eickmann, B., Hofmann, A., Planavsky, N. J., Asael, D., Pambo, F. and Bekker, A. 2018. Two-step deoxygenation at the end of the Paleoproterozoic Lomagundi Event. *Earth Planet. Sci. Lett.* **486**, pp. 70-83

Ostrander, C.M., Nielsen, S.G., Owens, J.D., Kendall, B., Gordon, G.W., Romaniello, S.J. and Anbar, A.D. 2019. Fully oxygenated water columns over continental shelves before the Great Oxidation Event. *Nature Geosci.* **12**, pp.186-191.

Ouyang, G., She, Z., Papineau, D., Wang, X., Luo, G. and Li, C. 2020. Dynamic carbon and sulfur cycling in the aftermath of the Lomagundi-Jatuli Event: Evidence from the Paleoproterozoic Hutuo Supergroup, North China Craton. *Precambrian Research*. **337**

Ozaki, K., Reinhard, C.T. and Tajika, E. 2019. A sluggish mid-Proterozoic biosphere and its effect on Earth's redox balance. *Geobiology.* **17**(1), pp.3-11.

Ozaki, K. and Tajika, E. 2013. Biogeochemical effects of atmospheric oxygen concentration, phosphorus weathering, and sea-level stand on oceanic redox chemistry: Implications for greenhouse climates. *Earth and Planetary Science Letters.* **373**, pp.129-139.

Ozaki, K., Tajima, S. and Tajika, E. 2011. Conditions required for oceanic anoxia/euxinia: Constraints from a one-dimensional ocean biogeochemical cycle model. *Earth and Planetary Science Letters.* **304**(1-2), pp.270-279.

Pasek, M.A., Gull, M. and Herschy, B. 2017. Phosphorylation on the early earth. *Chemical Geology.* **475**, pp.149-170.

Pavlov, A.A. and Kasting, J.F. 2002. Mass-independent fractionation of sulfur isotopes in Archean sediments: strong evidence for an anoxic Archean atmosphere. *Astrobiology.* **2**(1), pp.27-41.

Pavlov, A.A., Kasting, J.F., Brown, L.L., Rages, K.A. and Freedman, R. 2000. Greenhouse warming by CH4 in the atmosphere of early Earth. *Journal of Geophysical Research: Planets.* **105**(E5).

Pickard, A.L. 2003. SHRIMP U-Pb zircon ages for the Palaeoproterozoic Kuruman Iron Formation, Northern Cape Province, South Africa: evidence for simultaneous BIF deposition on Kaapvaal and Pilbara Cratons. *Precambrian Research.* **125**, pp.275-315.

Planavsky, N.J. 2014. The elements of marine life. *Nature GEoscience.* **7**, pp.855-856.

Planavsky, N.J., Asael, D., Hofmann, A., Reinhard, C.T., Lalonde, S., Knudsen, A., Wang, W., Ossa Ossa, F., Pecoits, E., Smith, A.J.B., Beukes, N.J., Bekker, A., Johnson, T.M., Konhauser, K.O., Lyons, T.W. and Rouxel, O. 2014a. Evidence for oxygenic photosynthesis half a billion years before the Great Oxidation Event. *Nature Geosci.* **7**, pp.283-286.

Planavsky, N.J., Bekker, A., Rouxel, O., Kamber, B.S., Hofmann, A., Knudsen, A. and Lyons, T.W. 2010a. Rare Earth Element and yttrium compositions of Archeanand Paleoproterozoic Fe formations revisited: New perspectiveson the significance and mechanisms of deposition. *Geochimica et Cosmochimica Acta.* **74**, pp.6387-6405.

Planavsky, N.J., McGoldrick, P., Scott, C., Li, C., Reinhard, C.T., Kelly, A.E., Chu, X., Bekker, A., Love, G.D. and Lyons, T.W. 2011. Widespread iron-rich conditions in the mid-Proterozoic ocean. *Nature.* **477**(7365), pp.448-451.

Planavsky, N.J., Reinhard, C.T., Wang, X., Thomson, D., McGoldrick, P., Rainbird, R.H., Johnson, T., Fischer, W.W. and Lyons, T.W. 2014b. Low Mid-Proterozoic atmospheric oxygen levels and the delayed rise of animals. *Science.* **346**, pp.635-638.

Planavsky, N.J., Rouxel, O.J., Bekker, A., Lalonde, S.V., Konhauser, K.O., Reinhard, C.T. and Lyons, T.W. 2010b. The evolution of the marine phosphate reservoir. *Nature.* **467**(7319), pp.1088-1090.

Planavsky, N. J., Bekker, A., Hofmann, A., Owens, J. D. and Lyons, T. W. 2012. Sulfur record of rising and falling marine oxygen and sulfate levels during the Lomagundi event. *Proc. Natl. Acad. Sci,* **109**. pp. 1-6

Poulton, S.W. 2017. Early Phosphorus Redigested. *Nature Geoscience.* **10**, pp.75-76.

Poulton, S.W. and Canfield, D.E. 2005. Development of a sequential extraction procedure for iron: implications for iron partitioning in continentally derived particulates. *Chemical Geology.* **214**(3-4), pp.209-221.

Poulton, S.W. and Canfield, D.E. 2011. Ferruginous Conditions: A Dominant Feature of the Ocean through Earth's History. *Elements.* **7**(2), pp.107-112.

Poulton, S.W., Fralick, P.W. and Canfield, D.E. 2010. Spatial variability in oceanic redox structure 1.8 billion years ago. *Nature Geoscience.* **3**(7), pp.486-490.

Poulton, S.W., Krom, M.D. and Raiswell, R. 2004. A revised scheme for the reactivity of iron (oxyhydr)oxide minerals towards dissolved sulfide. *Geochimica et Cosmochimica Acta.* **68**(18), pp.3703-3715.

Poulton, S.W. and Raiswell, R. 2002. THE LOW-TEMPERATURE GEOCHEMICAL CYCLE OF IRON: FROM CONTINENTAL FLUXES TO MARINE SEDIMENT DEPOSITION. *American Journal of Science.* **302**, pp.774-805.

Poulton, S.W. and Raiswell, R. 2005. Chemical and physical characteristics of iron oxides in riverine and glacial meltwater sediments. *Chemical Geology.* **218**(3), pp.203-221.

Quirk, J., Leake, J.R., Johnson, D.A., Taylor, L.L., Saccone, L. and Beerling, D.J. 2015. Constraining the role of early land plants in Palaeozoic weathering and global cooling. *Proceedings of the Royal Society B.*

Raiswell, R. and Al-Biatty, H.J. 1989. Depositional and diagenetic C-S-Fe signatures in Early Paleozoic normal marine shales. *Geochimica et Cosmochimica Acta.* **53**, pp.1147-1152.

Raiswell, R., Benning, L.G., Tranter, M. and Tulaczyk, S. 2008. Bioavailable iron in the Southern Ocean: The significance of the iceberg conveyor belt. *Geochemical Transactions.* **9**(7).

Raiswell, R., Buckley, F., Berner, R.A. and Anderson, T.F. 1988. Degree of pyritization of iron as a paleoenvironmental indicator of bottom-water oxygenation. *Geoscience World.* **58**(5), pp.812-819.

Raiswell, R. and Canfield, D.E. 1996. Rates of reaction between silicate iron and dissolved sulfide in Peru Margin sediments. *Geochimica et Cosmochimica Acta.* **60**(15), pp.2777-2787.

Raiswell, R. and Canfield, D.E. 1998. Sources of iron for pyrite formation in marine sediments. *American Journal of Science.* **298**(3), pp.219-245.

Raiswell, R., Canfield, D.E. and Berner, R.A. 1994. A comparison of iron extraction methods for the determination of degree of pyritisation and the recognition of iron-limited pyrite formation. *Chemical Geology.* **111**(1-4), pp.101-110.

Raiswell, R., Hardisty, D.S., Lyons, T.W., Canfield, D.E., Owens, J.D., Planavsky, N.J., Poulton, S.W. and Reinhard, C.T. 2018. The iron paleoredox proxies: A guide to the pitfalls, problems and proper practice. *American Journal of Science.* **318**(5), pp.491-526.

Raiswell, R., Tranter, M., Benning, L.G., Siegert, M., De'ath, R., Huybrechts, P. and Payne, T. 2006. Contributions from glacially derived sediment to the global iron (oxyhydr)oxide cycle: Implications for iron delivery to the oceans. *Geochimica et Cosmochimica Acta.* **70**(11), pp.2765-2780.

Rasmussen, B., Bekker, A. and Fletcher, I.R. 2013. Correlation of Paleoproterozoic glaciations based on U–Pb zircon ages for tuff beds in the Transvaal and Huronian Supergroups. *Earth and Planetary Science Letters.* **382**, pp.173-180.

Rasmussen, B. and Buick, R. 1999. Redox state of the Archean atmosphere: Evidence from detrital heavy minerals in ca. 3250–2750 Ma sandstones from the Pilbara Craton, Australia. *Geology.* **27**(2), pp.115-118.

Rasmussen, B., Krapez, B., Muhling, J.R. and Suvorova, A. 2015. Precipitation of iron silicate nanoparticles in early Precambrian oceans marks Earth's first iron age. *Geology.* **43**(4), pp.303-306.

Redfield, A.C. 1958. The biological controls of chemical factors in the environment. *Am. Sci.* **46**, pp.205-221.

Reinhard, C.T., Planavsky, N.J., Gill, B.C., Ozaki, K., Robbins, L.J., Lyons, T.W., Fischer, W.W., Wang, C., Cole, D.B. and Konhauser, K.O. 2017. Evolution of the global phosphorus cycle. *Nature.* **541**(7637), pp.386-389.

Reinhard, C.T., Planavsky, N.J. and Lyons, T.W. 2013. Long-term sedimentary recycling of rare sulphur isotope anomalies. *Nature.* **497**(7447), pp.100-103.

Reinhard, C.T., Planavsky, N.J., Olson, S.L., Lyons, T.W. and Erwin, D.H. 2016. Earth's oxygen cycle and the evolution of animal life. *Proc Natl Acad Sci U S A.* **113**(32), pp.8933-8938.

Reinhard, C.T., Raiswell, R., Scott, C., Anbar, A.D. and Lyons, T.W. 2009. A Late Archean Sulfidic Sea Stimulated by Early Oxidative Weathering of the Continents. *Science.* **326**(5953), pp.713-716.

Robbins, L.J., Funk, S.P., Flynn, S.L., Warchola, T.J., Li, Z., Lalonde, S.V., Rostron, B.J., Smith, A.J.B., Beukes, N.J., de Kock, M.O., Heaman, L.M., Alessi, D.S. and Konhauser, K.O. 2019. Hydrogeological constraints on the formation of Palaeoproterozoic banded iron formations. *Nature Geoscience.* **12**(7), pp.558-563.

Robbins, L.J., Lalonde, S.V., Planavsky, N.J., Partin, C.A., Reinhard, C.T., Kendall, B., Scott, C., Hardisty, D.S., Gill, B.C., Alessi, D.S., Dupont, C.L., Saito, M.A., Crowe, S.A., Poulton, S.W., Bekker, A., Lyons, T.W. and Konhauser, K.O. 2016. Trace elements at the intersection of marine biological andgeochemical evolution. *Earth-Science Reviews.* **163**, pp.323-348.

Rosing, M.T. 1999. 13C-Depleted carbon microparticles in >3700Ma seafloor sedimentary rocks from West Greenland. *Science.* **283**, pp.674-676.

Rosing, M.T., Bird, D.K., Sleep, N.H. and Bjerrum, C.J. 2010. No climate paradox under the faint early Sun. *Nature.* **464**(7289), pp.744-747.

Rothe, M., Kleeberg, A. and Hupfer, M. 2016. The occurrence, identification and environmental relevance of vivianite in waterlogged soils and aquatic sediments. *Earth-Science Reviews.* **158**, pp.51-64.

Rothe, M., Kleeberg, A.B., Gruneberg, K., Friese, K., Perez-Mayo, M. and Hupfer, M. 2015. Sedimentary sulphur:iron ratio indicates vivianite occurrence: a study from two contrasting freshwater systems. *PLoS One.* **10**(11).

Rothe, M.T., Frederichs, M., Eder, A., Kleeberg, A. and Hupfer, M. 2014. Evidence for vivianite formation and its contribution to long-term phosphorus retention in a recent lake sediment: a novel analytical approach. *Biogeosciences.* **11**(18), pp.5169-5180.

Rouxel, O., Bekker, A. and Edwards, K.J. 2005. Iron isotopeconstraints on the Archean and Paleoproterozoic ocean redoxstate. *Science.* **307**, pp.1088-1091.

Ruttenberg, K.C. 1992. Development of a sequential extraction method for different forms of phosphorus in marine sediments. *Limnol. Oceanogr.* **37**(7), pp.1460-1482.

Ruttenberg, K.C. and Berner, R.A. 1993. Authigenic apatite formation and burial in sediments from non-upwelling, continental margin environments. *Geochimica et Cosmochimica Acta.* **57**(5), pp.991-1007.

Rye, R. and Holland, H.D. 1998. Paleosols and the evolution of atmospheric oxygen: A critical review. *American Journal of Science.* **298**, pp.621-672.

Ryther, J. H. and Dustan, W. M. 1971. Nitrogen, phosphorus, and eutrophication in the coastal marine environment. *Science*. **171**(3975), pp.1008-1013

Sagan, C. and Mullen, G. 1972. Earth and Mars: Evolution of Atmospheres and Surface Temperatures. *Science.* **177**(4043), pp.52-56.

Sahoo, S.K., Planavsky, N.J., Jiang, G., Kendall, B., Owens, J.D., Wang, X., Shi, X., Anbar, A.D. and Lyons, T.W. 2016. Oceanic oxygenation events in the anoxic Ediacaran ocean. *Geobiology.* **14**(5), pp.457-468.

Sahoo, S.K., Planavsky, N.J., Kendall, B., Wang, X., Shi, X., Scott, C., Anbar, A.D., Lyons, T.W. and Jiang, G. 2012. Ocean oxygenation in the wake of the Marinoan glaciation. *Nature.* **489**(7417), pp.546-549.

Saltzman, M. R. 2005. Phosphorus, nitrogen, and the redox evolution of the Paleozoic oceans. *Geology*. **33**(7), pp.573-576

Sarmiento, J.L. and Gruber, N. 2006. Ocean Biogeochemical Dynamics. [Online].

Sarmiento, J.L. and Toggweiler, J.R. 1984. A new model for the role of the oceans in determining atmospheric P CO2. *Nature.* **308**, pp.621-624.

Schidlowski, M., Eichmann, R. and Junge, C.E. 1976. Carbon isotope geochemistry of the Precambrian Lomagundi carbonate province, Rhodesia. *Geochimica et Cosmochimica Acta.* **40**(4), pp.449-455.

Schidlowski, M., Hayes, J. M. and Kaplan, I. R. 1983. Isotopic inferences of ancient biochemistries: carbon, sulfur, hydrogen, and nitrogen. Earth's Earliest Biosphere. Its origin and evolution, Princeton University Press, Princeton, pp. 149-186.

Schlanger, S.O. and Jenkyns, H.C. 1976. Cretaceous Oceanic Anoxic Events: Causes and consequences. *Geologie en Mijnbouw.* **55**(3).

Schröder, S. 2006. Stratigraphic and geochemical framework of the Agouron drill cores, Transvaal Supergroup (Neoarchean-Paleoproterozoic, South Africa). *South African Journal of Geology.* **109**(1-2), pp.23-54.

Schröder, S., Bedorf, D., Beukes, N.J. and Gutzmer, J. 2011. From BIF to red beds: Sedimentology and sequence stratigraphy of the Paleoproterozoic Koegas Subgroup (South Africa). *Sedimentary Geology.* **236**(1-2), pp.25-44.

Schulz, H.N. and Schulz, H.D. 2005. Large sulfur bacteria and the formation of phosphorite. *Science.* **307**(5708), pp.416-418.

Schwartzman, D.W. 2015. The Case for a Hot Archean Climate and its Implications to the History of the Biosphere. *arXiv.*

Scott, C., Lyons, T.W., Bekker, A., Shen, Y., Poulton, S.W., Chu, X. and Anbar, A.D. 2008. Tracing the stepwise oxygenation of the Proterozoic ocean. *Nature.* **452**(7186), pp.456-459.

Scott, C.T., Bekker, A., Reinhard, C.T., Schnetger, B., Krapez, B., Rumble, D. and Lyons, T.W. 2011. Late Archean euxinic conditions before the rise of atmospheric oxygen. *Geology.* **39**(2), pp.119-122.

Sharp, Z. 2017. *Principles of Stable Isotope Geochemistry, 2nd Edition.*

Shields, G.A. and Mills, B.J.W. 2017. Tectonic controls on the long-term carbon isotope mass balance. *PNAS.* **114**(17), pp.4318-4323.

Simms, M.J. 2004. British Lower Jurassic Stratigraphy: an introduction. **30**, pp.3-45.

Simonson, B.M. 2003. Origin and evolution of large Precambrian iron formations. *Geological Society of America Special Paper.* **370**, pp.231-244.

Sleep, N.H. 2010. The Hadean-Archaean Environment. *Cold Spring Harbor Perspectives in Biology.* **2**(6).

Slomp, C.P., Epping, E.H.G., Helder, W. and Raaphorst, W.V. 1996. A key role for iron-bound phosphorus in authigenic apatite formation in North Atlantic continental platform sediments. *Journal of Marine Research.* **54**(6), pp.1179-1205.

Slomp, C.P., Thomson, J. and De Lange, G.J. 2002. Enhanced regeneration of phosphorus during formation of the most recent eastern Mediterranean sapropel (S1). *Geochimica et Cosmochimica Acta.* **66**(7), pp.1171-1184.

Slomp, C.P. and Van Cappellen, P. 2007. The global marine phosphorus cycle: sensitivity to oceanic circulation. *Biogeosciences.* **4**, pp.155-171.

Sperling, E.A., Halverson, G.P., Knoll, A.H., Macdonald, F.A. and Johnston, D.T. 2013. A basin redox transect at the dawn of animal life. *Earth and Planetary Science Letters.* **371-372**, pp.143-155.

Sperling, E.A., Wolock, C.J., Morgon, A.S., Gill, B.C., Kunzmann, M., Halverson, G.P., Macdonald, F.A., Knoll, A.H. and Johnston, D.T. 2015. Statistical analysis of iron geochemical data suggests limited late Proterozoic oxygenation. *Nature.* **523**, pp.451-454.

Stookey, L.L. 1970. Ferrozine---a new spectrophotometric reagent for iron. *Analytical Chemistry.* **42**(7), pp.779-781.

Strickland, J.D.H. and Parsons, T.R. 1972. A practical handbook of seawater analysis. *(2nd edition), Fisheries Research Board of Canada, Ottawa, Bulletin.* **167**, pp.45-64.

Stüeken, E. E., Kipp, M. A., Koehler, M. C. and Buick, R. 2016. The evolution of Earth's biogeochemical nitrogen cycle. Earth-Science Reviews. 160, pp. 220-239

Sturm, A., Fowle, D.A., Jones, C., Leslie, K., Nomosatryo, S., Henny, C., Canfield, D.E. and Crowe, S.A. 2019. Rates and pathways of CH4 oxidation in ferruginous Lake Matano, Indonesia. *Geobiology.* **17**(3).

Sumner, D.Y. and Grotzinger, J.P. 2004. Implications for Neoarchaeanocean chemistry from primary carbonate mineralogy of the Campbellrand-Malmani Platform, South Africa. *Sedimentology.* **51**, pp.1-27.

Sun, S., Konhauser, K.O., Kappler, A. and Li, Y.-L. 2015. Primary hematite in Neoarchean to Paleoproterozoic oceans. *Geological Society of America Bulletin.* **127**(5-6), pp.850-861.

Tajika, E. and Harada, M. 2019. Great Oxidation Event and Snowball Earth. *Astrobiology.*

Taylor, S.R. and McLennan, S.M. 1985. The Continental Crust: Its composition and evolution.

Thomazo, C., Ader, M. & Philpott, P. Extreme 15N-enrichments in 2.72-Gyr old sediments: evidence for a turning point in the nitrogen cycle. *Geobiology* **9**, pp.107–120

Thompson, J., Poulton, S.W., Guilbaud, R., Doyle, K.A., Reid, S. and Krom, M.D. 2019. Development of a modified SEDEX phosphorus speciation method for ancient rocks and modern iron-rich sediments. *Chemical Geology.* **524**, pp.383-393.

Tissot, F.L.H., Chen, C., Go, B.M., Naziemiec, M., Healy, G., Bekker, A. and Dauphas, N. 2018. Controls of eustasy and diagenesis on the 238U/235U of carbonates and evolution of the seawater 234U/238U during the last 1.4 Myr. *Geochimica et Cosmochimica Acta.* **242**, pp.233-265.

Tissot, F.L.H. and Dauphas, N. 2015. Uranium isotopic compositions of the crust and ocean:Age corrections, U budget and global extent of modern anoxia. *Geochimica et Cosmochimica Acta.* **167**, pp.113-143.

Tostevin, R., Clarkson, M.O., Gangl, S., Shields, G.A., Wood, R., Bowyer, F., Penny, A. and Stirling, C.H. 2019. Uranium isotope evidence for an expansion of anoxia in terminal Ediacaran oceans. *Earth and Planetary Science Letters.* **506**, pp.104-112.

Tostevin, R., Wood, R.A., Shields, G.A., Poulton, S.W., Guilbaud, R., Bowyer, F., Penny, A.M., He, T., Curtis, A., Hoffmann, K.H. and Clarkson, M.O. 2016. Low-oxygen waters limited habitable space for early animals. *Nat Commun.* **7**, p12818.

Trendall, A.F., Compston, W., Williams, I.S., Armstrong, R.A., Arndt, N.T., McNaughton, N.J., Nelson, D.R., Barley, M.E., Beukes, N.J., de Laeter, J.R., Retief, E.A. and Thorne, A.M. 1990. Precise zircon U□Pb chronological comparison of the volcano-sedimentary sequences of the Kaapvaal and Pilbara cratons between about 3.1 and 2.4 Ga. *Third International Archaean Symposium.* pp.81-83.

Tribovillard, N., Algeo, T.J., Lyons, T.W. and Riboulleau, A. 2006. Trace metals as paleoredox and paleoproductivity proxies: An update. *Chemical Geology.* **232**, pp.12-32.

Tsandev, I. and Slomp, C.P. 2009. Modelling phosphorus cycling and carbon burial during Cretaceous Oceanic Anoxic Events. *Earth and Planetary Science Letters.* **286**, pp.71-79.

Tsandev, I., Slomp, C.P. and Van Cappellen, P. 2008. Glacial-interglacial variations in marine phosphorus cycling: Implications for ocean productivity. *Global Biogeochemical Cycles.* **22**.

Tyrrell, T. 1999. The relative influences of nitrogen and phosphorus on oceanic primary production. *Nature.* **400**, pp.525-531.

Van Cappellen, P. and Ingall, E.D. 1994. Benthic phosphorus regeneration, net primary production, and ocean anoxia: A model of the coupled marine biogeochemical cycles of carbon and phosphorus. *Paleoceanography.* **9**(5), pp.677-692.

Van Cappellen, P. and Ingall, E.D. 1996. Redox Stabilization of the Atmosphere and Oceans by Phosphorus-Limited Marine Productivity. *Science.* **271**.

Warke, M. R., Di Rocco, T., Zerkle, A. L., Lepland, A., Prace, A. R., Martin, A. P., ueno, Y., Condon, D. J. and Claire, M. W. 2020. The Great Oxidation Event preceded a Paleoproterozoic "snowball Earth". *PNAS.*

Wallace, M.W., Hood, A.v., Shuster, A., Greig, A., Planavsky, N.J. and Reed, C.P. 2017. Oxygenation history of the Neoproterozoic to early Phanerozoic and the rise of land plants. *Earth and Planetary Science Letters.* **466**, pp.12-19.

Wallmann, K. 2003. Feedbacks between oceanic redox states and marine productivity: A model perspective focused on benthic phosphorus cycling. *Global Biogeochemical Cycles.* **17**(3), pp.n/a-n/a.

Wang, D., Ling, H.F., Struck, U., Zhu, X.-K., Zhu, M., He, T., Yang, B., Gamper, A. and Shields, G.A. 2018. Coupling of ocean redox and animal evolution during the Ediacaran-Cambrian transition. *Nature Communications.* **9**(2575).

Watson, A.J., Bakker, D.C.E., Ridgwell, A., Boyd, P.W. and Law, C.S. 2000. Effect of iron supply on Southern Ocean CO 2 uptake and implications for glacial atmospheric CO 2. *Nature.* **407**, pp.730-733.

Watson, A.J., Lenton, T.M. and Mills, B.J.W. 2017. Ocean deoxygenation, the global phosphorus cycle and the possibility of human-caused large-scale ocean anoxia. *Philosophical Transactions of the Royal Society A: Mathematical, Physical and Engineering Sciences.* **375**(2102).

Westermann, S., Stein, M., Matera, V., Fiet, N., Fleitmann, D., Adatte, T. and Föllmi, K.B. 2013. Rapid changes in the redox conditions of the western Tethys Ocean during the early Aptian oceanic anoxic event. *Geochimica et Cosmochimica Acta.* **121**, pp.467-486.

Weyer, S., Anbar, A.D., Gerdes, A., Gordon, G.W., Algeo, T.J. and Boyle, E.A. 2008. Natural fractionation of 238U/235U. *Geochimica et Cosmochimica Acta.* **72**(2), pp.345-359.

Wignall, P.B. and Newton, R.J. 1998. Pyrite framboid diameter as a measure of oxygen deficiency in ancient mudrocks. *American Journal of Science.* **298**, pp.537-552.

Wignall, P.B., Newton, R.J. and Little, C.T.S. 2005. The timing of paleoenvironmental change and cause-and-effect relationships during the Early Jurassic mass extinction in Europe. *American Journal of Science.* **305**(10).

Xiong, Y., Guilbaud, R., Peacock, C.L., Cox, R.P., Canfield, D.E., Krom, M.D. and Poulton, S.W. 2019. Phosphorus cycling in Lake Cadagno, Switzerland: A low sulfate euxinic ocean analogue.

Yang, J., Junium, C. K., Grassineau, N. V., Nisbet, E. G., Izon, G., Mettam., C., Martin, A. and Zerkle, A. L. 2019. Ammonium availability in the Late Archaean nitrogen cycle. *Nature Geoscience*. **12**, pp. 553-557.

Ying, J.F., Zhou, X.H., Su, B.X. and Tang, Y.J. 2011. Continental growth and secular evolution: Constraints from U-Pb ages and Hf isotope of detrital zircons in Proterozoic Jixian sedimentary section (1.8-0.8Ga), North China Craton. *Precambrian Research.* **189**(3), pp.229-238.

Zahnle, K., Arndt, N.T., Cockell, C.S., Halliday, A., Nisbet, E.G., Selsis, F. and Sleep, N.H. 2007. Emergence of a habitable planet. *Space Science Reviews.* **129**, pp.35-78.

Zahnle, K., Catling, D.C. and Claire, M.W. 2013. The rise of oxygen and the hydrogen hourglass. *Chemical Geology.* **362**, pp.26-34.

Zahnle, K., Claire, M.W. and Catling, D.C. 2006. The loss of mass-independent fractionation in sulfur due to a Palaeoproterozoic collapse of atmospheric methane. *Geobiology.* **4**(4).

Zegeye, A., Bonneville, S., Benning, L.G., Sturm, A., Fowle, D.A., Jones, C., Canfield, D.E., Ruby, C., MacLean, L.C., Nomosatryo, S., Crowe, S.A. and Poulton, S.W. 2012. Green rust formation controls nutrient availability in a ferruginous water column. *Geology.* **40**(7), pp.599-602.

Zerkle, A. L., House, C. H., Cox, R. P. and Canfield, D. E. 2006. Metal limitation of cyanobacterial N2 fixation and implications for the Precambrian nitrogen cycle. *Geobiology*. **4**(4)

Zerkle, A.L., Claire, M.W., Domagal-Goldman, S.D., Farquhar, J. and Poulton, S.W. 2012a. A bistable organic-rich atmosphere on the Neoarchaean Earth. *Nature Geoscience.* **5**(5), pp.359-363.

Zerkle, A.L., Claire, M.W., Domagal-Goldman, S.D., Farquhar, J. and Poulton, S.W. 2012b. A bistable organic-rich atmosphere on the Neoarchaean Earth. *Nature Geosci*. **5**(5), pp.359-363.

Zerkle, A.L., Poulton, S.W., Newton, R.J., Mettam, C., Claire, M.W., Bekker, A. and Junium, C.K. 2017. Onset of the aerobic nitrogen cycle during the Great Oxidation Event. *Nature*. **542**(7642), pp.465-467.

Zhao, M., Reinhard, C. T., Planavsky, N. 2018. Terrestrial methane fluxes and Proterozoic climate. *Geology*, **46**(2). pp. 139-142.

Zhang, S., Wang, X., Wang, H., Bjerrum, C.J., Hammarlund, E.U., Costa, M.M., Connelly, J.N., Zhang, B., Su, J. and Canfield, D.E. 2016. Sufficient oxygen for animal respiration 1,400 million years ago. *Proc Natl Acad Sci U S A.* **113**(7), pp.1731-1736.

Zhang, S. Wang, X., Wang, H., Hammarlund, E. U., Su, J., Wang, Y. Canfield, D. E. 2017. The oxic degredation of sedimentary organic matter 1400 Ma constrains atmospheric oxygen levels. *Biogeosciences*, **14**, pp. 2133-2149

Zhang, S., Wang, X., Wang, H., Bjerrum, C. J., Hammarlund, E. U., Haxen, E. R., Wen, H., Ye, Y. and Canfield, D. E. 2019. Paleoenvironmental proxies and what the Xiamaling Formation tells us about the mid-Proterozoic ocean. *Geobiology*.

Model Appendix from Alcott et al., 2019

Table 10.1: Present day reservoirs with the corresponding flux equations. Present day steady-state values and fluxes are presented below.

Reservoir	Eq No.	Label	Initial Size (moles)	Differential Equation	Source
Proximal Water	1	W_P	$36x10^{12}$	$River_W - circ_{PD}$	[1]
Distal Water	2	W_D	$3600x10^{12}$	$circ_{PD} + circ_{DPD} - circ_{DS}$	[1]
Surface Water	3	W_S	$4{,}983x10^{13}$	$circ_{DPS} + circ_{DS} - circ_{SDP} - Evap$	[1]
Deep Ocean Water	4	W_{DP}	$1.3x10^{18}$	$circ_{SDP} - circ_{DPS} - circ_{DPD}$	[1]
Proximal Carbon	5	C_P	$4.5x10^{12}$	$PP_P - POCmin_P - POCbur_P - xp_{PD}$	[1]
Distal Carbon	6	C_D	$243x10^{12}$	$xp_{PD} + PP_D - POCbur_D - POCmin_D - xp_{DS}$	[1]
Surface Carbon	7	C_S	$3{,}816x10^{12}$	$xp_{DS} + PP_S - POCmin_S - xp_{SDP}$	[1]
Deep Ocean Carbon	8	C_{DP}	$5.6x10^{16}$	$xp_{SD} - RespPOC - POCbur_{DP}$	[1]
Proximal Oxygen	9	O_P	$4.5x10^{12}$	$O_{P_0} \cdot \boldsymbol{O_A}$	[1]

Distal Oxygen	10	O_D	$243x10^{12}$	$O_{D_0} \cdot \boldsymbol{O_A}$	[1]
Surface Oxygen	11	O_S	$1.615x10^{16}$	$O_{S_O} \cdot \boldsymbol{O_A}$	[1]
Deep Ocean Oxygen	12	O_{DP}	$2.21x10^{17}$	$O_{SDP} - OResp - O_{DPS} - O_{DPD}$	[1]
Atmosphere Oxygen	13	O_A	$3.7x10^{19}$	$POCburT - AtmosW - genred$	[2]
Proximal SRP	14	P_P	$9.7x10^{9}$	$W_P - PPP_P + POPmin_P - PFe_P - Pauth_P - SRP_{PD}$	[1]
Distal SRP	15	P_D	$5x10^{12}$	$SRP_{PD} - PPP_D + POPmin_D - PFe_D - Pauth_D - SRP_{DS} + SRP_{DPD}$	[1]
Surface SRP	16	P_S	$47x10^{12}$	$SRP_{DS} - PPP_S + POPmin_S - SRP_{SDP} + SRP_{DPS}$	[1]
Deep Ocean SRP	17	P_{DP}	$2{,}790x10^{12}$	$SRP_{SDP} + POPmin_{DP} - PFe_P - Pauth_{DP} - SRP_{DPS} - SRP_{DPD}$	[1]
Proximal POP	18	OP_P	$4.3x10^{10}$	$PPP_P - POPmin_P - POPbur_P - POP_{PD}$	[1]
Distal POP	19	OP_D	$2.3x10^{12}$	$POP_{PD} + PPP_D - POPmin_D - POPbur_D - POP_{DS}$	[1]
Surface POP	20	OP_S	$36x10^{12}$	$POP_{DS} + PPP_S - POPmin_S - POP_{SDP}$	[1]
Deep Ocean POP	21	OP_{DP}	$530x10^{12}$	$POP_{SDP} - POPmin_{DP} - POPbur_{DP}$	[1]

Table 10.2: Present day flux values and corresponding equations.

Flux	Eq No.	Label	Initial flux (moles/yr)	Equation	Source
River input	22	$River_W$	$37x10^{12}$	$constant$	[1]
Proximal-Distal water	23	$circ_{PD}$	$37x10^{12}$	$constant$	[1]
Low latitude upwelling water	24	$circ_{DPD}$	$3.78x10^{14}$	$kDpD \cdot W_{DP}$	[1]
Distal-Surface ocean water	25	$circ_{DS}$	$4.15x10^{14}$	$circ_{PD} + circ_{DPD}$	[1]
High latitude upwelling water	26	$circ_{DPS}$	$3.78x10^{15}$	$kDpS \cdot W_{DP}$	[1]
High latitude downwelling water	27	$circ_{SDP}$	$4.158x10^{15}$	$kSDp \cdot W_S$	[1]
Evaporation of surface water	28	$Evap$	$37x10^{12}$	$River_W$	[1]
Proximal Primary Production OC	29	PP_P	$3.975x10^{13}$	$kPP_P \cdot \boldsymbol{P_P} \cdot RedCP$	[1]
Proximal OC mineralisation	30	$POCmin_P$	$3.277x10^{13}$	$kcmin_P \cdot \boldsymbol{C_P}$	[1]

Proximal OC burial	31	$POCbur_P$	2.3x10^{12}	$kcbur_P \cdot PP_P$	[1]
Proximal-Distal export prod.	32	xp_{PD}	4.685x10^{12}	$POP_{PD} \cdot RedCP$	[1]
Distal Primary Production OC	33	PP_D	5.6x10^{14}	$kPP_D \cdot \boldsymbol{P_D} \cdot RedCP$	[1]
Distal OC burial	34	$POCbur_D$	1.7x10^{12}	$kcbur_D \cdot (xp_{PD} + PP_D)$	[1]
Distal OC mineralisation	35	$POCmin_D$	5.349x10^{14}	$kcmin_D \cdot \boldsymbol{C_D}$	[1]
Distal-Surface export prod.	36	xp_{DS}	2.811x10^{13}	$POP_{DS} \cdot RedCP$	[1]
Surface Ocean Primary Production	37	PP_S	3.869x10^{15}	$kPP_S \cdot \boldsymbol{P_S} \cdot RedCP$	[1]*
Surface OC mineralisation	38	$POCmin_S$	3.404x10^{15}	$kcmin_S \cdot \boldsymbol{C_S}$	[1]*
Surface-Deep export prod.	39	xp_{SDP}	4.931x10^{14}	$kxp_{SDP} \cdot (xp_{DS} + PP_S)$	[1]*
OC Respiration	40	$RespPOC$	4.921x10^{14}	$kResp \cdot \boldsymbol{C_{DP}}$	[1]*
Deep Ocean OC burial	41	$POCbur_{DP}$	1 x10^{12}	$POPburd_{DP} \cdot \frac{(CP_{anoxic} \cdot CP_{oxic})}{([\boldsymbol{O_{DP}}] \cdot CP_{anoxic}) + ((1 - [\boldsymbol{O_{DP}}]) \cdot CP_{oxic})}$	[1]*
Surface-Deep oxygen downwelling	42	O_{SDP}	1.347x10^{15}	$circ_{SDP} \cdot [O_s]$	[1]*
Oxygen Respiration	43	$OResp$	6.403x10^{14}	$kResp \cdot (\frac{\boldsymbol{C_{DP}}}{redCO}) \cdot (\frac{O_{DP}}{(kmO_2 + O_{DP})})$	[1]*
Deep-Surface oxygen upwelling	44	O_{DPS}	6.426x10^{14}	$circ_{DPS} \cdot [O_{DP}]$	[1]
Deep-Distal oxygen upwelling	45	O_{DPD}	6.426x10^{13}	$circ_{DPD} \cdot [O_{DP}]$	[1]
Total OC burial	46	$POCburT$	5x10^{12}	$POCbur_P + POCbur_D + POCbur_{DP}$	[4]
Oxidative Weathering	47	$AtmosW$	5x10^{12}	$kAtmosW \cdot (\sqrt{\boldsymbol{O_A}})$	[4]
Oxygen consumption via reduced gases	48	$genred$	0	Varied depending on model run	[4]
Riverine P input	49	W_P	9x10^{10}	Varied depending on model run	[1]
Proximal Primary Production (P)	50	PPP_P	3.75x10^{11}	$\frac{PP_P}{RedCP}$	[1]
Proximal POP	51	$POPmin_P$	3.216x10^{11}	$\boldsymbol{OP_P} \cdot kpmin_P$	[4]

mineralisation					
Proximal Iron bound P burial	52	PFe_P	8.973x10^{9}	$kFeP_P \cdot P_P$	[4]
Proximal Authigenic P burial	53	$Pauth_P$	1.768x10^{10}	$kpmin_P \cdot OP_P \cdot kCaP_P$	[4]
Proximal-Distal SRP transport	54	SRP_{PD}	9.969x10^{9}	$circ_{PD} \cdot [P_P]$	[4]
Distal Primary Production (P)	55	PPP_D	5.283x10^{12}	$\frac{PP_D}{RedCP}$	[1]
Distal POP mineralisation	56	$POPmin_D$	5.055x10^{12}	$\boldsymbol{OP_P} \cdot kpmin_D$	[4]
Distal Iron bound P burial	57	PFe_D	6.762x10^{9}	$kFeP_D \cdot P_D \cdot (1 - fanoxic_{dist})$	[3]
Distal Authigenic P burial	58	$Pauth_D$	1.032x10^{10}	$kCaP_D \cdot \boldsymbol{O_D} \cdot (1 - fanoxic_{dist})$	[3]
Distal-Surface SRP transport	59	SRP_{DS}	5.764x10^{11}	$circ_{DS} \cdot [P_D]$	[1]
Deep-Distal SRP transport	60	SRP_{DPD}	8.113x10^{11}	$circ_{DPD} \cdot [P_{DP}]$	[1]
Surface Ocean Primary Production (P)	61	PPP_S	3.650x10^{13}	$\frac{PP_S}{RedCP}$	[1]*
Surface POP mineralisation	62	$POPmin_S$	3.173x10^{13}	$OP_S \cdot kpmin_S$	[4]
Surface-Deep SRP transport	63	SRP_{SDP}	3.922x10^{12}	$circ_{SDP} \cdot [P_S]$	[1]
Deep-Surface SRP transport	64	SRP_{DPS}	8.113x10^{12}	$circ_{DPS} \cdot [P_{DP}]$	[1]
Deep POP mineralisation	65	$POPmin_{DP}$	5.028x10^{12}	$OP_{DP} \cdot kpmin_{DP}$	[4]
Deep Iron bound P burial	66	PFe_{DP}	6.75x10^{9}	$kFeP_{DP} \cdot [\boldsymbol{O_{DP}}]$	[3]
Deep Authigenic P burial	67	$Pauth_{DP}$	1.953x10^{10}	$kCaP_{DP} \cdot POPmin_{DP} \cdot (0.75 + (0.25 \cdot [\boldsymbol{O_{DP}}]))$	[3]
C:P ratio for respective box	68	$CPratio$	250 (oxic) 1100 (anoxic)	$\frac{1}{\left(\frac{1 - fanoxic_x}{CP_{oxic}}\right) + \left(\frac{fanoxic_x}{CP_{anoxic}}\right)}$	[1]
Proximal POP burial	69	$POPbur_P$	9.182x10^{9}	$kcbur_P \cdot \frac{PP_P}{CPratio_{proximal}}$	[4]

Proximal-Distal POP transport	70	POP_{PD}	4.419x10^{10}	$circ_{PD} \cdot [OP_P]$	[4]
Distal POP burial	71	$POPbur_D$	6.800x10^{9}	$kPOPbur_d \cdot \frac{PP_D + xp_{PD}}{CPratio_{distal}}$	[4]
Distal-Surface POP transport	72	POP_{DS}	2.651x10^{11}	$circ_{DS} \cdot [OP_D]$	[4]
Surface-Deep POP transport	73	POP_{SDP}	5.032x10^{12}	$kPOP_{SDP} \cdot (\frac{PP_S + xp_{DS}}{RedCP})$	[4]
Deep POP burial	74	$POPburd_D$	4x10^{9}	$kPOPbur_{DP} \cdot \left(\frac{xp_{SDP}}{CP_{oxic}}\right) \cdot (0.75 + (0.25 * [\boldsymbol{O_{DP}}]))$	[3]

OC-Organic Carbon, SRP-Soluble Reactive Phosphorous, POP-Particulate Organic Phosphorus

*Flux equation is the same as citation, however present day value was altered by Alcott et al. (2019)

[1] – Slomp and Van Cappellen (2007); [2] – Bergman et al. (2004); [3] – Tsandev and Slomp (2009); [4] – Alcott et al. (2019)

Table 10.3: Parameters and constants.

Parameter/ Constant	Constant	Value	Reference
Coastal Upwelling	*kDpD*	2.908x10^{-4}	Slomp and Van Cappellen, 2007
Open Ocean Upwelling	*kDpS*	0.0029	Slomp and Van Cappellen, 2007
Open Ocean Downwelling	*kSDp*	0.0834	Slomp and Van Cappellen, 2007
Proximal shelf primary production	kPP_P	3.75x10^{11}	Slomp and Van Cappellen, 2007
Proximal organic carbon remineralisation	$kcmin_P$	3.277x10^{13}	This work
Proximal organic carbon burial	$kcbur_P$	0.0579	Slomp and Van Cappellen, 2007
Distal shelf primary production	kPP_D	5.283x10^{12}	Slomp and Van Cappellen, 2007
Distal organic carbon burial	$kcbur_D$	0.003	Slomp and Van Cappellen, 2007
Distal organic carbon remineralisation	$kcmin_D$	5.349x10^{14}	This work
Surface ocean primary production	kPP_S	3.650x10^{13}	Slomp and Van Cappellen, 2007
Surface organic carbon remineralisation	$kcmin_S$	3.404x10^{15}	This work
Surface to Deep Ocean export production	kxp_{SDP}	0.1265	Slomp and Van Cappellen, 2007
Deep Ocean Respiration	*kResp*	4.921x10^{14}	Slomp and Van Cappellen, 2007
Deep ocean organic carbon burial	$kcbur_{DP}$	0.0019	Slomp and Van Cappellen, 2007

Monod constant for respiration	kmO_2	$1x10^{-4}$	Slomp and Van Cappellen, 2007
Oxidative Weathering	*kAtmosW*	$5x10^{12}$	Alcott et al., 2019
Carbon – Phosphorus Redfield ratio	*RedCP*	106	Slomp and Van Cappellen, 2007
Proximal Iron bound P burial	$kFeP_P$	0.925	Alcott et al., 2019
Proximal Authigenic P burial	$kCaP_P$	$1.279x10^{-12}$	Alcott et al., 2019
Distal Iron bound P burial	$kFeP_D$	0.0014	Alcott et al., 2019
Distal Authigenic P burial	$kCaP_D$	$1.035x10^{10}$	Alcott et al., 2019
Deep ocean Iron bound P burial	$kFeP_{DP}$	$6.75x10^{9}$	Alcott et al., 2019
Deep ocean Authigenic P burial	$kCaP_{DP}$	0.0039	Alcott et al., 2019
Distal Organic P burial	$kPOPbur_D$	0.003	Alcott et al., 2019
Surface to Deep Organic Phosphorus Export Production	$kPOP_{SDP}$	0.1369	Alcott et al., 2019
Deep Ocean Organic P burial	$kPOPbur_{DP}$	0.002	Alcott et al., 2019